The University Of Sheffield.

RF coils development and sequences optimisation for hyperpolarised ^{129}Xe MRI

Claudio Puddu

Section of Imaging
Division of Clinical Medicine
University of Sheffield
Sheffield, South Yorkshire, United Kingdom

A thesis submitted in partial fulfilment of the requirements for the degree of Doctor of Philosophy under supervision of Prof. Jim Wild and Rd. Madhwesha Rama Rao, PhD

March, 2024

The University of Sheffield

Acknowledgements

First, I would like to say a great thanks to my supervisor Jim Wild, for having accepted me to the University of Sheffield as a PhD student. I was glad to that believing him me and it was an honour to be his student. I am grateful for the scientific support that he gave me during all the PhD, but even more for his patience and comprehension.

I also want to give my gratitude to Madhwesha Rao, my second supervisor. I would like to sincerely thank him for all the time he had dedicated to me. He always tried to support me, to motivate me. I will never forget the precious lessons you taught to me; these will be very useful even outside academia.

I also would like to say thanks to Guilhem Collier, for his valuable help in several experiments, and the numerous discussions about MRI physics and sequence developments.

Olly and Ryan, you cannot imagine how much I appreciated the time you spent for me polarising gases, for your support and for the nice time we had in the lab.

Paul, Fung, Graham, Adam, thanks for all the suggestions that helped me to pursue this life journey called PhD. Thanks also for all the good times we spent together outside the university: playing, or watching football, at the pub or playing video games or pool.

Thanks to all the staff of the Academic Unit of Radiology, and especially Leanne always ready to find some scanner time and to fill these boring forms for me.

In the end, I would like to express my gratitude to all the members of POLARIS lab, to Jen for having filled all my SMF, to Alberto for his help to understand how to work with sharc (still not sure about that!), Martin, Laurie for all nice chat we had together. I do not want to forget (and never forget at all), the good time I had with every one of you after work at the pub, I really enjoyed this time and now I have become a huge fan of English beer!

Abstract

Chapter 1) MRI theory and Instrumentation

This chapter provides an overview of the fundamental physics of Nuclear Magnetic Resonance (NMR), as it pertains to Magnetic Resonance Imaging (MRI). It starts with a brief historical perspective of the development of MRI technology. The chapter then delves into the generation of the NMR signal, detailing the processes from nuclear spin polarisation to radio-frequency excitation, and concluding with signal detection. The latter part of the chapter is dedicated to the principle of MR imaging, with a description of the encoding process to localize the signal in space.

Chapter 2) RF coil theory

The second chapter of the thesis explores the theoretical foundations and practical development of RF coils. It starts with a detailed description of the Finite Element Method applied to the Maxwell equations. Then it will extensively cover the essential steps and concepts necessary to develop an RF coil, including Tuning, Matching, Quality factor. Following this will be shown the main differences between transmit and receive coil design and purpose. Finally, at the end, a quick introduction to Parallel imaging and the SENSE reconstruction method.

Chapter 3) Hyperpolarised ^{129}Xe MRI

The main features of Hyperpolarised MRI will be discussed in this chapter. Initially, there will be a brief introduction to Hyperpolarised gases and the physics of ^{129}Xe Hyperpolarisation. It will follow a description of the main sequences used for Hyperpolarised ^{129}Xe MR imaging, more specifically Spoiler Gradient Echo and Steady-State Free Precession. Finally, the chapter will describe the employment of ^{129}Xe as a contrast agent to image perfusion in the lungs, brain, and kidneys.

Chapter 4) Development of a whole-body setup for ^{129}Xe Hyperpolarised imaging

This section of the thesis focuses the development of a whole thorax RF setup for ^{129}Xe MR imaging. It will describe the development of the asymmetrical birdcage transmitter coil, construction, simulation, and testing on the workbench and the scanner.

Chapter 5) Development of a whole-body setup for ^{129}Xe Hyperpolarised imaging

Chapter 5 will show the results of the lungs imaging with the birdcage as a transceiver and then with the receiver array. It will conclude with demonstration of parallel imaging, with results of sequence simulation, reconstructions method and g-factor maps.

Chapter 6) Development of a six-channel array for dissolved phase hyperpolarised ^{129}Xe MR imaging in the brain at 3T

This last chapter involves the construction, testing and imaging of an RF coil setup for imaging of hyperpolarised ^{129}Xe in the brain. The transmitter coil was an 8-leg octagonal shaped birdcage, and the receiver coil was a 6-channel array built around a 3D printed helmet. An optimal coil array design was found through electromagnetic simulation for three different configurations. Subsequently, the birdcage and receiver array were constructed in the RF lab. The chapter concludes with brain perfusion imaging using the proposed RF coil design.

Publications and conference proceedings

Publications

Puddu, C., Rao, M., Xu, X., et al. *An asymmetrical whole-body birdcage RF coil without RF shield for hyperpolarized ^{129}Xe lung MR imaging at 1.5 T*. *Magn Reson Med*. 2021; 86: 3373– 3381. https://doi.org/10.1002/mrm.28915

Proceedings

Puddu, C., Rao M., Collier G., Maunder, A., Chang, H., F., Rodgers, O., Deppe, M., Xu,X., De Zanche, N., Robb, F., Wild, J.M., RF coil system for accelerated 129Xe hyperpolarised imaging, *Proceedings to ISMRM 2020, Online, 4098*

Puddu, C., Rao, M**.**, Rodgers, O., Maunder, A., Wild J.M. *6-channel RF array for hyperpolarized ^{129}Xe brain MRI at 3T, Proceedings to ISMRM 2020, Online, 4099*

Oral Presentation

Puddu,C., Rao,M., Maunder A., Xu X., De Zanche N., Robb, F., Wild J., A whole-body Transmit/Receive RF system for Hyperpolarised ^{129}Xe MRI, British Chapter of International Society of Magnetic Resonance in Medicine 2018

Additional papers

Chacon-Caldera, J., Maunder, A., Rao, M., Norquay, G., Rodgers O.I., Clemence M., **Puddu C.**, Shar, R.L., Wild J.M., ***Dissolved hyperpolarized xenon-129 MRI in human kidneys***. *Magn Reson Med*. 2020; 83: 262– 270. https://doi.org/10.1002/mrm.27923

Curreli N., Lodi M.B., Melis A., **Puddu C.**, Casu S., Fanti A., Djuric N., Retico A., Mazzarella G., *"Analysis of a Flexible Dual-Channel Octagonal Coil System for UHF MRI"* in *IEEE Access*, vol. 10, pp. 104589-104597, 2022, https://doi.org/10.1109/ACCESS.2022.3209676

Table of contents

Chapter 1: Introduction

MRI theory and instrumentation

This chapter will describe the basics of MRI physics, to give an overview of the phenomena behind an MRI experiment. Furthermore, an overview of the MRI scanner system is provided, with a description of the main components.

1.1 MRI origins

The physical phenomenon of Nuclear Magnetic Resonance (NMR), was discovered first by Isadoor Rabi [1] in 1937, and successively in 1945 Bloch [2], and Purcell [3] defined its physical appearance also in the condensed matter (i.e. paraffin and water). One year later, Bloch also formalized the mathematical equations to model the phenomena [4]. Until the '70s NMR was used mainly with the purpose of the study of material and molecules. It was in 1971 that, Raymond Damadian, a physician of the State University of New York, consider the approach to employ NMR to study human tissues. He discovered that tumorous cells in mice had longer T_1 and T_2 relaxation times, under the hypothesis that the cancerous cells contained more water [5]. In the following years, thanks to the improvement the cryogenics, he built the first whole-body superconductor magnet, and in 1974 he filed the patent for the first in vivo NMR apparatus. The machine, named FONAR (**F**ield f**O**cused **N**uclear m**A**gnetic **R**esonance **I**maging) was able to in 1977 to produce the first in-vivo MRI images using a sensitive point method [6]. In the same period, Paul Lauterbur proposed the employment of magnetic field gradients to localize the NMR signal from different locations using a rotating gradient field [7]. Applying a gradient field rotated by 45 degrees obtained four different signals which were back-projected to obtain a 2D image similar to a technique already used in Computer Tomography. This was the first employment of the magnetic field gradients, which is the basis of modern MR images acquisition. The usage of the gradient was successively refined by Peter Mansfield of the University of Nottingham in 1974, demonstrating how a linear gradient field could be used to localise NMR signal slice by slice [8]. Its experiments involved a stack of 1mm pieces of camphor placed into the magnet bore. Applying an RF pulse perpendicular to the stack, Mansfield was able to measure the signal from each different layer. Richard Ernst, in 1975,

invented 2D Fourier transforms to produce MRI imaging introducing the concept of frequency and phase encoding [9]. In 1980, two scientists of the University of Aberdeen, Edelstein and Hutchinson, employing the Ernst technique acquired a whole-body image in less than 5 minutes [10]. All these developments were fundamental to fastener the acquisition time of the scans and moving MRI from a clinical perspective. The first commercial clinical scanner was installed at the Royal Hammersmith Hospital in London while GE in 1984 was able to produce the first high field scanner (with a static magnet of 1.5T). MRI in the following years continued to gain interest and continued its development in the application of new techniques like fMRI (functional MRI) [11-12] and MRA (Magnetic Resonance Angiography) [13]. In 1994, Albert et al. reached an important milestone considering the purpose of the thesis, with the first experiments with ^{129}Xe for respiratory MR imaging [14]. Today, in the UK, in the period from April 2017 to March 2018 the number of MRI scans performed was more than 3.4 million with an increment of 24% considering the previous 5 years [15]. Thus, demonstrating that due to its continuous technological improvement (improved gradients, higher superconductor magnets, new RF coils technologies) Magnetic Resonance Imaging (MRI) has become one of the predominant clinical diagnostic methods.

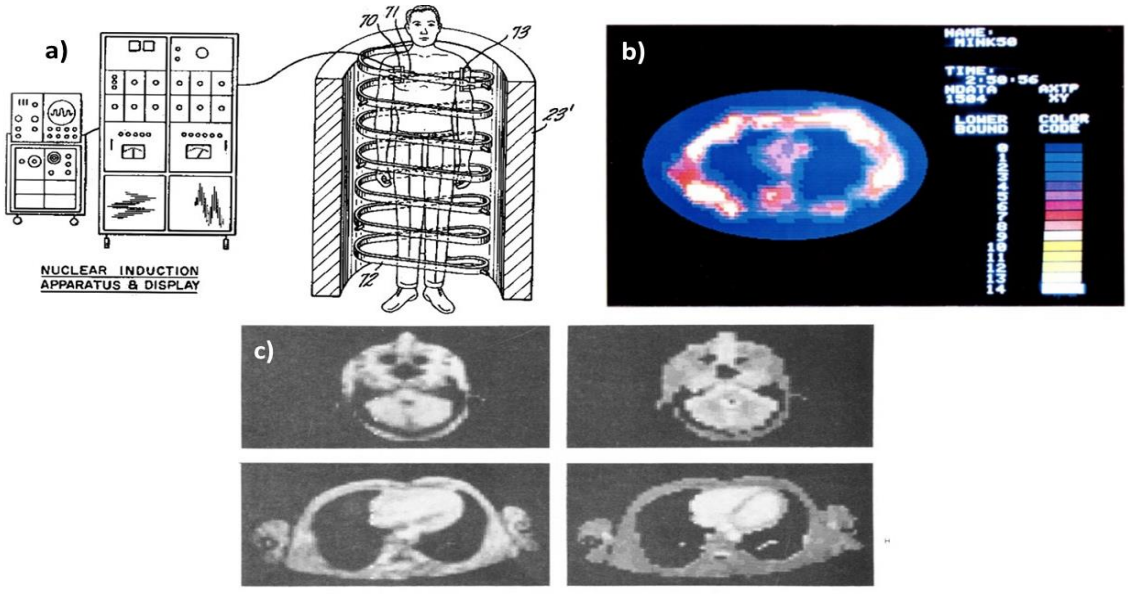

Figure 1: In a), there is the first MRI imaging apparatus filed by Damadian reproduced [16]***. Images b) shows the axial reconstruction of the signal (total scan time 5 hours). In c), one of the first images obtained by Eldestein and Hutchinson showing an axial slice of brain and thorax (Reproduced with permission from*** [10]***).***

1.2 Generation of NMR signal

1.2.1 Nuclear Spin and Polarisation

Magnetic resonance imaging is based on the physical principle of NMR (Nuclear Magnetic Resonance) which pertains to the nuclei of atoms. Nuclei are composed of protons and neutrons, and they have the property of spin, defined by a spin quantum number ($\vec{I}$). This property is governed by quantum mechanics and is an intrinsic physical property of each elementary particle. In MRI, the nuclei of interest such as ^{1}H, ^{3}He or ^{129}Xe have an odd number of protons and neutrons, having a total non-zero quantum spin ($\vec{I} \geq 1/2$). Since these nuclei are charged particles, they have a nuclear magnetic dipole ($\vec{\mu}$) moment of a nuclear spin (Figure 2a) defined by:

$$\vec{\mu} = \gamma \hbar \vec{I} \tag{1}$$

$\hbar$ is the reduced Plank constant ($h/2\pi$), and γ is the gyromagnetic ratio, specific for each nucleus defined as:

$$\gamma = {}^{q}/_{2m} \tag{2}$$

where q and m are defined respectively as the charge and mass of the nucleus under spin motion.

Table 1: Most common nuclei imaged in MR with spin values and Gyromagnetic Ratio.

Nuclei	Spin	Gyromagnetic Ratio [MHz/T]
^{1}H	**1/2**	**42.58**
^{3}He	**-3/2**	**-32.434**
^{23}Na	**3/2**	**11.262**
^{19}F	**1/2**	**40.08**
^{129}Xe	**-1/2**	**-11.77**

Considering a nucleus of spin $\vec{I}$, there are ($2\vec{I}$+1) energy state associated, ranging from -$\vec{I}$ to $\vec{I}$. At the equilibrium, in absence of any static magnetic field applied, these values are degenerate. If a static magnetic field (B_0) is applied (conventionally along the z-axis, considering a generic Cartesian system of coordinates), considering a nucleus with quantum spin $\vec{I} = 1/2$ (i.e. proton), the spin will have an orientation parallel ($\vec{I} = 1/2$) or

anti-parallel ($\vec{I} = -1/2$) to the direction of the static magnetic field, according to the Zeeman resonance theory. [17], [18]. These energy states correspond respectively to the lower and the higher energy state (Figure 2c). Under the influence of $\overrightarrow{B_0}$, the two degenerate energy states is lifted, resulting in a potential energy difference ΔE proportional to the static magnetic field, as described by formula (3):

$$\Delta E = \gamma \hbar \overrightarrow{B_0} \tag{3}$$

Considering a sample that contains N nuclei, there is an excess of the population occupying the low-energy level, and the difference in population between the two levels is responsible for the generation of the NMR signal. The difference ΔN, according to the Boltzmann statistic, is given by the nuclei with different energy states:

$$\Delta N = N_p - N_a = \frac{N}{2}\left[\exp\left(\frac{\gamma \hbar B_0}{2k_b T}\right) - \exp\left(-\frac{\gamma \hbar B_0}{2k_b T}\right)\right] \sim \frac{N\gamma \hbar B_0}{2k_b T} \tag{4}$$

Where, k_b is the Boltzmann constant, and T is the temperature. The total bulk magnetisation M_0, for $\vec{I} = 1/2$, in a volume containing N nuclei, will be therefore given by:

$$M_0 = \frac{N\gamma^2 \hbar^2 B_0}{4k_b T} \tag{5}$$

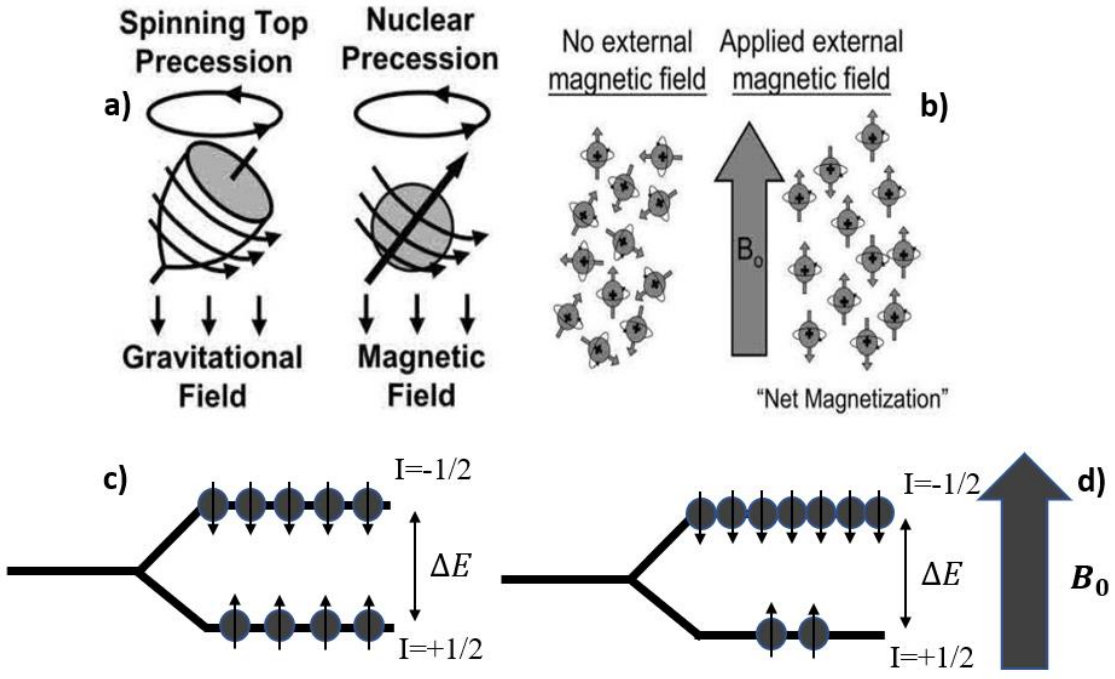

Figure 2: a)-b)Precession movement of the nuclei polarisation of the nuclei can be explained with an analogy: influenced by the static magnetic field and their intrinsic spin, the nuclei begin to rotate like a spinning top in the same direction of the static magnetic field. From [19]***, reproduced by permission. c) The Zeeman effect with the alignment of the nuclear spin with the two different energy levels, before and after the influence of B_0***

1.2.2 Excitation and rotational frame

A nuclear spin $\vec{\mu}$ under the influence of a static magnetic field $\overrightarrow{B_0}$ will have a torque given by:

$$\tau = \vec{\mu} \times \overrightarrow{B_0} \tag{6}$$

Combining equation 6 with equation 1 will defines the equation of spin motion:

$$d\mu/_{dt} = \gamma\vec{\mu} \times \overrightarrow{B_0} \tag{7}$$

the nuclei will undergo a processional movement with an angular frequency, known as the Larmor Frequency, defined by [20]:

$$\omega_0 = \gamma\overrightarrow{B_0} \tag{8}$$

The total magnetisation vector defines the change of macroscopic angular momentum $\vec{M}$, calculated as the sum of the magnetic moment per unit of volume:

$$d\vec{M}/_{dt} = \gamma\vec{M} \times \vec{B} \tag{9}$$

Equation 9 is defined in a rotating coordinate system ($x'y'z'$), rotating with a frequency ω, around the static laboratory frame of a coordinate (x, y, z):

$$d\vec{M}/_{dt} = \gamma\vec{M} \times \overrightarrow{B_{eff}} = \gamma\vec{M} \times [\overrightarrow{B_0} - \frac{\omega}{\gamma}] \tag{10}$$

Considering a $\overrightarrow{B_0}$ static field applied along the z-direction, if ω is equal to the Larmor frequency ω_0, according to equation 10, the terms $\overrightarrow{B_0}$ disappear. Therefore magnetisation $\vec{M}$ remains while is undergoing precession at the Larmor frequency. If a Radio Frequency (RF) field ($\overrightarrow{B_1}$) Larmor frequency ω_0, orthogonal to the direction of $\overrightarrow{B_0}$, is applied, the bulk magnetisation M_0 will be flipped onto the plane orthogonal to the direction of the static magnetic field. The angle α of the flip is known as flip angle or tip angle and is given by:

$$\alpha = \gamma \int_0^\tau B_1 \, d\tau \tag{11}$$

In which τ defines the period of the radio frequency pulse. Therefore, the total magnetic field is given by the sum of the static field $\overrightarrow{B_0}$ along the z-direction and by the rotating RF $\overrightarrow{B_1}$ field:

$$\vec{B} = \overrightarrow{B_1}(\cos(\omega t)\hat{x} - \sin(\omega t)\hat{y}) + \overrightarrow{B_0}\hat{z} \tag{12}$$

The rotating coordinate system is chosen so that the $\overrightarrow{B_1}$ field static along the x' axis. This configuration transform equation 12 into:

$$d\vec{M}/_{dt} = \gamma\vec{M} \times \overrightarrow{B_{eff}} = \gamma\vec{M} \times [\overrightarrow{B_0} - \frac{\omega}{\gamma} + \overrightarrow{B_1}\hat{x}] \quad (13)$$

The equation implies that the magnetisation occurs around both the direction of $\overrightarrow{B_0}$ and $\overrightarrow{B_1}$. If the rotation frame process at Larmor frequency ω_o, the magnetic field will be influenced only by $\overrightarrow{B_1}\hat{x}$, and the magnetisation will rotate solely around $\hat{x}$ with a frequency ω_1. However, if $\omega \neq \omega_o$, the system is off-resonance and the longitudinal field along $\hat{z}$ is not null during magnetisation process around $\overrightarrow{B_{eff}}$ with a frequency of ω_{eff}.

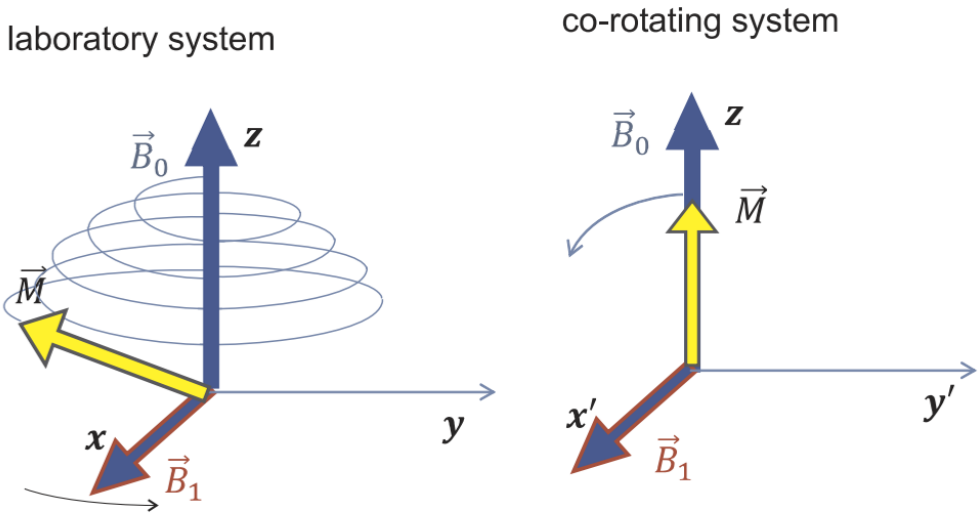

Figure 3: Evolution of the nuclear spin magnetisation in the presence of a longitudinal static field B_0, and transverse rotating field (a). In the laboratory frame the rotating frame, where a rotation about the *z*-axis is set to ω_0, the fields B_0 and B_1 are stationary, and the magnetisation $\vec{M}$ processes with frequency ω about B_1 (b). Reproduced from [21] **with permission**

1.2.3 Bloch equations and relaxation process

For a detailed explanation of the net magnetisation behaviour, we consider the Bloch equations. The Bloch equations are macroscopic equations that define the full magnetisation vector's movement and the laboratory frame and not of the single spin motion. At the equilibrium at t=0, we have M $\vec{M}$=$\vec{M}_0$=$(0,0,M_z)$. When is applied an orthogonal RF field defined as $B_1(t)$= $[B_1 cos\omega t, B_1 sin\omega t, B_0]$, the magnetisation is given by the vector product between B and M as along the three axes is defined as below:

$$\frac{dM_x}{dt} = \gamma(M_y B_0 - M_z B_1 sin\omega t) - \frac{M_x}{T_2} \quad (14)$$

$$\frac{dM_y}{dt} = \gamma(-M_x B_0 - M_z B_1 cos\omega t) - \frac{M_y}{T_2} \quad (15)$$

$$\frac{dM_z}{dt} = \gamma(M_x B_1 sin\omega t + M_y B_1 cos\omega t) - \frac{M_0 - M_z}{T_1} \quad (16)$$

Thus, it can be even written in matrix form:

$$\frac{d}{dt}\begin{bmatrix} M_x \\ M_y \\ M_z \end{bmatrix} = \begin{bmatrix} \frac{1}{T_2} & \gamma B_z & -\gamma B_1 sin\omega t \\ -\gamma B_z & -\frac{1}{T_2} & \gamma B_1 cos\omega t \\ \gamma B_1 sin\omega t & -\gamma B_1 cos\omega t & -\frac{1}{T_1} \end{bmatrix} \begin{bmatrix} M_x \\ M_y \\ M_z \end{bmatrix} + \begin{bmatrix} 0 \\ 0 \\ \frac{M_0}{T_1} \end{bmatrix} \quad (17)$$

After the shutoff of the transmitted RF transverse $\overrightarrow{B_1}$ field (RF pulse), the bulk magnetisation $\vec{M}$ starts to relax and to return to the equilibrium status through a process of relaxation. Under the influence of a static magnetic field $\overrightarrow{B_0}$, pointing in z-axis direction, magnetisation phenomena are regulated by the Bloch phenomenological equation, which includes the relaxation process as shown in equation 17. T_1 and T_2 are constant that define the relaxation time, related to the spin-lattice interaction between the molecules in the examined volume. Referring to equation 16, the change in magnetisation along the longitudinal z-axes, is governed by the T_1 relaxation time. More specifically, T_1 is the time that defines the spin-lattice relaxation. T_1 is related to the time of recovery of the magnetisation to thermal equilibrium, more precisely the time needed by the magnetisation to recover 63% of its value at equilibrium. The excited nuclei release the energy previously absorbed from the RF pulses to the other nuclei of the surrounding molecular structure. Consequently, all the energy absorbed is dispersed throughout the entire lattice, restoring the equilibrium state's magnetisation. Solving the differential equation 16, yields the longitudinal magnetisation M_z as a function of time:

$$M_z(t) = M_z(0)e^{-t/T_1} - M_0\left(1 - e^{-t/T_1}\right) \quad (18)$$

Considering the magnetisation in the transversal plane, after the shutoff of the B_1 field, the magnetisation is dominated by the T_2 relaxation time. Transverse relaxation is expressed as the T_2 relaxation (also known as spin-spin relaxation) and is associated to the decay of the bulk magnetisation vector due to nuclei dephasing. Following the cessation of the RF pulse, nuclei begin to lose phase coherence in the transverse plane due to the local inhomogeneity fields in the molecular structure. Specifically, T_2 is related to the time

required for transverse magnetisation to decrease by 37% of its initial values. Related to the T_2 decay is the T_2^*. T_2^*, is defined as the combined effect of T_2 with the contribution of the dephasing caused by static B_0 field inhomogeneity:

$$\frac{1}{T_2^*} = \frac{1}{T_2} + \frac{1}{T_2'} \tag{19}$$

Where $\frac{1}{T_2'}$ is the T_2^* component due to B_0 inhomogeneity. The magnetisation around the x and y plane is described by:

$$\frac{dM_x}{dt} = \omega_0 M_y - \frac{M_x}{T_2} \tag{20}$$

$$\frac{dM_y}{dt} = -\omega_0 M_x - \frac{M_y}{T_2} \tag{21}$$

The solution of the

$$M_x(t) = e^{-t/T_2}\gamma(M_x(0)cos\omega_0 t + M_y(0)sin\omega_0 t) \tag{22}$$

$$M_y(t) = e^{-t/T_2}\gamma(M_y(0)cos\omega_0 t - M_x(0)sin\omega_0 t) \tag{23}$$

Table 2: T1 and T2 times of ^{1}H for different tissues at 1.5T

Tissues	T_1	T_2
Skeletal Muscle	**880 ms**	**45 ms**
Lungs	**820 ms**	**139 ms**
Myocardium	**880 ms**	**75 ms**
Subcutaneous Fat	**260 ms**	**108 ms**
Gray Matter	**520 ms**	**90 ms**

Equations 18,22,23 describe the motion of the magnetisation vector, which assumes a spiral trajectory around the longitudinal axis, processing at the Larmor frequency. Transversal magnetisation decays exponentially according to T_2, while longitudinal magnetisation replenishes according to T_1.

Magnetisation decay in the transversal plane can also be expressed with the equation 24,25 as follows:

$$\frac{dM_{xy}(t)}{dt} = -i\gamma(M_{xy}(t)B_z(t)) - \frac{M_{xy}(t)}{T_2} \tag{24}$$

$$\boldsymbol{M_{xy}(t) = e^{-t/T_2} M_{xy}(0)} \tag{25}$$

1.2.4 Signal detection and contrast definition

After the shutdown of the B_1 field, the precession of magnetisation in the transverse plane, generate a time-varying magnetic flux. According to Faraday's law, this field induces an electromotive force (*e.m.f.*) also known as free induction decay FID, in a Radiofrequency coil placed nearby the sample:

$$e.m.f = \frac{d\phi}{dt} = \int_{sample} M(\vec{r},t) * \vec{B}(\vec{r})\, d^3r \tag{26}$$

where $\vec{B}$ is the magnetic field induced in the RF coil is defined as the magnetic field per unit volume ($\vec{r}$). Introducing the spin density definition $p(\vec{r})$ equation 26 can be expressed also as:

$$s(t) = \int_{sample} e^{-t/T_2} p(\vec{r}) e^{-i(\phi(\vec{r},t))}\, d^3r \tag{27}$$

The amplitude of the FID is proportional to the number of spins per unit at time t=0. However, the spin density and the relaxation time are directly dependent on the molecular composition of the tissue under exam. Therefore, the contrast of an image can be modulated based on the T_1 and T_2 and spin density. To acquire the desired contrast two parameters can be manipulated by the user during the scan:

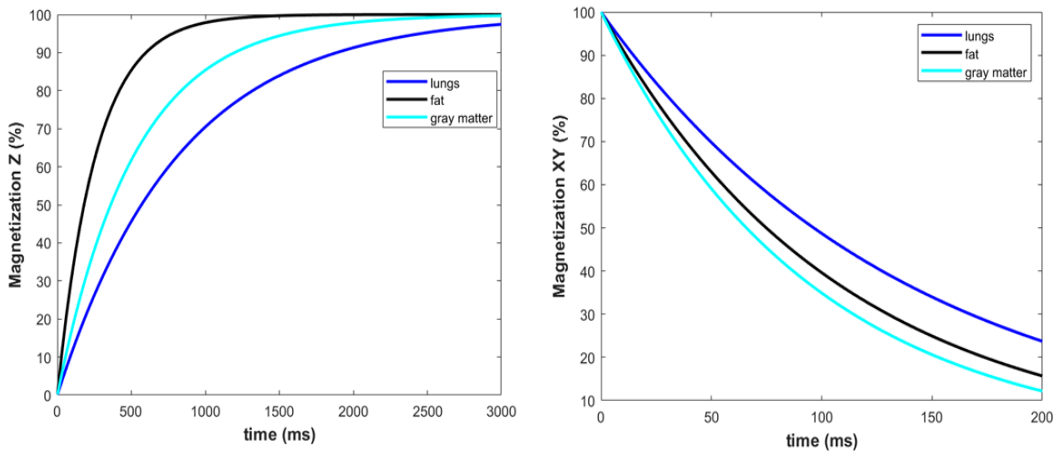

Figure 4: Course of longitudinal, and transverse Magnetisation as a function of time, for different tissues. Considering the two graph,s the best contrast, given by the difference of magnetisation between the tissues, is achieved by setting the time repetition or the time of echo respectively at the T_1 or T_2 times of different tissues.

- Time Repetition (TR) is the time between two RF pulses.
- TE is the time between the RF pulse application and the signal reception.

As an example, the signal over time $S(t)$ of a Spin-echo sequence is proportional to:

$$S(t) = M_{xy}(0)\left(1 - e^{\frac{-TR}{T_1}}\right) e^{\frac{-TE}{T_2^*}} \tag{28}$$

If the TR$\simeq T_1$ and a TE$\rightarrow$0 the images will be T1 weighted.

If the TE$\simeq T_2^*$ and a TR$\rightarrow\infty$, the images will be T_2^* weighted.

If the TR$\rightarrow\simeq\infty$ and a TE$\rightarrow$0, the images will be proton density weighted. T_1-weighted images are commonly used for the anatomical scans, where high contrast is needed to distinguish between tissues. Fat tissue will appear bright, while water-based, and liquid tissues look progressively darker. In contrast, T_2 weighted images enhance the signal of fluid-based tissue, while the fat-based or solid tissues appears darker.

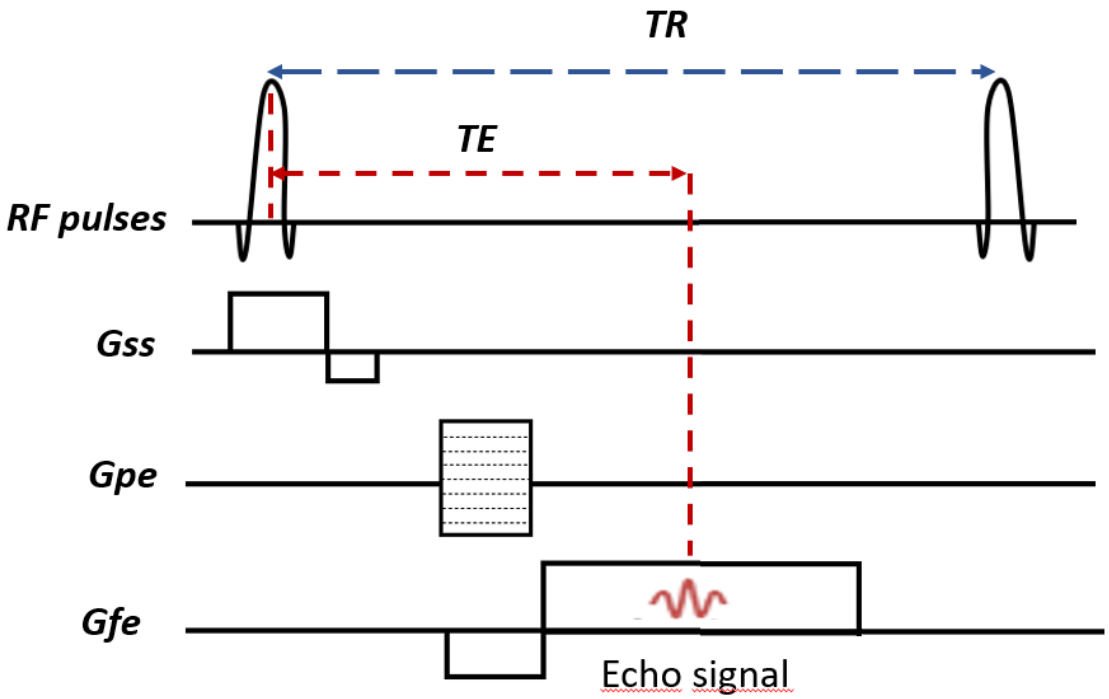

Figure 5: Example of an MRI sequence (Gradient echo); TR is defined with the time between two RF pulses, TE is the time between the RF pulse and the maximum amplitude of the echo signal. G_{SS} is the slice selection gradient, G_{PE} is the Phase Encoding gradient and G_{FE} is the frequency encoding.

1.3 Magnetic resonance imaging (MRI)

To accurately localize the exact origin of the signal from a nucleus at a given point in space, three local and spatial variations of the magnetic field strength along the three axes (G_x, G_y, G_z) must be applied. These variations ensure that the frequency and phase of a bulk magnetisation of the vector in the unit space are unique, enabling spatial resolution of the

acquired RF signal. The expression for the magnetic field including the local spatial variations is given by:

$$B(r) = B + r * G \tag{29}$$

Where r is the gradient position along the respective axes and G is the gradient strength expressed in T/m unit. The local variation of the precession frequencies along the gradient is given by:

$$\omega_0(r) = \gamma(B + r * G) \tag{30}$$

The gradients are all orthogonal to each other, and as a convention, the gradient on z-axes is known as the slice encoding gradient, while the gradients on x and y-axes are known as the frequency and phase encoding gradients.

1.3.1 Slice Encoding

The gradient G_z imposes a frequency shift along the z-axis. The excitation frequency along the z-axis, is given by:

$$\omega(z) = (\gamma B_0 + \gamma z G_z) \tag{31}$$

Referring to figure 6, Equation 31 implies that at the isocentre for z=0, the excitation frequency is equal to the exact Larmor frequency, while is higher to the hips and lower towards the chest. However, the gradient G_z is applied simultaneously with the transmitted RF pulse to create the so-called *slice selective excitation*. The RF pulse contains a narrow bandwidth of frequencies centred at the Larmor frequency ω_0. In this way, only the nuclei in that around of frequencies will be excited, and the slices at the peripherical region of the gradient will not be on resonance and will contribute to the signal formation. The pulse bandwidth depends directly on its duration $BW_{RF} = \frac{1}{\tau}$, and the excited spins will be restricted by the frequency range of the RF pulse window. Thus, the size of the excited slice will be given by:

$$\Delta z = 2\pi \frac{BW_{RF}}{\gamma G_z} = \frac{\Delta\omega_{RF}}{\gamma G_z} \tag{32}$$

As can be seen from 34, the slice selection thickness increases proportionally with the bandwidth of the pulse width, while the excitation area will decrease for higher values of Gradient.

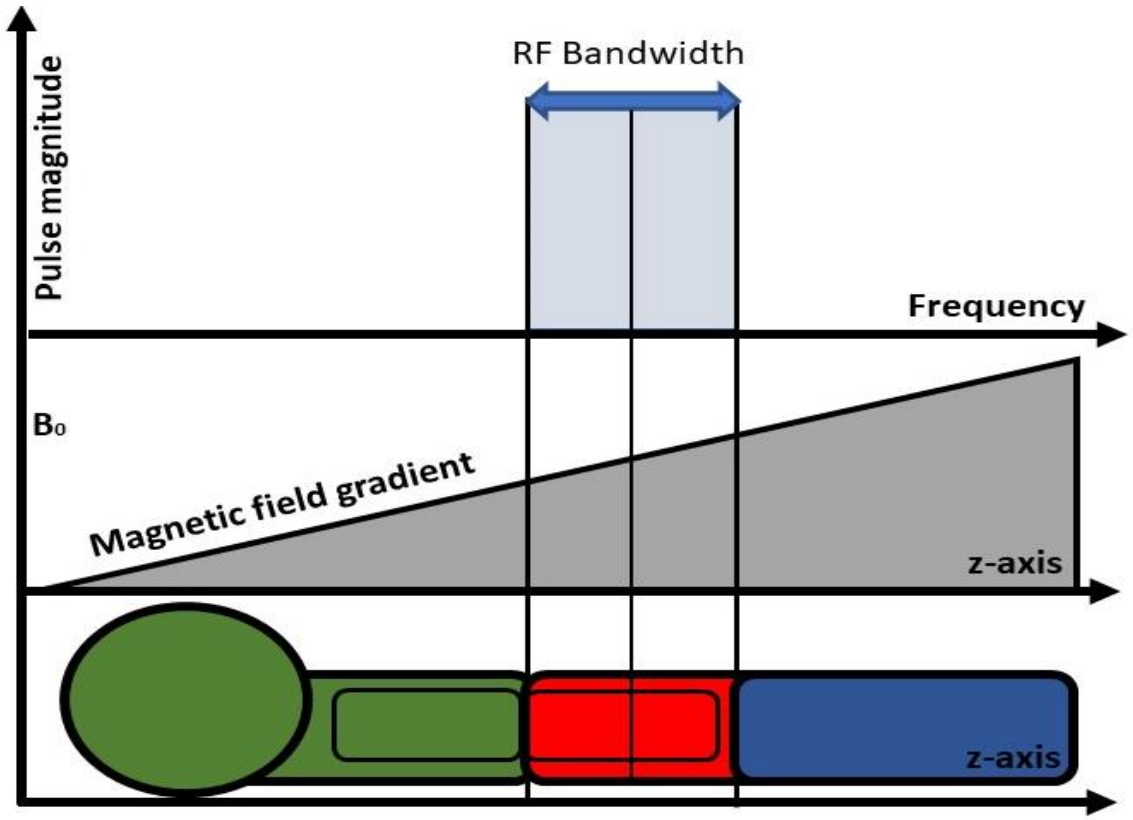

Figure 6: Slice selection gradient. The variation in the strength of the strength causes a slight change in the nuclei's precession frequency. In this way, it is possible to select the right portion of the sample that resonate at desired frequencies.

1.3.2 Phase Encoding

The gradient along z, applied along with the RF pulse, selects a slice along the transverse (slice) plane. However, two additional steps are needed to localise the signal. The signal localisation along the y-axes is known as a phase encoding or spin warping [10].

Phase encoding is applied after applying a gradient along y-direction for a period; the resonance of nuclei will change according to equation (33):

$$\omega(y) = (\gamma B_0 + \gamma y G_y) \tag{33}$$

Therefore, depending on their position on the y-axes, spins will spin faster or slower. Simultaneously, this will cause a dephasing between the spins progressively as long the gradient is applied. The change of phase along the y-axis of the is therefore expressed as:

$$\Delta\phi(y) = G_y \tau_y y \tag{34}$$

where τ_y are the time of the gradient window, and $\Delta\phi$ is defined in a range between $[-2\pi, 2\pi]$. In this way, at the shut-of the Gy gradient, the spins will keep the same frequency since they experience the same B_0, but they precess with a different phase

depending on their position along y-axes. The resolution in the phase encoding direction is expressed as:

$$FOV_y = \frac{2\pi}{\gamma \Delta G_y \Delta t} \tag{35}$$

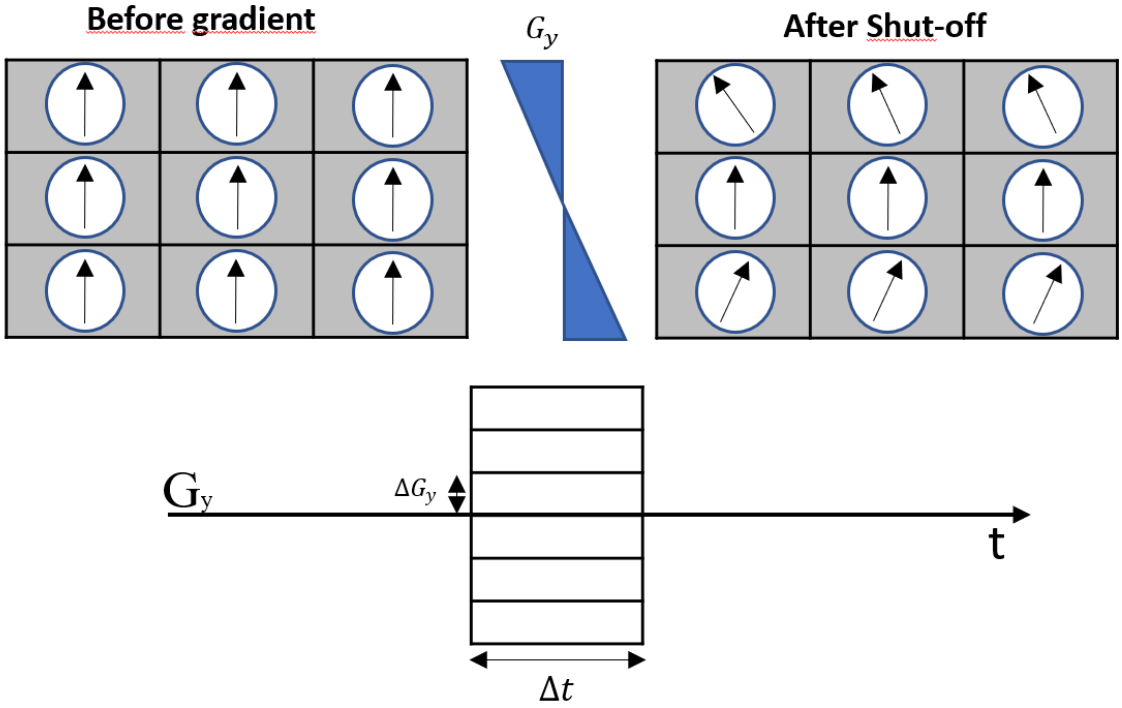

Figure 7: Before the phase encoding gradient, the nuclei will precess with the same phase, after the shut-off of the phase encoding gradients, there is a phase shift between the nuclei.

1.3.3 Frequency Encoding

The last step is to apply the gradient along the x-axes, usually referred to as frequency encoding gradient. Following the same concept of the slice and phase encoding, that causes a linear difference in the resonant frequency along the direction where it is applied:

$$\omega(x) = (\gamma B_0 + x\gamma G_x) \tag{36}$$

G_x causes a change in resonance frequency in the x-axes, a similar to the slice selection gradient. The frequency encoding is also referred to as the readout gradient because it is turned on during the signal acquisition. The acquisition of the signal has a duration defined as T_{acq} and is determined by the receiver bandwidth ($\pm BW$) and number of sampling points along the readout direction (n_x):

$$T_{acq} = \frac{n_x}{2BW} \tag{37}$$

The receiver bandwidth is inversely proportional to the readout gradient steep. A higher gradient would then allow a shorter echo time and therefore can be advantageous for scans involving nuclei with short T_2. The resolution of the phase encoding directions is defined as:

$$FOV_x = \frac{BW}{\gamma \Delta G_x} \tag{38}$$

1.3.4 Signal acquisition

After the application of three gradients (G_x , G_y,G_z), at the position (x, y) the received signal $S(t)$ by the RF coil is modulated by the change of phase along the 2D plane, caused by the gradients:

$$S(t) = \iint p(x,y) e^{\frac{-TE}{T_2^*}} e^{-j(\gamma G_y y T_y)}\, exp^{-j(\gamma G_x x t)} dxdy \tag{39}$$

Where $p(x,y)$ is the signal detected by the coil.

So now it is possible to consider the following change of variables:

$$k_x = \gamma \int_0^t G_x dt \qquad\qquad k_y = \gamma \int_0^\tau G_y d\tau \tag{40}$$

Solving the integrals in (40) and subsisting in the formula (39):

$$S(t) = \iint p(x,y) e^{-j(\gamma k_y \tau)}\, exp^{-j(\gamma k_x t)} dxdy \tag{41}$$

Except for the $e^{\frac{-TE}{T_2^*}}$ Equation 39, is a form of an inverse Fourier transform of the spin density $p(x,y)$. Then with the inverse Fourier transform, we obtain the value of the signal in terms of space:

$$p(x,y) = \iint S(k_x k_y) e^{-ik_x + ik_y}\, dk_x dk_y \tag{42}$$

Through a change of variable, using k-coordinates, we create a mathematical formalism known as k-space. The spatial frequency vector, k(t), in equation 41, delineates the trajectory inside the k-space in the presence of magnetic field gradients. Each point in the k-space define a spatial frequency, with its magnitude denotes indicating the extent to which this spatial frequency is represented in the imaged object. A 2D image is described in k-space with two spatial frequency dimensions (k_x and k_y); while a 3D *k*-space corresponds to a 3D k-space with an additional dimension (k_z). During a sequence execution, the phase encoding gradient selects the start position in the k-space, and then

the frequency encoding enables the signal sampling following a specific pattern. For example, (Figure 8a) a sequential sampling the phase encoding gradient defines the row; and the frequency encoding starts acquiring the signal from left to right, then the phase encoding gradient is applied again on the upper row, and the frequency encoding will sample from right to left. However, other arbitrary patterns can be applied, such as the radial pattern with a heavier sampling density at the centre of k-space (Figure 8b).

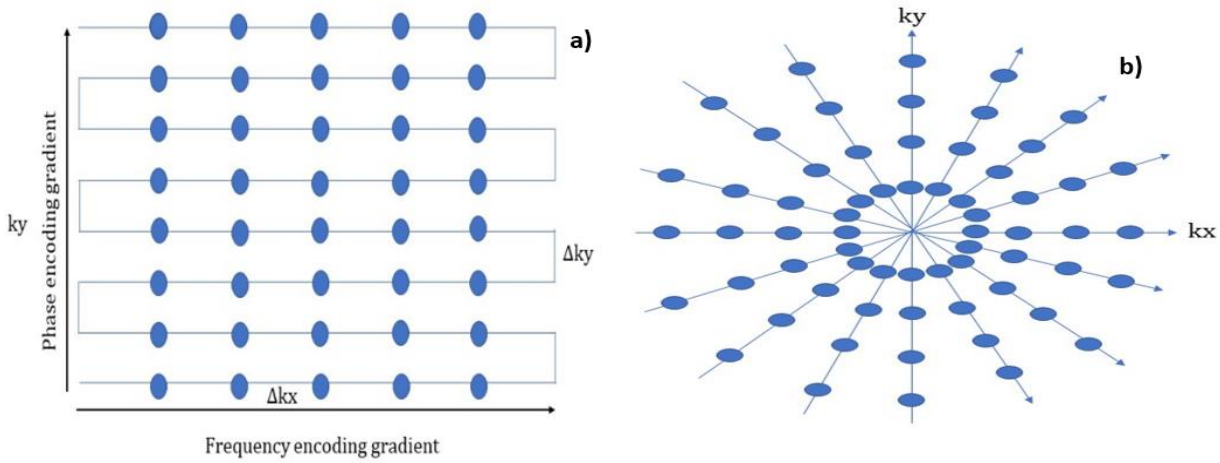

Figure 8: Example of K-space sampling with sequential encoding (on the left) and radial encoding (on the right).

1.4 SNR in MRI

The Signal to Noise Ratio (SNR) is one of the key parameters to evaluate the quality of images in MRI. In conventional MRI, the signal for a single voxel with a uniform distribution of spins SNR is proportional to [22]:

$$S \propto B_0^2 B_1 V_{voxel} \tag{43}$$

Where V_{voxel} is the volume of the voxel. V_{voxel} is chosen during the setup of the sequence and depends on the spatial sampling, along with the proton density in the three image directions: V_{voxel}=$\Delta x \Delta y \Delta z$. In k-space, Δx Δy is defined as:

$$\Delta x = \frac{\pi}{k_x max} \qquad \Delta y = \frac{\pi}{k_y max} \tag{44}$$

$kmax$ is directly related to the number of samples in k space along with the frequency and phase encoding directions. Additionally, the Δz is proportional to the bandwidth of the transmit RF pulse. Since it is proportional to B_1 intensity, even the flip angle has a direct

influence on the signal level, as expressed by equation (11). The noise equation is expressed as the thermal noise N [23]:

$$N = \sqrt{4kTR(BW_{rx})} \tag{45}$$

Where k is the Boltzmann constant, T is the absolute temperature, R is the coil resistance, and BW_{rx} is the bandwidth of the receiver coil. A more detailed explanation about the meaning of the resistance R will be explained in the next chapter.

1.5 MRI system

The main components of an MRI scanner are three: the static magnet that produces the B_0 static magnetic field, the gradient coils, and the RF equipment, which comprises the RF coils and the transmit and receiver chain. All these components are controlled by a computer system (spectrometer) that synchronizes magnet shimming, pulsed gradients, RF transceiver operation, and data acquisition.

1.5.1 Static magnet

A static magnet is the most significant part of the scanner bore; it has to offer a strong magnetic field and at the same time, a high field uniformity inside the gantry. Most of the commercial clinical scanners employ superconductive magnets which work at very low temperatures approaching 0 Kelvin. The magnets are composed of filaments of superconductive material (one of the most used is the Niobium-Titanium, or Niobum-Tin) wires that are wounded in a copper core that protects the superconducting filaments [24], [25]. The magnet is then submerged in a structure called a cryostat. It is a structure filled with liquid helium (with an evaporation temperature of 4 K) and surrounded by a layer of liquid nitrogen at 77 K. A vacuum chamber then surrounds all the systems to isolate the system from the external environment. The homogeneity of a magnetic field is measured in parts per million (ppm) considering a spherical domain volume. The size of the volume is determined by the diameter of the spherical volume (DSV). In general, a clinical MR scanner has around 50 ppm homogeneity, considering 45 cm DSV [26]. However, undesired higher values of local inhomogeneities of the static field are present due to the magnet's intrinsic properties and by the presence of ferromagnetic structures near the magnet and by the magnetic properties of the sample itself. To preserve the field

homogeneity, MRI systems are equipped with conducting shimming coils that create a superimposed field that compensates the field inhomogeneities. Shimming could be passive, active, or a combination of both [27]. Passive shimming is achieved, placing a series of ferromagnetic objects with proper size and position along the scanner bore [28]. However, it does not guarantee application flexibilities because each patient creates a different pattern of inhomogeneity. Active shimming instead, relies on a set of coils in which the current flow is adjusted to create a pattern of spherical harmonics, that compensate the local inhomogeneity of the magnetic field [29], [30]. This process could be automatic using an iterative methods algorithm or manually adjusted by the user.

1.5.2 Gradient coil

As previously mentioned, gradient coils are fundamental instrumentation for signal localisation. Each coil is composed of two layers: the first inner one, is the coil; and the shield. The shield has the task to minimize the stray field of the coil within the cryostat and to reduce the undesired eddy currents that could lead to an intefering field. All the coils system (one for each axes) are usually embedded in a cylindrical epoxy structure (Figure 9c). The design of a z -gradient coil, is a Maxwell coil (Figure 9a), which is composed of two parallel loops with opposed current flow.

The optimal linearity of the gradient is obtained when two loops are placed at a distance of $\sqrt{\boldsymbol{3}}r$, where r is the radius of loops. The transverse plane gradient coils, instead, are two unique configurations of a saddle coil. These coils are also known as Golay coil (Figure 9b), which are placed orthogonally to each other, and are comprised of four coils with an inner arc and outer arc. Only the inner arcs contribute to creating a gradient perpendicular to $\boldsymbol{B_0}$ field. The increment of the number of arcs creates a fingerprinting-like pattern that improves the linearity of the gradients; and therefore, its efficiency [31], [32]. Gradient coils can guarantee a frequency shift of around ±3 KHz, and they must have low resistance (> 150 $\boldsymbol{m\Omega}$ DC) and inductance (> 1000 $\boldsymbol{\mu H}$) [33], [34]. They are fed with Gradient Power Amplifiers which deliver a train of pulses of several hundred Ampere of current (<500 $\boldsymbol{A}$) to the gradient coil in a concise range of times (range of ms). Conventional gradient pulses have a typical trapezoidal shape, and their strength is expressed in milli-Tesla per metre ($\boldsymbol{mT/m}$) while the gradient slew rates are calculated by dividing the peak gradient by the rise times. Usual values of slew rates are around a range between 20 to 150 $\boldsymbol{T}/_{(\boldsymbol{m}*\boldsymbol{s})}$.

However, these rapid switching of the generates by the amplifier generates eddy currents in the nearby electric components.

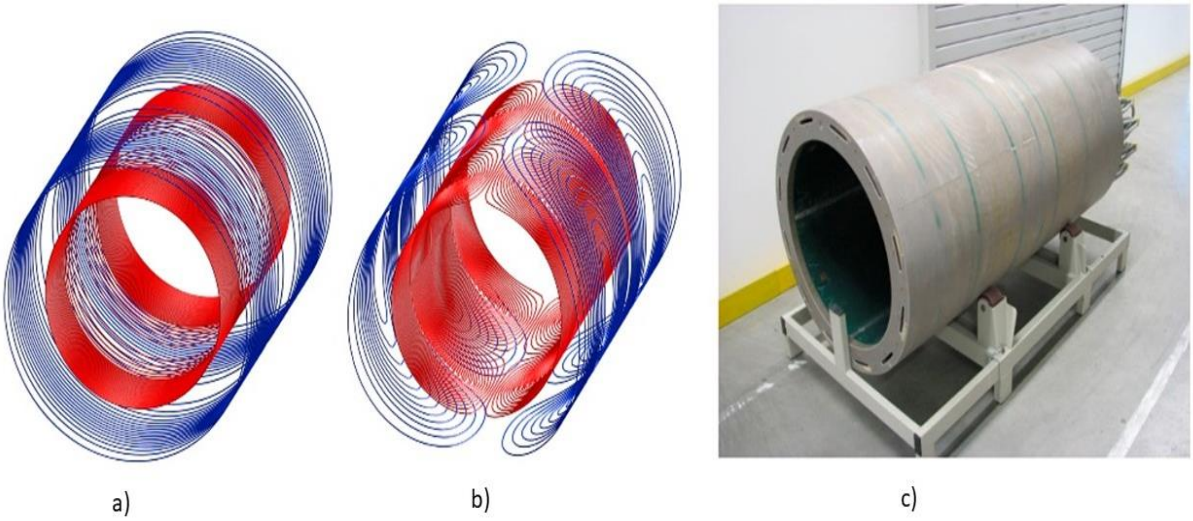

Figure 9: Gradients Coil: a) is the Helmotz gradient coil for the z coil, b) are the x and y gradients Golay coils, c) show the epoxy model where the three gradient coils are embedded. Reproduced with permission from [32].

Eddy currents, generate a magnetic field that combines with the magnetic field produced by the gradient field, modifying the shape of gradients pulse. Eddy currents can be compensated by pre-emphasis, to have a final waveform like the expected pulse shape. An alternative approach is to use active shielding with an additional coil surrounding the gradient coils that work as active shimming.

1.5.3 Computer system and electronics

A brief introduction of the scanner console and electronics is necessary to have a complete overview of the scanner's hardware.

Figure 10 offers a complete overview of the scanner's main components, and of the principal blocks that contributing to the signal generation and processing.

One of the main hardware components is the pulse sequence programmer (spectrometer), which controls and synchronises all the components: gradients, the transmit chain, and the receive chain. The RF signal is first generated by the synthesizer, creating a stable oscillating clean signal at the desired Larmor frequency; the phase is then adapted in the phase shifter. Then the signal passes through the pulse gate circuit. The switch of the gate circuit is controlled by the pulse controller that acts on the length and the timing. The transmit signal then arrives at the amplifier, which boosts the signal from a low level (mW)

to the power of several kW. At the end of the transmit chain, there is the T/R switch. It has the task to direct the high-power RF signal from the RF amplifier to a transmit/receive RF coil, and the low power nuclear magnetic resonance (NMR) signal from the RF coil to the low noise pre-amplifier (LNA).

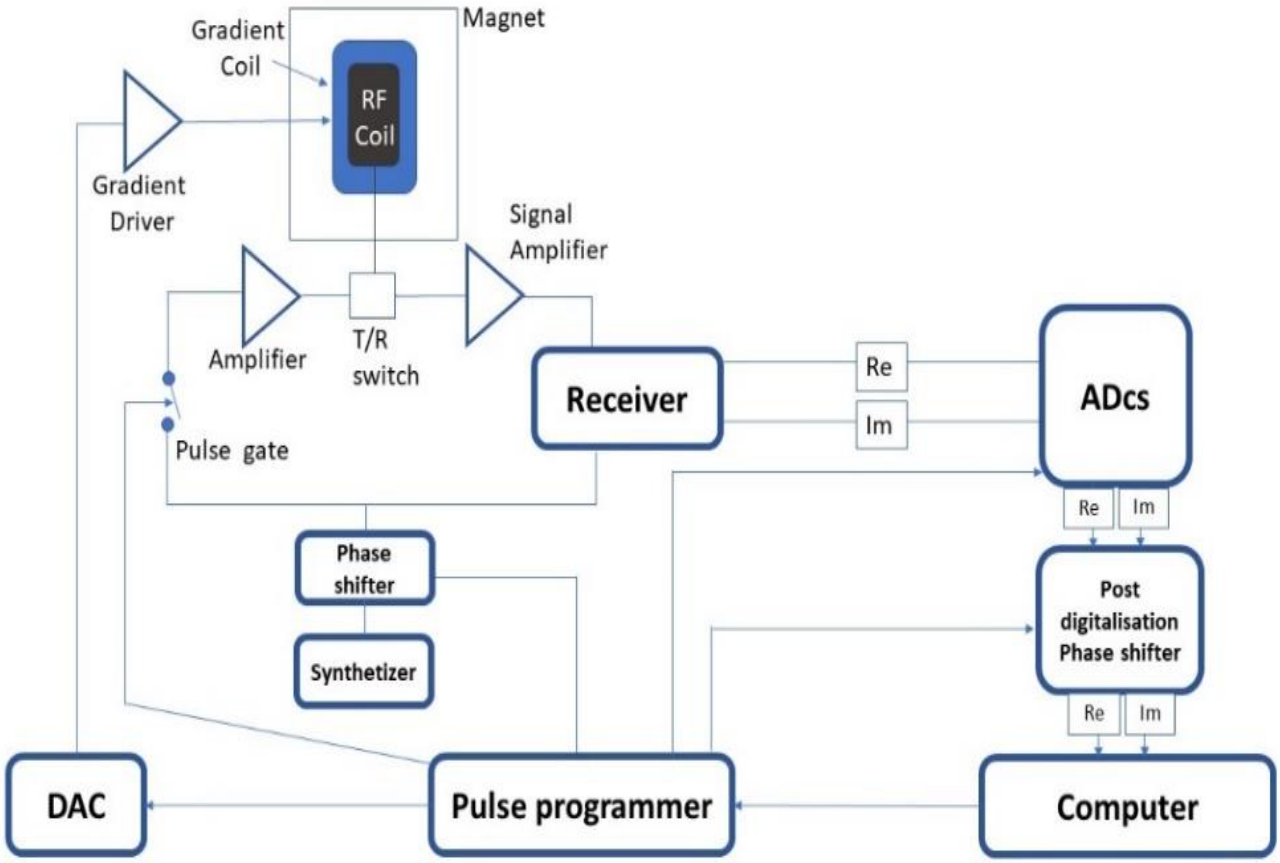

Figure 10: Schematic of the MRI hardware.

Another critical task of the T/R switch is to protect the receive chain preamplifier from the high power delivered during the RF transmission and allow the receiver coil's NMR signal to the receive preamplifier without unwanted additional noise. Regarding the receive chain, the signal from the RF coil is first enhanced by the preamplifier, which must have a small noise figure due to the weak signal of the free induction decay received in the RF coil. The second step of the receive chain is the spectrometer that converts the signal to form the Larmor frequency to the baseband frequency, to allow the signal's digitalisation. The signal is low passed and then digitally converted in the ADC, which sampling steps are determined by the prescribed receive Bandwidth (BW). The last elements are the signal

phase shifter, which adjust the incoming signal according to the pulse programmer. Finally, the signal arrives at the computer where it undergoes Fourier transformation.

Chapter 2:
RF coils

RF coils are essential components of MRI system, tasked with transmitting the RF field that excites the spins in the anatomy of interest and receiving the resulting resonant free induction decay signal. The design, efficiency, and electromagnetic evaluation of RF coil are fundamental for the quality of an MRI scan. Due to the relevance of the argument in the thesis, following paragraphs will provide an extended outlook on the theory and the state of the art of RF coils.

2.1 Finite element methods

Giving the diverse possibilities of designs, applications, and operating frequencies, electromagnetic analysis and simulations are crucial steps in the developments of RF coil. Analytical methods can predict the magnetic and electric fields of an RF coil structure accurately just in the case of simple geometries. However, for complex geometries and configurations, complex numerical methods are required to evaluate parameters such as magnetic and electric fields, resonance frequencies, transmission and reflection losses [35], [36]. The two most used mathematical methods are the Finite Difference Time Domain Methods (FTDT), and Finite Elements Methods (FEM). FDTD solves the problem in the time domain through a process called leapfrog time stepping. It calculates the electric field vector components in a volume of space at a given instant in time, then the magnetic field vector components in the same spatial volume, are solved at the next instant in time, proceeding until the field reaches a steady state solution. Despite its widespread use, FDTD method encounters issues with complex coil shapes, such as those with curved geometry with a small radius [37].

FEM works in the frequency domain and is widely employed in various EM simulation software, including ANSYS EM, which was used for all the simulations in this thesis. For this reason, a more extended overview of the methods will be provided. The relationship between magnetic $H(r)$ and electric field $E(r)$ considering a free source environment in the frequency domain is defined by the following Maxwell equations:

$$\nabla \times E(r) = -j\omega\mu H\,(\mathrm{r}) \tag{46}$$

$$\nabla \times H(r) = -j\omega\varepsilon(r)E(r) + \sigma E(r) + J(r) \tag{47}$$

ω, ε, μ are respectively angular frequency, the dielectric constant, and the diamagnetic constant in the free space. **J** is defined as the surface density current, which is the source of the field. Solving (48) and (49) for E in the absence of a source yields:

$$\nabla \times [\nabla \times \mathrm{E(r)}]\text{-}k^2\mathrm{E(r)}=0 \tag{48}$$

Where $k^2=i\omega\mu\sigma + \omega^2\varepsilon\mu$. Applying the dot product on both sides with an infinitesimal and an arbitrary variation of E, and then integrating over the volume V, the resulting function $F(E)$ is expressed as follows:

$$F(E) = \frac{1}{2}\int_V [\nabla \times \mathrm{E}][\nabla \times \mathrm{E}] - k^2 E \cdot E\, dV \tag{49}$$

With the electric boundary condition as follows:

$$\begin{cases} \partial F(\boldsymbol{E}) = 0 \\ n\, x\, \boldsymbol{E} = 0 \end{cases} \tag{50}$$

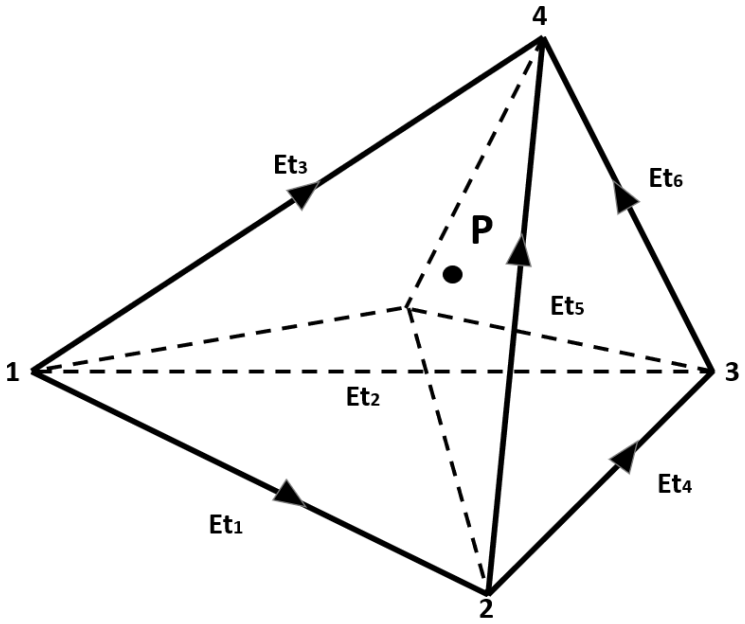

Figure 11: Shape functions defined in a tetrahedral finite element

The first step of FEM method is to discretize the volumes by creating a mesh composed of finite elements of known shape. In a 3D volume domain, the most common discretisation uses tetrahedral shape due to its versatility and simplicity in constructing surface with

triangular shape. Each element is considered a homogeneous domain of integration, where the solution is found by a linear combination of simple functions, known as shape function. The interpolation variables for the shape functions can be chosen as the tangent electrical field of the edges of each of the tetrahedrons, as shown in figure 11. Initially, we define the volume of the tetrahedron as V and label the nodes of the tetrahedron as 1,2,3 and 4. By connecting an arbitrarily chosen point P (x, y, z) in the tetrahedron, the volume is divided into four smaller sub volumes $V_{1,\,2,3,4.}$

$$V_1 = \frac{1}{3!}\begin{bmatrix} 1 & x_{\square} & y_{\square} & z_{\square} \\ 1 & x_1 & y_2 & z_2 \\ 1 & x_2 & y_2 & z_2 \\ 1 & x_3 & y_3 & z_3 \end{bmatrix} V_2 = \frac{1}{3!}\begin{bmatrix} 1 & x_1 & y_1 & z_1 \\ 1 & x_2 & y_2 & z_2 \\ 1 & x_3 & y_3 & z_3 \\ 1 & x_4 & y_4 & z_4 \end{bmatrix} \tag{51}$$

$V_{3,4,}$ are obtained similarly. The volume coordinates P (L_1, L_2, L_3, L_4) are defined as:

$$L_i = \frac{V_i}{V} \quad \text{where } i=1,2,3,4 \tag{52}$$

With the interpolating functions of E defined by:

$$N_i = (L_{i1}\boldsymbol{\nabla} L_{i2} - L_{i2}\boldsymbol{\nabla} L_{i1})l_i \tag{53}$$

Where l_i denotes the length of the edge *i*. In the end, the electric field in the tetrahedron can be expressed as:

$$E = \sum_{i=1}^{6} N_i E_{t_i} = [E]^T[N] \tag{54}$$

Assuming the volume V is sampled into a chosen number of tetrahedra without gaps or overlap, inserting, 54 into the functional expressed in 49 gives:

$$F(E) = \frac{1}{2}[E]^T[A][E] \tag{55}$$

Where M is the number of tetrahedra that discretize the volume V and A is given by:

$$A = \int_V^{\square}\{[\nabla \times \mathrm{N}][\nabla \times \mathrm{N}]^T - k^2[N] * [N]^T\}\, dV \tag{56}$$

The integral involved in A can be evaluated analytically and numerically since the integrands are simple linear or quadratic. The extended solution can be found in reference [45]. If a source is applied to the domain, the function (56) changes as follows:

$$\mathbf{F}(\boldsymbol{E}) = \frac{1}{2}\int_V^{\square}[\nabla \times \mathrm{E}][\nabla \times \mathrm{E}] - k^2 E \cdot E]\boldsymbol{dV} + \boldsymbol{j}k_0 Z_0 \int_V^{\square} \mathrm{J} \cdot \mathrm{E}\, \boldsymbol{dV} \tag{57}$$

Where Z_0 is defined as $\sqrt{\frac{\mu_0}{\varepsilon_0}}$, representing the impedance in the free space. In this case, applying the FEM we obtain:

$$F(\boldsymbol{E}) = \frac{1}{2}[\boldsymbol{E}]^{\boldsymbol{T}}[\boldsymbol{A}][\boldsymbol{E}] - [\boldsymbol{E}]^{\boldsymbol{T}}[\boldsymbol{b}] \quad (58)$$

Applying the boundary condition, equation (58) is solved for [E]. Once E is solved, it is possible to obtain the field at each point of volume V, and from this, all the other parameters of interest such as H-field and B_1 field. To limit the volume of the analysis, , terminating boundary that surrounds the Volume are usually applied. Boundaries are generally modelled as a perfect electric conductor (PEC), or radiative. FEM has become one of the most widely used numerical methods to solve complex engineering problems; however, the complexity to generate a mesh and the matrix calculation can be computationally challenging. Nonetheless, the incorporation of lumped models such as a resistor, capacitors, and inductances are straightforward, including excitation through lumped, voltage or current port enforcing the electric field across the gap.

2.2 Far field near field and balanced circuits

This section briefly describes two concepts of the antenna theory necessary to understand the next paragraphs.

2.2.1 Near field/Far field

The far field and near field, are regions describing the behaviour of the Electromagnetic field around an antenna. The near field is more prominent in proximity of the antenna, while the far field dominates at further distances.

Near field regions can be divided into two zones:

Reactive zone

This region is of particular interest for RF coil antenna. In the Reactive Zone, there is not a specific relationship between the magnetic field and the electric field, and both their phase and amplitude vary over time. Electromagnetic waves are radiated outside the antenna, and a reactive component absorbed is also present, which is absorbed and emitted again. It is important to underline that an external object, such as anatomical tissue or a sample placed in the proximity of the field, causes a strong coupling and energy absorption by the

sample. Commonly, this zone extends from the antenna surface to a distance of 0.62 $\sqrt{\frac{D^3}{2\pi}}$, where D is the linear dimension of an antenna.

Radiative Zone (also known as the Fresnel Region)

In this region, reactive fields are no longer dominant anymore. The energy in the radiative field is purely radiative. However, unlike the far field region, the shape of the radiation pattern varies with the distance. This zone usually extends from the end of the reactive zone to $\frac{2D^2}{\lambda}$

Far field Region or Fraunhofer zone

The Far field region starts after the radiative zone and extends to the infinity. In this zone, the magnetic field and the electric field are orthogonal to each other, and their pattern is independent of distance.

2.3 RLC circuits, tuning and matching

RF coils must resonate at the same Larmor frequency as the nucleus of interest. The simplest example of a resonant circuit is described by an RLC circuit. The lumped components must be chosen to achieve the desired resonance frequencies by adjusting the discrete values of capacitance or inductance. An example of a series RLC circuit is shown in figure 12a. R represents the Ohmic losses of the coil, while the sum of the inductive L and capacitive C reactance at the resonance frequency is zero. Therefore, the resonance condition is satisfied by:

$$j\omega L + \frac{1}{j\omega C} = 0 \quad \Longrightarrow \quad \omega = \frac{1}{\sqrt{LC}} \tag{59}$$

The concept is similar for the parallel RLC circuit shown in figure 12b. For this configuration, the values of complex admittance are mutually opposite, and the resonance condition is satisfied by:

$$j\omega C - \frac{1}{j\omega L} = \quad \Longrightarrow \quad \omega = \frac{1}{\sqrt{LC}} \tag{60}$$

Where the total ohmic losses of the circuit are given by the conductance of the coil conductors, $\frac{1}{R}$.

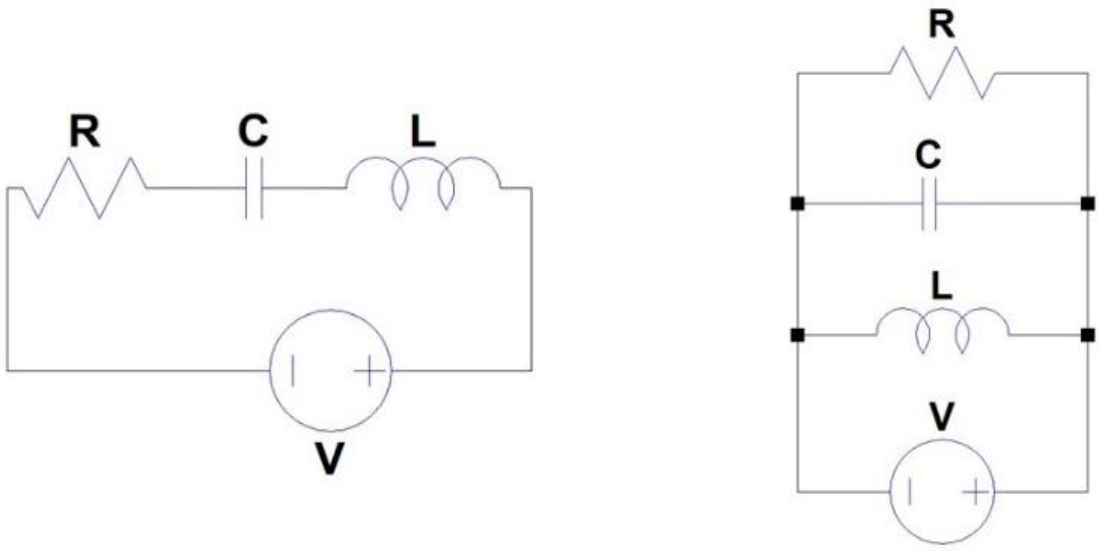

Figure 12: RLC in series and parallel

2.3.1 Circuit Balancing

A balanced circuit is an electrical or electronic circuit where the signal or power is sent symmetrically in two wires, unlike the unbalanced circuit, where the voltage is seen in one wire and a common ground. Balanced circuits are used for immunity to high power or electromagnetic interference. In a balanced circuit, the electric interference (i.e. common mode currents) flows in the two-lines with opposite signs, cancelling each other out. Baluns (Balanced to unbalanced) are electrical circuits designed to transform the circuit from unbalanced to balanced. Balun circuits can take different forms and designs, and sometimes they also function to transform impendence.

2.3.2 Quality factor and coil losses

The quality factor is the main parameter used to determine the efficiency of an RF coil and to describe its losses. Quality factors can be expressed in terms of transmitted power efficiency:

$$Q = \frac{Power\ stored}{Power\ loss\ per\ cycle} \tag{61}$$

Practically, the Q factor is the measured dividing the peak frequency f_0 (for MRI application, we assume the Larmor frequency of interest) by the bandwidth at the half-power (-3dB on a decibel scale) see figure 13 (47):

$$Q = \frac{\omega_0}{\Delta\omega} \tag{62}$$

The quality factor in an RLC series circuit can also be calculated as:

$$Q = \frac{\omega L}{R} \tag{63}$$

For a parallel RLC circuit, the Q factor is calculated as:

$$Q = R\omega C \tag{64}$$

where R indicates the total losses of RF coils. R coil has an inverse relationship with SNR as seen in (30). R is composed of many elements that contribute to the increased noise [38]:

$$R = R_{\text{coil}} + R_{\text{sample-el}} + R_{\text{rad}} + R_{\text{sample-ind}} \tag{65}$$

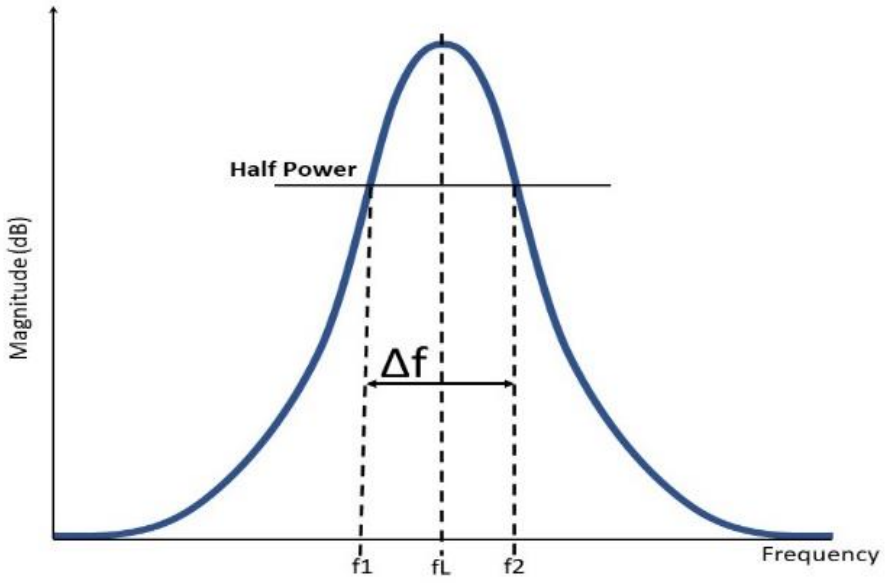

Figure 13: Quality factor, in the lab, is measured by checking the bandwidth S_{12} peak of two loops connected to the VNA (Vector Network Analyser).

$R_{coil,}$ represents the Ohmic losses of the coil, attributed to the random movement of electrons along the conductors (Johnson Noise) [39]. However, the current is not uniform along the conductor but tends to flow along its surface, to a depth defined by the so-called skin effect, with a thickness described by:

$$\delta = \sqrt{\frac{2}{\sigma f \mu_0}} \tag{66}$$

Here, σ, f, μ_0 respectively representing the conductivity of the material, f the tuning frequency and $\mu_0$the diamagnetic constant in the free space. Formula (66) implies that R_{coil} depends directly on the frequency f. As a rule of thumb, the thickness of the conductor must be five times bigger than the skin depth to minimize the resistance. Another issue to consider is that the current tends to concentrate where the curvature is larger; resulting in a more uniform current density in circular conductors. This phenomenon is referred to

as the lateral skin effect. A consideration also include the intrinsic quality factor of the capacitors and the soldering, which should be minimized as much as possible.

R_{rad}, represents the radiation losses of the coil. if the current path is longer than the wavelength at the Larmor frequency, the coil starts to behave as a transmission line, losing near field efficiency due to radiative dissipation. This problem can be mitigated by reducing the conductor length between λ/20 and λ/10, where λ is the wavelength. The wavelength is inversely proportional to the resonant frequency of the coil, making radiative losses a serious consideration, especially in high field MRI. Another source of radiative loss is the common mode currents between the cables, interaction of the coil with RF bore shield, and components of the bore. This issue can be addressed by balancing the coil circuit and placing cable traps that minimize the current flow outside the cables.

$R_{sample\text{-}el}$ is caused by the electric field penetrating the sample where the resistance of the sample causes dissipation of the transmitted energy. Also, movements of the electrons between the sample and the RF coils create stray capacitance. For better visualisation of the phenomena, Gadian and Robinson [40] proposed an equivalent circuit model (represented in Fig. 14) where L_C and C_C represent the conducting tissue and C_s the stray capacitance in parallel with the coil circuit. In conclusion, the last elements in equation 65, $R_{ind,}$ refers to the resistive inductance caused by the eddy current induced in the sample and subsequently to the RF coils, resulting in noise. As shown in figure 14, L_I represents the inductive loop within the sample and M the mutual inductance between the coil and the patient. C_i and R_i represent the electrical losses of the sample. Calculation of the quality factor of a coil in unloaded and loaded condition gives an estimation of the coil losses due to the sample:

$$\frac{Q_{unloaded}}{Q_{loaded}} = \frac{R_{coil}+R_{rad}}{R_{coil}+R_{rad}+R_{sample}+R_{ind}} \tag{67}$$

It is essential to know that R_{sample} and R_{ind} cannot be minimized and depend strictly on the dielectric and conductibility of the sample, as well as its shape. Therefore, most of the effort in the development of the RF coil must focus on minimising R_{coils} and $R_{rad.}$ Another useful measure for the factor of merit of the coil is the filling factor, which is the ratio of the magnetic energy stored inside a sample volume (V) to the total energy of the coils. This can be expressed by:

$$n_f = \frac{\int_{V_{LOAD}} |B|^2 \, dV}{\int_V |B|^2 \, dV} \sim \frac{B_1^2}{QP} \tag{68}$$

Where B_1 is the magnetic field at a specific point, and P is the coil input power.

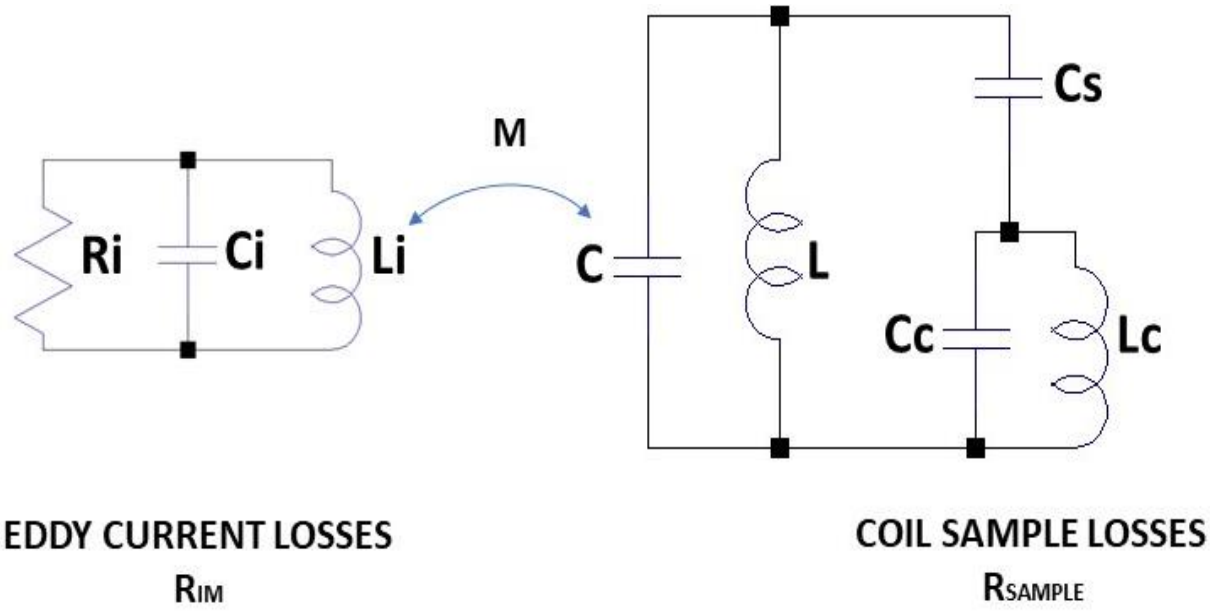

Figure 14: Circuital model of an RF coil loaded with a sample

2.3.3 Impedance matching

The power transmitted by the RF coil to the sample is proportional to the transmitted power of the source. However, this dependence relies on difference between the input impedance of the coil and the impedance of transmission lines, which, is conventionally set to 50 Ω in experimental setups. The reflection coefficient Γ of a transmission line is given by:

$$\Gamma = \frac{Z_c - Z_0}{Z_c + Z_0} = \frac{V_r}{V_i} \tag{69}$$

Where Z_c is the coil impedance, Z_0 is the transmission line impedance, V_i is the amplitude of the incident wave, and V_r is the reflexed wave amplitude. The reflection coefficient is generally defined in dB (decibel units):

$$\Gamma_{dB} = -20log|\Gamma| \tag{70}$$

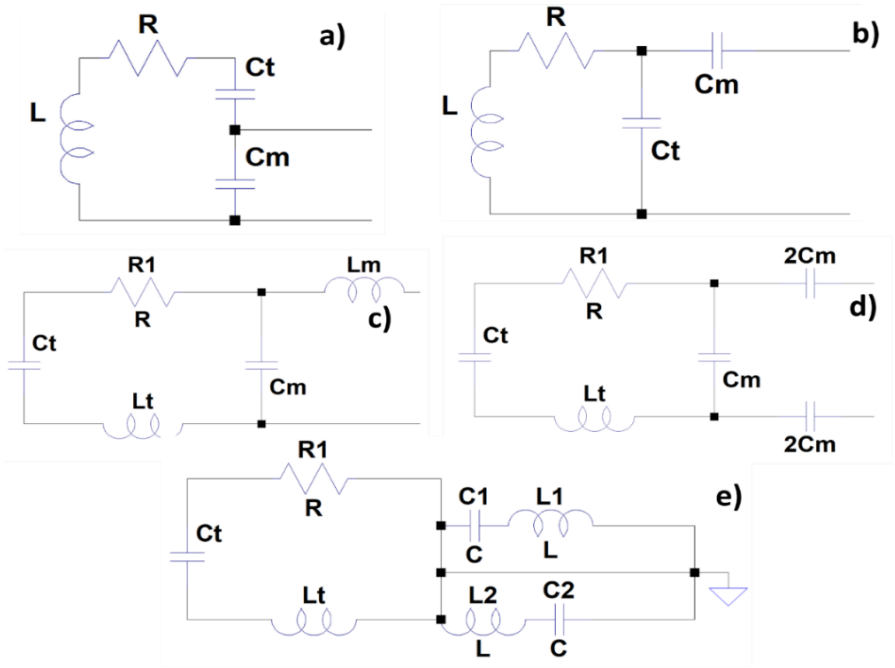

Figure 15: Example of matching circuits. Capacitive parallel matching a), series capacitive matching b), LC matching c), capacitive balanced matching d), Lattice balun e).

Generally, values Γ_{dB} of below -13 dB indicate that the delivered power is around 95% or more, which is considered acceptable for a matched coil. The procedure to match the input impendence of the coil to 50 Ω involves a small transformer circuit composed of a series of capacitances and inductances. There are several different topologies of the matching circuit, such as capacitive matching in series or parallel, inductance matching in series or parallel or eventually a combination of them as the LC matching or lattice Baluns [41] (Figure 15). However, a balanced matching circuit is preferable because the coil should be driven symmetrically. This means that the phase of current at the two terminals of the coil must be opposed, with a null complex impedance component of the current flowing in the transmit cable. As previously mentioned in paragraph 2.3.2, this approach offers two advantages: it reduces both the radiative losses of the coaxial cable (commonly known as Antenna effect) and the common-mode currents. As demonstrated in [42], a perfectly balanced coil doubles the quality factor. Practically, the input impedance of a coil is measured on the workbench by creating a break in the coil conductor and connecting the coil to a network analyser after calibrating the cable. Depending on the input impedance, a different variety of matching strategies can be used to match the coil to the load and feeding source. A useful lab tool for this purpose is the Smith Chart shown in figure 16 [43]. It helps to visualize whether a matching circuit is capable of properly matching the coil, an

operation that alternatively involves complex mathematical operations. Each point of the Smith Chart represents a value of normalized impedance, where the x-axis represents the real values of impedance as resistance or conductance. The circles represent values with constant resistance or conductance, while the arcs represent values with constant susceptance or reactance. The upper half of the chart corresponds to the positive complex impedance (inductive), while the lower half corresponds to the negative complex impedance (capacitive). Starting from the values of input impedance, one can move toward the Smith chart to find the optimal combination of capacitance and inductance.

Table 3: Transmitted power for different values of Γ_{dB}

Γ_{dB}	Transmitted power
-2dB	20.57 %
-5dB	68.38 %
-8 dB	84.15 %
-10 dB	90.00%
-13 dB	94.99%
-20 dB	99.00%
-30 dB	99.99%

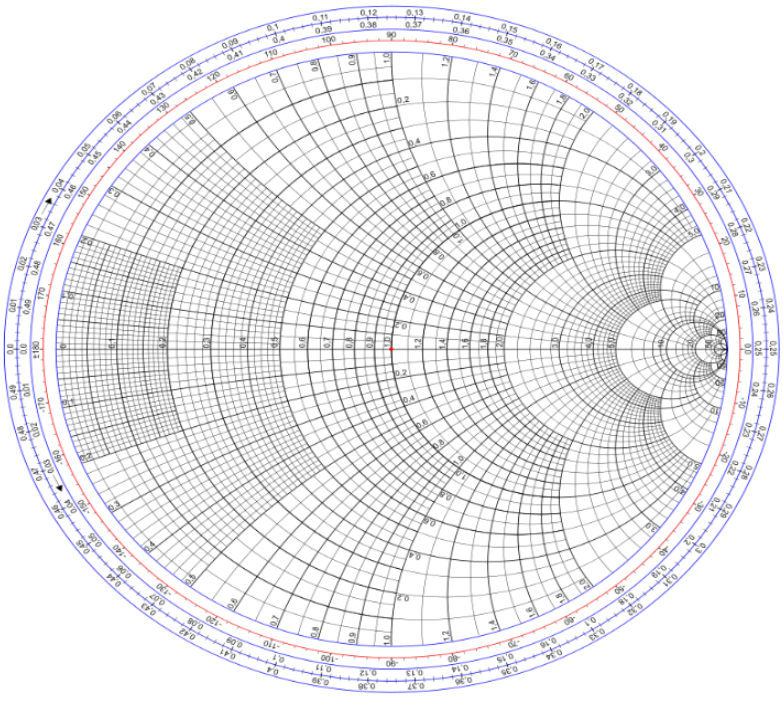

Figure 16: Smith Chart. Reproduced from *https://commons.wikimedia.org/wiki/File:Smith_chart_gen-2012-03-02.svg*

2.4 B_1 fields

The harmonic RF magnetic field $B_1(r,t)$ generated by a RF coil is expressed as follows [44]:

$$B_1(r,t) = B_1(r)e^{i\omega t} \tag{71}$$

B_1 can be decomposed into the three orthogonal Cartesian components (*x,y,z*) using phasor notation. Assuming that the component B_z is parallel to the static field B_0 [45], only the *x* and *y* component are used to excite the nuclear spin. The circular polarisation in the transverse plane, opposite to the nuclei's precession relates to the transmit field and is expressed as [46]:

$$B_1^+ = \frac{B_{1x}+iB_{1y}}{2} \tag{72}$$

The circular polarisation in the transversal plane, related to the received field, is expressed as:

$$B_1^- = \frac{\left(B_{1x}-B_{1y}\right)^*}{2} \tag{73}$$

At higher field strengths, B_1^+ and B_1^- are not symmetrical due conduction currents induced in the sample. These currents generate larger out-of-phase contributions that can alter the polarization of B_1 and its spatial distribution, leading to asymmetric B_1^+ and B_1^- maps.

2.4.1 Coil polarisation

The B_1 field transmitted by an RF coil, is conventionally perpendicular B_0 field direction. Depending on the coil design, the field produced by the coil can be linear, quadrature, or circular. Linear polarisation can be produced only by one single loop, while a dual Helmholtz can produce a quadrature polarisation. A birdcage type resonator, when fed in quadrature with two feed ports shifted by 90° degrees, produces circular polarisation [48]. The difference and advantage of quadrature polarisation are detailed in the studies by Chen [49] and Glover et al. [45].

A general transverse field, assuming a propagation along the z+ direction, is described by:

$$B_{xy} = xB_x + yB_y \tag{74}$$

The field is comprised two components: a clockwise field and a counterclockwise field. The counterclockwise field B_{CCW} is mathematically described as [50]:

$$B_{CCW} = \frac{(B_{1x}+jB_{1y})}{\sqrt{2}} \tag{75}$$

While the clockwise component of the magnetic field B_{CCW} is given by:

$$B_{CW} = \frac{(B_{1x} - jB_{1y})}{\sqrt{2}} \quad (76)$$

Assuming a linear polarisation along the x axis, the field would have only the B_{1x} component. This component, being out of phase with the nutation direction of the protons, would cause additional heating during transmission phase. Conversely, a circular polarisation comprises the B_{1y} component, which cancels out the counter rotating component. Additionally, circularly polarized excitation reduces the RF drive power by a factor of 0.5 to 0.7 over linear drive since the nonproductive counter-rotating mode is not excited. A factor of 0.5 would be expected for a symmetric object, while the smaller benefit is predicted for an object with elliptical cross section. Furthermore, a quadrature coil increases SNR by $\sqrt{2}$ during the receive phase, since the orthogonal components of the precessing magnetisation are sampled independently and simultaneously.

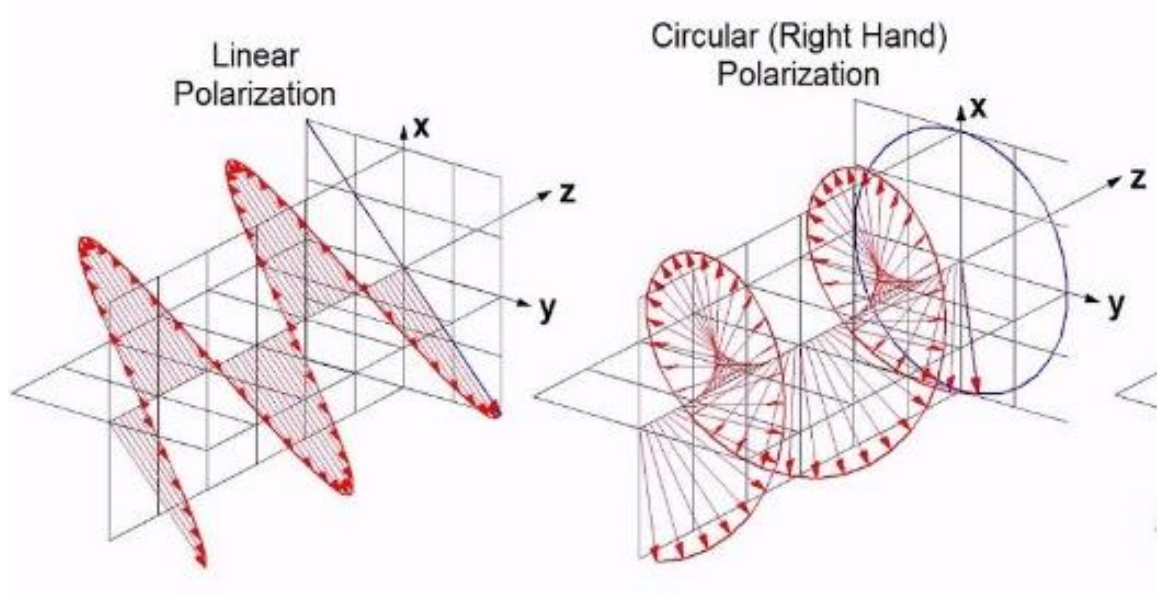

Figure 17: Linear polarisation (on the left), circular polarisation on the right.

2.5 Specific Absorption Rate

The electric field produced during the transmission of the B_1 field induces currents that results in the heating of the sample. Monitoring this effect is essential to prevent potential risks to the patient, including heating or burning. The Specific Absorption Rate (SAR) measures the rate of the energy absorbed per unit mass of a sample exposed to electromagnetic energy. Mathematically, SAR is defined as:

$$SAR = \frac{1}{V}\int_{sample} \frac{\sigma(r)|E(r)|}{\rho(r)} dr \quad (77)$$

Where V is the sample volume, σ (S/m) is the sample conductivity, *E* (V/m) is the root mean square electrical field, and ρ(r) (Kg/m^3) is the tissue density. SAR is expressed in W/kg and depends on the coil, the intensity of transmit field, sample features (dimensions, geometry, tissues), type of sequence and the static field strength. Two types of SAR can be measured: average SAR and local SAR. Average SAR is the total energy transferred into the sample per time unit divided by the whole sample mass. Local SAR is the total energy transferred in a small portion of the sample divided by its mass (this is usually 1 g or 10 g of the tissue). In MRI, the transmitted B_1 field is not continuous over time, and the SAR must be weighted based on the RF pulse encoding used in the pulse sequence, as described by Collins et al. [47]. The energy absorbed by the patient or a generical sample during a scan is defined as:

$$SAR = \frac{\sum_{n=1}^{N}(SAR_{\tau n/\alpha n} * \tau n)}{TT} \quad (78)$$

where τ_n and α_n represent the flip angle and the pulse duration of the sequence of the nth pulse in a sequence with a total N pulse, while TT represents the total scan time, while $SAR_{\tau n/\alpha n}$ is obtained through:

$$SAR_{\tau/\alpha} = f(3ms/\tau)^2 \left(\alpha/_{90^\circ}\right)^2 SAR_{3ms/90^\circ} \quad (79)$$

Where $SAR_{3ms/90^\circ}$ is the SAR measured with a transmitted B_1 field necessary to obtain a 90° flip angle with a pulse time of 3 ms. *f* is a normalisation factor depending on the pulse shape. The SAR limits for MRI applications are described by IEC 60601-22-33:2010 and are shown in Table 4.

Table 4: SAR limit, according to the IEC 60601-22-33:2010

Operating mode	Whole-body SAR Average SAR	Head SAR Average SAR	Head SAR Local SAR (10g)
Normal	2 W/Kg	3.2 W/Kg	10W/Kg
First level Controlled	4 W/Kg	3.2 W/Kg	20W/Kg

2.6 Volume Coils

Volume coils are commonly used to deliver RF energy to the sample. They surround the anatomy of interest, and they must offer a homogeneous B_1^+ field, ensuring the transmission

of a uniform flip angle inside their volume. Birdcage coils (Figure 18a) are a class of resonators that produce a circularly polarised, transverse, and highly uniform magnetic field within a cylindrical volume. Their geometrical structure comprises an even number of equally spaced legs or rungs, terminated by two end rings. The circuit forms a ladder network composed of N identical sections (where N is defined as the number of rungs) (Figure 19), with a current intensity I_n expressed as:

$$I_n = I_0 e^{(\frac{i2\pi n}{N})} \tag{80}$$

The different paths of the current along the network produce several resonant modes proportional to N, of which only one corresponds to the desired homogeneous magnetic field [51]. There are three different birdcage topologies based on the position of the capacitors: low pass [52] (capacitors only in the legs), high pass (Figure 20) (capacitors only in the end rings), and hybrid or band-pass [53] (capacitor in the end rings and the legs).

The choice of topology depends on the specific application, the working frequency, and the geometrical dimensions and ergonomic considerations.

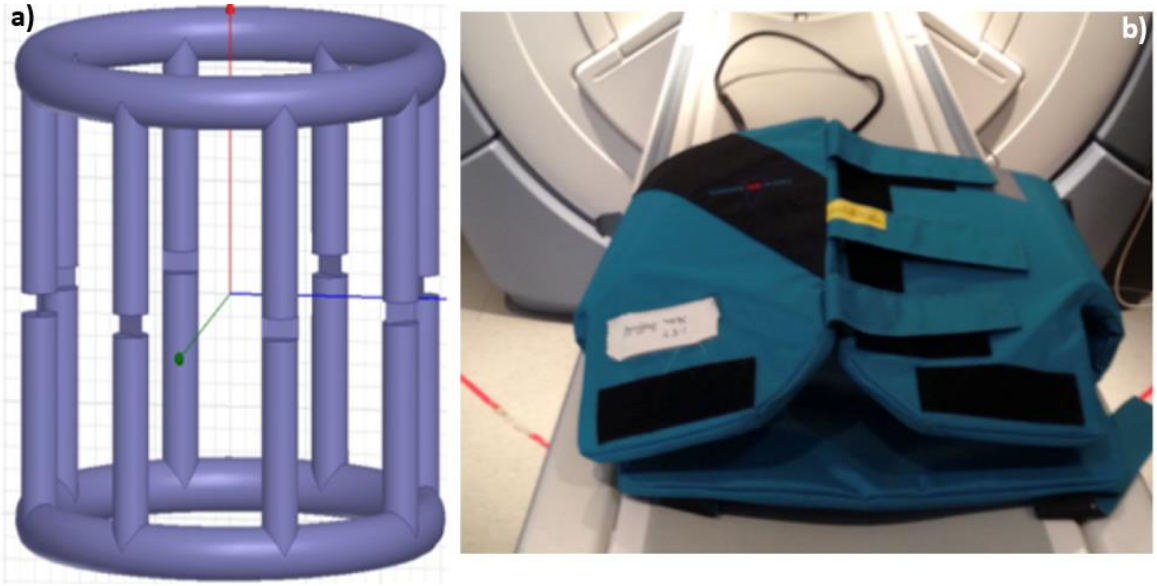

Figure 18: Vest coil commonly used for clinical MRI scans on the left (vest coil CRMS, Wisconsin, USA) and a 3D cad of a low pass birdcage: the gap in the middle of the legs are the capacitors. ©University of Sheffield.

The dimension of the birdcage must be chosen carefully because the field homogeneity improves with the coil length, while the field intensity at the isocentre of the volume is reduced. For hyperpolarised gas applications in the thorax, a larger coil may have advantages in B_1 homogeneity. Conversely, a geometry with *l=d* (where l is the coil length

and d the end rings diameter) optimizes the SNR profile in the range of ^{129}Xe Larmor resonant frequencies at 1.5 and 3 T (specifically at 25.9 MHz) [54]. Birdcages can be fed linearly or in quadrature; however, quadrature feeding, as previously described, produces a circularly polarised B_1 field. Typically, a hybrid quadrature driven circuit is used to drive the input power with a 90 degrees phase shift between the two inputs ports. At higher frequencies, birdcage coils are not the optimal choice due to their large electrical dimension (λ/20~11,7 cm at 128 MHz), and alternative designs such as TEM (Transverse Electromagnetic coil) body coil are preferred [55]. One commonly used design of transmit coil in hyperpolarised gases MRI is the dual Helmholtz coil (Figure 18b), commonly known as a vest coil because it wraps around the patient's chest like a jacket. This design is flexible, adaptable to different patient morphologies, and optimise the coil filling factor. The two loops are fed with a 90 degrees phase difference, creating a quadrature feed. However, this design, does not offer an optimal homogeneity of the transmitted B_1^+ and therefore, the transmitted flip angle could vary within the ROI. Although field homogeneity can be improved through capacitive or inductive decoupling, birdcage coils remains the best option to ensure a high degree of B_1 uniformity [56].

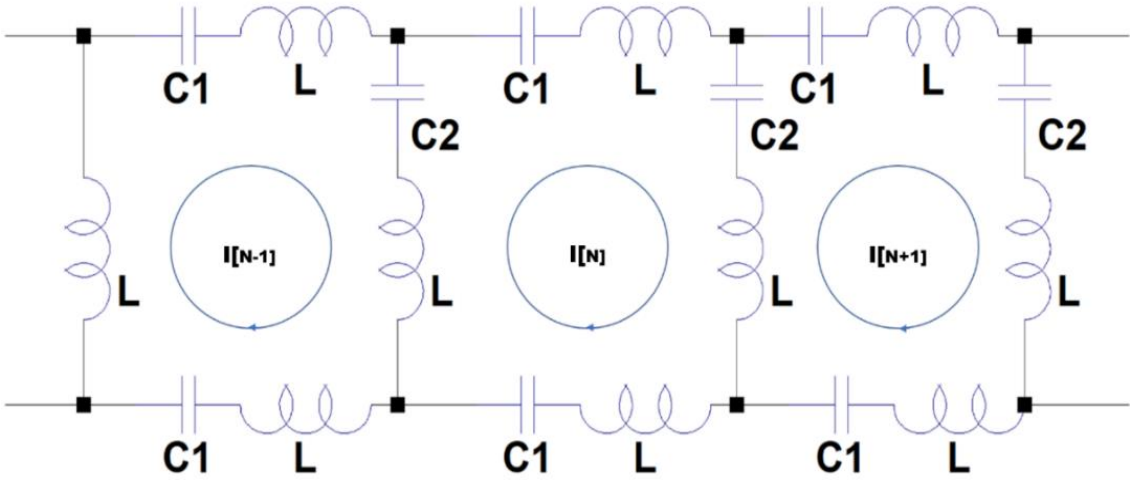

Figure 19: Example of birdcage circuits.

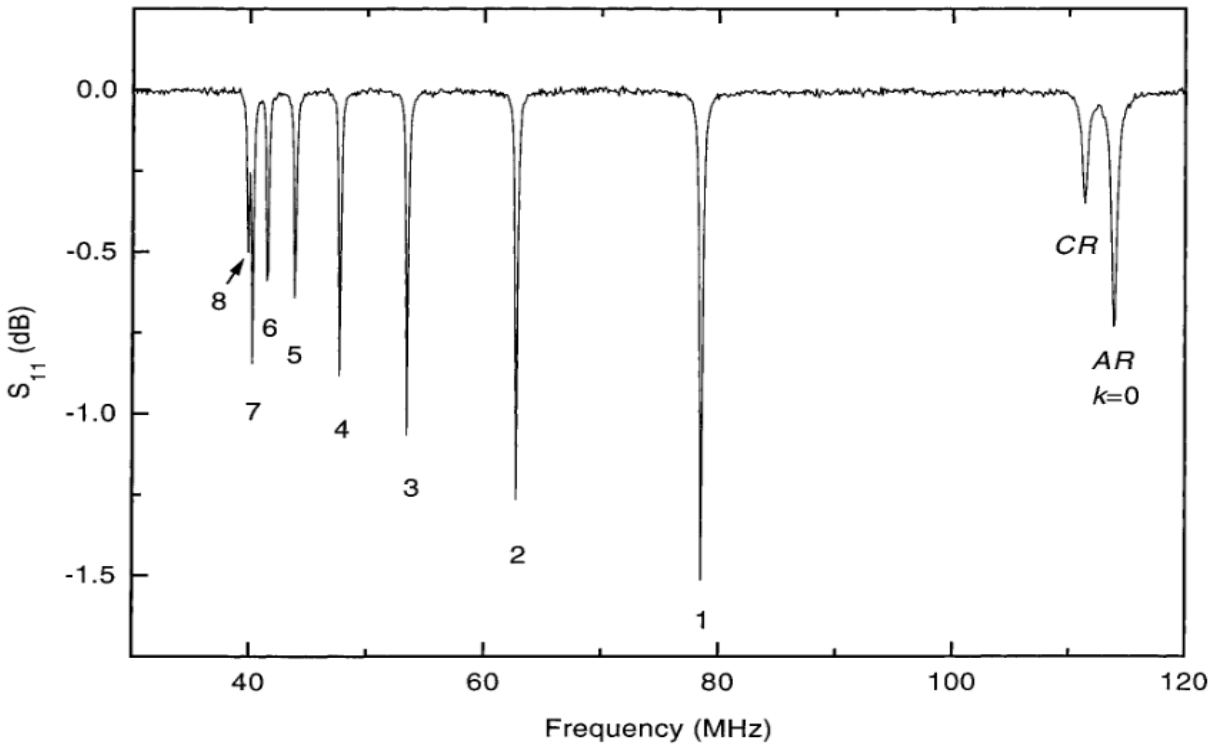

Figure 20: Resonant modes of a 16 legs high-pass birdcage coil, AC and CR indicate the end rings modes, the right resonant homogeneous modes in the third one from the right Reproduced with permission from [51]***.***

2.7 Surface receive and array coils.

RF surface coils are strategically placed near the surface of the sample with to ensure high sensitivity and high SNR in proximity to the sample surface [57]. Additionally, they function as a spatial filter that eliminate noise outside the region of interest. However, due to their smaller size when compared to volume transmitters, surface coils have a limited field of view (FOV) and restricted spatial discrimination in deeper regions [58]. The dimensions and geometry of the loops are crucial factors determining the strength of the induced signal. A surface coil with a small diameter ensures high spatial discrimination and high SNR at the centre of the Region of Interest (ROI) near the surface, at the expense of a limited field of view.

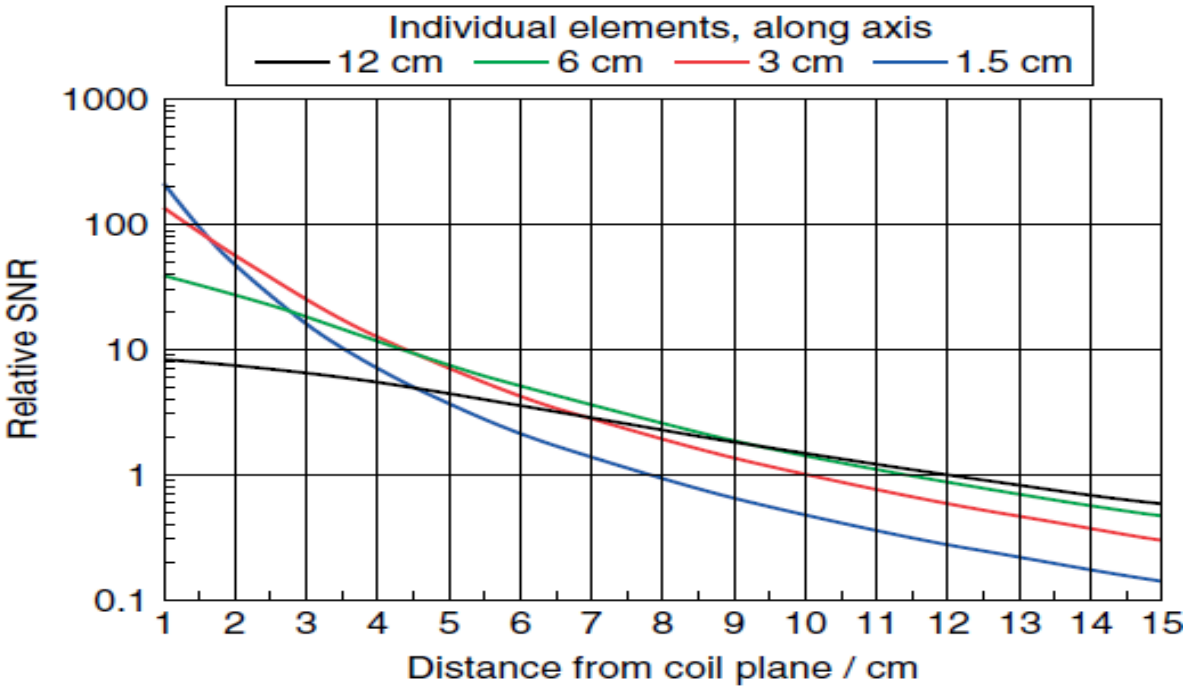

Figure 21: SNR for different lengths of the side of square-shaped coil at different distances from the sample. The smaller coil gives the best performance in proximity to the sample, while the larger coil has the best sensitivity if the coil is placed 10 cm far or more from the sample. Reproduced from [59] ***with permission.***

A decrease in signal strength is noticeable when placing the coil far away from the sample (Figure 21). In this case, sample losses are no longer more dominant compared to the coil losses. On the other hand, a larger coil offers a higher field of view and a stronger SNR in further region of the sample. The expression to evaluate the SNR of a surface coil is given by [60]:

$$SNR \propto \frac{\omega^2}{a\left[1+\left(\frac{x^2}{a^2}\right)\right]^{3/2}} \tag{81}$$

Where ω is the working frequency, a is the coil radius, and x is the distance from the surface of the sample.

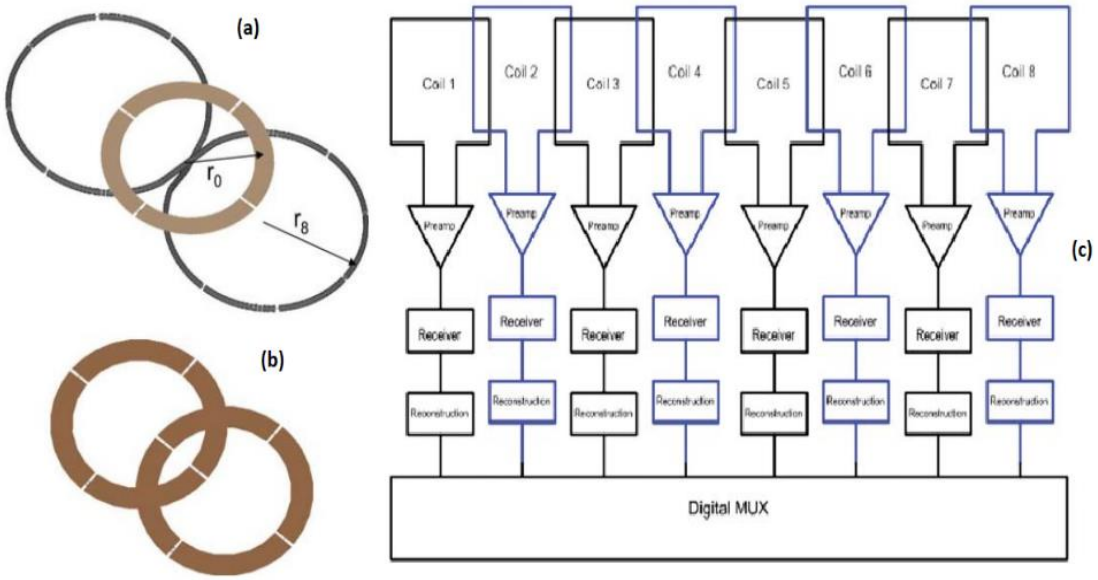

Figure 22: Three designs of Rx coils: (a) butterfly coil, (b) two-channel coil with two overlapped loops, reproduced with permission from [61]***; (c) Schematic of a phased array coil reproduced with permission from*** [62]***.***

Other standard models of surface coils are the butterfly or figure-of-eight coils, consisting of two adjacent loops with a current phase shift of 180° between the two components (see Fig. 22) [61]. These quadrature coils offer higher SNR (proportional to $\sqrt{2}$) with respect to similar designs, but they suffer from strong field inhomogeneity in the centre of the coil. It has been shown that placing a decoupled loop in the middle of the coil improves field uniformity [63]. A widely used design is the phased-array, [64] an array of single elements that combines the inherent sensitivity of individual surface coils and extends the FOV of the receiver antenna. However, each channel, must be decoupled from the other to avoid any mutual inductance, which can shift the tuning frequency and result in a loss of coils sensitivity. Figure 23 illustrates the mutual interactions among two loops single loops. Considering the mutual inductance, the voltage of the first coil is expressed by:

$$\boldsymbol{V_1 = \left(R + i\left(\omega L - \frac{1}{\omega C}\right)\right) I_1 + i\omega M_{12} I_2} \qquad (82)$$

In this equation, L and C ar the tuning capacitance and the self inductance of the coil, respectively, R represents the intrinsic noise of the loops, M_{12} is the mutual inductance between the coils, and I_2 is the current induced by the second loops. Therefore, $M_{12}I_2$, which represent the mutually induced noise, must be minimized by forcing M_{12} or I_2 to 0. $M_{12} = 0$ can be achieved through geometric decoupling between near elements. Overlapping the nearest neighbour elements create a virtual spine array, combining the

magnetic flux of the two coils. Alternatively, mutual inductance can be manipulated using lumped elements through capacitive [65], [66] or inductive decoupling approaches. However, these methods work only for a two-element array because they do not eliminate the RF interactions with further elements. Interaction with further elements, as well with the nearest neighbour, can be significantly reduced by minimizing the induced current (I_2=0 in equation 82), through the so-called preamplifier decoupling. A low impedance preamplifier (generally between 0.5 Ω and 3 Ω) is placed at the terminal of the coil circuit, as shown in Figure 24. The low impedance of the preamplifier Rp, in series with a matching circuit L_m and C_m resonant at the Larmor frequency, creates a parallel resonant circuit with the coil that yields high impedance, thus limiting the flow of the parasitic current I_2 on coil 1. The lower the input impedance of the coil, the higher the decoupling achieved. In addition to this decoupling function, preamplifiers have the primary task of amplifying the small, received e.m.f. signal in the coil; by almost 20-30 dB (almost 1000 higher, from the range of μV to the range of mV). However, preamplifiers are the first stage of the receiver chain, and due to the intrinsic weak nature of the signal, the noise added in the amplification stage has a significant influence on signal degradation. The noise of the preamplifier is characterized by the noise figure (NF) [67]; which depends on the device, the impedance of the source, and the impedance that the coil presents to the preamplifier. Figure 25 shows a simple preamplifier noise model, where V represent the e.m.f. induced in the RF coil, R is the coil resistance, N_p the noise generated inside the preamplifier, and N_s is the Johnson Noise defined as formula 47.

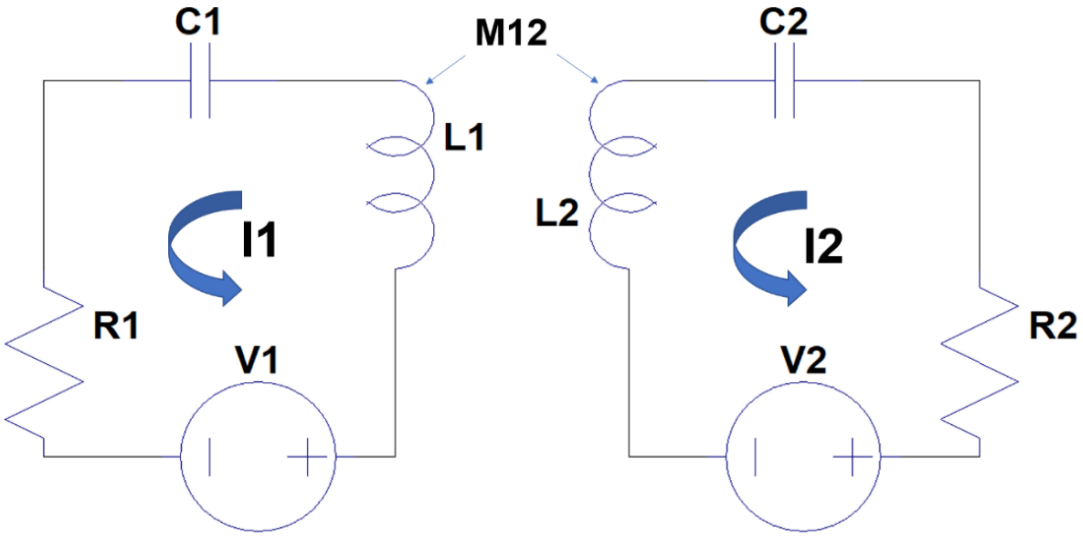

Figure 23: Mutual Inductance between two coils

Having defined these quantities, the Noise Figure is given by:

$$NF = 10log_{10}\left(\frac{N_P^2+N_S^2}{N_p^2}\right) \quad (83)$$

Currently, commercial preamplifiers have a noise figure between 0.2-0.5 dB and are integrated close to the coil circuit to minimize the noise interference in the cable path between the coil and device. However, if the number of array elements is high the preamplifier may be placed far away from the array and connected with a cable with a length of lambda/2. If the working frequency is low (i.e. in the range of 1.5T and 3T ^{129}Xe Larmor frequency), the required cable length needed becomes impractically large (8.45 meters at 17.65 MHz) and therefore an integrated phase shifter is needed.

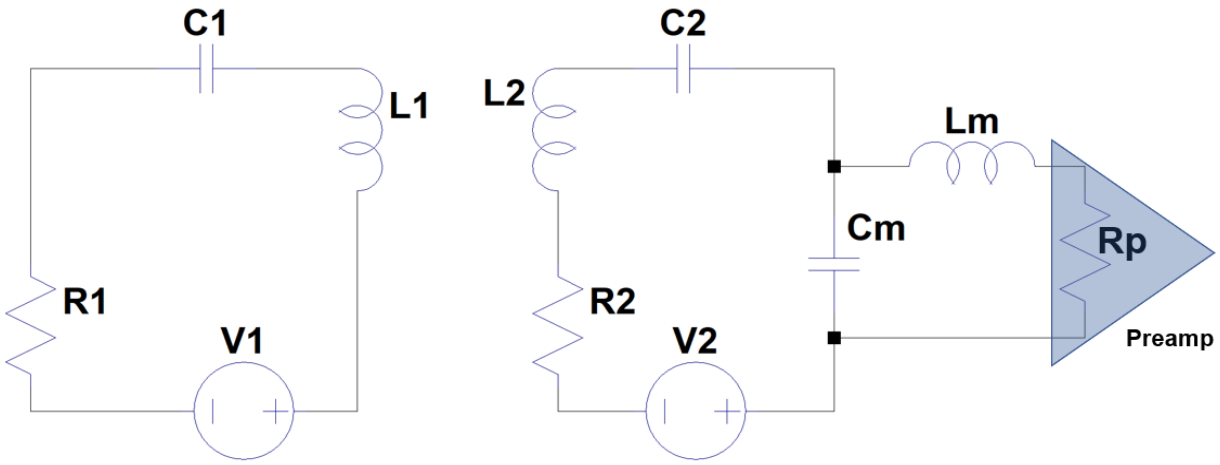

Figure 24: Preamplifier decoupling, Lm, Cm and Rp are Matching capacitance, Matching inductance, and Preamplifier resistance

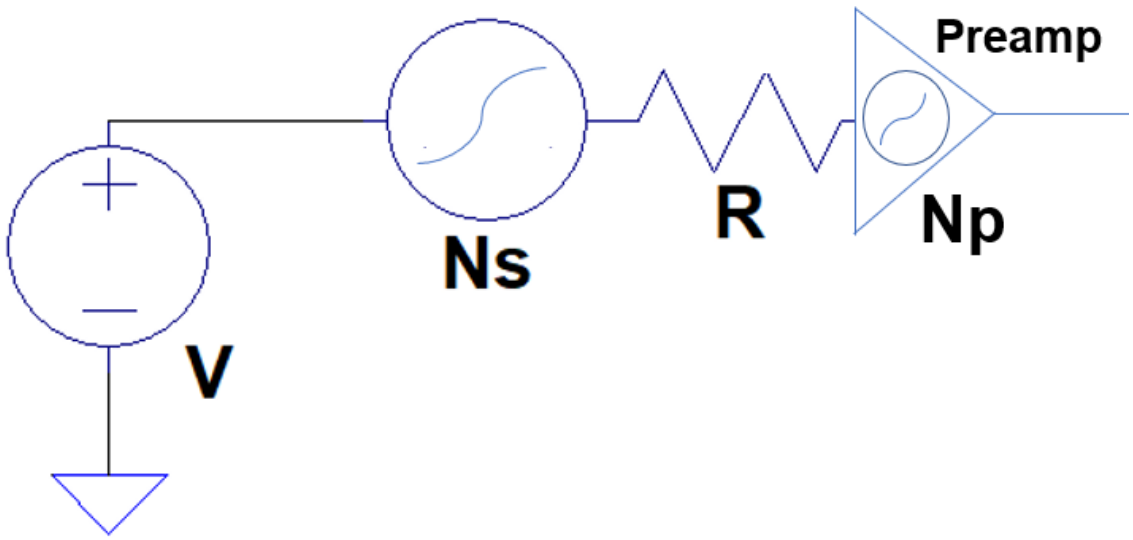

Figure 25: Noise model for a preamplifier.

Even with effective decoupled of each element through overlapping of the nearest neighbour elements and additional preamplifier decoupling, residual coupling is still exists, contributing to the increase in the total noise. One method to quantify the degree of standard coupling of among the elements is the noise covariance matrix, which is a NxN size matrix (where n is the number of array channels). The non-diagonal elements of the matrix represent the coupling between the different channels. An improved phased array design by Corea et al. [68], [69], uses inkjet conductors and capacitors, avoiding the use of commercial discrete capacitors. This design, which favours the flexibility and the conformal fitting for the patient, is becoming the state of the art of the development of the arrays for research and industrial environment, such as AIR coil by GE [70], [71].

2.7.1 Decoupling circuit

Decoupling the transmit and receive fields and blocking the mutual currents between two coils, is crucial for maintaining image quality and patient safety. A high impedance circuit designed to detune the coil can achieve this decoupling. However, this approach could lead to degrade image quality, due to the reduced coil sensitivity and may compromise patient safety due to the induced current and heat [94], [95]. Usually, active detuning RF circuits for MRI employ PIN diodes. Unlike standard PN diodes, PIN diodes consist of two heavily doped type-P and type-N regions separated by a non-doped intrinsic region I (Figure 26a). The high electric field in region I, facilitates charge transport between the region P and N, allowing the fast switching of the Diode and the control of the polarisation with a small amount of DC (Direct Current).

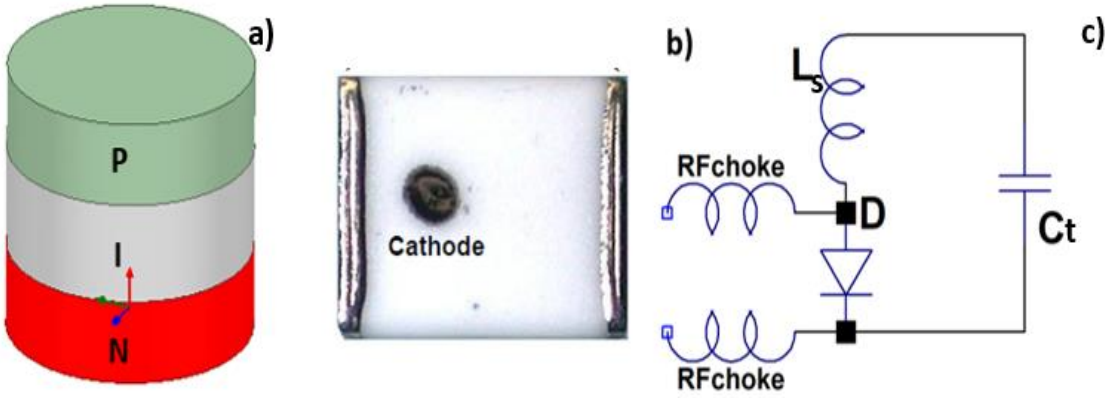

Figure 26: 3D examples of a Pin diode a), an example of packaged PIN diodes, that in the specific case of MRI application must be nonmagnetic in order to not interfere with the coil magnetic field, c) Active decoupling circuit that required DC to activate the diodes.

At RF frequencies, a forward biased PIN diode can be modelled as a small impedance, with the value inversely proportional to the current. Alternatively, reverse biased PIN diodes can be modelled as a parallel combination of capacitance and resistance in the KΩ range [49], creating, a high impedance along the coil conductors. However, if PIN diodes are placed in series, their intrinsic parasitic capacitance can degrade the coil Q factor. Moreover, the high RF transmitted RF power (around 10 KW) could potentially damage the component. To mitigate these issues, a PIN diode is usually inserted into a shunt LC circuit with a tuning capacitor and inductance Ls. When the diodes are forward biased, this parallel circuit causes a large impedance (or zero Conductance) to appear across the Ct, causing the RF loop current to decrease to zero (Figure 26c). Nonetheless, the DC path needs to be isolated from the RF current placing the RF chokes at the terminal of the diode.

2.8 Multi-Tuned coils

In the early days of MRI technology, the concept of multi-tuned RF coils emerged as a solution for receiving signals from nuclei with different gyromagnetic ratios (see Table 1, paragraph 1.2)[74]. These coils enable multinuclear MR imaging and spectroscopy without need to remove the coil or reposition the patient, facilitating the transmission and reception of signal from two or more nuclei [75].

Multi-tuned circuits are also desirable in hyperpolarised MRI of the lungs, where they enable the merging anatomical imaging of proton with the functional imaging of airways. One of the simplest ways to achieve a double resonance coil is by orthogonally placing two elements tuned to different Larmor frequencies. However, this design has limited spatial sensitivity, and orthogonal decoupling is feasible only for two or three elements [76]. Several alternative designs have been proposed in literature, including the development of nested birdcage coils [77], birdcages with alternate tuning in each leg, and coils employing PIN diodes or MEMS to switch the tuning frequencies. However, the most common strategy to achieve multi tuning is through the employment of LC trap circuits [78]. These are additive, passive resonating circuits, designed to selectively block undesired signal derived from another coil resonant at different frequencies (Fig. 27a). Practically, the trap circuit is created by placing an inductance in parallel with the tuning capacitor. Assuming an LC circuit as in figure 22, considering a coil tuned at the resonance frequency of ^{129}Xe $j\omega_{Xe}$, with proton trap we have:

$$\frac{1}{j\omega_{Xe}C} + j\omega_{Xe}L + \left(\frac{1}{\frac{1}{j\omega_{Xe}L_T} + j\omega_{Xe}C_T}\right) = 0 \qquad (84)$$

Here L, and C represents the inductance and the capacitance of the RF coil, whilst L_T and C_T are the trap capacitance and inductance respectively. Removing complex values from the denominators, we get:

$$\frac{j\omega_{Xe}C - j\omega_{Xe}^3 LC^2}{\omega_{Xe}^2 C^2} + \frac{j\omega_{Xe}L_T C_T}{1+\omega_{Xe}^2 C_T L_T} = 0 \qquad (85)$$

And therefore:

$$\omega_{Xe}^4(C_T L_T LC) + \omega_{Xe}^2(LC + C_T L_T + L_T C) + 1 = 0 \qquad (86)$$

This resonance will return a result of two resonant frequencies, ω_{High} and ω_{Low}. As a result, at the highest frequencies, the trap acts as a capacitive impedance, while at the lowest it acts as an inductive impedance. The added inductance can be adjusted by adding a tuning capacitance to achieve the coil at the desired resonant frequencies. However, this inductive impedance must be minimised because it has a direct influence on the coil quality factor. An alternative method is to use the LCC trap, which helps the control of the inductive reactance by adding a capacitor in series with the trap impedance (Figure 27b) [79]. An accurate model of a multi tuned receiver coil for ^{1}H, ^{3}He, and ^{129}Xe utilising trap circuits was demonstrated by Rao et al. [80]. Despite decrease in SNR resulting due to the addition of multiple traps, the feasibility of the same breath imaging for all the nuclei was successfully demonstrated [81].

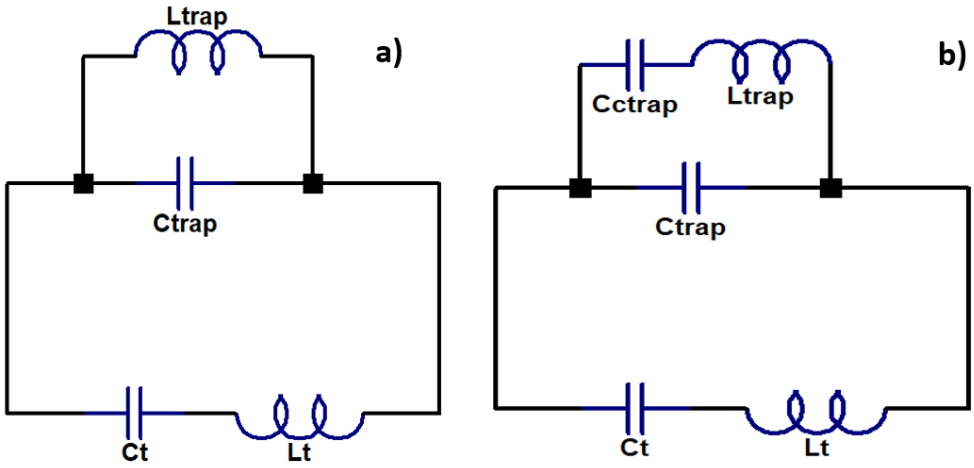

Figure 27: Example of trap circuit, L and C are the tuning components of the coil, Lt and Ct the trap circuits a), On the left the LCC trap circuit in ref [72].

2.9 Parallel imaging

In standard MR imaging, the signal from each element of an array coil, is typically combined using a sum of squares reconstruction [64]. Parallel imaging exploits the unique sensitivity of individual elements in an array coil to reduce the scan time [82], [83] by reducing the number of phase encoding (Figure 28). This is particularly advantageous for applications that demand short scan times, such as hyperpolarised MRI or cardiac imaging, which are often performed during a breath hold manoeuvre. Two principal methods of parallel imaging are employed: the first method, SENSE [83] reduces the phase FOV of the image by a factor R and uses sensitivity maps of the RF coil to reconstruct the full image from the aliased data. The second method, referred to as Generalized Auto-calibrating Partially Parallel Acquisition (GRAPPA), reconstructs the missing phase-encoding lines in the k-space through a linear combination of the data from nearby points [84]. In parallel imaging Signal to noise ratio SNR_p can be evaluated as:

$$SNR_p = \frac{SNR}{g\sqrt{R}} \tag{87}$$

Here SNR indicates the Signal to Noise ration of the image acquired without parallel imaging, R the acceleration factor and g is the geometry factor that describes the pattern of spatial noise enhancement. The g-factor is specific to each coil design and must be minimised as much as possible through accurate receiver coil design. Typical acceptable values for the g-factor range from approximatively 1.1 and 1.4 [85]. Nonetheless, parallel imaging is attractive in Hyperpolarised MRI, offers significant advantages beyond the reduction of scan time. The reduced number of acquired k-space lines not only limits the number of transmitted RF pulses needed for phase encoding, but also reduces the loss of valuable gas hyperpolarisation. Consequently, this allows for the use of higher flip angles, which affects the typical SNR trade-off observed in parallel imaging in proton MRI [86].

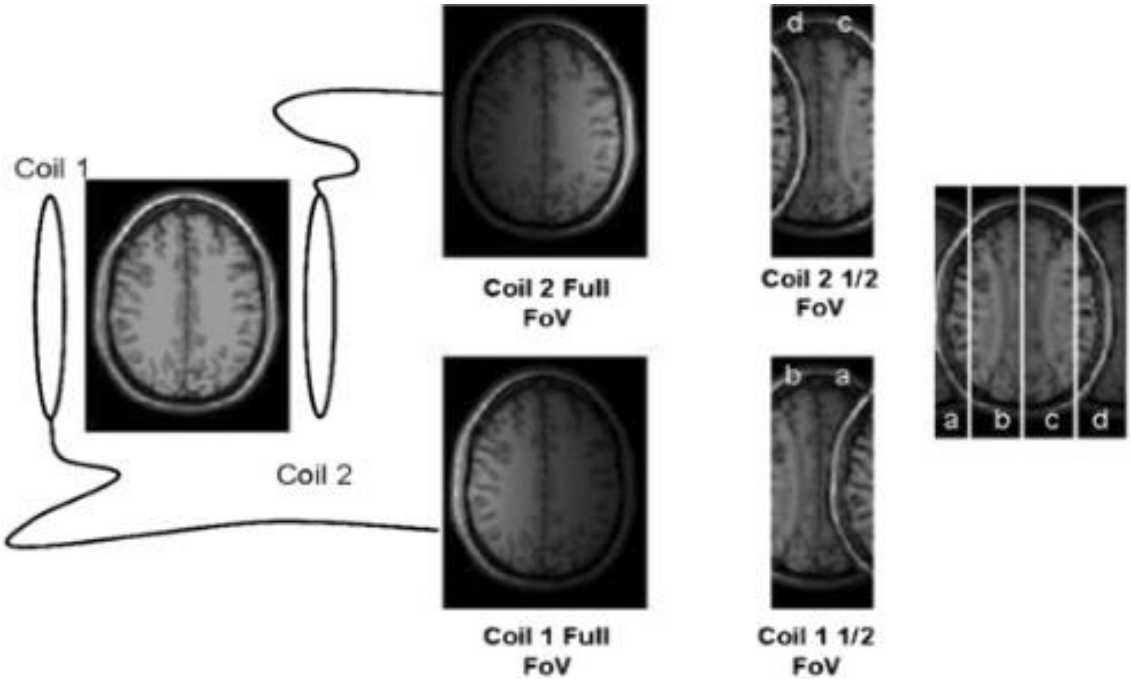

Figure 28: Parallel imaging reconstruction Due to the reduced FOV, each image from a single element shows strong aliasing. Thanks to the parallel imaging algorithms are possible to reconstruct the image with full FOV. Reproduced from [87] ***with permission.***

2.9.1 SENSE (Sensitivity encoding) parallel imaging reconstruction.

SENSE reconstruction imaging was first introduced by Pruessman et al. [106] and took advantage of the inherent coil sensitivities of each element in an array. Reduction of the k-space is achieved by decreasing the sampling of the k-space while maintaining the same resolution. The ratio between the sampled k-space line and the real resolution of the k-space, along with the reduction of the acquired lines, is expressed by the acceleration factor R, which represents the gap between each acquired phase-encoding line. Reconstruction of the images in the Cartesian space will result in aliased images.

The second part of SENSE reconstruction involves recreating the full FOV images. The critical point is that each single coil image occur with different weights according to their local sensitivities [83]. The coil sensitivities are used to calculate the U unfolding matrix, expressed as:

$$U = (S^H \Psi^{-1} S)^{-1} S^H \Psi^{-1} \tag{88}$$

Ψ^{-1} is the noise correlation matrix and S is the coil sensitivity matrix defined as:

$$S_{\gamma,\rho} = s_\gamma(r_p) \tag{89}$$

Here, γ index count the coils, ρ indexes the super-imposed pixels, r defines the position of the pixel, and s_γ the spatial sensitivity of the coil. With the unfolding matrix, the separation of the signal then can be performed through:

$$v = Ua \tag{90}$$

Where v has the dimension of the superimposed pixels. SENSE can be applied independently in any position of the imaging volume, and the formulas 88, 89, 90 are independent by the number of encoding directions. The main change in a 2D SENSE reconstruction is to place the correct values of the image in the corrected matrix and vector [88].

Chapter 3: Hyperpolarised ^{129}Xe MRI

In vivo, Hyperpolarised MRI was first employed in the second half of the 1990s [89]–[91], and has since been widely used in lung MRI as a contrast agent to reveal various aspects of anatomical and functional information. Currently, this technique is in the process of translating towards clinical practice for the early diagnosis and understanding of a variety of lung diseases [92]. This chapter will cover the physical properties of Hyperpolarised gases and most commonly used methods to polarise them. Additionally, various techniques and features of hyperpolarized MRI will be described.

3.1 Hyperpolarised Gases

Proton Magnetic Resonance Imaging (MRI) is a well-established imaging modality often used in the clinical assessment of certain patient groups. However, the proton density of lungs is low compared to other organs [93], resulting in a very low signal when imaged using standard proton imaging techniques; unless they display some pathology such as fibrosis or collapsed segments. For this reason, the use of hyperpolarised (HP) gases as a contrast agent for lung imaging has steadily gained interest in the last 20 years. HP gases, such as Xenon-129 ^{129}Xe, and Helium ^{3}He, are inert gases isotopes (see table 5 for their physical properties), with an artificially enhanced magnetisation, resulting in signal approximately 10^5 higher compared to thermal polarisation. Due to the increased signal and sensitivity of the technique to detect airway obstruction, HP MRI is a powerful tool to evaluate diseases such as chronic obstructive pulmonary disease (COPD), asthma and idiopathic pulmonary fibrosis (IPF) [94]. Helium-3 and Xenon-129 are the most common HP gases used in research; however due to the scarcity (1.37×10^{-4} %) and high price (~1000 $ per litre) of ^{3}He [95], many centres moved towards using ^{129}Xe. ^{129}Xe has a large natural abundance in the atmosphere (26.44%) and is cheaper (the price of ~100 per litre $). Despite its lower resonant frequency (17.65 MHz at 1.5 T), which results in a lower signal-to-noise ratio (SNR) when compared to ^{3}He (48.7 MHz at 1.5 T), ^{129}Xe MRI offers similar anatomical and functional information, thanks to advances in polarisation techniques, pulse sequences, and RF coils. Additionally, ^{129}Xe is highly soluble in blood, allowing

imaging of different aspects of lung function, including ventilation, perfusion and gas transfer [96]. As a results, ^{129}Xe MRI has become an important instrument for the assessment of additional lungs diseases such as IPF (Idiopathic Pulmonary Fibrosis) [97] and for the quantify capillary gas uptake [98]. Moreover, the long T1 ^{129}Xe in the blood plasma (21.7 seconds) allows it to be transferred to other organs and tissues [99]. In recent years, dissolved phase ^{129}Xe has been proven as a useful method to image blood and tissue perfusion in several organs, such as brain, kidneys, or liver.

Table 5: Principal properties of the Hyperoplarised gases compared with proton

Properties	^{1}H	^{3}He	^{129}Xe
Isotope abundance (%) [a]	99.99	1.37×10^{-4}	26.44
Nuclear spin, *I* [a]	1/2	1/2	-1/2
Gyromagnetic ratio (MHz/T) [a]	42.58	32.43	-11.7
Spin density (10^{19} atoms/cm^3) [b]	6690	2.37	2.37
Chemical Shift (ppm)[c]	----	~0.8	~250
Self-diffusion coefficient (cm^2/s) [d,e]	2×10^{-5}	2.05	0.062
Ostwald solubility in blood [f]	----	0.0083	0.146

3.2 Hyperpolarisation physics – a brief introduction

At equilibrium, ^{3}He and ^{129}Xe isotopes have a low spin density due to their physical density compared to ^{1}H atoms in the body. A standard sample of Hyperpolarised gas (around 500mL/1L) contains about 0.0037 moles per atom per litre, whereas the spin density of proton in water is about 110 moles of ^{1}H per litre. However, the achievable magnetisation can be enhanced by a 10^5 factor [90] when compared to the thermal equilibrium (Fig. 29), thanks to the Hyperpolarised technique. The two main methods to hyperpolarise gases are spin exchange optical pumping (SEOP) [100] and metastability exchange optical pumping (MEOP) [101]. SEOP is generally the preferred technique because, unlike MEOP [102], guarantees larger volumes of gas extraction and works for both ^{3}He and ^{129}Xe. For this

reason, only the SEOP will be briefly reviewed as this work is focused on RF coils for hyperpolarised ^{129}Xe.

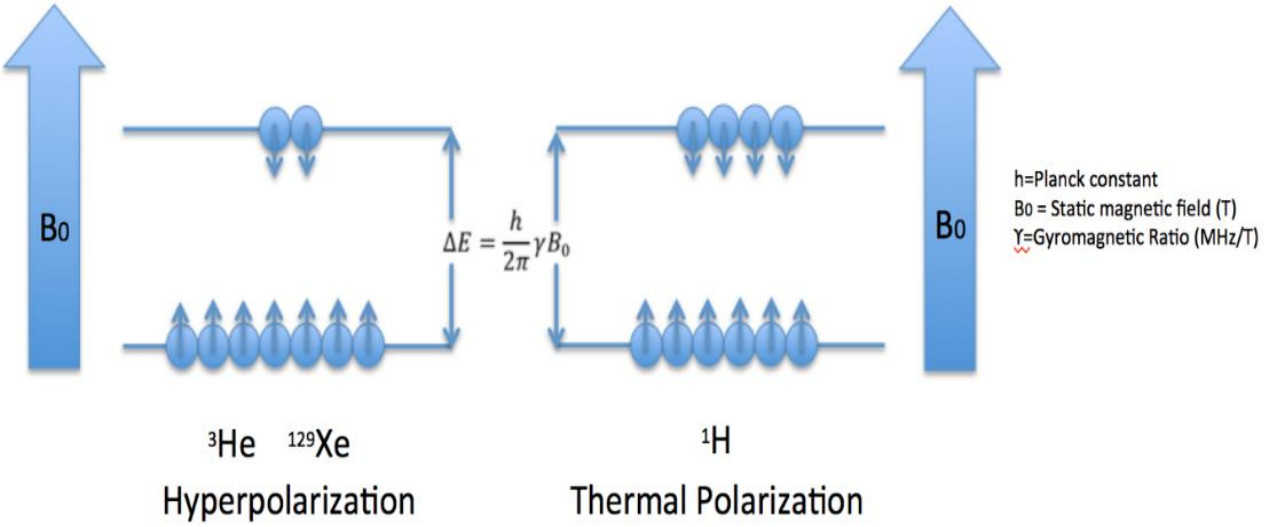

Figure 29: Polarisation comparison-The different levels of polarisations for Hyperpolarised gases (a) and thermal level (b), the greater difference between the spin up and spin down nuclei obtained by Hyperpolarisation of the nuclei permit to achieve a higher net magnetisation with a sensible increase in the signal.

The SEOP process takes place in an inert optical glass cell, containig an alkali metal, a noble gas, and an additional gas used as a spin exchange buffer. This process can be divided into three main steps:

- The cell is heated in an oven to reach the saturation, vaporising temperature of the alkaline metal. Rubidium (Rb) is usually preferred, due to its low melting point [103]. Vaporised rubidium is then excited by a 794.7 nm circularly polarized laser (σ^+) light. This wavelength is chosen to match the D_1 transition of the Rb valence electron, exciting the the electron spins and changing the energy state from the spin down sub-level ($m_j = -1/2$) of the $^2S_{1/2}$ ground state to the spin up sub-level ($m_j = 1/2$) $^2P_{1/2}$ [104]. In the excited level $^2P_{1/2}$ the electrons with spin m=1/2 and spin m=1/2 are equally distributed through collisional mixing and have the same probability to relax to the correspondent ground level (Figure 30). However, at the ground level, $^2P_{1/2}$ due to the continuous excitation by the laser light, there is a net excess of polarised electron with positive spin ($m_j = 1/2$).
- The Rubidium atoms randomly diffuse in the glass cell and collide against Xenon atoms, transferring polarisation from Rubidium electrons to Xenon-129 nuclei, equalizing the sublevel of the excited state of the Rubidium. Two different processes

could be involved in the spin exchange between alkali-metal atoms and noble gases: the "*two body*", or the "*three body*" interactions (Figure 31).

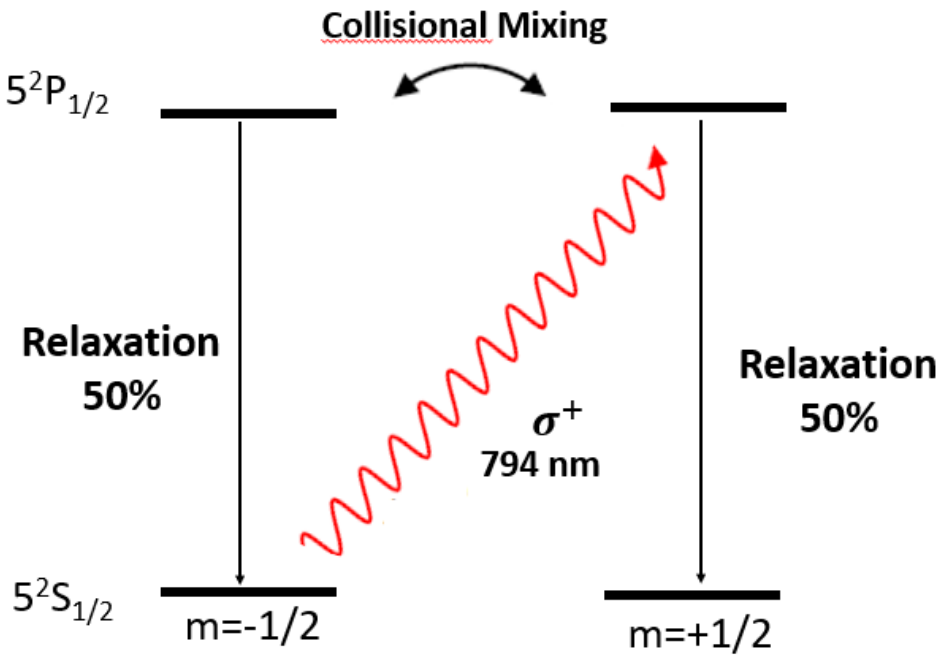

Figure 30: Polarisation of the Rb atoms. Excited by the laser light the electrons move from the ground state 5S to the excited 5P. At this state, there is a levelling between the spin with m=1/2 and m=-1/2 due to collisional mixing. However, after the relaxation due to the continuous excitation of the -1/2 electrons at the ground state 5S there is a net excess of electrons with spin +1/2.

Two body collisions, which take around 10^{-12} seconds, dominate the exchange between Rb and ^{3}H the spin exchange. In contrast, three-body collision dominate the interactions between Rb and ^{129}Xe and involve an additional molecule (specifically N_2). The N_2 buffer gas placed in the cell, favours the creation of Van der Waals bonds that takes a duration of 10^{-8} sec) [105]. The size of the electron clouds significantly influences the probability of spin exchange interactions, making the SEOP process longer for ^{3}He, and potentially lasting several hours [106]. Higher temperature and pressure increase the probability of "*two body*" interactions polarisation [107]. However, the large electron cloud of the Xe atom increases the likelihood of destroying spin polarisation. To minimise this effect, a gas mixture with 2-3% of ^{129}Xe is mixed with buffer gases (N_2 and ^{4}He).

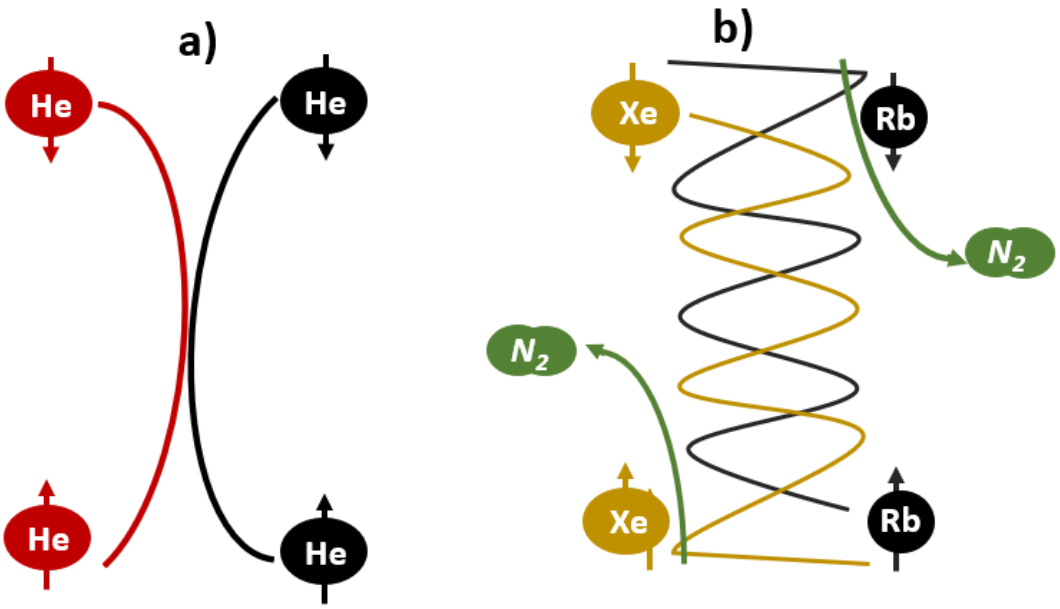

Figure 31: Draw of the spin exchange process. (a) Spin exchange through a binary collision between Rb-^{3}He binary. (b) For ^{129}Xe, spin exchange can occur through the formation of van der Waal molecules from 3-body collisions between Rb, ^{129}Xe, and N_2 molecules

After spin exchange, the rubidium atoms in the cell continues to absorb the laser light, allowing the process to repeat. Several factors can influence the probability to polarize the xenon nucleus, including the temperature, noble gas density, and pressure in the cell [108]. There are two practical approaches to SEOP process known as "continuous flow" and "stop flow". In continuous flow mode [109], [110] a high-density mixture of gases (5 amg) is used to obtain a large volume of polarised gas, with the rubidium being excited with a broad linewidth laser light (~2–3 *nm* FWHM). The disadvantage of this method is the low partial pressure of the hyperpolarised gases, which requires that the xenon be distilled and collected via a freezing process to separate it from the buffer gases. In stopped flow mode [111],a very powerful laser array with a low gas concentration is used. This method takes less time than the continuous flow mode and achieves a higher level of polarisation [112]. The main challenges include the need to extract gas from the mixture, typically achieved by cryogenic cooling, the high cost of the high-power laser, and the maintenance of the system. A revisited photon efficiency and optimisation process achieving level of polarisation of 35% at a 2 bar pressure and 0.1 nm narrow bandwidth laser was discussed in [113]. This method was very efficient offering a good SNR with a modest amount of Xe (400 ml) being inhaled. Other methods to hyperpolarize gases include Parahydrogen Induced Polarisation (PIHP) and

Dynamic Nuclear Polarisation (DNP) [114]–[116]; the details of these methods are not discussed as these methods are not used in this work.

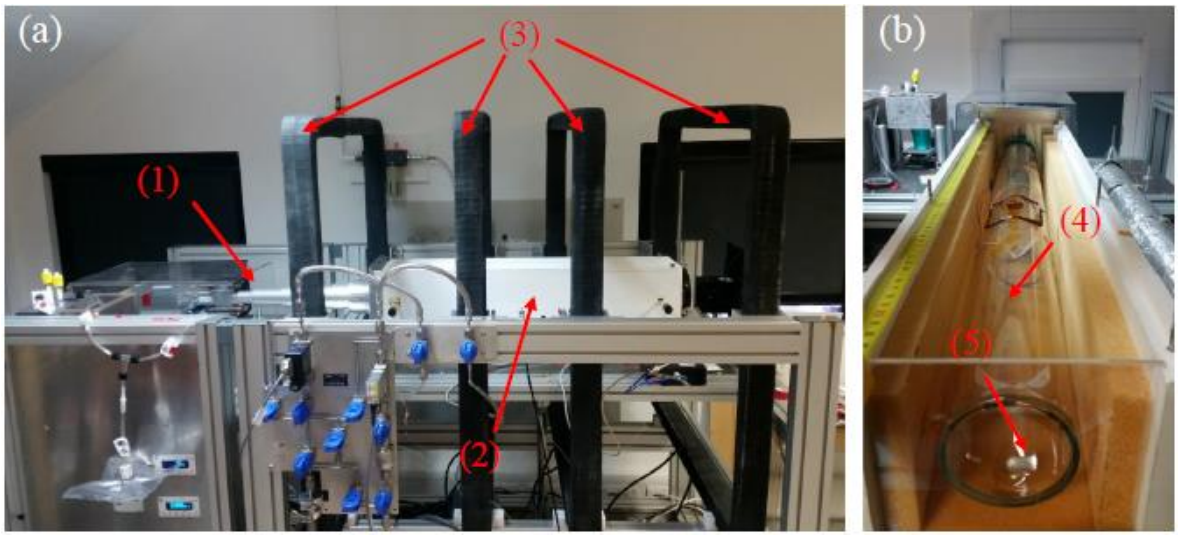

Figure 32: Photo of ^{129}Xe spin-exchange optical pumping polarizer, with permission [117]***. (a) The photo of ^{129}Xe spin exchange optical pumping polariser used in the Sheffield MRI facility. (1) Laser diode (170 W, 794.77nm wavelength) (BrightLock 200W, QPC, CA, US); (2) The temperature-controlled ceramic oven. (3) Coils to generate the B_0 field. (b) Ceramic oven with the lid off. (4) SEOP cell (Volume = 3500 ml, 7.5 cm diameter, 80 cm length); (5) the pool of rubidium is visible at the cell gas entrance. Gas mixture used throughout 3% Xe, 87% He, 10% N2. ©University of Sheffield.***

3.2.1 MRI sequences used - Gradient Echo Sequences (GRE)

Gradient echo sequences were first introduced by Haase et all. [118]. This sequence employs a single transmitting RF pulse for each phase encoding step, with an arbitrary flip angle, producing the echo signal through the phase inversion of the readout gradient. Even if a smaller signal is received due to the smaller flip angle, the short repetition time allows faster acquisition time. Unlike the spin echo sequences, gradient refocusing directly uses the FID following the RF pulse. As a result, the transverse decay of the GRE signal is therefore determined by the T_2*. Unwanted phase dispersions by means of T_2* processes could eventually be minimized by using short TE and small voxels [27]. In proton MRI with thermal recovery of the magnetisation, the signal of GRE (when TR>> of T_2) is a function of the flip angle, T_1 of the sample and TR. When the TR is less than the T1, the choice of the flip angle is crucial to obtain the maximum signal. Assuming a FA of 90°, the longitudinal magnetisation does not recover fast enough to the equilibrium state. Therefore, there exist an optimal flip Angle, known as the Ernst Angle α_E, that maximizes the signal of a Gradient Echo as a function of T1 of the sample and TR [119]:

$$\alpha_E = arcos(e^{-TR/T_1}) \quad (91)$$

When is important the define two tissues, even if the signal is maximised for a specific Ernst angle, the contrast is maximized at a higher flip angle [120] (Fig. 35).

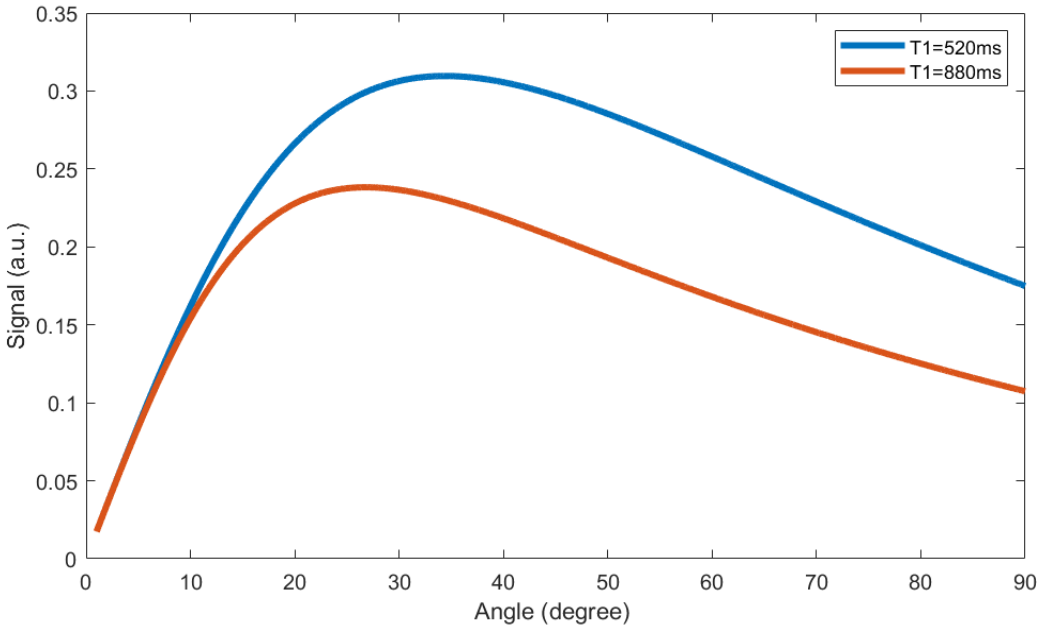

Figure 33: Ernst angle for musculoskeletal tissue (T_1=880ms) and grey matters (T_1=520ms) assuming a TR of 200 ms.

Another class of gradient echo sequences, known as Spoiler Gradient echo (SPGR), is used when the TR<T_2 and therefore the transverse magnetisation does not fully decay between each RF pulse. The signal now become directly dependent not only on TR, T_1 and FA, but also on the T_2^*. The residual transverse magnetisation can be "spoiled" or preserved in the next iteration of the sequence. Spoiling of the transversal magnetisation can be achieved in two different ways: applying an additional spoiler gradient to dephase additional transversal magnetisation, or through a change of phase of the RF pulse, which accelerates the dephasing process (Figure 34). The gradient spoiling method is performed by applying a readout along the slice selection gradient (and sometimes on the frequency encoding direction) with random or linear varying amplitudes after the signal acquisition. Gradient spoiling, however, is inherently non uniform and could lead to the creation of eddy

currents. RF spoiling, instead, randomly, or quadratically increment the phase of the RF pulse at each TR.

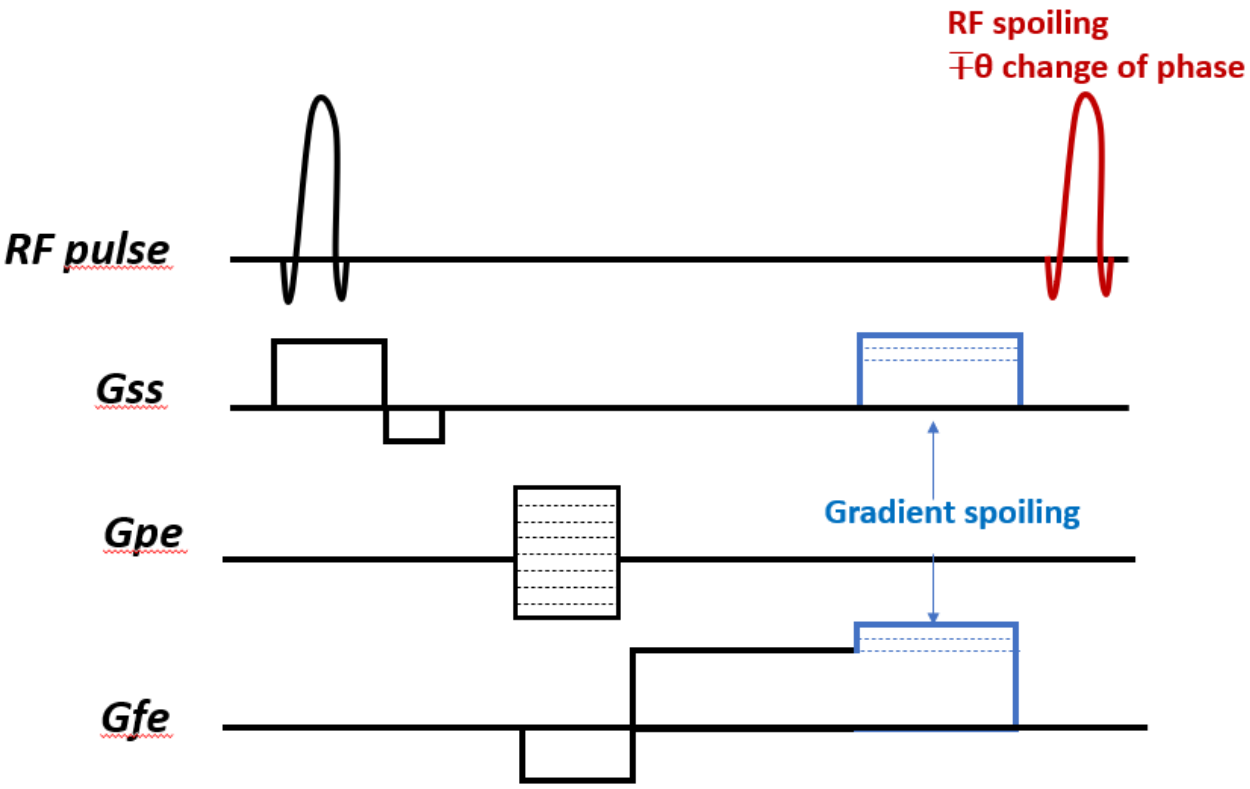

Figure 34: Example of a Spoiler Gradient echo with the two different methods of spoiling.

This method is more effective than the gradient spoiling in eliminating the transversal magnetisation and is spatially invariant. However, this comes at the price of a lower SNR since residual transversal magnetisation does not contribute to signal formation [121]. The typical signal of a perfectly spoiled SPGR is given by:

$$S_{SPGR} = \frac{\sin(\alpha)(1-e^{-TR/T_1})(e^{-TE/T_2^*})}{1-\cos(\alpha)(e^{-TR/T_1})} \quad (92)$$

The alternative method is to recycle the transverse magnetisation and reuse it in the next acquisition. These sequences are more commonly known as Steady State Free Precession (SSFP) and employ an additional rephasing gradient at the end of each TR to enforce consistency in the phase gradient area between repetitions; this ensures that spins are phase coherent. As a result, this leads to the formation of a steady-state transverse magnetisation after a few RF pulses. Once the steady state is reached, the signal is composed by a FID and successively by an echo that occurs before the next TR.

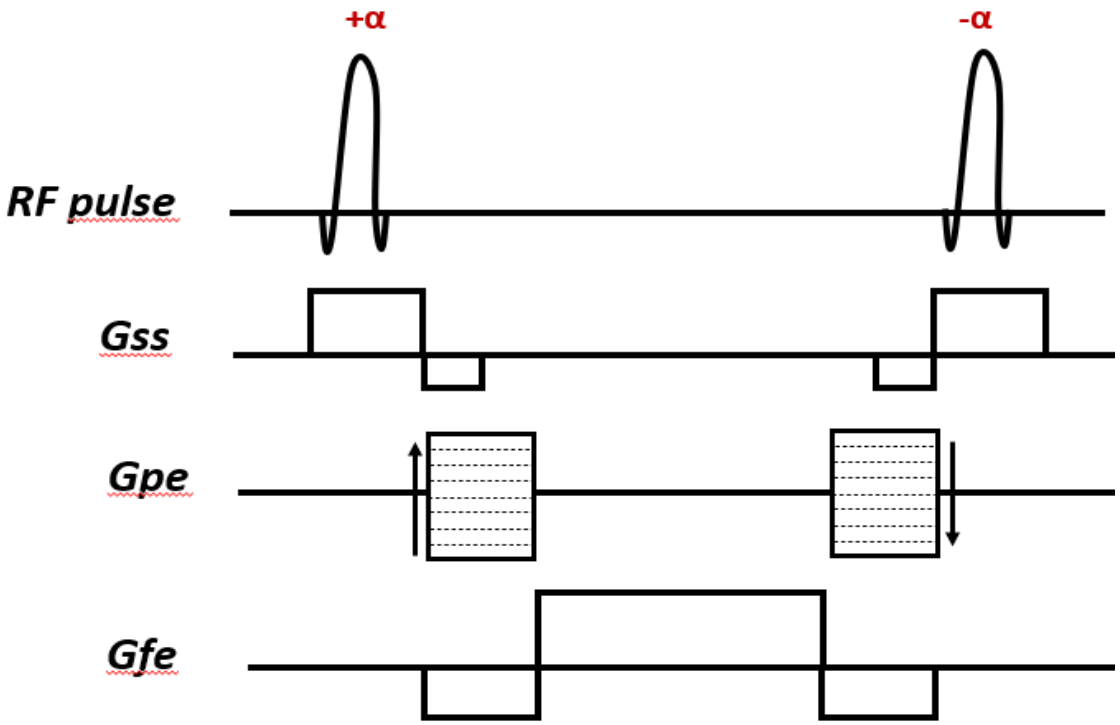

Figure 35: Example of a balanced steady state free precession sequence. The net gradient area along the three axes is zero.

Unlike other classed of GRE sequence, the net area of the gradient is fully balanced along the three axes, resulting in more efficient refocusing of the steady state magnetisation and thus an increased signal. However, bSSFP exhibits a strong sensitivity to local field inhomogeneities or susceptibility of the static magnetic field. If the sum of the phase accumulated at each TR due to the field inhomogeneities is equal to 180 degrees, the signal in these regions almost completely vanishes. In the final images, artefacts appear as dark bands. However, the problem could be minimised at low B_0, with an optimal shimming or with reduced TR [122], since the accrued phase depends on the TR of the sequence. For a frequency offset υ between the scanner synthesizer and local precession frequency, the dephasing ϑ is given by:

$$\vartheta = 2\pi\upsilon TR \tag{93}$$

The short repetition times needed by bSSFP can only be achieved with sufficiently fast switching and strong gradients. This is the reason why bSSFP imaging did not become widely used until the late 90's when the necessary gradient performance became available. The signal of a bSSFP based on its coherent steady-state magnetisation, offers the highest possible signal-to-noise ratio (SNR) per unit time of all known sequences [122]. SSFP

images show a mixture of T_1 and T_2 contrast, as expressed by formula 94 that defines the maximum peak signal [123], particularly in the case of high Flip Angle:

$$M_{ss} = \frac{1}{2} M_0 \sqrt{\frac{T_1}{T_2}} \tag{94}$$

Even though is not often used in common standard clinical practice, with the usage of low flip angle, the bSSFP images tend to be proton density weighted.

3.3 HP ^{129}Xe MRI sequence considerations

Due to the non-renewable polarisation, Hyperpolarised gases show different signal and magnetisation behaviour compared to ^{1}H under NMR experiments and require special consideration in terms of RF pulsing and k-space trajectory. Thus, different properties of hyperpolarised ^{129}Xe and ^{3}He are reflected in alternative optimised acquisition strategies. These properties will be described point by point in this paragraph.

1) Non-renewable longitudinal magnetisation

The bulk magnetisation of proton spins under thermal polarisation used in standard ^{1}H MRI has a T_1 recovery that permits recycling of the signal sufficient for imaging after each RF pulse. This is different for hyperpolarised gases because, after the application of the pulse, the magnetisation does not return to the previous hyperpolarised state (Fig 36). Instead, they return to a thermal polarisation state, and since the densities of gases are much lower when compared to the presence of protons, the level of the thermal equilibrium polarisation after the recovery time is very weak and challenging to image in. vivo. Therefore, the induced hyperpolarisation of the ^{129}Xe nuclei decays according to its spin-lattice relaxation time and the RF induced depolarisation. As a result, high flip angle sequences such as Spin echos or Inversion recovery are not generally feasible for hyperpolarised MRI imaging.

For these reasons, sequences with a lower flip angle (FA) (1°-20°) such as SPGR and bSSFP, are generally used to preserve the magnetisation after each RF pulse. The decay of the longitudinal magnetisation in a SPGR imaging experiment is described by considering a constant flip angle for each RF pulse:

$$M_z(n) = M_0 \sin(\alpha) \cos(\alpha)^{(n-1)} e^{[(-n)TR/T1]} \tag{95}$$

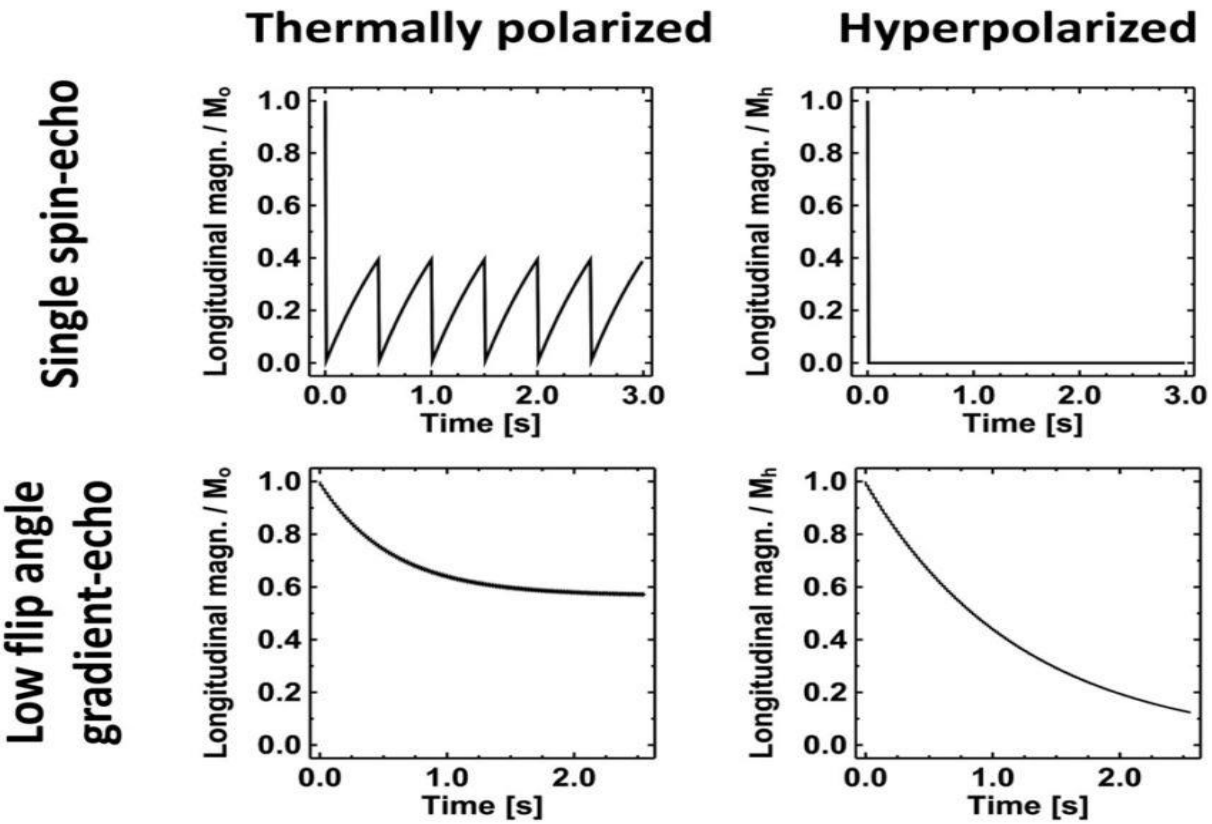

Figure 36: ***Signal decay | Comparison of the signal decay of thermal and Hyperpolarised nuclei after the application of high flip angle sequence (Spin echo) and the application of low flip angle GRE sequence. Reproduced from*** [95] ***with permission***

Where, M_0 is the initial longitudinal magnetisation, *n* is the number of RF pulse repetitions, and the exponential relaxation term is substituted by an exponential decay. The decay of gas hyperpolarisation in an SPGR sequence, as can be seen in equation (95) mis mainly governed by the transmitted flip angle and number of RF pulses. In a 2D SPGR sequence, the number of RF pulses corresponds to the number of phase encoding steps.

It can be demonstrated that for sequential phase encoding and constant flip angle schemes, the optimal angle to maximize the SNR is given by [124], [125], [126]:

$$\theta = \arctan \sqrt{1 \Big/ \left(\frac{N_y}{2} - 1\right)} \tag{96}$$

Where N_Y indicates the number of phase encoding steps. The decay of the longitudinal magnetisation is also commonly known as “k-space” filter. As shown in Fig. 38, for a sequential acquisition, an exponential decay of the “k-space” filter is expected, leading to a blurring effect related to the different weighting associated with each k-space line.

Centric acquisition of the k-space offers a higher SNR compared to sequential acquisition, at the price of smaller spatial discrimination and an enhanced blurring effect [127], due to the higher weight given to the central line of the k-space. However, a good compromise between sharpness of the images and SNR is to choose a flip angle that can maintain 20-30% of the initial longitudinal magnetisation at the end of the acquisition. A varying flip angle strategy can be eventually employed to minimize the blurring effect and increase the sharpness of the images [128]:

$$\theta = \arctan \sqrt{1/(N_y - n)} \tag{97}$$

Furthermore, a comparison between 2D and 3D sequences were analysed with a phantom and in vivo [129]. 3D acquisitions, due to the inherent higher averaging factor $\sqrt{N_z}$, and the reduced influence of the slice encoding dephasing given by diffusion, showed an increase of SNR when compared to the 2D sequence.

2) The Flip Angle must be calibrated for each single image acquisition.

Commercial scanners used for ^{1}H clinical application are provided with software that calculates and optimizes the transmitted flip angle with a prescan. In contrast, all coils employed for Hyperpolarised applications are specifically customized for the purpose, and there is no intrinsic signal until HP xenon is inhaled. Before each experiment, the flip angle must be calculated by the user when the coil is loaded by the patient. This can be done by inhaling a modest dose of HP gas and calculating the decay of a series of pulse acquires, composed of the RF pulse, the frequency encoding, and a spoiler gradient. The resulting signal will have a decay profile function as a function of the number of RF pulses, according to equation 95. The TR is always chosen very short (10 *ms*), to make the T_1 relaxation contribution negligible considering the timescale of a 2D imaging experiment [129], [130] Under this assumption, the decay is fitted using the $\cos(\alpha)^{(n-1)}$ function. In this way is possible to calculate the average flip angle over the whole thorax and adjust the RF power with to transmit the desired flip angle.

3) T_1 of hyperpolarised gas nuclei is heavily dependent upon spin-spin relaxation with paramagnetic molecular oxygen

The T_1 relaxation of the hyperpolarised gases become shorter proportionally with the quantity of molecular oxygen in the gas mixture. In fact, according to equation (98), T_1 decay is related to the partial pressure of the Oxygen ρ_{O2} in the tissues due to the dipolar interaction with the paramagnetic oxygen [131]:

$$\frac{1}{T_1} = \kappa \rho_{O2} \tag{98}$$

Where κ is a coefficient dependent on the temperature. The oxygen molecules are paramagnetic, and therefore the dipole-dipole interactions between Xenon and the residual oxygen in the lungs (after inhalation of the Xe the gas concentration are 80% Xe, 20% O_2 [132]) cause a T1≈20sec for the nucleus in the lungs. This is a strict constraint for the time of scanner acquisition. As a result, before each in vivo experiment, the patient is requested to clear the airways, breathe out the remaining air in the lungs, and inhale the Xe dose immediately before the start of the sequence. Also, the entire SEOP process must be executed under low oxygen conditions, and the Tedlar bag in which the Xe is stored must be pre vacuumed to remove O_2. Even if relaxation due to the paramagnetic oxygen is the main factor that determines the T_1 relaxation, additional phenomena contribute to the spin-lattice relaxation of hyperpolarised gas. During the SEOP and after, the relaxation is also influenced by the dipole-dipole interaction between the gas and the nuclei of the polymeric material of the gas bag ("wall effect"). However, when the Tedlar bag filled with hyperpolarised ^{129}Xe is left in a homogenous magnetic field, T_1 relaxation could least around 2-3 hours [133]. Differently, in the presence of gradient field or static field inhomogeneities, the T_1 can be drastically reduced to the orders of a few minutes [134].

4) During the scan breath holding is required to reduce the respiratory motion

Another important factor to consider is that the patient must keep the breath hold for several seconds with the purpose to minimise respiratory motion. In addition, breath hold reduces the quantity of Oxygen uptake in the lungs during the sequence. The average time of breath hold, and the T1 of ^{3}He and ^{129}Xe in the lungs, are constraints that have to be equally considered during a hyperpolarised ^{129}Xe MRI experiment.

5) The flip angle is not uniform over the whole thorax

The difference of magnetic susceptibility between the diamagnetic lung parenchymal and the air (which contains molecular oxygen) in the static magnetic field, brings some local inhomogeneities of B_0. This is due the presence of multiple numerous capillary alveolar interfaces, which are smaller than the typical size of an image voxel (2-5 mm). This small-scale fields lead to a rapid dephasing of the proton spin (T_2^* of 2ms at 1.5T). This effect, combined with the low proton density of the lung parenchyma makes the proton imaging of the airways and lung challenging. On the contrary, T_2^* of hyperpolarised Xe and He is longer due to diffusional narrowing (typically > 20 ms [135], [136]) and make it possible to obtain images with good SNR with specific Spoiler gradient echo or steady state free precession imaging. However, macroscopic susceptibility artefacts or banding artefacts persist, especially in the peripheral region of the lungs (i.e in the proximity of the diaphragm or main pulmonary blood vessels).

6) Gases are diffusive

Diffusion coefficients of pure ^{3}He and ^{129}Xe gas are respectively $D_{0;He}$ =2 cm^2/s; $D_{0;Xe}$=0.14 cm^2/s. These values are several orders of magnitude lower than the Diffusion coefficient of water in human tissues (i.e. $D_{0;H2O}$ =2*10^{-5} cm^2/s). In the lungs, the Apparent Coefficient Diffusion of the Xe mixed with air is $D_{0;Xe}$=0.04 cm^2/s and is sensitive to the underlying alveolar dimension. Thus, in the lungs, on a timescale of a few milliseconds, ^{129}Xe atoms collide with the alveolar walls several times, limiting the diffusion and leading to MR signal attenuation (S) described by:

$$S = S_0 e^{-bD} \tag{99}$$

S_0 is the initial signal, and *b* represent the diffusion weighting parameter dependent on the gradient amplitude, duration, and time interval between the two-phase encoding steps. Therefore, during the development of a specific sequence for hyperpolarised Xe MRI, *b* values of the slice, phase, and frequency encoding must be considered. In 2D SPGR applications, frequency encoding gradients usually exhibit the largest b-values. For 3D sequence, the b values depend on the number of phase encoding acquisition along z-axes n_z. However, in general, these studies employ a low number of n_z, and large FOV and is reasonable to assume $e^{-bD} \sim 1$.

3.4 Hyperpolarised ^{129}Xe in Dissolved phase MRI

Due to its high solubility coefficient in tissues, numerous studies have evaluated the potential of xenon imaging and spectroscopy in the dissolved phase for the assessment of gas exchange and blood perfusion. Following the inhalation of the gas, the xenon is taken up via passive diffusion, passing through a barrier composed of alveoli, epithelium, interstitial tissue, and capillary endothelium, into the blood vessels (Figure 37). Despite its complexity, the mean thickness of a healthy alveolus is 0.77 μm and the whole process takes only 1.5 *ms* [137]. As discussed previously, due to its relatively low solubility, only 1-2% of the Xenon can be found in the dissolved phase in the blood, which is transported to other organs [95]. However, the supply of Xe from the alveoli to the circulatory system acts as a continuous reservoir, permitting to obtain enough signal for spectroscopy and imaging. This paragraph will focus on a brief overview of ^{129}Xe dissolved phase imaging and spectroscopy in the lungs and other distal organs.

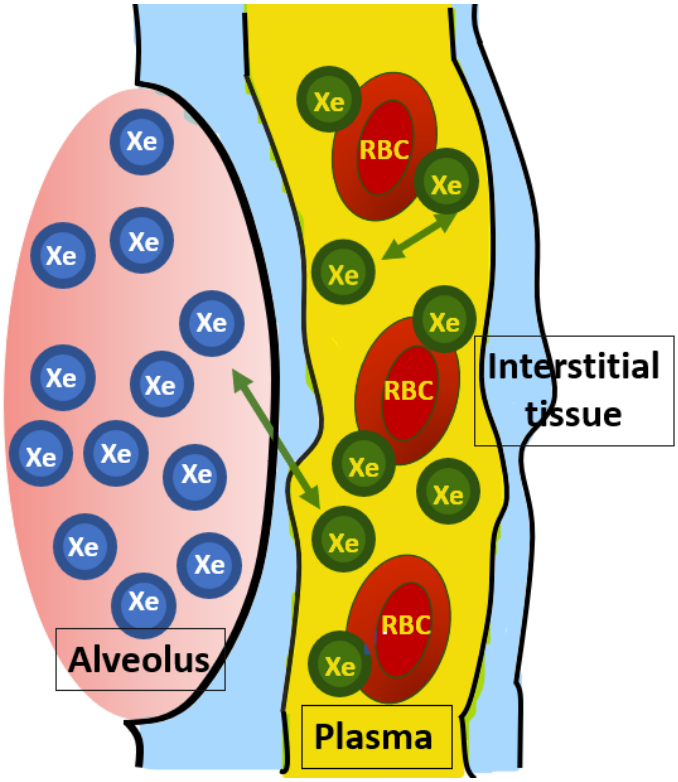

Figure 37: Representation of ^{129}Xe diffusive gas exchange across the alveolar membranes into the capillary

3.4.1 Dissolved phase Hyperpolarised ^{129}Xe MRI in the lungs

The first in vivo spectra of hyperpolarised ^{129}Xe in the dissolved phase was acquired in 1997 [138]. The spectra identified two different peaks, respectively to 197 ppm and 220 ppm

correspondent to dissolved Xenon in the tissues (lung parenchyma/plasma) and red blood cells [95] respectively. This phenomenon is the basis of the imaging technique known as xenon transfer polarisation (XTC) [139] (Fig. 38).

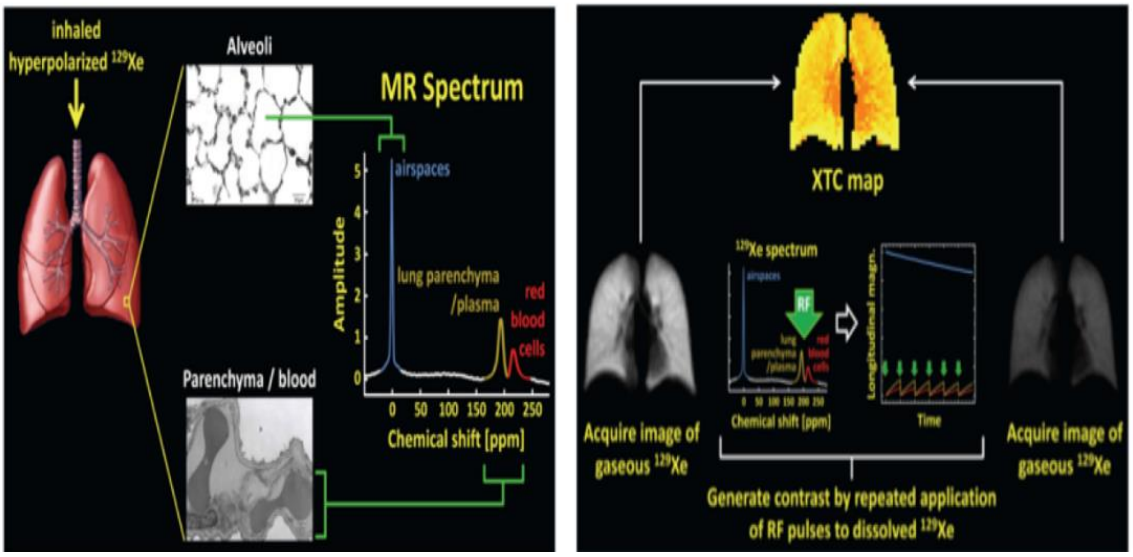

Figure 38: Xtc technique on the left the spectrum of ^{129}Xe in the lung; is noticeable a large chemical shift between the gas phase and the dissolved phase in the blood, on the right is shown the sequence of the XTC. Reprinted with permission from [92].

Initially, a gradient echo sequence is used to obtain gas-phase ventilation images of the lung. Subsequently, a RF pulse transmitting a high flip angle (20°), centred at the dissolved phase Xenon frequency, is applied, completely depolarizing the longitudinal magnetisation by the end of acquisition. During the application of the RF pulse, due to the ongoing exchange and uptake of Xenon between blood and alveoli, the gas-phase polarisation also decreases, allowing a second image to be acquired. By comparing the intensity of the two images, is it possible to evaluate the quality of exchange/uptake ratio in the lung. XTC was subsequently extended by applying multiple RF pulses at dissolved phase frequency (MXCT), enabling the possibility to obtain information regarding the tissue volume ratio of the alveoli (MXCT-F) and the mean functional thickness of the alveolar walls (MXCT-C) [140]. Through chemical shift saturation recovery (CSSR), Stewart et al. [141] demonstrated an enhancement of the tissue peak in patients with idiopathic pulmonary fibrosis (IPF) and systemic sclerosis, with a decreased red blood cell peak compared to

healthy volunteers. A relationship between the increased septal thickness of the alveolar wall and diseases was shown in [142].

Additionally, two barrier compartments were identified by decomposing the dissolved phase spectrum in the time domain which improved spectral fitting and suggested an overestimation of the IPF-blood barrier peaks in previous studies. The feasibility of direct dissolved xenon imaging was demonstrated by Cleveland et al. [143] and subsequently, simultaneous imaging of ventilation and dissolved phase imaging was studied by [144]. The large chemical shift of the spectrum allows the application of a large FA (~20°) pulse centred in the dissolved phase frequency and a low FA pulse (~0.5°) for the gas phase, which is the xenon reservoir for the dissolved phase signal. The dissolved and gas phase imaging are separated along the frequency encoding direction due to a chemical shift of ~200ppm. Kaushik et al. [145] using a 3D radial acquisition reduced the TE to 1ms (below the T_2^* (2ms) of ^{129}Xe in dissolved phase in the lung), separating the dissolved phase and gas phase pulses application and image acquisitions in two different TRs. Thanks to this strategy, the feasibility of same breath imaging of tissue and RBC is possible through the usage of 1 point Dixon radial imaging [146]. The sequence was used to evaluate a regional diagnosis of IPF comparing the results with CT and Pulmonary Function tests [98]. Another method is based on an iterative decomposition of echo asymmetric with a least-squares estimation (IDEAL) and consists of the acquisition of images at multiple echo times to improve the separation of gaseous, TP- and RBC-dissolved ^{129}Xe. IDEAL has also been tested with spiral and radial k-spaces trajectories; for example in Sheffield where we use a 4-echo implementation [147].

3.4.2 Dissolved phase ^{129}Xe in blood

T_1 relaxation of the dissolved phase Xe in blood has been reported in several studies. These studies are performed with blood samples with different oxygenation. At a static magnetic field of 1.5T, Wolber et al. reported a nonlinear descendent relationship of longitudinal magnetisation with the increase of blood oxygenation (2.88 ± 0.27s deoxygenated and 5.71 ± 0.35 s oxygenated blood). Norquay et al. conducted a similar experiment with a wider range of blood oxygenation, matching the previous experiment. When the blood is equilibrated with carbon monoxide, haemoglobin locks into a shape similar to the fully oxygenated haemoglobin, increasing T1 to 11±2 seconds as reported [96]. Dissolved phase

Xenon can also be a useful instrument to evaluate blood oxygenation through NMR spectroscopy [149]. The analysis of the chemical shift for different levels of blood oxygenation reveals a noticeable shift of the red blood cell peak and a nonlinear relationship between the dissolved ^{129}Xe signal decay and blood oxygenation. It was found that the higher the blood oxygenation (0.90-1 sO_2), the larger shift of the peak [148] (Fig. 39). However, the plasma peak remains at the same frequency and is used as a reference, showing a chemical shift of 6ppm between deoxygenated and fully deoxygenated blood [150]. Additionally, periodic modulation of the signal and chemical shift between RBC and tissue peak, close to the cardiac pulsation frequency, was observed. This could be attributed to changes in blood flow in the capillaries during the cardiac cycle. These findings provide additional information for the assessment of various respiratory and cardiovascular diseases such as COPD, IPF, pulmonary arterial hypertension, where knowledge of lung blood oxygenation is of interest.

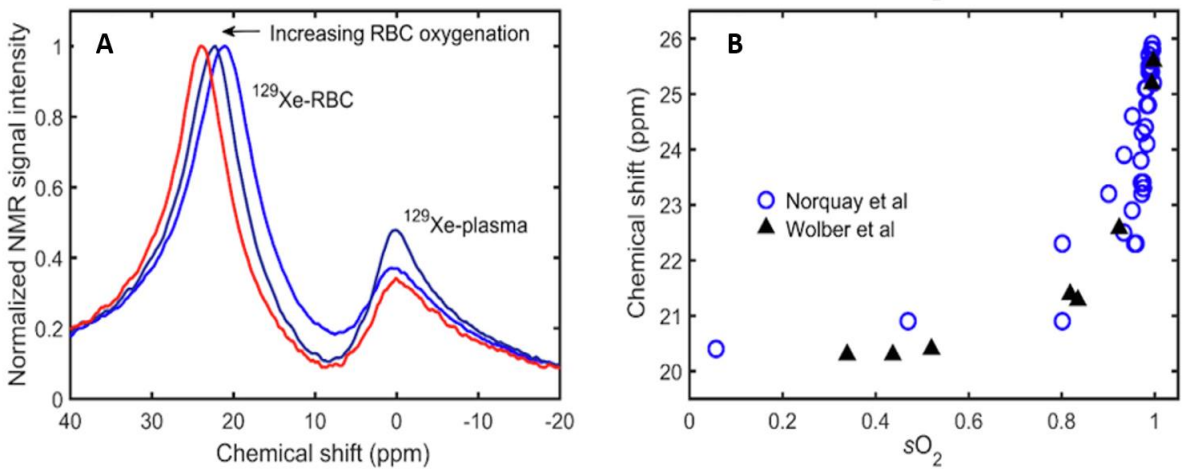

Figure 39: Chemical shift of the ^{129}Xe based on blood oxygenation. Reproduced under creative commons license from [149]

3.4.3 Dissolved phase ^{129}Xe in brain and kidneys

The long T1 of ^{129}Xe in the blood means that dissolved phase ^{129}Xe in the cardiocirculatory system to be transported to other tissues. Currently, clinical assessment of the brain are performed using functional MRI and CT with contrast agent such as iodine and gadolinium injected intravenous. Recently, concerns have been raised regarding patient safety with these contrast agents. In contrast, ^{129}Xe is safe, inert, and non-invasive, and can be easily inhaled. Due to these advantages, recent studies have explored its potential as non-invasive biomarker in the most vascularized organs such as kidneys and brain.

Spectroscopy of dissolved phase Xenon in the human brain has been performed [151], where five distinct peaks are noticeable (Fig. 40a):

- The peak at 188 ppm corresponds to soft muscular tissues.
- The peak at 192 ppm corresponds to white matter.
- The peak at 196 ppm corresponds to grey matter.
- The peak at 200 ppm corresponds to cerebrospinal fluid.
- The peak at 217 ppm corresponds to the red blood cell.

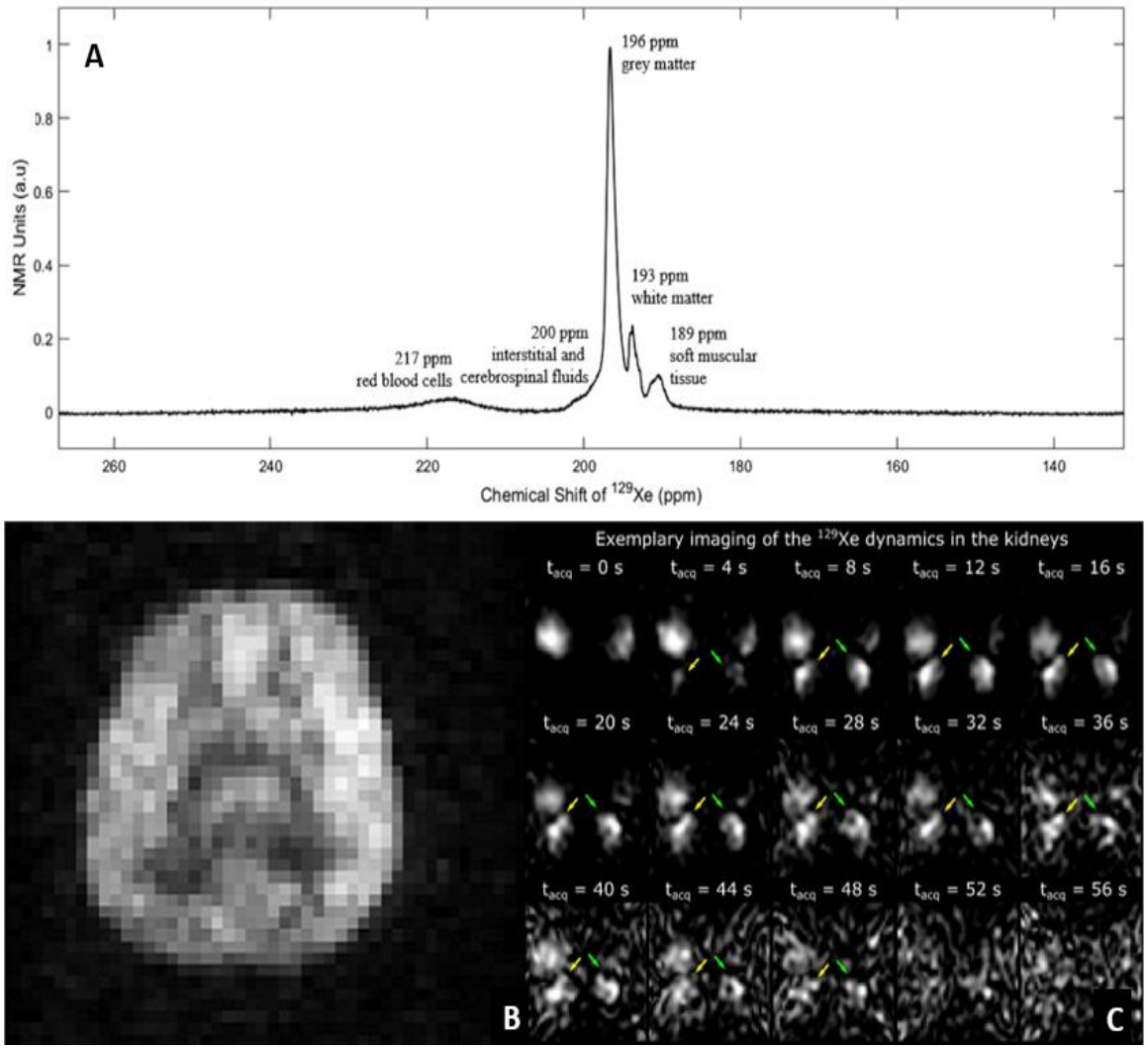

Figure 40: a) Dissolved phase spectra of hyperpolarised ^{129}Xe brain reprinted from [151] ***under creative commons license, brain imaging of ^{129}Xe in dissolved phase reproduced with permission from*** [152]***, and dynamic imaging of dissolved phase ^{129}Xe in the kidneys reproduced under creative commons license from*** [153].

Also, a dynamic spectrum over time has been acquired over a span time of 30 sec, with the highest peak corresponding to grey matter, detected around 22-24 seconds. Figure 40b,

show imaging of Xe perfusion over the whole brain, consisting of a map of the uptake of inhaled gas into the brain tissue across the intact blood-brain barrier. This highlights the regional blood flow volume and the mean transit time of the gas across the brain blood barrier. In recent years, many studies have evaluated the sensitivity of dissolved brain images to ischemia in rats, sensory stimuli, stokes, and Alzheimer in humans. Very recently, the dynamic kidney spectrum and imaging for dissolved phase have been studied [154]. Dissolved phase Xe spectra in the kidneys exhibit 5 peaks. The peaks at 197ppm and 217ppm correspond to tissue/plasma and RBC, respectively. The peak at 188.6 has been attributed to fat in the lower abdomen, outside the kidneys. Finally, the peak at 192ppm still need to be determined, but is assumed to be kidney specific. Additionally, the same study successfully performed the dissolved phase kidney dynamic imaging, at 3T (Fig 40c). These results confirm the potential of dissolved phase xenon imaging as a useful method for assessment of tissue perfusion, even in less vascularized tissues, such as the liver [155] and warrant further investigation.

Chapter 4:
Development of a whole-body RF coil setups for ^{129}Xe HP MRI of the lungs

Work from this chapter has been published in part in:

An asymmetrical whole-body birdcage RF coil without RF shield for hyperpolarized ^{129}Xe lung MR imaging at 1.5 T. Puddu C., Rao M., Xu X., Deppe M.H., Collier G., Maunder A., Chan H.F., De Zanche N., Robb F., Wild J.M. Magn Reson Med. 2021 Dec;86(6):3373-3381.

Clinical ^{129}Xe studies are usually performed with a flexible, dual channel quadrature Helmholtz coil vest design [151][152][158][159][160]. Although this design is capable of a high sensitivity, it lacks to transmit a very homogeneous B_1 field, that can sensibly vary with the patient morphology. In contrast, a birdcage type design can ensure a more B_1 field homogeneity throughout the coil volume, and therefore a uniform flip angle along with the anatomy of interest. This experimental chapter of the thesis will describe the development and testing of an asymmetrical ^{129}Xe birdcage RF coil for ^{129}Xe lung ventilation imaging at 1.5T (Figure 40). Birdcage will be used in conjunction with an 8-channel receiver array both fully compatible with the ^{1}H system transmit/receive body coil. The coil was developed and built to operate on the 1.5T GE Signa HDx 1.5 T scanner (GE, Milwaukee, WI, USA).

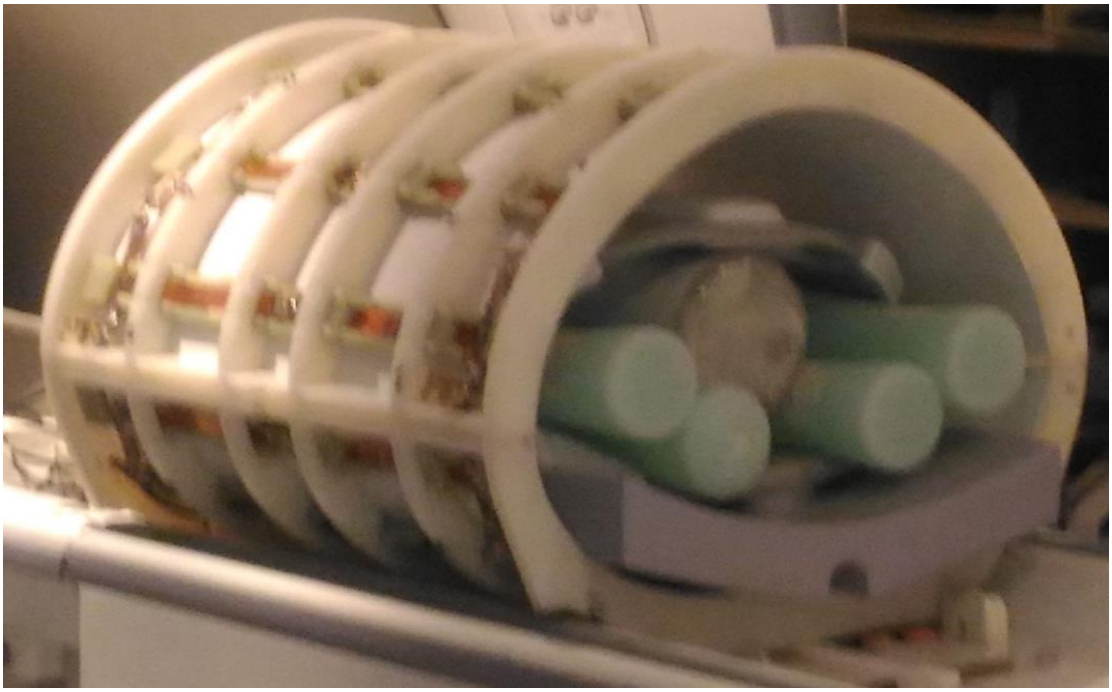

Figure 41: Asymmetrical Birdcage coil on the 1.5T scanner in combination with the 8-channel array. ©University of Sheffield

4.1 Literature review

Given the low Larmor frequencies of hyperpolarised nuclei, (17.65 MHz for ^{129}Xe and 48.64 MHz for ^{3}He at 1.5 T), large transmit coil designs inspired by birdcage topology are commonly utilised . To optimize the space within the bore, enhance patient comfort, and optimise coil filling factor, elliptical and asymmetrical designs have explored in the literature [161], [162]. Due to the non-symmetrical shape of these coil designs, to preserve uniformity of the field, careful balancing of the lumped components along the perimeters of the coil conductors is required [163]. This design approach has been successfully demonstrated for ^{3}He [164] lung MRI by our group and ^{23}Na [165]. Deppe et al. [166] combined this Tx asymmetrical elliptical body coil design with a flexible Rx 32 channel array to perform ^{3}He parallel imaging, facilitating volume imaging with high SNR and rapid scan time. Moreover, a similar design was implemented for ^{129}Xe MRI [167]. The elliptical design was also employed to develop a small animal coil for proton imaging at Ultra-High Field [168]. However, none of these implementations however demonstrated successful parallel functionality of the ^{1}H body coil for simultaneous ^{1}H anatomical imaging, which vital for assessment of structure from ^{1}H MRI alongside X-nuclear function.

4.2 Asymmetrical Birdcage coil: design

The topology of the birdcage was optimized for patient comfort and future accommodation of a receive array. Additionally, the coil size is maximized to fully utilise the magnet bore, providing the advantage of scanning more of the anatomy compared to the vest coil.

Several initial design considerations were taken into account:

a. The coil must be large enough to accommodate a medium sized patient and ensure uniform excitation over the entire FOV.

b. There should be additional space to accommodate an array receiver coil for either a ^{129}Xe and/or ^{1}H multiple receiver array.

c. The rigid structure of the coil former offers a consistent, homogeneous magnetic field with less potential variation due to differences in subject size and coil loading, when compared to the flexible transmit-receive vest coil designs, which fit the size of the torso of the patient.

d. The coupling of ^{129}Xe RF coils with the scanner's built-in proton body coil was to be considered in the design process by making all possible measurements inside the magnet bore. This enables anatomical ^{1}H imaging of the chest with the ^{129}Xe coils in-situ, allowing for the acquisition of co-registered ^{1}H and ^{129}Xe images in the same scan session or even in the same breath hold.

e. Due to the non-recoverable polarisation of the ^{129}Xe, small flip angles are typically employed in gas phase ^{129}Xe lung MRI. ^{129}Xe, can also be imaged in its dissolved phase in the blood using the gas in the lungs as a polarisation reservoir. In this case, the transmit coil must be able to deliver a wide range of flip angles, homogeneously and linearly with delivered RF pulse power up to 4kW.

4.3 Asymmetrical Birdcage coil: topology and structure

As mentioned in the introduction, the aim was to develop a birdcage with an asymmetrical elliptical topology. The birdcage base fits on the scanner, positioned 16 cm below the centre of the gantry. The topology is the same as described in [169], featuring a 12 leg

asymmetrical band pass birdcage coil, as shown in Figure 42. The design is optimized to work with the 1.5T GE Signa HDx magnet in Sheffield (GE Healthcare, Waukesha, Wisconsin), which has a 60 cm inner-bore diameter. The dimensions are as follows: length 47 cm (head-feet direction), common elliptical diameter 50.8 cm (left-right direction), and asymmetrical diameter 36.4 cm (anteroposterior direction), with the top half being 30 cm and the bottom half of 14.8 cm. The conductors are copper bars, each of 47 cm long, 1.5 cm width and 0.3 cm thick. The shape was calculated using a conformal mapping approach, that transforms the evenly distributed position from the circumference of a circle into a cylinder, resulting in a arbitrary cross section that produces a uniform transmit field. Assuming, that *f(x)* is an analytical function of the transform, the transformation domain also includes regions with optimal current distributions that solve the limit:

$$\lim_{x\to\infty} \frac{f(x)}{x} = 1 \tag{100}$$

The conformal mapping transformation can be solved through the following series expansions:

$$f(x) = x + \sum_{k=1}^{\infty} \frac{c_k}{x^k} \tag{101}$$

Where c_k identifies the transformation complex coefficients and x are the coordinates in the circle plane.

The theoretical basis for the calculations are more expressed in detail in the papers by De Zanche et al. [170][171]. The mechanical support was already constructed for previous studies, is a glass reinforced and flame retarding fibreglass epoxy, commonly known as FR_4. The structure can be split into two halves along the coronal plane to facilitate the patient positioning, and four nonmagnetic beryllium copper rods at the corners ensure the connection (Figure 43). Printed circuit boards (PCB) were soldered along the legs and end rings to allow the placement of tuning capacitors. The quadrature coil connection is ensured with two BNC connectors at the bottom end ring, specifically between the legs 5-6 and 7-8, at 90° of difference in the circular polarisation for a quadrature feed via a hybrid circuit (see figure 43). The circuitry of the coil is covered with thick Acrylonitrile butadiene styrene (ABS) cover sheet with 3 mm of thickness. A more detailed explanation of

geometrical design, as well as of technique for the capacitance estimation is described in full in [164]. Values of tuning capacitors are shown in Table 4.

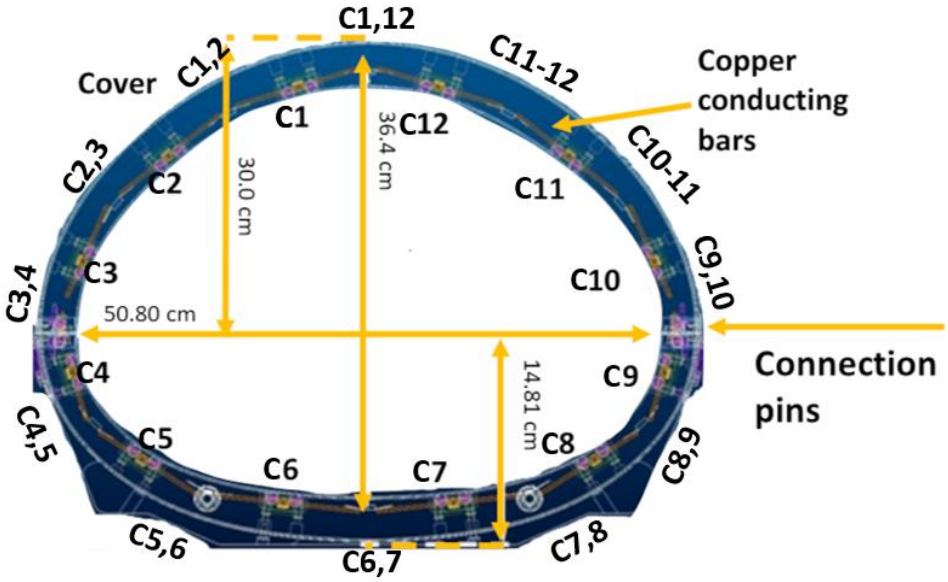

Figure 42: Axial section of the coil with the diameters and radii dimensions. Reproduced under creative commons license from [172]***.***

However, compared to the asymmetrical birdcage coil previously developed for hyperpolarised ^{3}He MRI, the ^{129}Xe birdcage does not employ an RF shield. It is designed to be transparent to ^{1}H RF transmit-receive coil within the scanner bore.

Additionally, as mentioned earlier, the birdcage features a band-pass design. This design choice is optimal to achieve maximal control of coil tuning at of 17.7 MHz, compared to 48.6 MHz for the previous ^{3}He design.

Table 6: Values of the tuning capacitors

END RINGS CAPACITOR VALUES						
C_1	**C_2**	**C_3**	**C_4**	**C_5**	**C_6**	**C_7**
450 pF	630 pF	780 pF	680 pF	910 pF	620 pF	550 pF

Due to symmetry about the y-z plane, only half of the values are shown (i.e. $C_1 = C_{12}$, $C_6 = C_9$).

LEGS CAPACITOR VALUES					
C^{1-2}	**C^{2-3}**	**C^{3-4}**	**C^{4-5}**	**C^{5-6}**	**C^{6-7}**
1700 pF	4400 pF	2200 pF	750 pF	860 pF	640 pF

Due to symmetry about the y-z plane, only half of the values are shown (i.e. $C^{1-2}=C^{1-12}$, $C^{5-6}=C^{8-9}$).

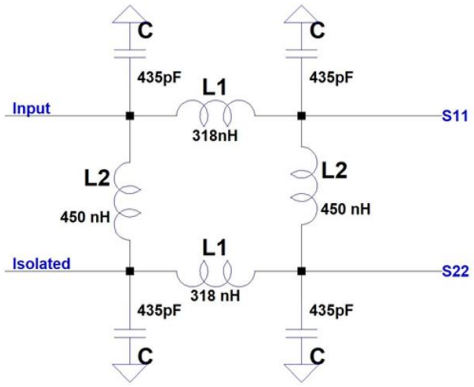

Figure 43: ^{129}Xe body coil mesh with copper conductors with 12 rungs which separate into two parts at the red line indicators. In the figure are also evidenced the mesh 6 and 9 where are placed the matching circuit. On the right the schematic of the hybrid coupler ©University of Sheffield.

4.4 Asymmetrical Birdcage coil: EM simulation

Before assembling the coil, a complete simulation of the RF setup was performed using FEM ANSYS HFSS 17.2 solver software. The simulation aimed to evaluate several aspects of the coil design:

a). B_1^+ field homogeneity of the ^{129}Xe birdcage. The ^{129}Xe birdcage was loaded with a human body model (σ= 0.14 S/m and ε_r= 81) with air spaces for the lungs, evaluating the homogeneity of the transmitting field of the asymmetrical birdcage along the coronal, axial and sagittal planes.

b). The ^{129}Xe birdcage RF coil was simulated for its ^{1}H RF transparency in 4 different configurations: one configuration without PIN diodes (tuned ^{129}Xe coil); and three configurations with 4, 8 and 12 PIN diodes applied, respectively, to de-tune the ^{129}Xe coil. To evaluate the transparency, the RF coils were positioned in their normal operating conditions; the ^{129}Xe birdcage RF coil was set in the detuned mode without excitation, and the ^{1}H body coil was tuned to the ^{1}H resonance with RF excitation to mimic the state of the RF coils during ^{1}H transmit and receive phase. The transparency of ^{129}Xe birdcage was assessed by the distortion it would cause to the ^{1}H B^+_1 magnitude and homogeneity.

c). The isolation S-parameters between the RF coils in all four configurations were simulated over a frequency span of 10 to 100 MHz. The ^{1}H body RF coil was tuned, and the ^{129}Xe birdcage RF coil was detuned as per the diode configurations mentioned earlier.

d). SAR was simulated in MATLAB (MathWorks, Natick, MA) as described in Collins et al. [26] using the EM fields exported from Ansys HFSS 17.2 for all the 4 diode configurations mentioned earlier.

The 3D model used in all the simulations is shown in figure 44. The setup is as follows:

1) A cylinder of vacuum with a height of 83 cm and diameter of 70 cm with an zero thickness that defines the domain volume of the simulation. The RF shield is defined by assigning a radiative domain to the coil to emulate the proton coil RF shield and truncating infinite free space to a finite calculation domain.

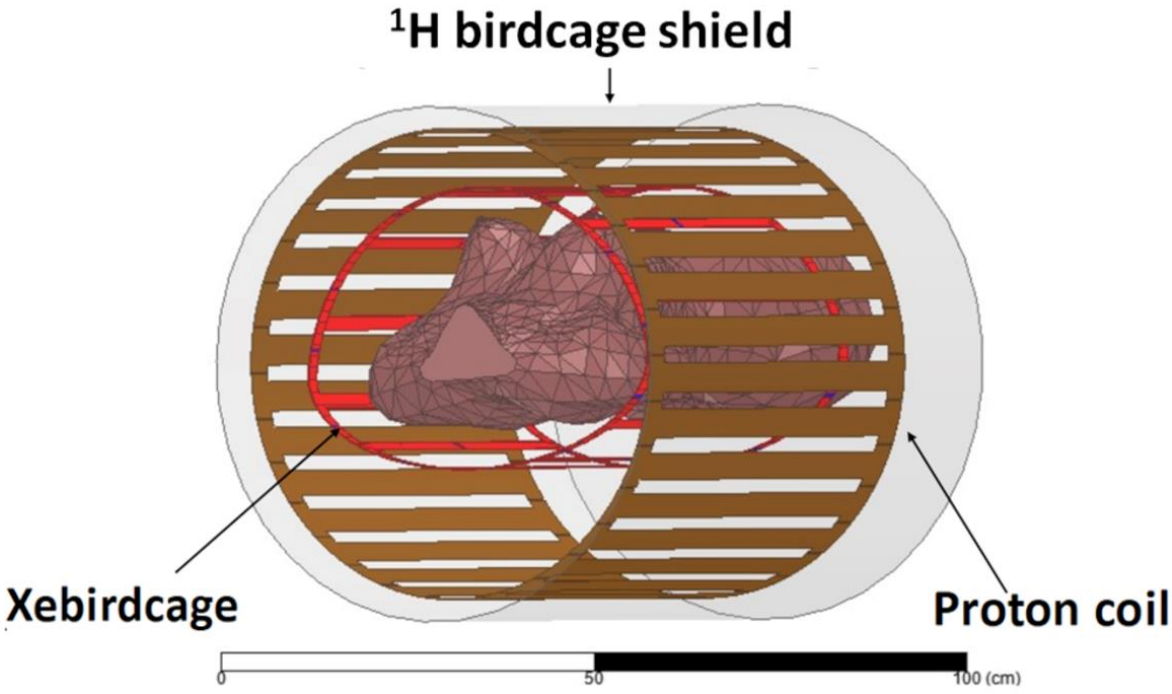

Figure 44: 12 Legs asymmetrical birdcage coil simulation with human body phantom. In the image can be seen in grey the RF shield, in brown the proton coil, in red the Xe coil. Reproduced under creative commons license from [172]

2) The ^{1}H body coil is embedded in the 1.5T scanner. The proton birdcage features a high-pass topology with the capacitors placed along with the end rings. It has a diameter of 64 cm and height of 64 cm. The conductors are defined as a finite conductivity copper domain with zero thickness and 3 cm of width. RLC ports were placed along the end rings to add the capacitors. A capacitor value of 252pF ensures a resonant frequency of 63.85 MHz. The coil is fed with a feeding port placed in the upper end rings.

3) The ^{129}Xe asymmetrical elliptical body has a bandpass configuration, with the dimension as described in the previous paragraph. The conductors are modelled with copper material. Capacitors were placed along the end rings and legs using lumped RLC ports. Two

feeding ports are placed in the upper end rings between the 5-6 and 8-9 legs. The results of the individual experiments will be explained and discussed in the next paragraphs.

4.4.1 Simulations of the homogeneity of the ^{129}Xe asymmetrical birdcage coil

To evaluate the magnetic field homogeneity of the ^{129}Xe birdcage, the coil was fed with two 1V ports with a difference of phase of 90° degrees. The magnetic field homogeneity was evaluated in three scenarios: with the empty coil, with the birdcage loaded with the female human phantom of ANSYS EM software, and with a truncated conical volume that resembles the size of the average human lungs.

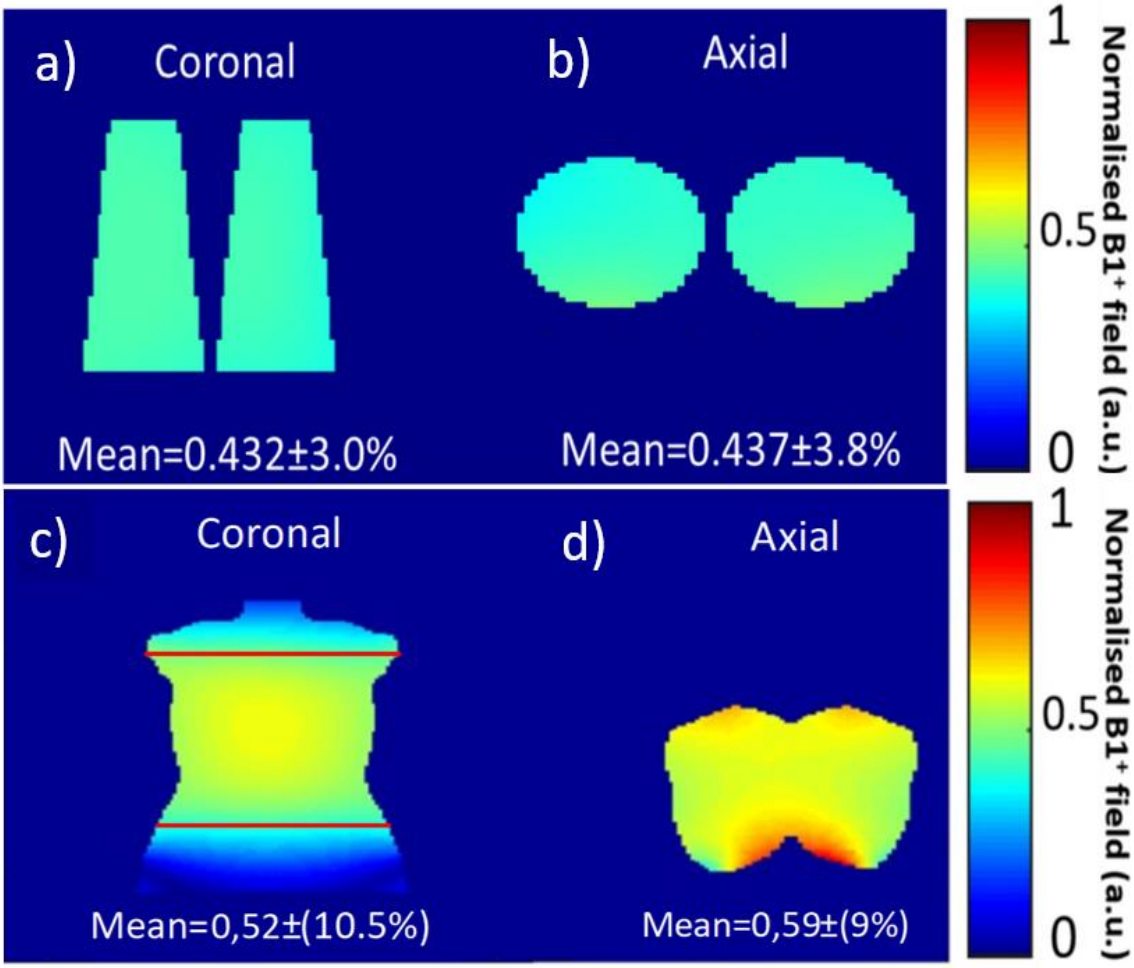

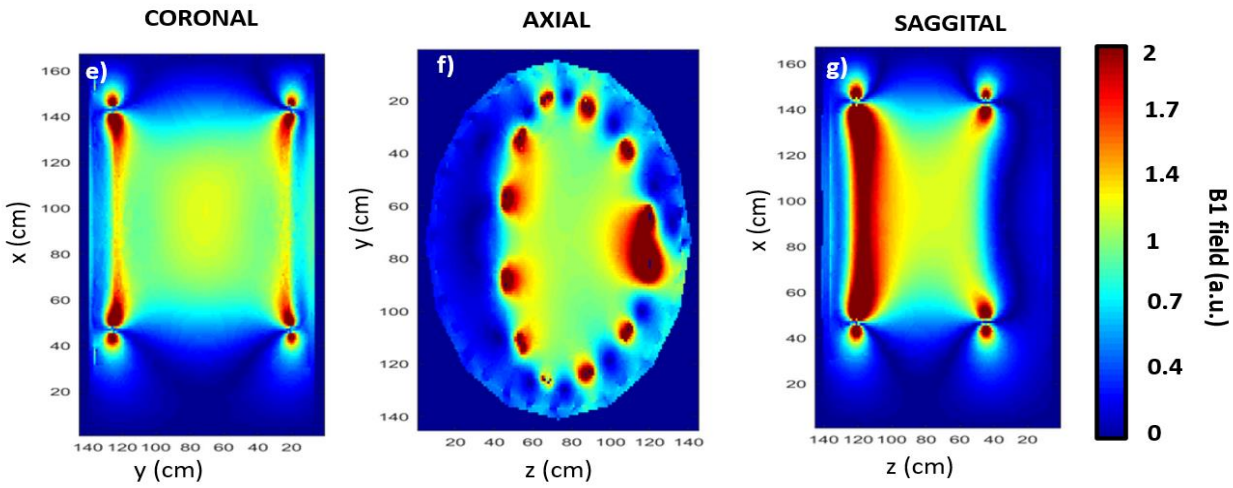

Figure 45: B1⁺ field uniformity along the axial and coronal central planes of the asymmetrical birdcage in the cones that mimic the shape of the average human lungs a-b), B1+ field uniformity over the whole thorax along the central axial and coronal planes c-d) red lines in figure c indicates the region inside the field of view of the coil where the standard deviation of B1 field was measured, a profile of the transmitted B1 field of the empty coil trough the three central planes (e-f-g). Figures a-b-c-d adapted from [172]***, under creative commons license.***

The truncated cone had an upper circular base with a diameter of 20 cm, a lower circular base with diameters of 8 cm, and a height of 20 cm. The frequency of the simulation was set at 17.66 MHz with 12 passes of convergence with a delta S of 0.02. The magnetic field H along the three axes was exported to MATLAB to calculate the B_1^+ fields. To evaluate the field uniformity, the mean and the standard deviation were calculated. The B_1^+ mean and standard deviation of the empty unloaded birdcage were calculated in a cubical region centred in the isocentre of the birdcage's plane. The results of the three simulations are reported in figure 45. The B_1^+ field shows a high degree of uniformity in the lungs with a standard deviation of 3.0% of the transmitted magnetic field on the coronal planes and 3.8% on the axial plane, where a small gradient along the anterior-posterior direction can be observed. Across the whole thorax, the magnetic field homogeneity decreases to 10.5% due to the larger area of analysis. In the axial plane, a high B_1 intensity is noticeable, due to the proximity of the anatomy to the coil conductors. Figure 45 e-f-g shows the magnetic field profile of the empty birdcage along the three axes, confirming the transmitted field homogeneity of the coil. Nonetheless, in the sagittal plane, an increase in the of B_1 field values in the posterior direction can be noticed. This could be attributed to a key feature of the coil geometry and a positive aspect of its design, as this behaviour was already

reported in a previous shielded elliptical birdcage design for ^{3}He lung MRI from our group [173].

4.4.2 Specific Absorption Rate simulation (SAR)

The positioning of the Xe coil inside the volume of the birdcage coil require careful consideration, as it acts as an RF shield, limiting the B_1 field transmitted from the coil to the sample. Therefore, it is crucial to evaluate the SAR at 63.8 MHz and the tuning frequency of the proton birdcage. The feeding ports of the ^{129}Xe coil were shorted by assigning a copper finite conductivity, and four diodes were positioned along the legs 2-3, 10-11,5-6,7-8. The ^{1}H birdcage was fed with 25V, necessary to produce a B_1^- field intensity of 2μT in the centre of the birdcage coil. For the body model phantom, a tissue density of 1.01 g/cm^3, the average tissue density of the human body, was used. In agreement with the IEC 60601-2-33 guidelines [174], Local SAR was calculated considering a mass of 10g. As mentioned in paragraph 2.5, the transmitted field is not continuous over time, and the SAR must be weighted based on the RF duty-cycle of the specific sequence. The SAR field was exported from ANSYS EM and calculated in MATLAB, assuming a Flip angle of 10 degrees, a total scan time of 12 seconds, a rectangular RF pulse shape with a temporal width of 324μS (according to the scanner settings), with 8000 phase encoding steps representative of a very high-resolution high RF duty cycle implementation of a 3D SPGR sequence typically used to image the lungs. The results of the SAR simulation and maps of the local SAR are summarised in table 7 and figure 46.

Table 7: Value of Average SAR and maximum vale of local SAR in the 3D body phantom

Average SAR	**1.23 W/Kg**
Local SAR	**9.93 W/K9**

Simulated SAR values showed an average SAR of 1.23 W/Kg over the whole thorax, which is below the values suggested by the IEC guidelines limit of 2 W/Kg. However, the local SAR reached a maximum value of 9.39 W/Kg, which is close to the maximum level allowed by the IEC. Nonetheless, this imposes a strict limit on the transmitted flip angle or number of RF pulses that can be employed in the sequence. Typically, around 2000 RF pulses are used per 3D SPGR sequence with a sequence TR of around 5 ms (e.g. 80 RF phase encodes in

plane and 24 phase encodes in slice direction). It can be noteworthy that the higher values of local SAR are near the shoulder, in the proximity to the end rings of the Xe birdcage, where the E fields are strongest.

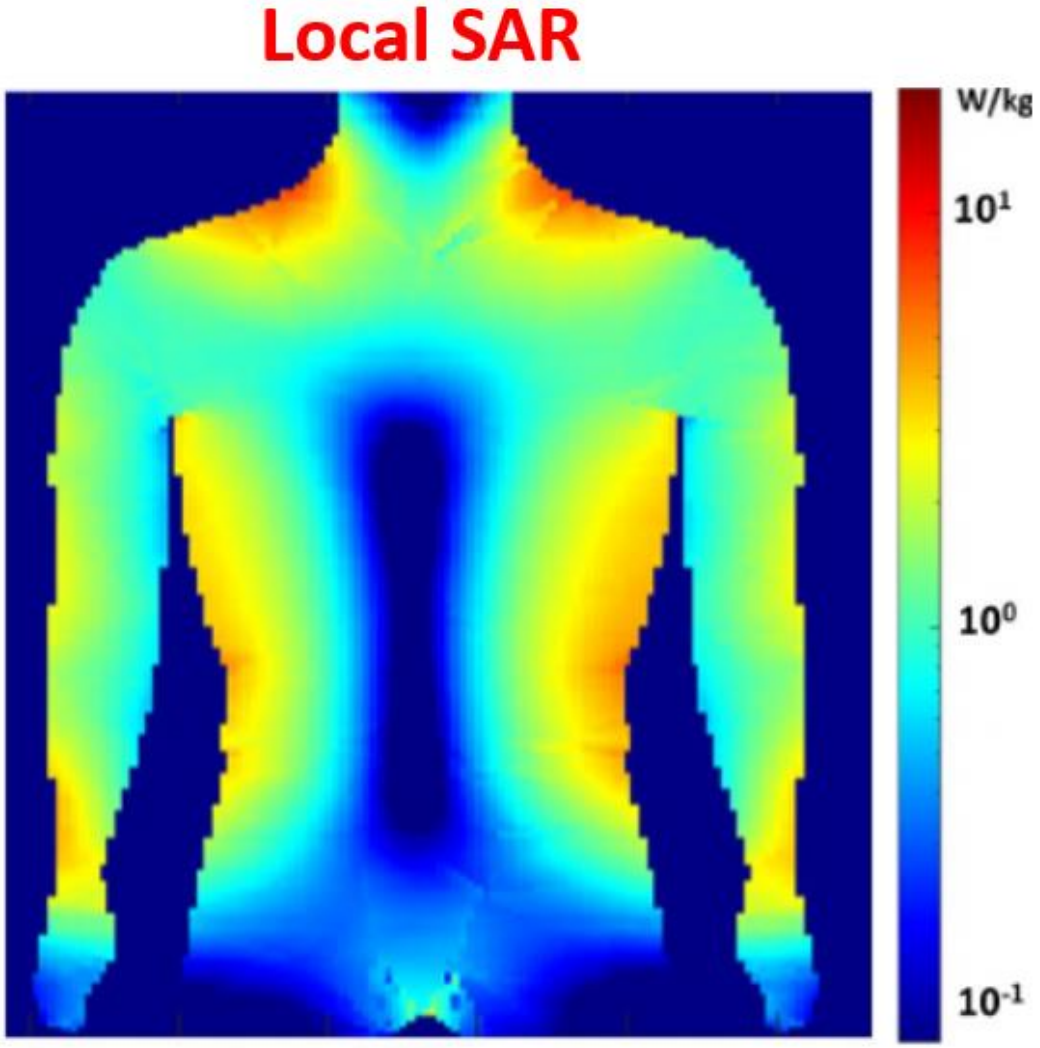

Figure 46: Local SAR maps in the coronal plane. Adapted from [172] ***under creative commons license.***

4.4.3 Magnetic field Interaction of the ^{1}H with the ^{129}Xe asymmetrical birdcage coil

These simulations were performed to evaluate the best diode configuration for detuning the ^{129}Xe coil and evaluate the geometric distortion to the $B_1^+(r)$ introduced by the proton birdcage at 63.85 MHz due to the electromagnetic interaction with the ^{129}Xe coil. The ^{129}Xe coil nested inside the birdcage proton birdcage acts as an RF shield, causing distortion, inhomogeneity, and limiting the intensity of the transmitted magnetic field. During proton body coil transmission in the scanner, the birdcage is detuned by the PIN diodes, which are switched off during the receiver phase. The simulation was performed with different coil

detuning setups to identify the design that offered the best solutions in terms of homogeneity and efficiency. First, the proton birdcage was simulated in a stand-alone configuration and then with the Xe birdcage nested inside. The ^{129}Xe coil was simulated with four different diode configurations: no diodes (coil tuned at ^{129}Xe Larmor frequency), 4 diodes, 8 diodes, and 12 diodes respectively, placed on the birdcage legs (see figure 47).

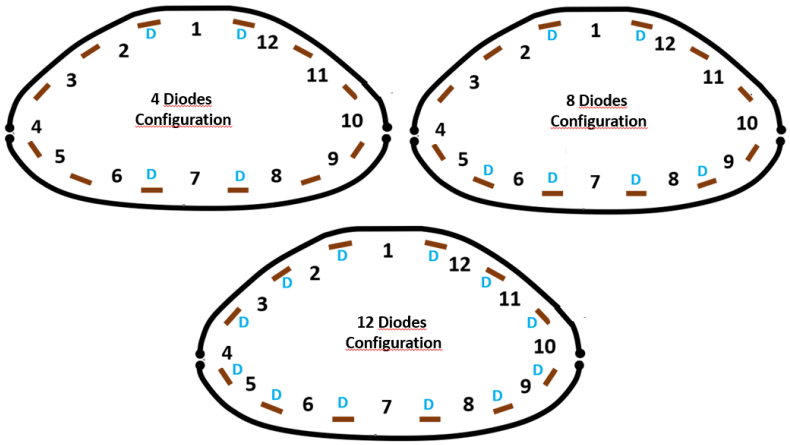

Figure 47: Simulated diodes configuration, respectively with 4, 8 and 12 diodes.

The diodes were placed in series with the tuning capacitor and modelled as the equivalent circuit for reversed biased PIN diodes, consisting of a 3-pF capacitance and 5 kΩ resistance in parallel. The ^{1}H birdcage was fed with a 1W port, while the feeding ports of ^{129}Xe birdcage were shorted with two ports of finite conductivity of copper. The simulation frequency was centred at 63.85 MHz with 12 passes of convergence and a Delta S of 0.1. The H magnetic field of each simulation were exported and analysed in MATLAB. The B_1^+ field was calculated using equation (72). The results of simulations are shown in figure 48. The mean field values and the standard deviation were calculated on the axial plane in the centre of the volume of the asymmetrical birdcage. The size of the region is 25x15 cm and is highlighted in the rectangular region.

Summary of results of simulations

- The birdcage coil exhibited a high uniformity with a standard deviation of1.90% and was used as the benchmark to evaluate the other setup.
- The setup without diodes offered the best field homogeneity (standard deviation of 3.83%); however, the transmitted field value was 55% lower when compared to the configuration with the only proton birdcage.

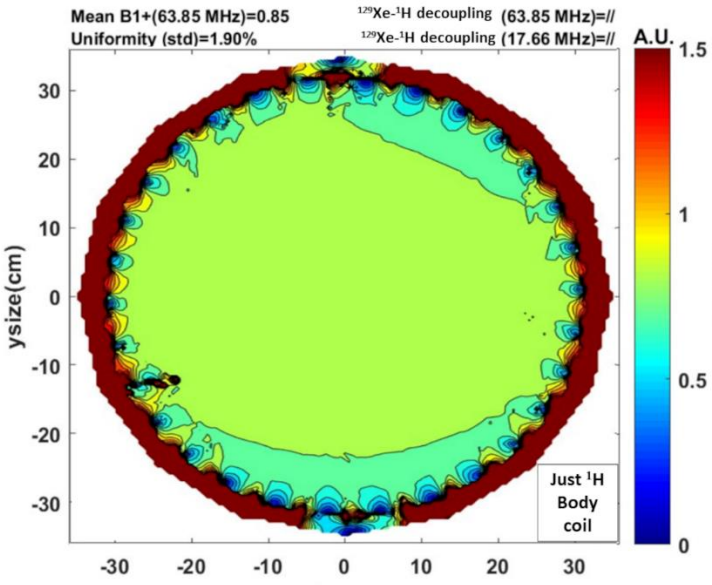
Mean B1+(63.85 MHz)=0.85
Uniformity (std)=1.90%
129Xe-1H decoupling (63.85 MHz)=//
129Xe-1H decoupling (17.66 MHz)=//
A.U.
1.5
1
0.5
0
ysize(cm)
Just 1H Body coil

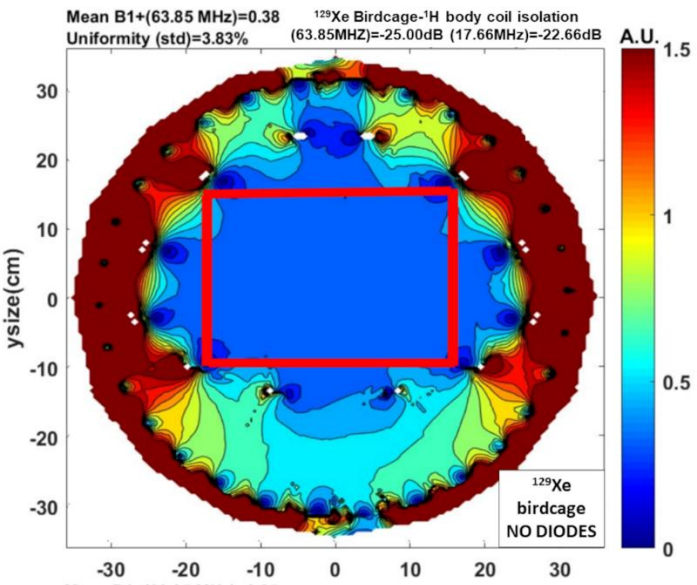
Mean B1+(63.85 MHz)=0.38
Uniformity (std)=3.83%
129Xe Birdcage-1H body coil isolation
(63.85MHZ)=-25.00dB (17.66MHz)=-22.66dB
A.U.
1.5
1
0.5
0
ysize(cm)
129Xe birdcage NO DIODES

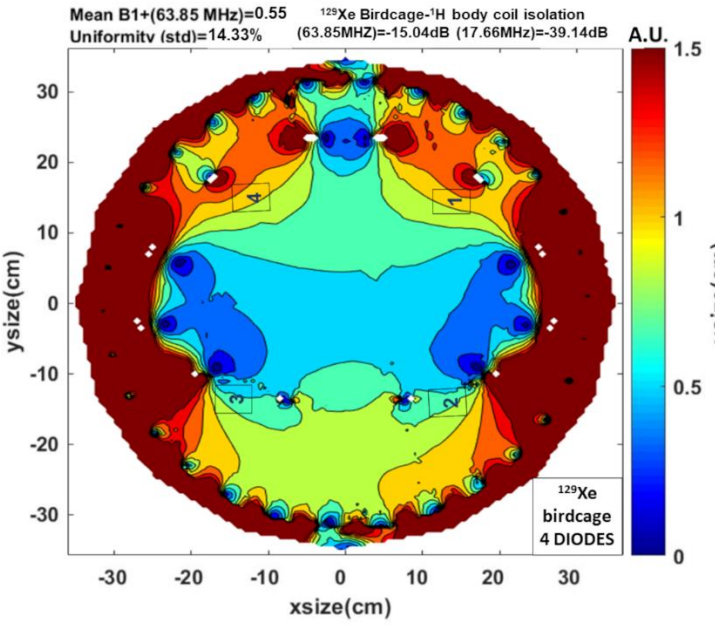
Mean B1+(63.85 MHz)=0.55
Uniformity (std)=14.33%
129Xe Birdcage-1H body coil isolation
(63.85MHZ)=-15.04dB (17.66MHz)=-39.14dB
A.U.
1.5
1
0.5
0
ysize(cm)
xsize(cm)
129Xe birdcage 4 DIODES

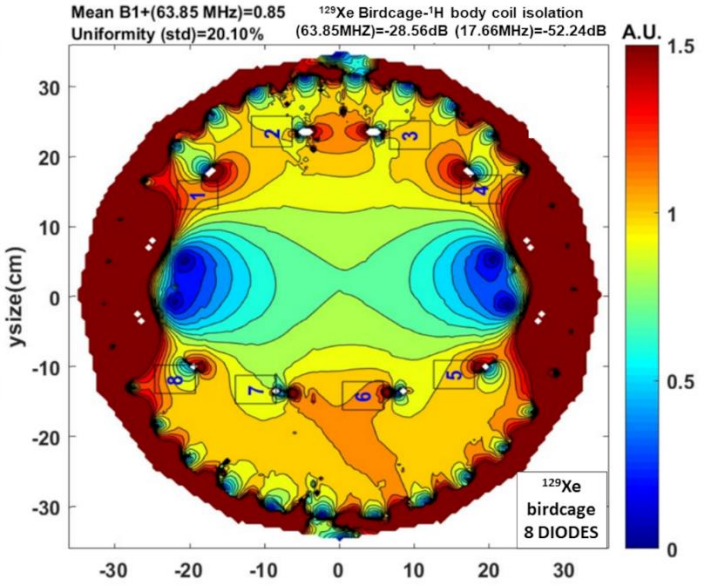
Mean B1+(63.85 MHz)=0.85
Uniformity (std)=20.10%
129Xe Birdcage-1H body coil isolation
(63.85MHZ)=-28.56dB (17.66MHz)=-52.24dB
A.U.
1.5
1
0.5
0
ysize(cm)
129Xe birdcage 8 DIODES

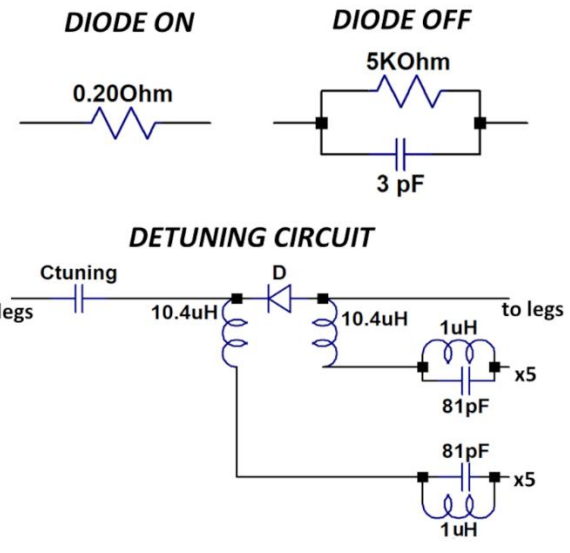
DIODE ON
DIODE OFF
0.20Ohm
5KOhm
3 pF
DETUNING CIRCUIT
Ctuning
D
to legs
10.4uH
10.4uH
1uH
x5
81pF
81pF
x5
1uH
to legs

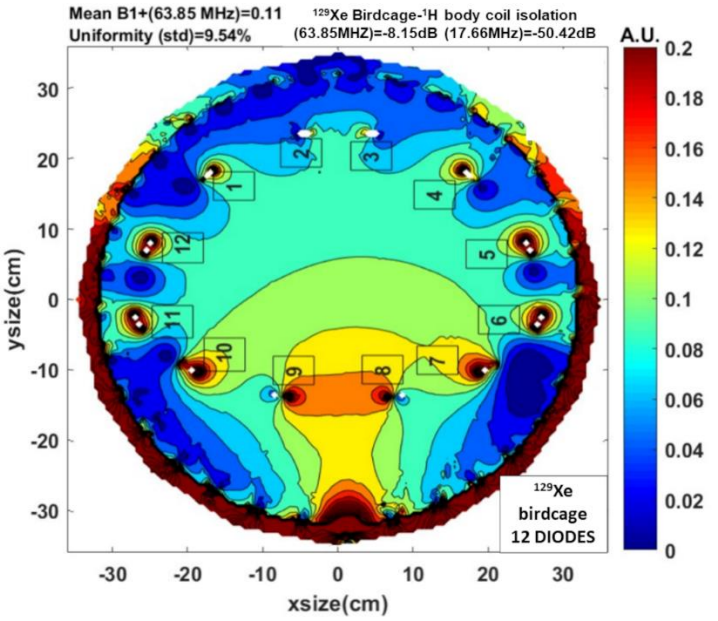
Mean B1+(63.85 MHz)=0.11
Uniformity (std)=9.54%
129Xe Birdcage-1H body coil isolation
(63.85MHZ)=-8.15dB (17.66MHz)=-50.42dB
A.U.
0.2
0.18
0.16
0.14
0.12
0.1
0.08
0.06
0.04
0.02
0
ysize(cm)
xsize(cm)
129Xe birdcage 12 DIODES

Figure 48: Simulated B_1^+ field on the axial plane of the 1H body coil at 63.8 MHz without and with ^{129}Xe birdcage RF coil nested inside for various detuning circuit configurations. The mean and SD of B_1^+ uniformity of the ^{1}H body coil within the ^{129}Xe RF coil as outlined by the red rectangle for all the configurations are 0.85% and 1.9% (without 129 Xe RF coil), 0.38% and 3.8% (no diodes), 0.55% and 14.3% (4 diodes), 0.85% and 20.1% (8 diodes) and 0.11% and 9.5% (12 diodes), where mean values were normalized to an obtained maximum regional value. Location of the detuning circuits on the legs in series with capacitors are marked as boxed numbers and its equivalent circuit is also shown. The RF isolation between ^{129}Xe and ^{1}H RF coils measured as transfer s- parameters (S_{21}) for all the configurations are indicated. Also in the figure the equivalent circuit of the diodes in ON and OFF configuration. Reproduced from [172] ***under creative commons license.***

- 4-Diode configuration has a B_1^+ field homogeneity with a standard deviation of 14.33%, with a mean value of transmitted field 33% lower compared with the only proton birdcage configuration.
- The configuration with 8-diodes, has the worst magnetic field homogeneity (with a standard deviation of 20.10%), especially in the centre of the birdcage volume. The mean field is the same as the only proton birdcage due to the high values of the field in the peripherical region of the coil.
- The magnetic field of the B_1^+ field with 12 diodes is significantly lower than only proton configuration, despite the good homogeneity (SD=9.54%).

4.4.4 S-parameters simulation of the ^{1}H with the ^{129}Xe asymmetrical birdcage coil

These simulations were aimed to determine the coupling parameters between the two birdcage coils to prevent cross-coupling at the two frequencies of interest (63.85 MHz and 17.66 MHz). As previously mentioned, the coil with diodes at the ^{129}Xe frequency is detuned; so effective detuning is expected at 17.65MHz. However, the primary concerns lies at 63.85 MHz, where the absence of proton traps in the ^{129}Xe coil, can lead to a significant power transmission between the two coils, potentially inducing eddy currents and local inhomogeneities, that may results in elevated SAR values. Table 8 shows the isolation values between the two coils. At 63.85 MHz, the best isolation was achieved with the 8 diodes configuration, however, this setup exhibited a high B_1^+, inhomogeneity. In contrast, the 12-diode configuration provided an S_{12} of -8.15 dB, insufficient for optimal isolation between the two birdcages. Conversely, 4 diodes configuration, provided an S_{12} isolation of -15.04 dB, which provided adequate isolation. At 17.66 MHz except in the case of No Diodes configuration, every configuration had an S_{12} below -39 dB.

Table 8: Isolation values of the two birdcages at the Xe and H Larmor frequency at 1.5T

^{129}Xe COIL CONFIGURATION	**S12 (17.66 MHz)**	**S12 (63.85 MHz)**
NO Diodes	*-22.66 dB*	*-25.00 dB*
4 Diodes	*-39.14 dB*	*-15.04 dB*
8 Diodes	*-52.24 dB*	*-28.56 dB*
12 Diodes	*-50.42 dB*	*-8.15 dB*

In conclusion, the design chosen for construction was the one with 4 Diodes, capable of offering the best compromise in terms of field homogeneity and coil isolation.

4.5 ^{129}Xe Coil building and testing on the Workbench

To assess the Xenon birdcage homogenous mode, bench testing was conducted on Vector Network Analyser (VNA) Agilent E5061A Network Analyser (Agilent, Santa Clara, CA). Two BNC connectors and RF168 cables were placed in between the $6^{th}/7^{th}$ (S_{22} port, 0º phase) and $8^{th}/9^{th}$ ($S_{11,}$ port, 90º phase) legs of the lower end ring to feed the coil in quadrature. A 2-loop probe was used to evaluate the resonant modes of the coil by observing the S_{12} parameters. The quality factor was measured by evaluating the S_{12} coupling of two loop probes placed nearby the coil, with and without load. The measured quality factors were 192 (Q-unload) and 107 (Q-load), resulting in an r-ratio of 1.72 (see Figure 48). Coil matching at 50 Ω was ensured by two balun matching circuits (see figure 49), with inductance and capacitance values of 43 nH and 188 pF, respectively. The initial input impedance of 46 Ω was measured by breaking the conductors of the 6^{th} and 9^{th} legs. Each port was connected to the VNA through a cable, while the other port was loaded with a 50 Ω impedance. The coil was loaded with two boxes containing a water solution containing $CuSO_{4.}$ The setup was then connected to the VNA to evaluate the matching and the matching and the tuning parameters on the workbench. The results are shown in figure 49.

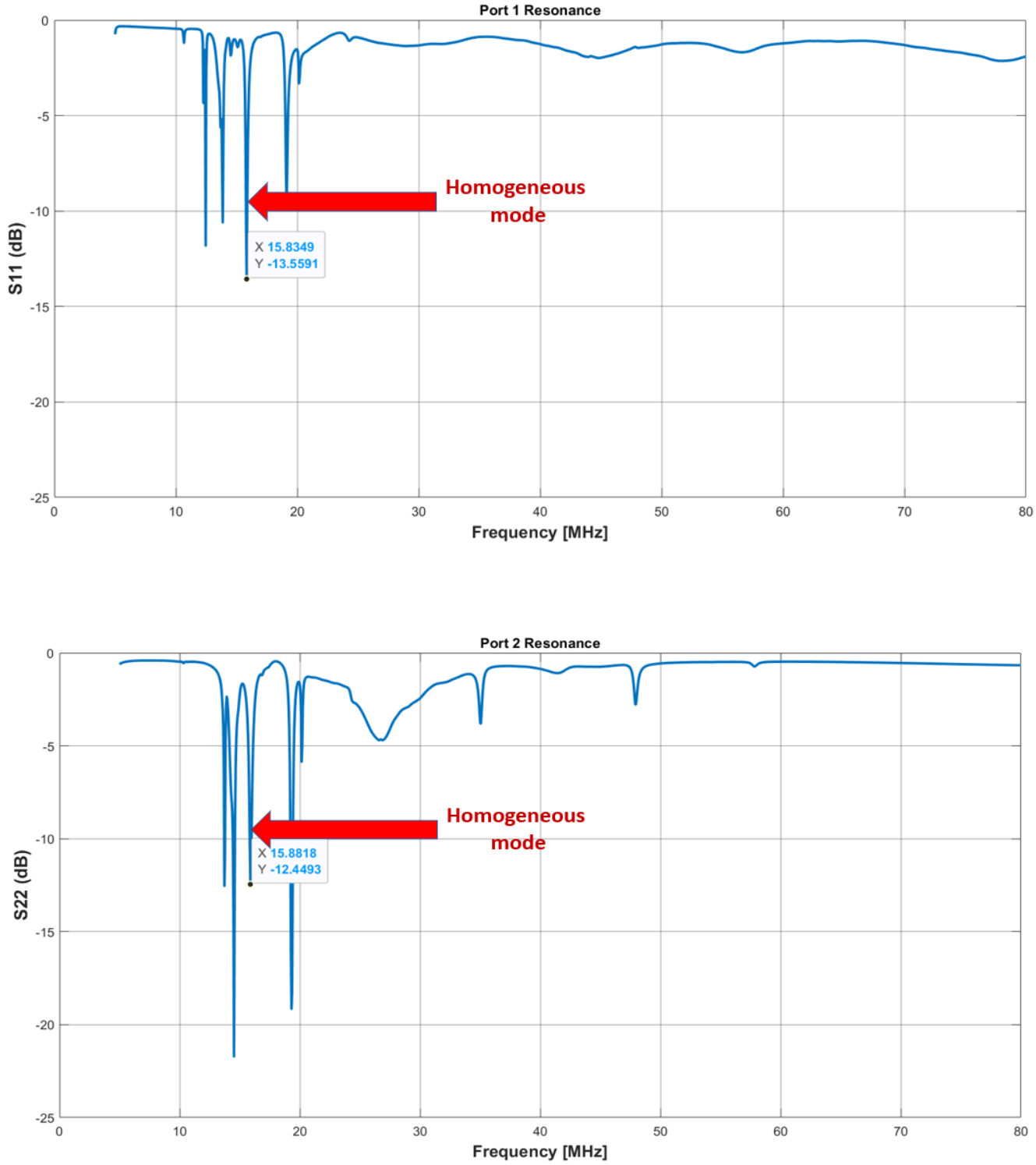

Figure 49: Resonant frequency parameters of the Xe birdcage measured in the RF lab. The coil in the lab has a detuning of around 1.8 MHz compared to the resonant frequency in the scanner

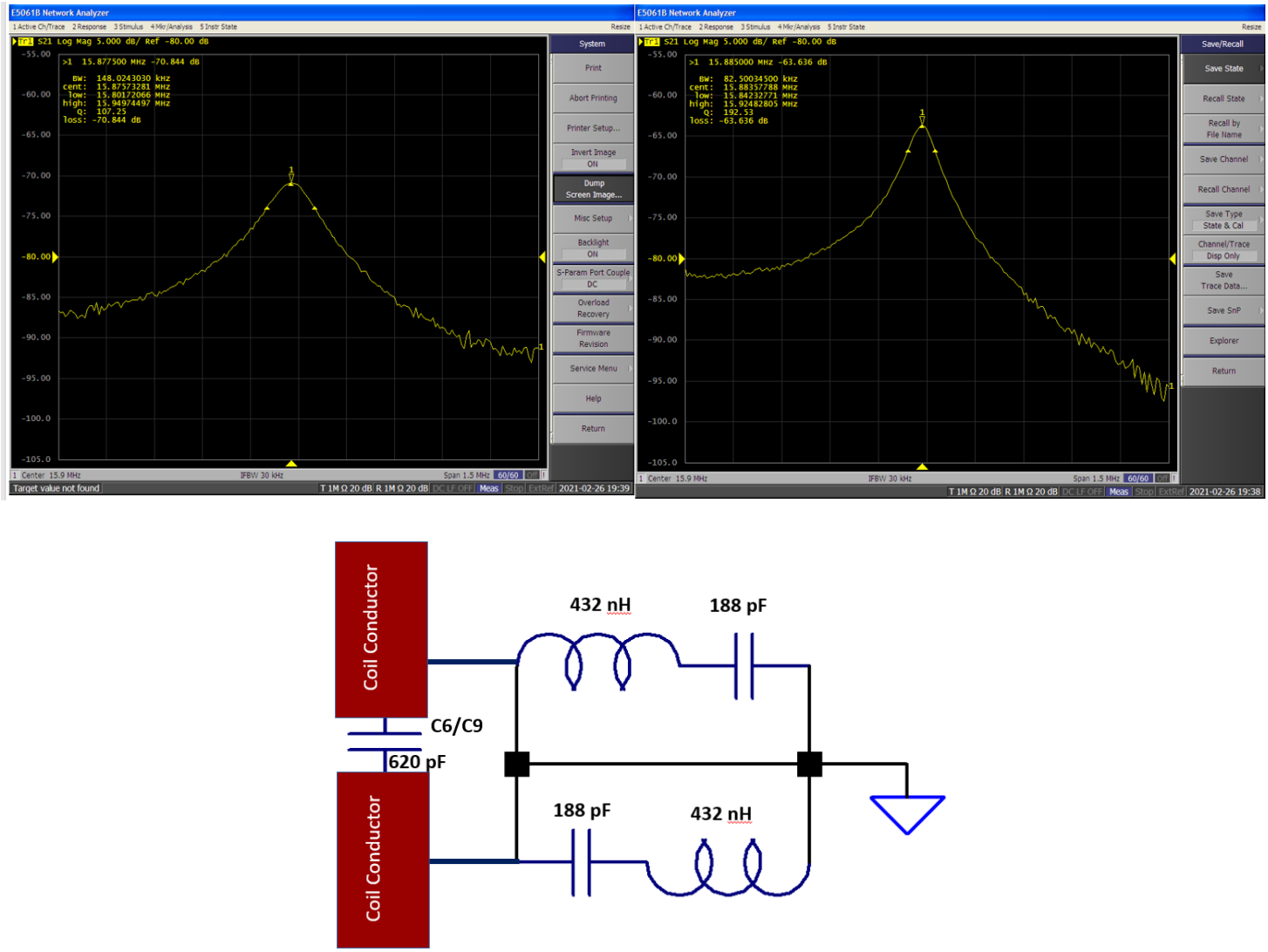

Figure 50: Q factor measurements of the asymmetrical birdcage coil. On the left Q-load, on the right Q-unload. Below is shown the matching circuit used to match the coil.

4.5.1 Hybrid quadrature coupler

Hybrid couplers are commonly used for power division or combining in circuits where a 90-degree phase shift of the two sources is required. In his study, a hybrid coupler was required to combine the two-quadrature channels of the Xe birdcage and connect them to the 1.5T scanner spectrometer. The circuit comprises four ports: an input port (1), an isolated port (4), a direct transmission port (2), and a coupled port 3, which receives power from both the input port and port 2 at -3dB. Thus, the total power entering from port 1 is equally split between ports 2 and 3. For our purpose, we selected a compact lumped component hybrid coupler, as shown in figure 51 a-b, soldered onto an in-house etched FR4 board. The values of the lumped components L1, L2, and C were calculated using the formulae below [175]:

$$L2 = \frac{Z_0}{2\pi f} \qquad L1 = \frac{Z_0}{\sqrt{2}2\pi f} \qquad C = \frac{1}{2\pi f Z_0}$$

(102)

Where Z_0 is the input impedance (assumed to be a perfect matched impedance of 50 Ohms), and f is the working frequency (17.66 MHz). The circuit and measured S parameters on the VNA are shown in figure 51 c-d below.

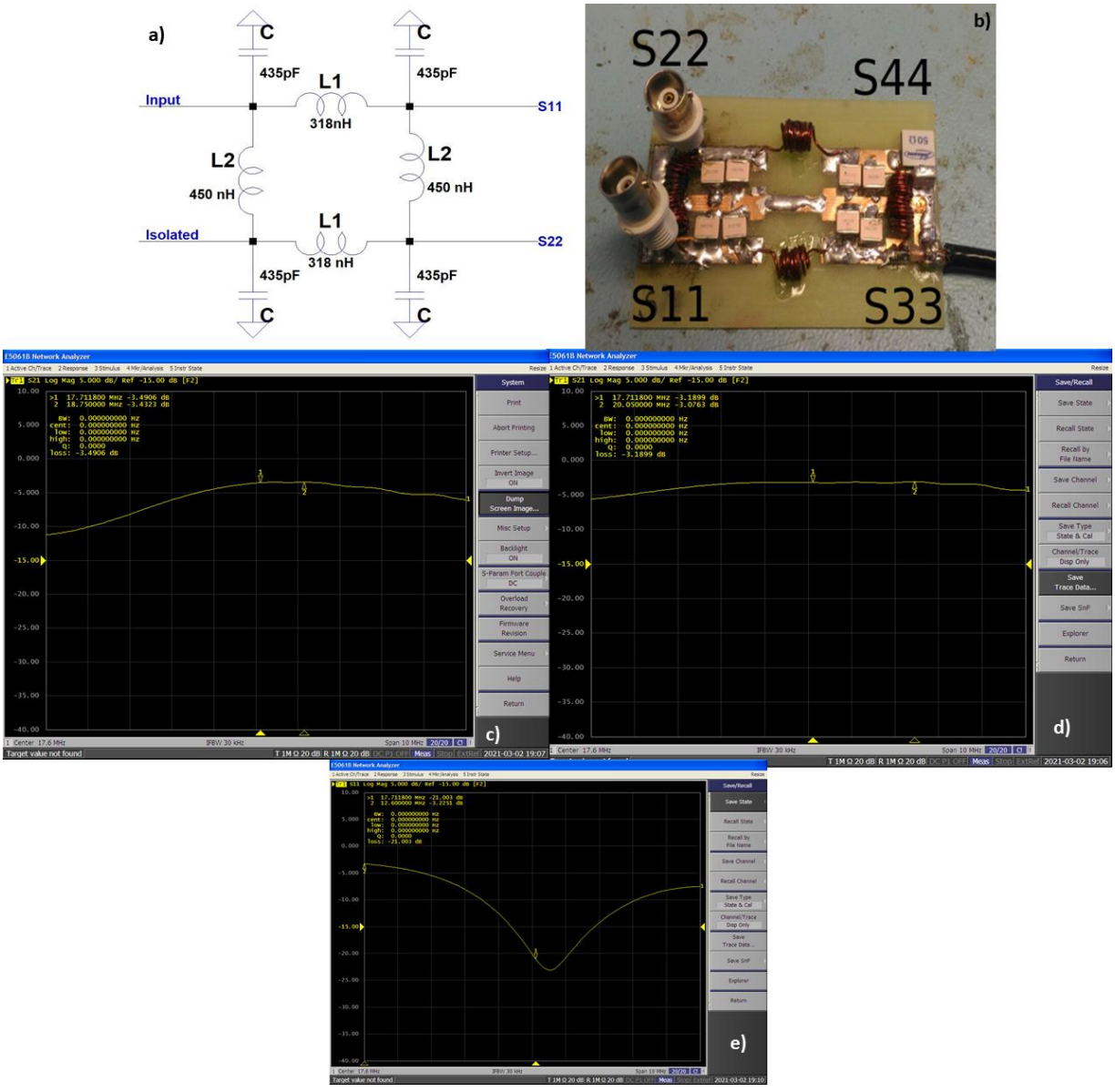

Figure 51: Lumped components values of the hybrid coupler, the parameters were calculated considering input impedances of 50 Ω at 17.66 MHz, b) real model of the branch line coupled, c) S23 measured values (-3.49 dB), d) S13 values (-3.18 dB), e) S33 (-21 dB). The measurements were taken on a calibrated VNA. The non used ports were loaded with a 50 Ω load.

4.5.2 Active decoupling circuit

To prevent coupling between the birdcage and the array system during signal reception, a decoupling circuit is necessary. The circuit detunes the birdcage coil during the receive phase, thereby reducing coupling with the 8-element array. The decoupling circuit uses PIN diodes driven by a DC current. To handle the high current and to avoid inadvertent detuning of the transmit coil during the transmission, six RF chokes are added along the DC current path. The working voltage of the circuit is 5/-15 V, and the current must be higher than 1200 mA when the diodes are forward biased and fall below 300 mA when the diodes are reverse biased. The circuit schematic is shown in Figure 53. The first five inductances are low coil inductance with low resistance, and the remaining one is a chip inductor. The chip inductor value was initially 7.5 µH obtained with two parallel 15 µH inductances. However, the current observed in the power supply was below the required current limit (800 mA) due to the high resistance (5.4 Ω) of the inductors. The value of the chip inductance was changed to 10.4µH. Testing the circuit with a multimeter showed that thee DC current for each diode was approximatively 500 mA with a voltage of 4.850 V. The total current of the circuit, including the hybrid power coupler, was around 2A. The efficiency of the decoupling was measured by placing two loops inside the coil and checking the S_{12} parameter.

Figure 52: Efficacy of the Decoupling circuit, on the left the coil resonance with diode OFF, on the right the coil resonance with Diode ON.

The decoupling provided by the circuit when the diodes are reverse biased is approximatively -20 dB, as determined by varying the positions of the two coupled loops inside the coil volumes. The results obtained at VNA are illustrated in Figures 52.

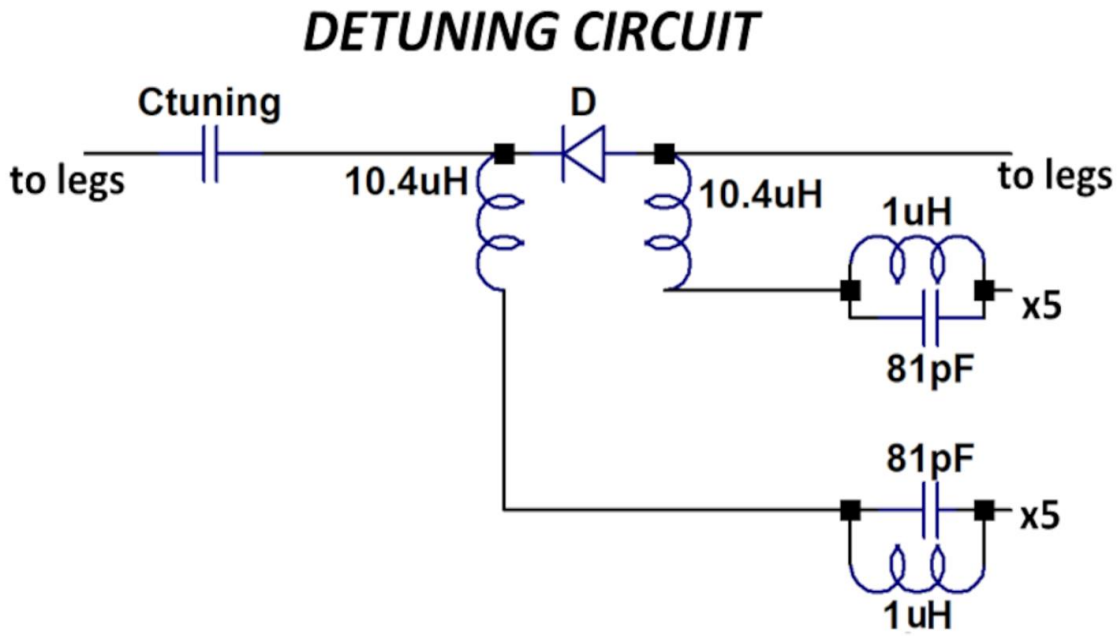

Figure 53: Schematic of the DC circuit. CT is the tuning capacitance and the values are ***different in every leg, RF choke circuits within parallel capacitance both resonate at 17.65 MHz, the DC circuit is connected before the matching circuit.***

4.5.3 Birdcage testing in the scanner bore

To evaluate and verify the tuning and matching parameters of the asymmetrical Xe birdcage coil, it was necessary to replicate the measurements previously performed on the RF bench with the coil inside the 1.5T scanner bore. The test setup included a DC power supply to feed the decoupling circuit and a portable Vector Network Analyser VNA (Anritsu MS2036C), both carefully placed outside the scanner room. Due to the cable length used to connect the coil to the VNA, which added almost -2dB at 63.85 MHz, pre-calibration of the cables was necessary. The measurement span ranged from 5MHz to 80 MHz with 1500 sampling points. This wide span was chosen to detect any resonant modes around 63.85 MHz that might indicate coupling with the proton body coil. The asymmetrical birdcage was positioned inside the scanner bore and loaded with a human subject (healthy male, 30 years old, 78 Kg), to simulate the scanning conditions. Diode detuning was assessed by measuring the S-parameter transmission loss using magnetic flux probes with diodes

turned on and off. Results of the measurements are shown in figure 54 and summarised in table 9.

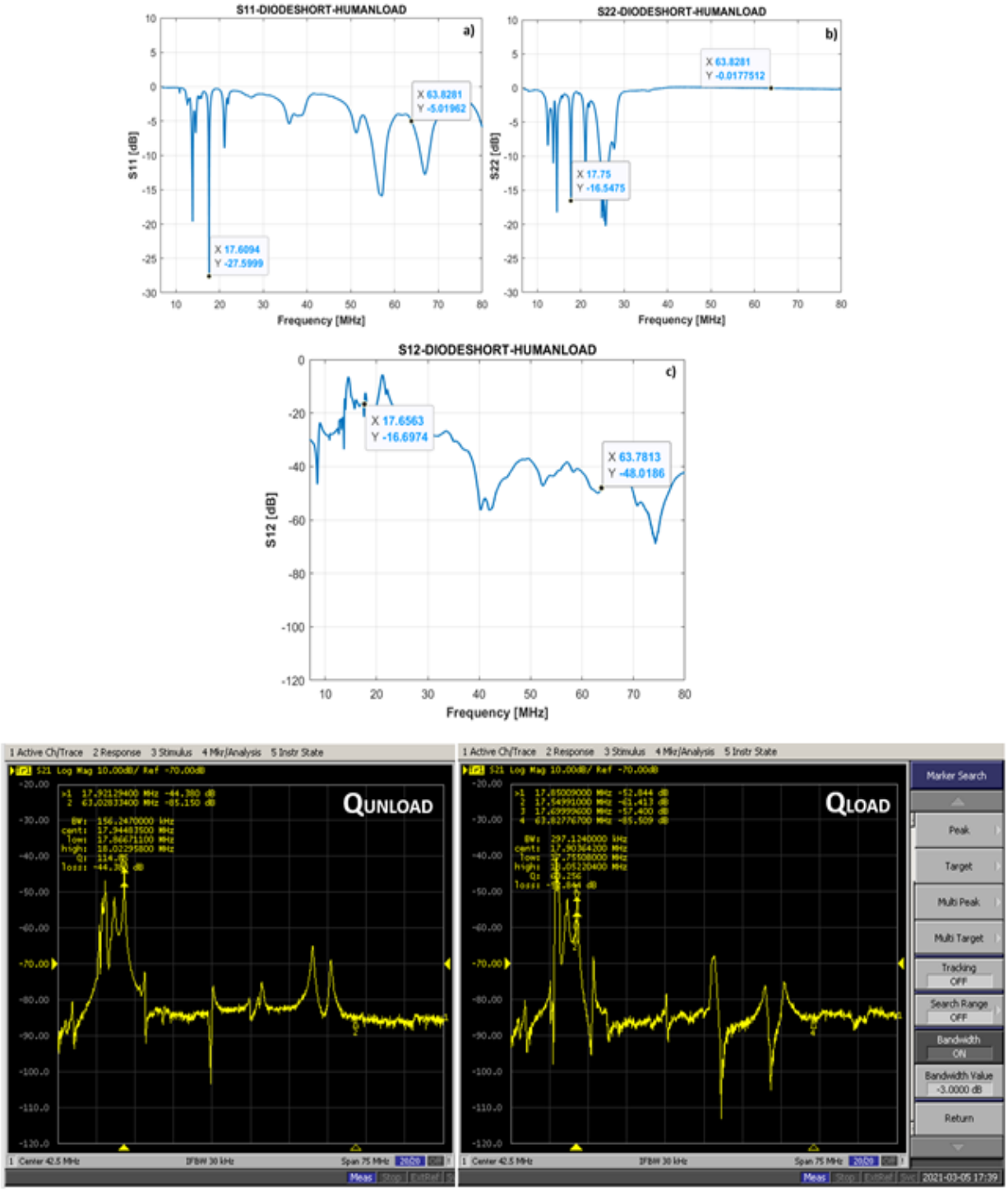

Figure 54 In figure a) S11 parameters, b) S22 measurements, c) S12 coupling parameter. Below the Q values of the coil with and without load and unloaded respectively.

Table 9: Measured S-parameters and Quality factor of the ^{129}Xe Asymmetrical birdcage coil

Parameter	17.66 MHz at peak	63.85 MHz
S11(dB)	*-27.59*	*-5.01*
S22(dB)	*-16.54*	*-0.01*
S12(dB)	*-16.69*	*-48.01*
QFactor	**Unload**	**Load**
R_ratio=1.9	***114***	***60***

4.5.4 Flip angle mapping of ^{129}Xe in phantoms and lungs

To confirm the B_1^+ magnetic field uniformity of the birdcage, experimental measurement of the flip angles across the coil volume were necessary. Flip angle mapping was first performed first on a large square shaped Tedlar bag (50x50 cm) filled with 400 ml of ^{129}Xe gas. The coil was loaded with two rectangular shaped phantoms placed below the bag. Flip angle mapping was acquired in a 2D plane using an SPGR sequence, with the same slice scanned 10 times consecutively. The raw data were exported to MATLAB and Fourier transformed. The flip angle map was calculated by fitting the rate of the depolarisation pixel per pixel using the following formula:

$$S_n^{\square} = S_0^{\square} \sin(\alpha) \cos(\alpha)^{(n-1)} \tag{103}$$

where S is the signal amplitude at n-th RF pulse, α is the flip angle, and S_0 is the initial amplitude. The same experiment was subsequently repeated in vivo with a healthy male volunteer (178cm, 70Kg, 29 years old). The sequence was the same for every experiment: an SPGR sequence with Matrix:32x32X10, TE=4.6ms, TR=50ms, BW=±2kHz, FOV=40cm^2. Only the first four images (with total scan time of 6.4 sec) were used to fit the Flip Angle to avoid the T1 decay of the hyperpolarised ^{129}Xe. Results of the experiments are visible in figure 54. In vivo flip angle maps (Figures 55a-55b) demonstrate good field uniformity with calculated flip angle of 4.23 and 4.68 degrees in the coronal and axial planes, respectively. Both planes exhibit good field uniformity with a maximum standard deviation of 13%. Along the axial plane, a small gradient of the B_1 field is noticeable, which already had been evaluated in the EM simulation. The good field uniformity is also confirmed by the B_1

mapping of the Tedlar bag (Figure 55 c), which shows flip angle values in the same range as the in vivo mapping (5.01 degrees), with a calculated standard deviation of 10%.

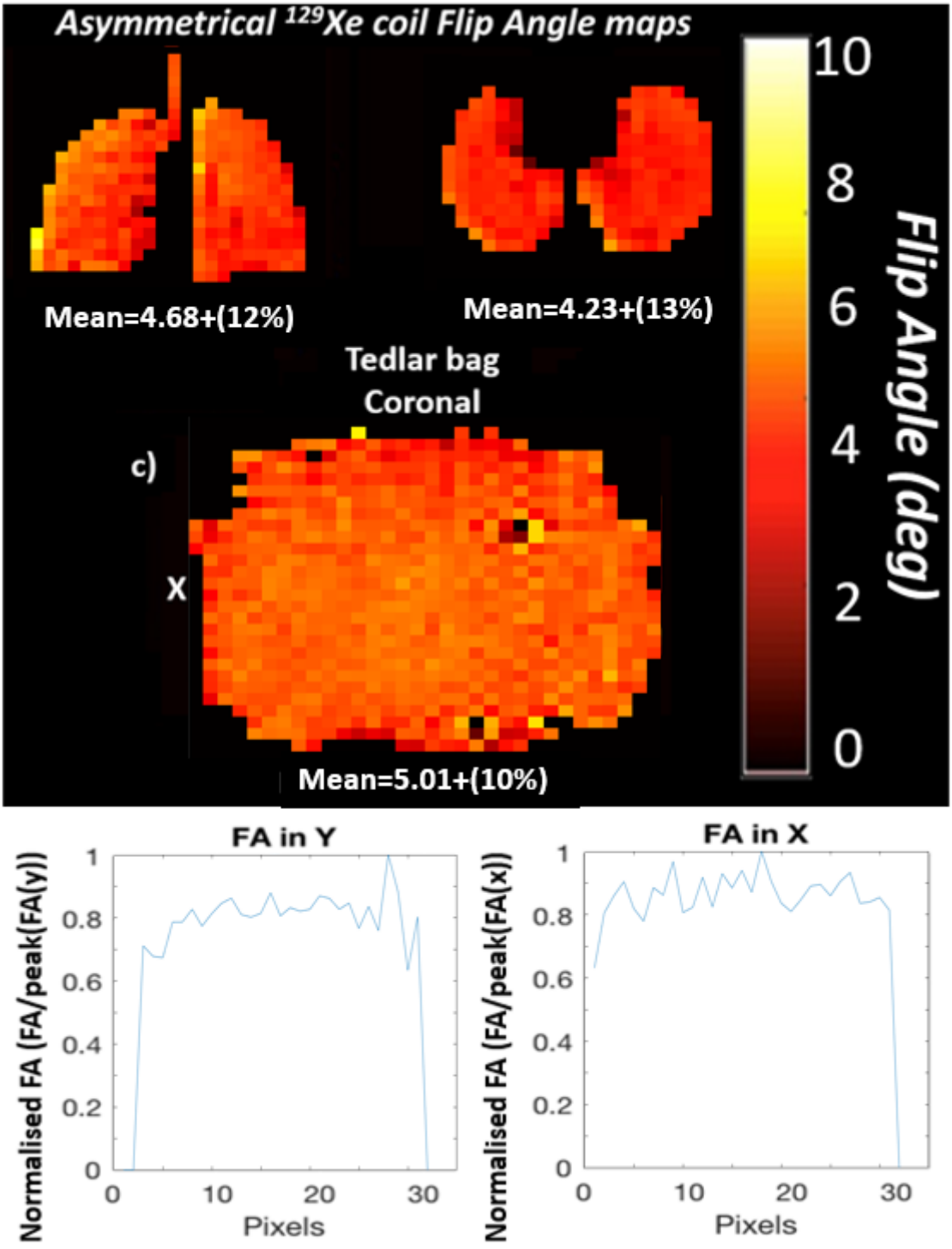

Figure 55: a) In vivo coronal Flip Angle maps, b) in vivo axial Flip Angle maps, c) Flip Angle maps of the Tedlar bag filled with 500ml of ^{129}Xe, below are shown the normalised FA (FA/peak(FA)) profile in the centre of the bag. Figures a-b-c adapted from [172] ***under creative commons license.***

As analysed in the simulations shown in Figure 54, the transmitted B_1 of the ^1H body coil was significantly reduced by 40% when the xenon coil was positioned inside the scanner bore. To assess the impaired efficiency of the proton birdcage, a T1 mapping was performed with and without the ^{129}Xe birdcage inside the scanner gantry. The phantom used for the experiment was an aqueous saline solution containing with 3.6 g/L NaCl and 1.96 g/L $CuSO_4$-$5H_2O$ with a radius 15.5 cm and a height of 42cm. The imaging sequence was a 2D spoiler gradient echo on the axial and coronal planes: Matrix 128x128, TR=300ms, TE=30ms, FOV=40x40 cm^2, 8 mm slice thickness, BW=15.63 KHz, nominal FA=30^o. The same slice was acquired consecutively, changing the RF power. The RF power of the scanner can be measured using the following formula:

$$Power = 2Kw * \left(\frac{ia_{rf1}}{32767}\right)^2 * TG \tag{104}$$

Where 2KW is the maximum power of the RF preamplifier of the scanner, iarf1 is a linear B_1 scaling parameter that can be set manually in the scanner (with maximum values of 32767), and TG is the transmit gain of the scanner. TG is calculated automatically by the scanner using the formula below (105):

$$TG = 10^{(-(200-TGc)/100)} \tag{105}$$

Where TGc is the calculated gain by the scanner. During experiment, TGc was found to be 197, and the iarf1 (the spectrometer B_1 amplitude scale factor) was manually set with values from 0 to 30000 in steps of 5000. The acquired raw files were exported to MATLAB, and the flip angle was calculated pixel by pixel using the formula described in reference [176]:

$$S_{SPGR} = \frac{\left(1-e^{TR/T1}\right)\sin(\alpha)}{1-e^{TR/T1}\cos(\alpha)} \tag{106}$$

The T1 of the aqueous saline phantom was already previously measured as 39.5 ms [177]. The calculated ^1H flip angle maps of the phantom with and without the xenon coil in situ can be seen in figure 56. The ratio of the calculated flip angle without and with the asymmetrical coil inside the scanner gantry is four times lower on the axial axis and three times lower on the coronal axis. Additionally, there is also an increased inhomogeneity of the magnetic field. The large decrease is likely related to the dual action of RF shielding by the Xe coil on both the transmitted B_1^+ and received B_1^- of the proton body coil. In

conclusion, as evaluated in the measurements of the S-parameters, there was still substantial residual coupling between the two coils.

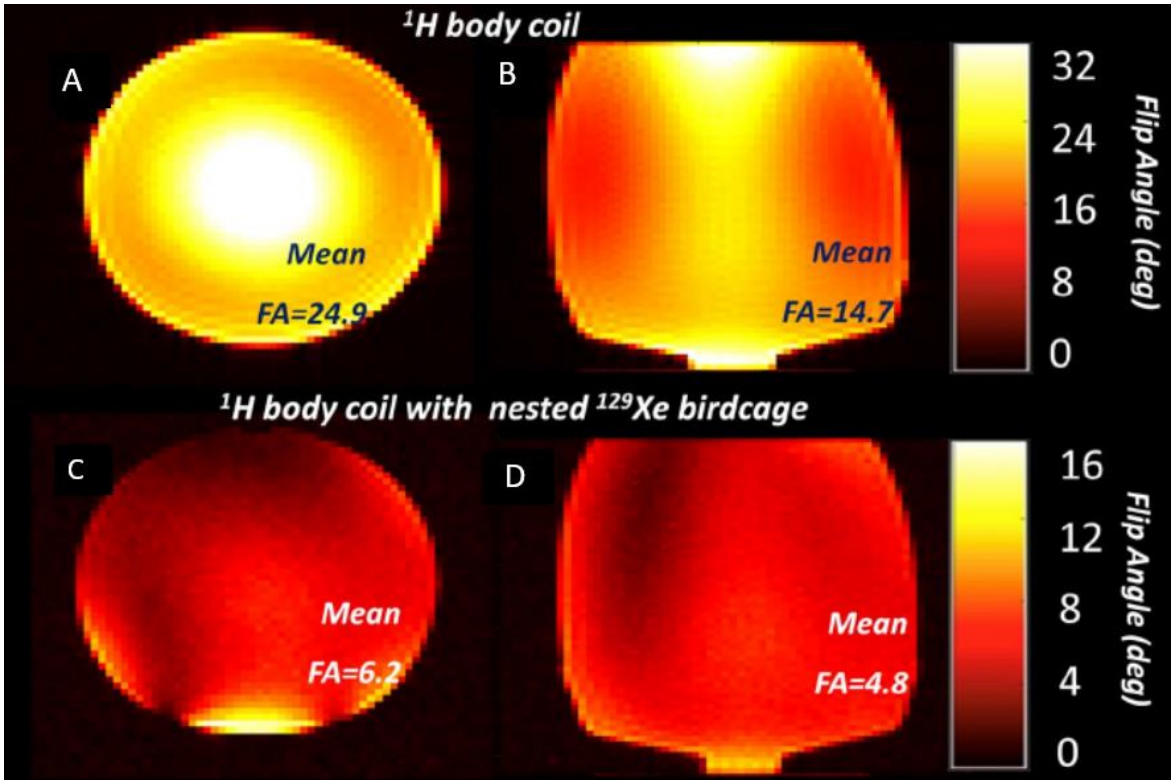

Figure 56: Flip Angle Maps of the saline solution phantom: a) and b) measured flip angle without the ^{129}Xe coil. c) and d) measured flip angle with the ^{129}Xe inside the gantry. Reproduced from [172] ***under creative commons license.***

First, the coil was tested in transceiver mode, and then as a transmit-only coil in conjunction with the 8-channel array as a receiver. Using the array also enabled parallel imaging and shortened scan times. The sequence design strategy, calculation of the optimal flip angle, and testing will be described at the end of this paragraph.

Chapter 5: In vivo imaging with the asymmetrical birdcage coil and an 8-channel receiver array

Work from this chapter has been published in part in:

An asymmetrical whole-body birdcage RF coil without RF shield for hyperpolarized ^{129}Xe lung MR imaging at 1.5 T. Puddu C., Rao M., Xu X., Deppe M.H., Collier G., Maunder A., Chan H.F., De Zanche N., Robb F., Wild J.M. Magn Reson Med. 2021 Dec;86(6):3373-3381.

After the developing the coil through stages of EM simulation, RF lab measurements, and testing in the scanner, its performance was tested trough in vivo measurements. First, the coil was tested in transceiver mode, then as a transmit-only coil in conjunction with the 8-channel array receiver. The array implementation also enabled parallel imaging and reduced scan times. The sequence design strategy, calculation of the optimal flip angle, and testing will be then described at the end of the paragraph.

5.1 Ventilation imaging with the birdcage Transmission/Receive configuration

Initially, the Xe birdcage was tested in a transmit receive/configuration, without the insertion of the DC decoupling circuit and the 8-channel array as a receiver coil. The first tests were conducted using a SPGR sequence for ventilation imaging to evaluate the preliminary image quality of the coil. The imaging sequence was a 2D SPGR with matrix 64x64x9, TE/TR=9.06/50 ms, BW=±2kW kHz, slice thickness = 20 mm, FOV=40cm^2. The patient was a 28-year-old healthy male volunteer and inhaled a dose of 450ml ^{129}Xe, topped up to 1L with 550ml N_2 (Figure 57).

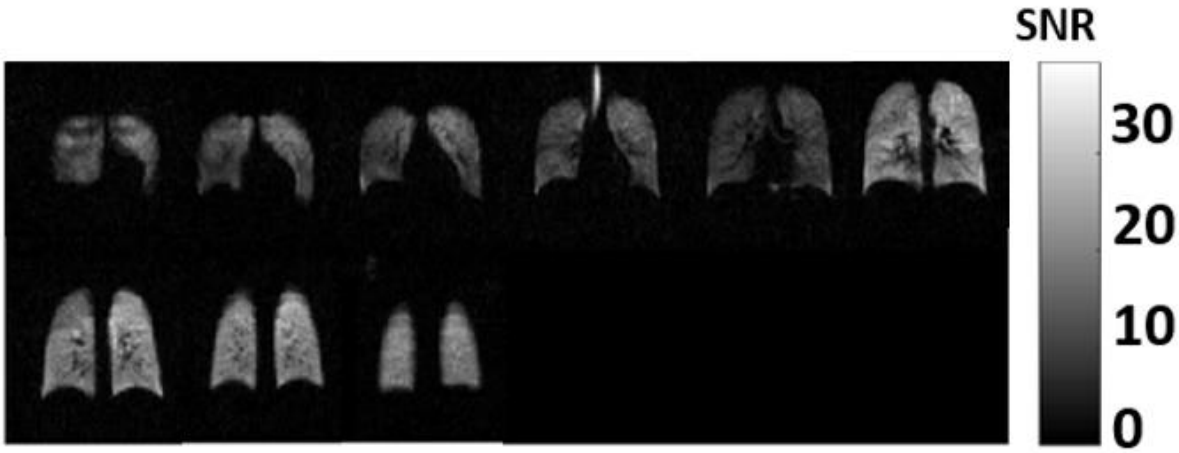

Figure 57: SPGR Lung Ventilation Images in SNR units. ©University of Sheffield.

Additionally, images were acquired with a 3D bSSFP sequence with a matrix size of 100x100x24, slice thickness=10 mm, TR/TE=6.7/2.2ms, FOV=40cm^2, BW=±8kHz, FOV=40cm^2. Two different scans were performed: the first with a 26-year-old healthy male volunteer with a dose of 500ml hyperpolarised ^{129}Xe (Figure 58) topped up to 1L with N_2 and the second with a 25-year-old healthy male volunteer using a dose of 750ml hyperpolarised ^{129}Xe topped up to 1L with N_2 (Figure 59). Each dose had ~30% polarisation. Before each scan, a calibration sequence was performed to determine the input power required to achieve a FA of 10°. Images were reconstructed using homodyne reconstruction in MATLAB. The SNR of the magnitude images was evaluated by excluding the airways via thresholding. The data within the threshold was defined as the signal used to calculate SNR using the formula below:

$$SNR = \frac{M}{\sigma} \tag{107}$$

Where σ is the standard deviation of the background noise in the bottom part of the images and M the average value of the pixel in the Region of interest. The standard deviation of the region without signal is calculated as in the equation below [178]:

$$\sigma = \frac{N}{\sqrt{\pi/_2}} \quad (108)$$

and N the mean value of the of background noise.

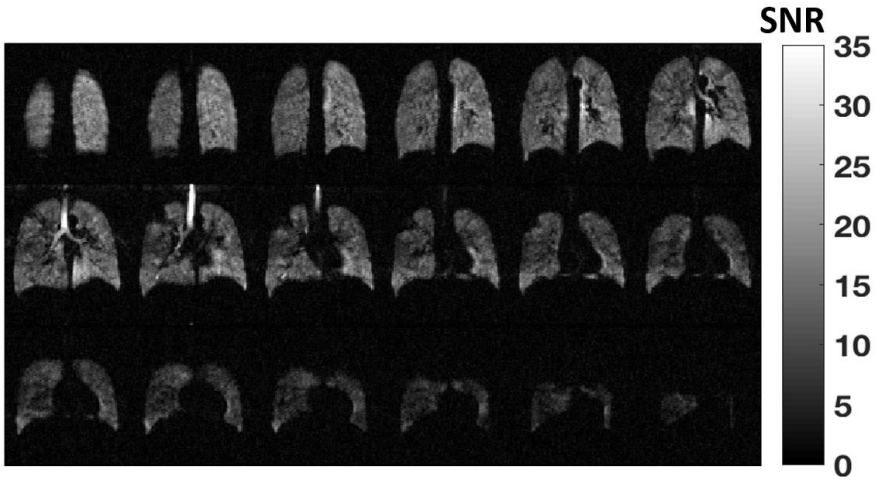

Slice	SNR ± Standard deviation
Posterior	**15±4.2**
Central	**12±3.8**
Anterior	**9±2.5**

Figure 58: SSFP scan with 500 ml dose of ^{129}Xe, the colour bar is expressed in SNR units. in the following table the mean values of SNR for the posterior, central and anterior slices. ©University of Sheffield.

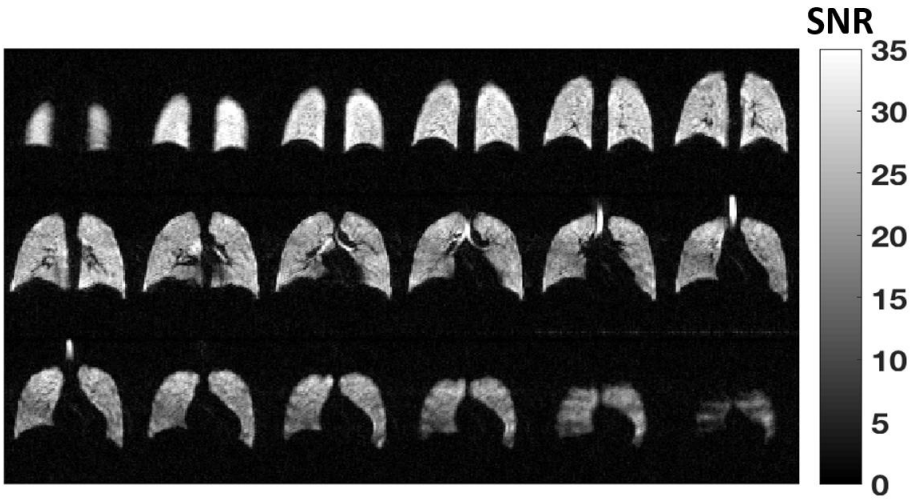

Slice	SNR ± Standard deviation
Posterior	**26±5.3**
Central	**21±5**
Anterior	**18±4.8**

Figure 59: SSFP scan with 750 ml dose of ^{129}Xe, the colour bar is expressed in SNR units. in the following table the mean values of SNR for the posterior, central and anterior slices. ©University of Sheffield.

The mean SNR was 8-9 for the 2D SPGR sequence. An SNR improvement is evident with the 3D SSFP sequence, which is the optimised in-house acquisition sequence for ventilation imaging [179]. The SNR with the 500ml ^{129}Xe dose was 15,12,9 in the posterior, central, and anterior slice, respectively. As expected, for the scan acquired with the 750ml ^{129}Xe dose, there was an improvement in the images signal, with a calculated SNR of 26,21,18 posterior, central, and anterior slice respectively. For all acquisitions, is possible to notice an SNR degradation from the posterior to the anterior slice, which can be attributed to the gravity dependant gradient in ^{129}Xe ventilation [180].

5.2 Hyperpolarised ^{129}Xe MRI with the asymmetrical birdcage coil as transmitter and the 8-channel array as a receiver.

Following the implementation of the DC circuit in the asymmetrical birdcage to act as a transmit-only coil, the next step of the development of the RF setup was the testing of the 8-channel receiver array in the scanner.

5.2.1 Receiver coil design

Although the asymmetrical birdcage can effectively work as a transceiver antenna, using a dedicated receiver antenna has two main advantages that will be discussed later in the chapter. The receiver coil is based on a repurposed 8 channel GE cardiac coil anterior arrays, retuned to resonate at the ^{129}Xe Larmor frequency at 1.5T. The array was divided into two separate modules, with four channels covering the anterior part chest and the other four channels covering the posterior part of the chest (Figure 60). Each single channel element was composed of a passive decoupling circuit and an active decoupling circuit with two tuning capacitors. Each loop had a squared shape with a dimension of 30x30cm (total size of the single module 60x60cm) enclosed in a semi flexible structure, favouring a conformal fit with the patient's anatomy. The design was optimised to achieve optimal performance for parallel imaging. The two halves are connected through a common connector.

.

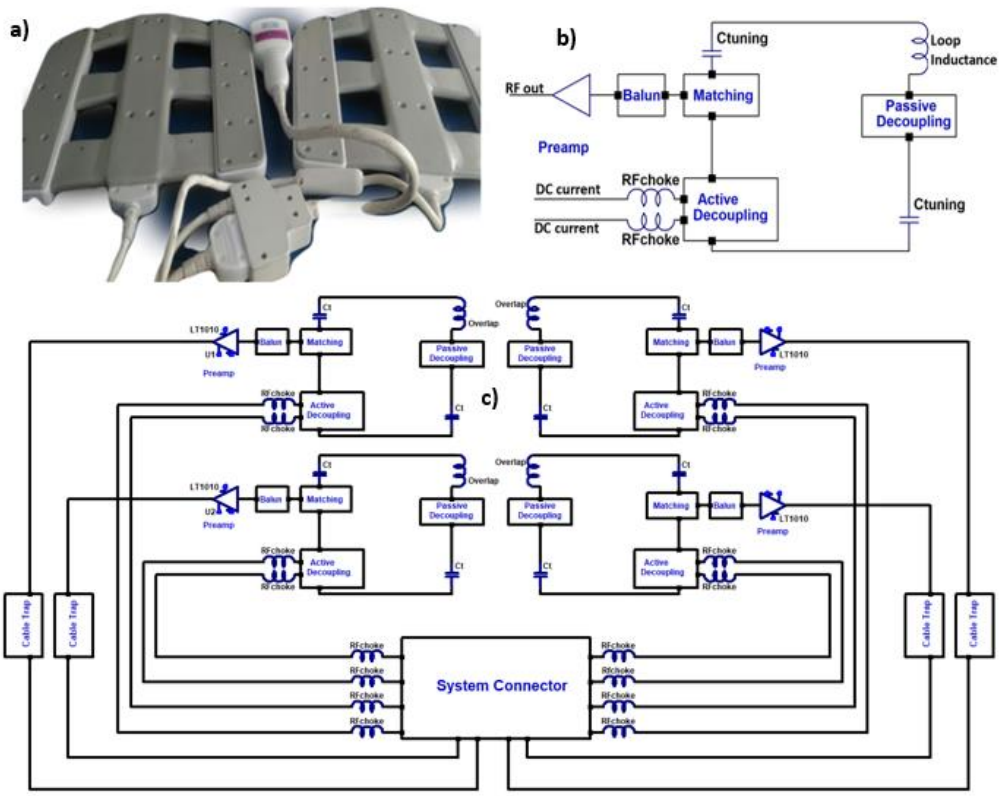

Figure 60: a) 8 channel coil, b) Electrical circuit of a single channel, c) blocks diagram of 4 channels together with a system connector. Figure a) adapted from [172] ***under creative commons license.***

Initially, each channel of the coil was tested on the VNA; the working frequency was analysed by checking the S_{12} coupling with a copper loop. The preamplifier and the Direct Current (DC) circuit were tested with a bias tee connection on a 5 Volts power supply. Additionally, a spectroscopy scan was carried out using a cylindrical thermal phantom of compressed ^{129}Xe (2 bar with 1 bar O_2) placed in the centre of the array. The parameters of the spectral acquisition were: central spectral frequency 17657320 MHz, Transmit Gain (TG)=120, TR=5s, Number of averages=5, spectral width=1200Hz and 256 sampling points. The raw data of spectra were then processed in MATLAB. The pre-processing of the signal used a Gaussian apodization and a Zero padding of 1024 points. The spectrum of each channel was reconstructed with a Fast Fourier Transform and combined using equation (109) in accordance with [181]:

$$S_{km}^{c} = [w_k]^T [S_{km}] \tag{109}$$

Where S_{km}^{c} is the combined spectra, w_k weighting function and S_{km} *is* the single coil spectrum. If the coil sensitivity is unknown the weighting function can be calculated as:

$$[w_{k,noise}] = \frac{[S_{km(ref)}]}{\|S_{km(ref)}\|} \quad (110)$$

Where m_{ref} is the reference spectral peak point of the spectrum. The spectrum results are shown in figure 61.

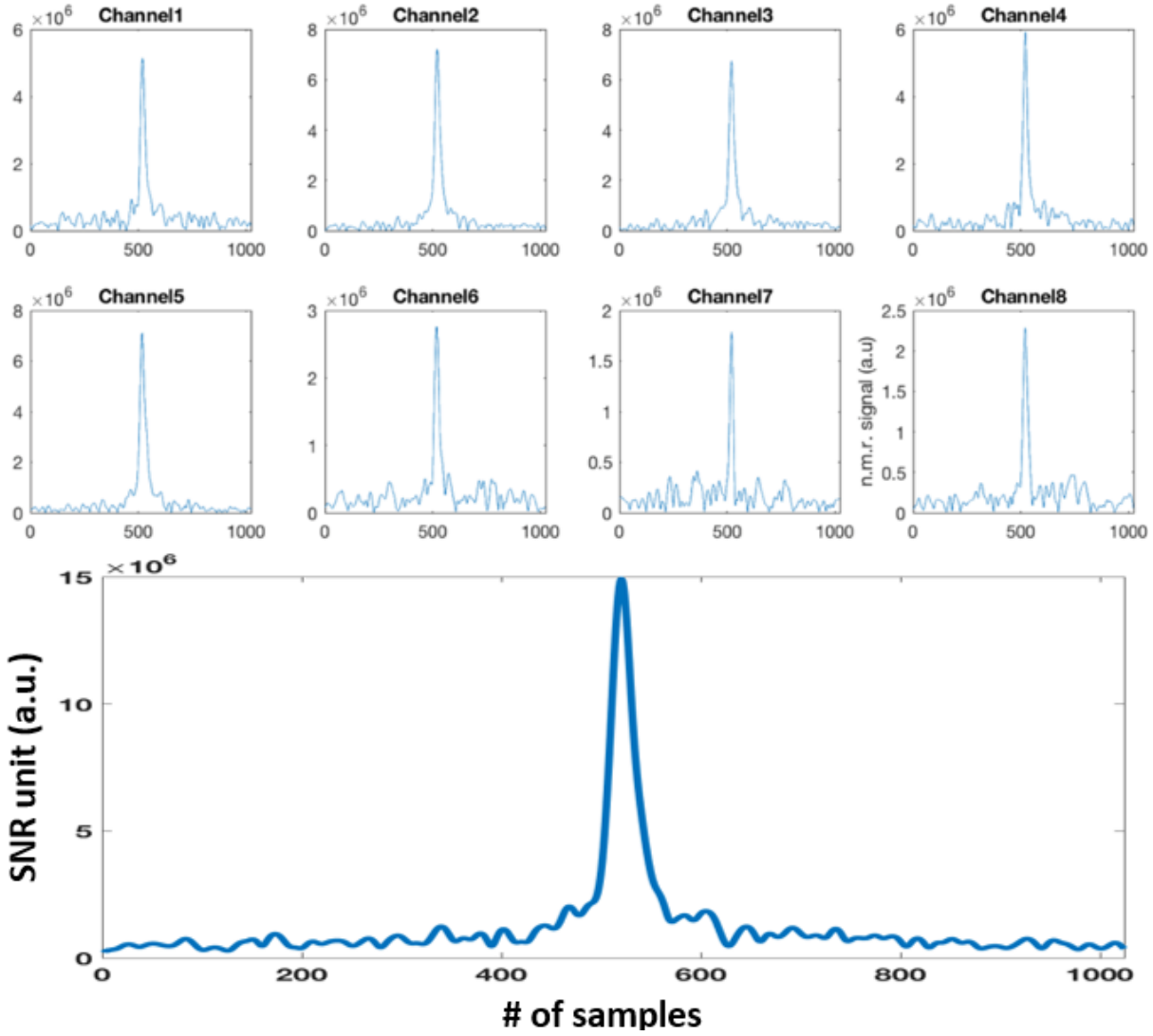

Figure 61: At the top are shown the spectra from each channel, and the sum of squares reconstruction of the spectrum in the bottom. The evaluated SNR was 166 obtained by the division of the signal intensity of the peak and the standard deviation of the first fifty points of the background noise.

5.2.2 Calibration of the 8-channel array

Following image analysis, a non-uniformity of the pixel signal intensity along the ROI was noticed, due to the different signals acquired in each channel. The calibration code normally used is tailored for the vest coil (CMRS, Wisconsin USA) a dual Helmholtz quadrature combined channels. However, for the 8-element array, the script provided the optimal required voltage only for the first channel, not for the other elements. Considering

an N element array, the prescribed power varies between each element due to the different positions and sensitivity. To address this issue, multiple calibration scan with the birdcage/array configuration were acquired to develop a method for combining all the channels and calibrating the correct input for all elements. For this purpose, two healthy male volunteers of 26 and 28 years old respectively were scanned. The prescribed input power was for a FA decay of 10°. The method involved taking the single FID of every element then fits the spectral decay of every channel. Subsequently, the mean of the flip angle decays was calculated to find an optimal flip angle for all elements. Table 10 shows the flip angle for each elements of two volunteers The same method was used in the paper of Deppe et al. [182] for an asymmetrical ^{3}He birdcage coil in combination with a 32 channel array.

Table 10: Flip angle (in degrees) for each channel and means prescribed for each scan

Channel	1st	2nd	3rd	4th	5th	6th	7th	8th	Mean FA
1st volunteer	4.82	4.96	4.82	4.91	3.54	5.36	4.61	5.26	**4.78**
2nd volunteer	5.84	4.97	4.73	4.90	4.52	4.63	4.25	5.93	**5.10**

5.2.3 In vivo ventilation imaging with 8-channel array

An in-vivo scan was performed to evaluate the image quality with the 8-channel receiver array. The image acquisition parameters were: Matrix 100x100, TR/TE=6.7/2.2ms, FOV=40cm^2, BW=±8kHz, FOV=40cm^2. The patient, a 25-year-old healthy male volunteer, inhaled a ^{129}Xe dose of 750ml. Prior to the scan, a calibration sequence was performed. The raw data were then exported to MATLAB and reconstructed using a homodyne reconstruction. The data were combined using the sum of squares method as in reference [64] :

$$I = \sqrt{p^T \Psi^{-1} p^*} \tag{111}$$

Where p is the pixel value matrix and Ψ is the noise correlation matrix between all the channels. The noise correlation matrix represents intrinsic correlations between the noise signals of various coils and is independent of the overall amplifier gain in each channel. The correlation matrix is given by equation 112:

$$\Psi_{ij}^{corr} = \frac{R_{ij}}{\sqrt{R_{ii}R_{jj}}} \quad (112)$$

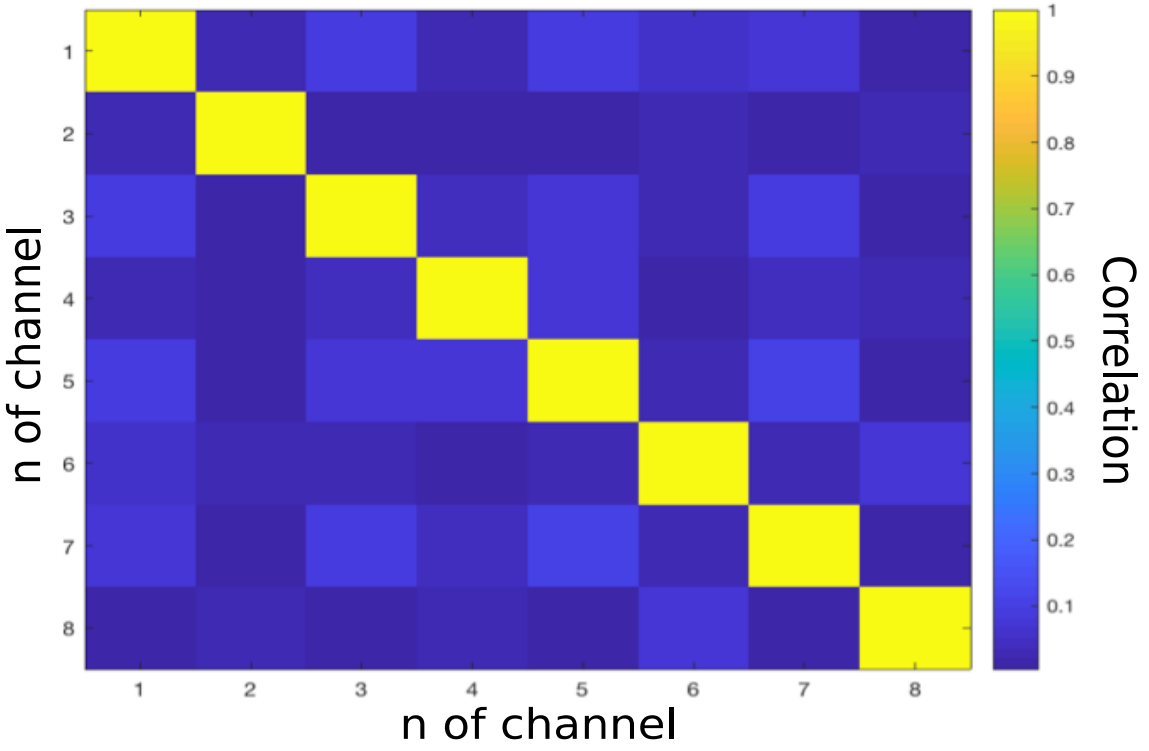

Figure 62: Noise correlation elements between the 8 channel coil elements

Figure 62 shows acceptable decoupling between the elements of the array, as each channel has a correlation below 10%. The maximum coupling observed was 9.65% between channels 5 and 7. SNR was evaluated as per method described by Kellman et al. [183], with the results presented in Figure 63. The posterior and anterior slices exhibit higher SNR compared to the central slices, likely due to the proximity of the array to the body. In contrast, the central slices show a lower SNR. Nevertheless, these results confirm the advantage of using separate coils for transmitting and receiving the signal, resulting in enhanced SNR.

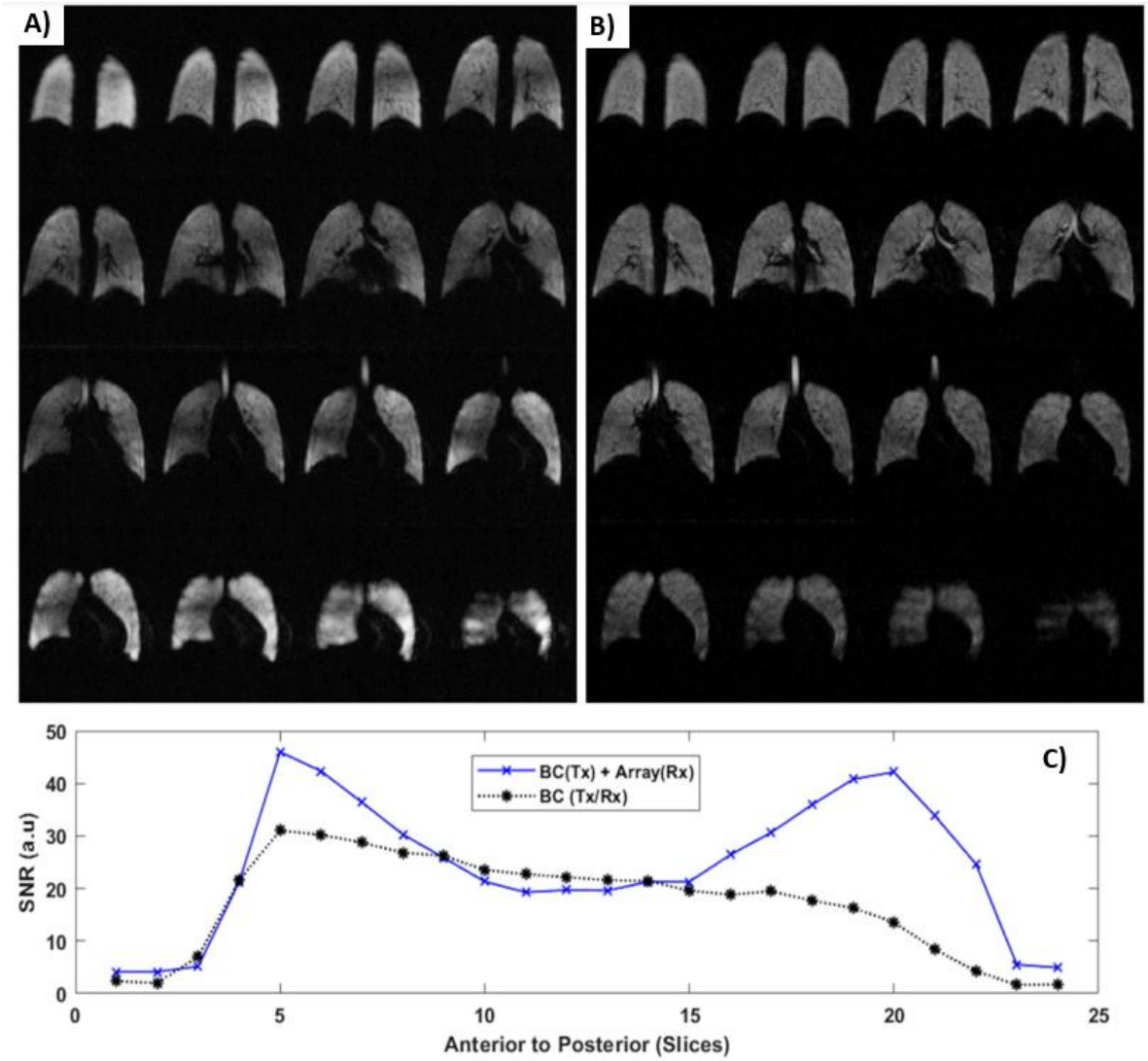

Figure 63: a) Ventilation lung imaging with Hyperpolarised ^{129}Xe MRI with the birdcage and coil array; b) ventilation imaging with birdcage as a transceiver coil, c) comparison of means SNR values calculated for each slice between the two images setup. Reproduced from [172] ***under creative commons license.***

5.3 Parallel imaging

The implementation of the 8-channel array enabled parallel RF encoded imaging with accelerated methods, aiming to reduce scan time and minimise the breath-hold time of the patient. Additionally, the reduced number of phase encoding steps allows the usage of a higher flip angle, which mitigate the typical SNR of this kind of acquisition. This section describes the accelerating imaging with auto calibrating SENSE acquisition and evaluation of the optimal flip angle for both acquisitions with SPGR and bSSFP sequences.

5.3.1 Acquisition Strategy

The SENSE algorithm reconstructs accelerated images by utilising sensitivity maps of each channel. These maps are usually low-resolution images, of the anatomy acquired with the accelerated imaging technique. However, for hyperpolarised ^{129}Xe, an additional scan would require an extra dose of ^{129}Xe increasing protocol scan time. To address these issues, a self-calibrating parallel imaging technique, as proposed by McKenzie et al [184] was used. Autocalibration lines in the centre of the k-space were acquired during the accelerated imaging acquisition. The size of auto calibrating k-space volume was 16x20 in the two-phase encoding directions of the sensitivity maps (original scan matrix 80x80x20). Additionally, a 3D low pass Kaiser window [β=3.0] was applied to k-space volume domain to attenuate the higher frequencies and to prevent non-physical truncation artefacts [184][182]. Two different acceleration patterns were considered along the right left direction with acceleration fact R=2 and R=4 (with a neat acceleration factor of 1.6 and 2.28 considering also the autocalibration lines acquisition). The acceleration patterns of the two accelerated acquisitions can be seen below in figure 64.

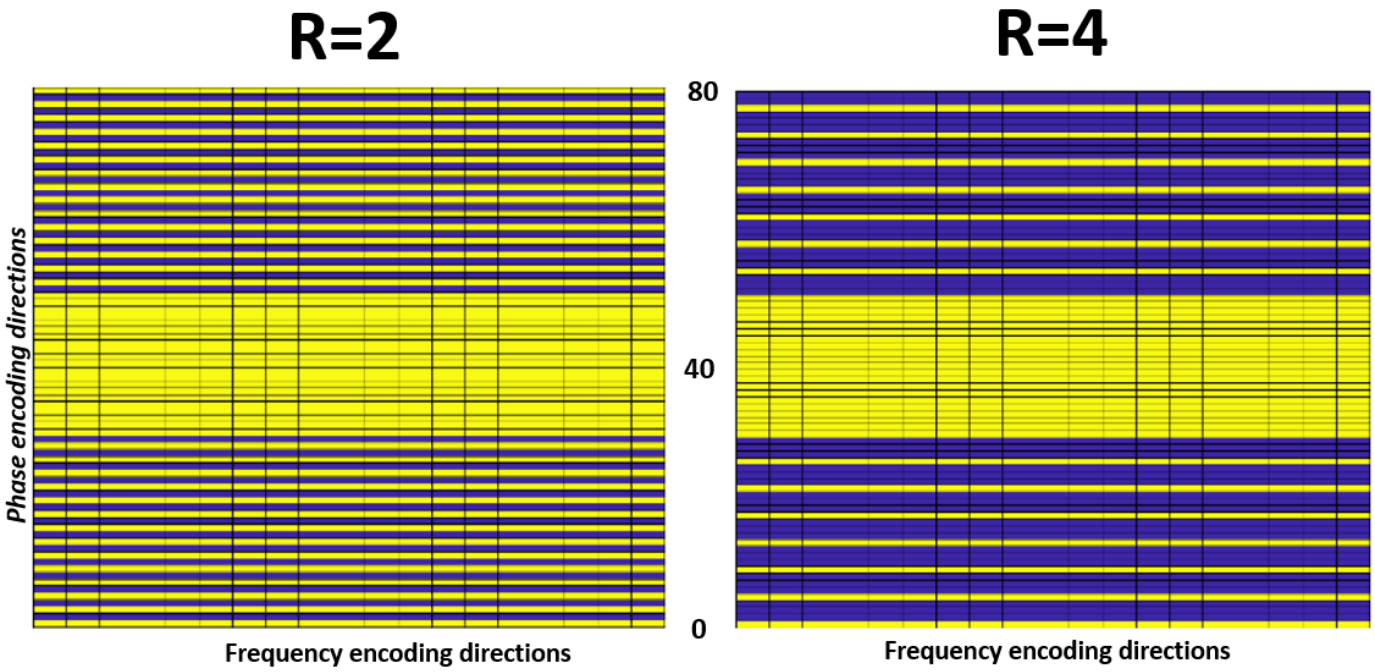

Figure 64: On the left the accelerating patterns for R=2, on the right accelerating pattern for R=4. The central yellow lines are the autocalibrating lines, the skipped k-space lines are written in blue.

5.3.2 Flip Angle assessment and imaging with the 3D Spoiler Gradient echo sequence

As described in paragraph 3.3, each RF pulse results a decay of ^{129}Xe polarisation while allowing for the usage of a larger flip angle. It was crucial to maintain the consistent RF depolarisation k-space filter to ensure uniform signal depletion across k-space and to avoid wasting the remaining polarisation (20% of the polarisation was assumed to remain as a conservative measure). The initial calculation of the optimal flip angle was calculated using formula 95 from paragraph 3.3. Minor adjustments were applied to achieve the same k-space filter in the centre of the k-space. R=4R=4, the calculated flip angle was adjusted from 3.20° to 3.59°, and for R=2R=2R=2, it was adjusted from 2.61° to 2.86°. The results of the simulations are visible in figure 65.

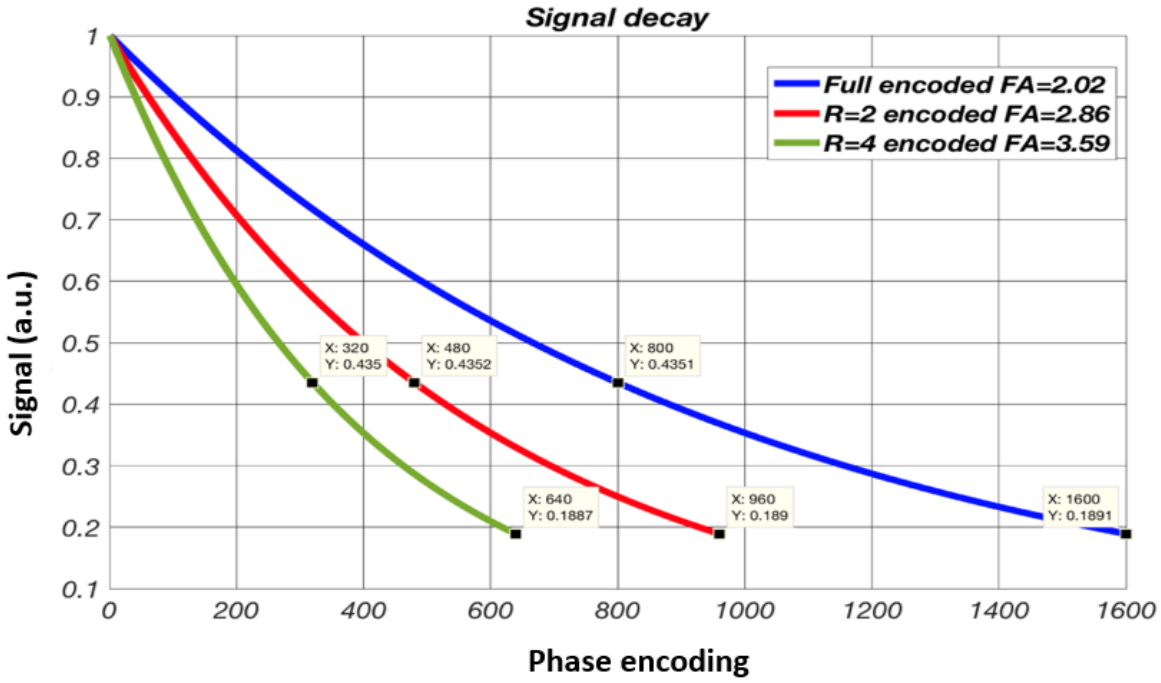

Figure 65: SPGR flip angle decay for different acceleration factors. It can be seen that despite the reduced number of phase encoding steps the k-space filter remain the same.

For all three different accelerated acquisitions, the k-space filter maintained the same shape, with a signal intensity reflecting approximately 43% additional polarization at the centre of the k-space. Additionally, the residual polarisation at the end of acquisition was around 19% for all three accelerated acquisitions.

5.3.3 3D SPGR acceleration imaging

The sequence was a 3D coronal Spoiled Gradient echo with the following parameters: 100 mm coronal/axial slices, a field of view of 40 cm^2, acquisition matrix of 80x80x20, a receiver bandwidth (BW) of 5.95 kHz. Under sampling was performed along left-right direction. An auto calibration region of size 16x20 was acquired in the centre of k-space, respectively along with the phase and the slice encoding directions. Experiments were conducted on a healthy male volunteer (29 years old, 70kg), who inhaled a gas mixture of 500 ml of ^{129}Xe and 500 ml of N_2 for each scan. Sensitivity maps were obtained by the filtering the auto calibration region with a Kaiser window to attenuate the higher frequencies. The cropped k-space was then zero-filled to the full encoded matrix size, Fourier-transformed and used to reconstruct the aliased images with 2D SENSE. The reconstructed images, expressed in SNR units, with the corresponding g-factor maps are shown in Figures 66 and 67, with the full encoded images (R=1) as serving as reference. Image reconstruction for R=2 showed a good reconstruction (mean SNR~25 in the central slices) with no visible artefacts. However, a decrease in image quality was observed at an acceleration factor of R=4, with visible aliasing artifacts in the posterior slices and a local g-factor greater than 3.

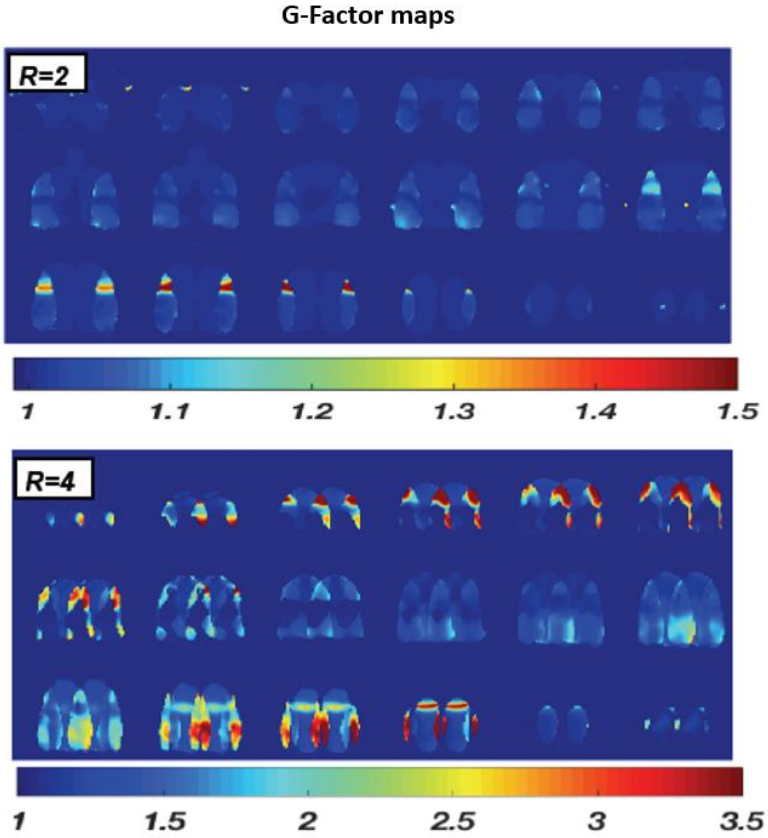

Figure 66: G-factors map for R=2 and R=4.

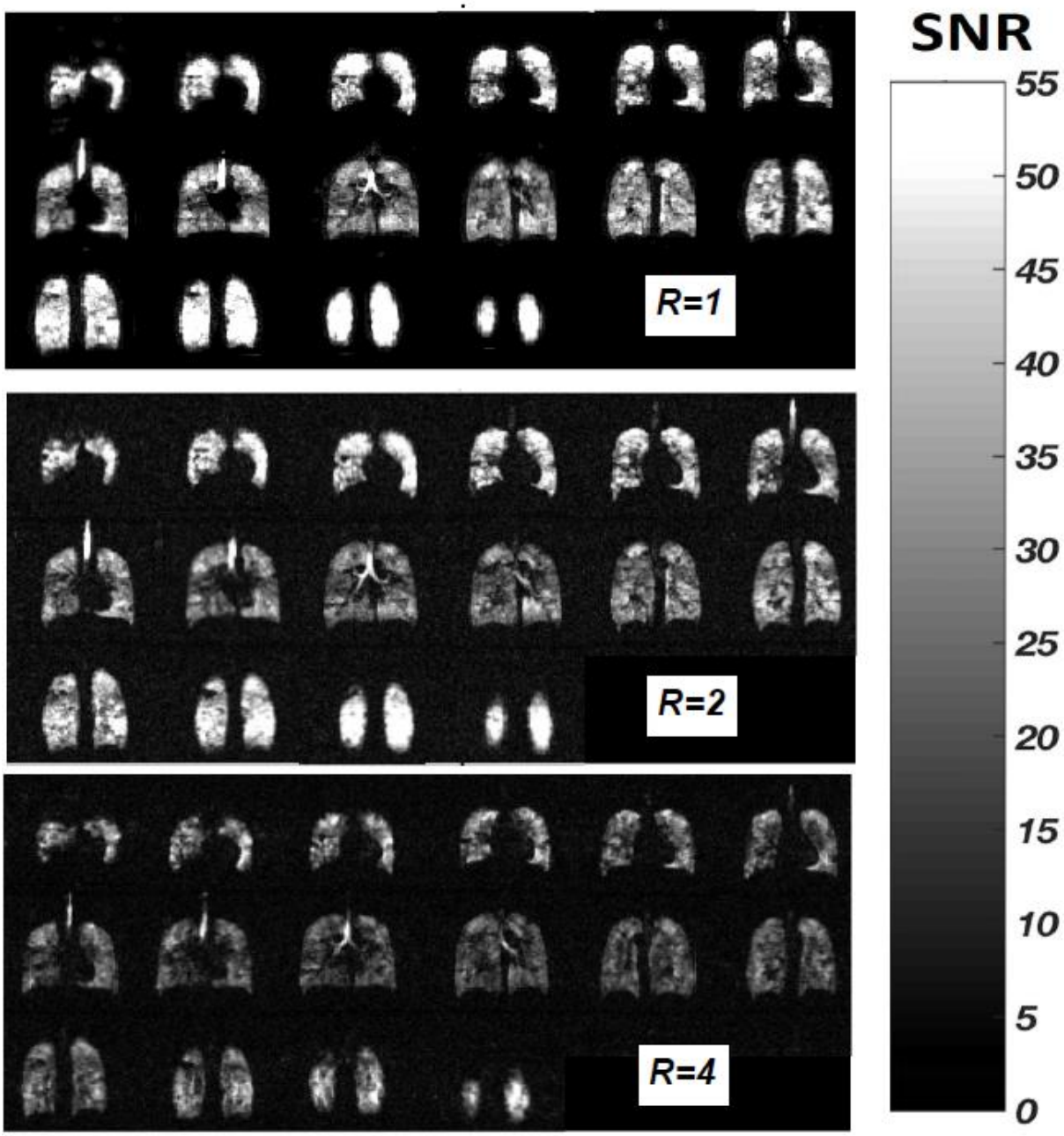

Figure 67: SNR with different acceleration. Is possible to notice a SNR degradation of the SNR related to the increase of the acceleration factor. Also, residual aliasing artefacts are visible in the lateral sides of the lungs.

5.3.4 Flip Angle assessment and imaging with the 3D Steady State Free precession sequence

As described in paragraph 3.2, the Steady State free precession sequence allows for the usage of a higher flip angle due to the magnetisation recycling. The behaviour of the HP ^{129}Xe longitudinal magnetisation during a 3D SSFP sequence can be simulated using a matrix operator approach. This method, extensively described for ^{1}H and ^{3}He [128], [185]

accounts for flip angle excitation, off resonance effect caused by the B_o inhomogeneity, and pulse sequence parameters. The magnetisation at the encoding steps n+1 is given by:

$$M_{n+1} = AM_n + B \tag{114}$$

B represents the relaxation matrix linked to the T_1 decay of magnetisation and is not considered for hyperpolarised gases application. The propagation matrix A, is a product of matrices representing rotation free precession, and relaxation of the magnetisation during a single-phase encoding step:

$$A = PCR_{\pi}(n)R_{\alpha}PC \tag{115}$$

Here, P denotes the free precession matrix during a period τ for a spin with a frequency offset of Δf_0:

$$\begin{bmatrix} \cos(2\pi\Delta f_0\tau) & \sin(2\pi\Delta f_0\tau) & 0 \\ -\sin(2\pi\Delta f_0\tau) & \cos(2\pi\Delta f_0\tau) & 0 \\ 0 & 0 & 1 \end{bmatrix} \tag{116}$$

For the case of no frequency offset, P simplifies to the identity matrix. The matrix C accounts for relaxation in the longitudinal and transverse planes:

$$\begin{bmatrix} \exp(-\tau/T_2(\tau)) & 0 & 0 \\ 0 & \exp(-\tau/T_2(\tau)) & 0 \\ 0 & 0 & \exp(-\tau/T_1) \end{bmatrix} \tag{117}$$

$\boldsymbol{R_{\alpha}}$ is the rotation matrix representing the RF excitation of a given by flip angle α pulse around the x-axis:

$$\begin{bmatrix} 1 & 0 & 0 \\ 0 & \cos(\alpha) & \cos(\alpha) \\ 0 & \cos(\alpha) & \cos(\alpha) \end{bmatrix} \tag{118}$$

Finally, $\boldsymbol{R_{\pi}}(n)$ denotes the phase cycling matrix of the sense of rotation of the alternate pulses [122]. The initial magnetisation before the first RF pulse is given by: $M_S^- = PCR_{\alpha/2}M_0$, where $M_0 = [0,0,M_0]$ represents the initial hyperpolarization level of the gas. Simulations were performed in MATLAB with the following sequence parameters: Matrix 80x80x20, BW=±8.06kHz, TR=6.4ms, TE=3.1ms. The simulation assumed no off-resonance effect, with T_1 of 20 sec, and a T_2 of 80ms [186]. The Autocalibration region was enlarged to a matrix of 20x20x20 to obtain a perfectly isotropic volume of the sensitivity maps. SSFP

sequence decay simulations identified optimal FA of 10.3º, 14.1º, 17.5º for fully sampled encoded, R=2 (1000 RF pulses with neat acceleration factor 1.6), and R=4 (700 RF pulses, neat acceleration factor=2.28), respectively. As can be seen in figure 68, the k-spaced filter maintained a consistent signal in the central lines of the k-space (around 47% of the initial polarisation), preserving around 22% of the residual polarisation at the end of the sequence.

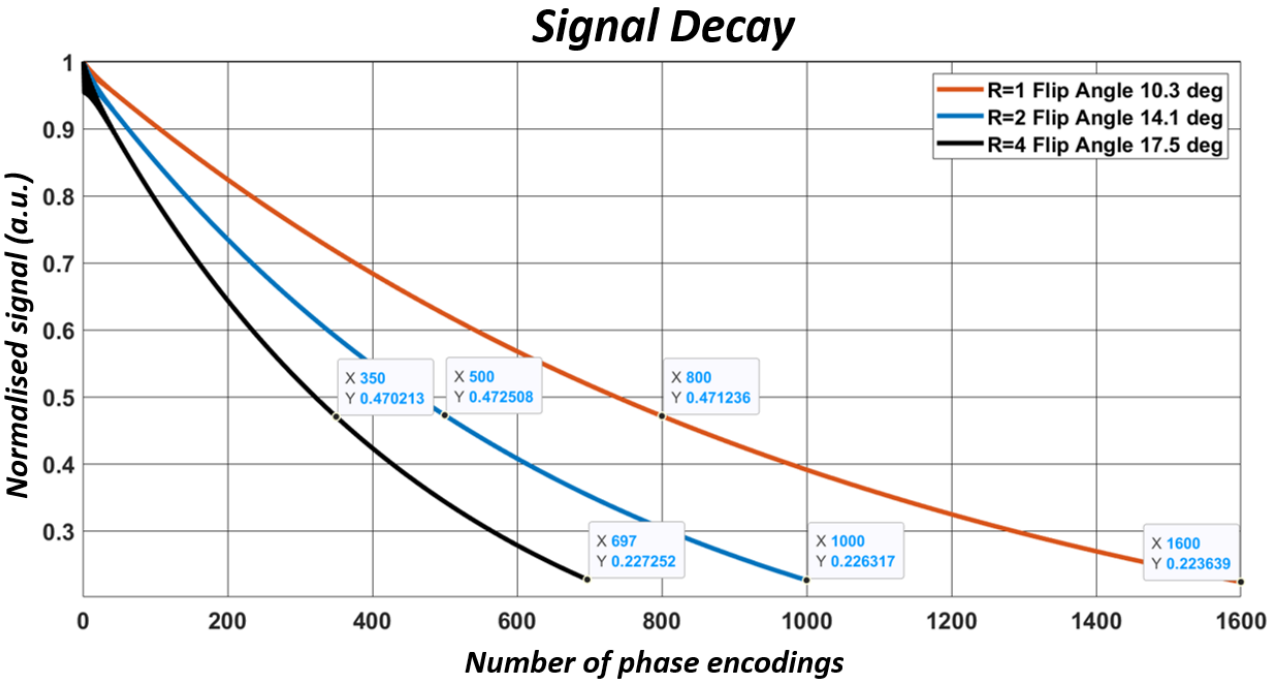

Figure 68: Flip angle evaluation of the accelerated imaging sequence with SSFP.

5.3.5 3D SSFP parallel accelerated imaging

The sequence used for parallel imaging was a 3DSSFP conducted on a healthy male volunteer, 29 years old, 75 kg, with matrix of 80x80x20, TR/TE=6.4/3.1ms, BW=8.06kHz, FoV=40x40cm^2; slice thickness=1cm. Parallel imaging was performed with acceleration factor of R=2 and R=4 along Left/Right direction. An Auto Calibration region with size 20x20 lines was acquired in the centre of k-space for both acceleration factors. Prior to the ventilation scans, anatomical proton images of the lungs were acquired for co-registration purposes (3D Coronal SPGR matrix 80x80x20, BW=83kHz; FOV=40x40cm^2 TR/TE=1.5ms/0.6ms, 5 Averages total scan times 12s). Figures 69, 70, and 71 illustrate the results of the image acquisitions, including the g-factor maps for the different acceleration factors and the image co-registration between the anatomical and ventilation scans.

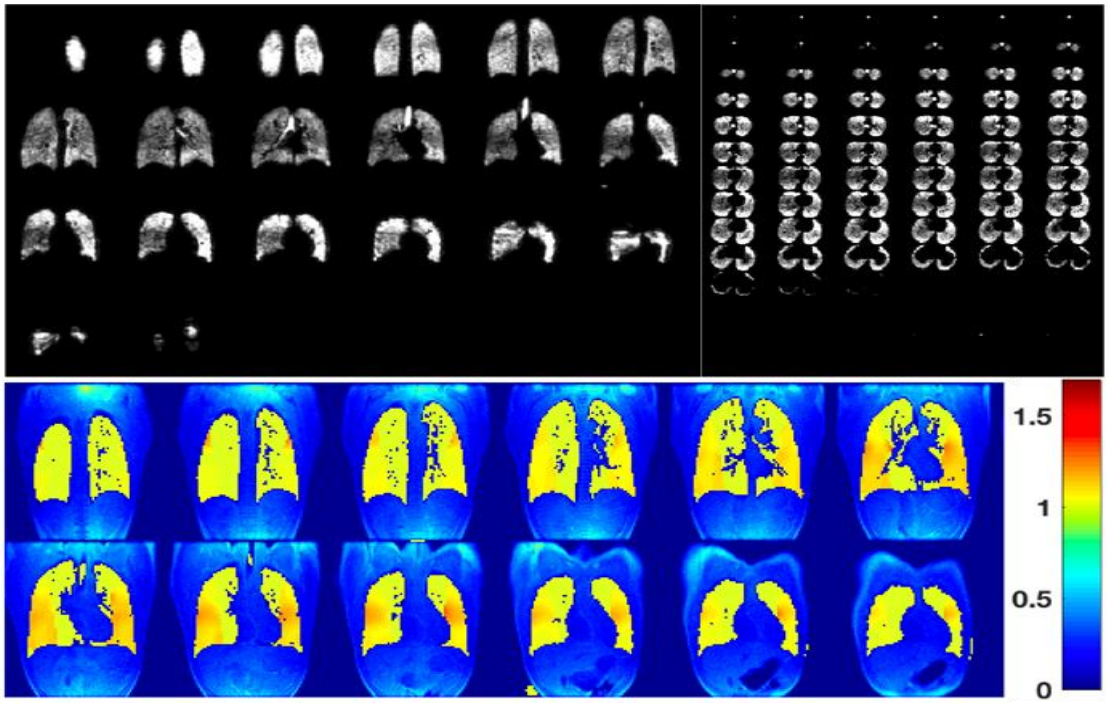

Figure 69: Reconstructed images with 2D SENSE on coronal and axial planes: R=2 image. Below are the g-factors maps. Figure adapted from [172] ***under creative commons license.***

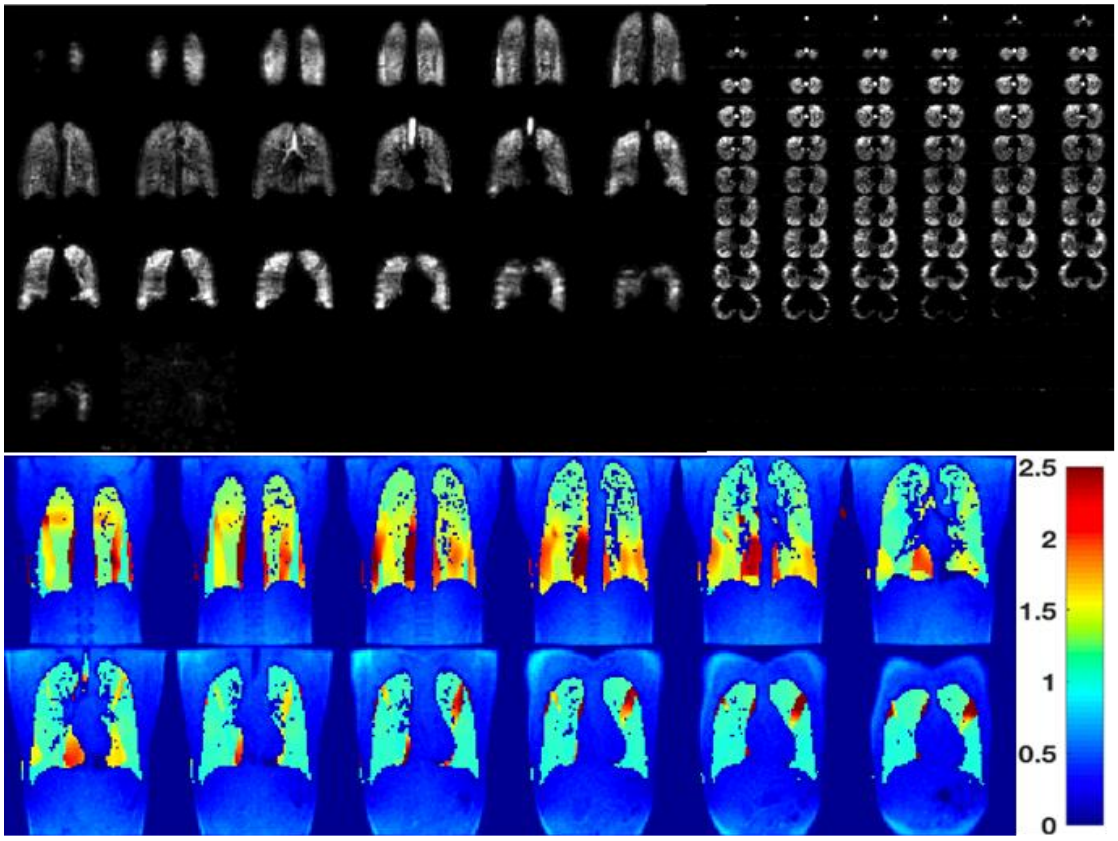

Figure 70: Reconstructed images with 2D SENSE: R=4 image. ©University of Sheffield.

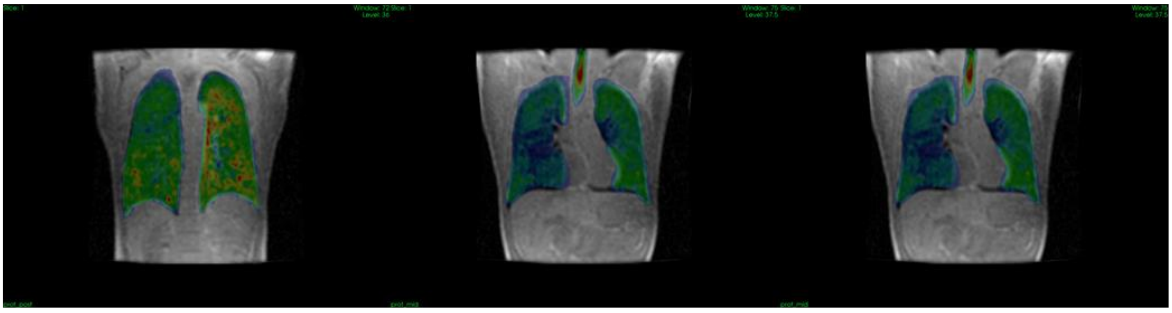

Figure 71: ^{1}H *Anatomical and ^{129}Xe ventilation phase co-referenced images with the birdcage inside the bore. Reproduced from* [172] *under creative commons license.*

^{1}H images acquired with birdcage in-situ show an optimal co-registration with the ^{129}Xe images (Figure 71). Images reconstruction for R=2 shows no visible reconstruction artefacts with a mean g-factor of 1.2. However, a decrease in image quality is noticeable an acceleration factor of R=4, where also some aliasing artefacts are visible, especially in the posterior slices (local g-factor>3).

5.4 Conclusion

In this chapter, we have demonstrated the development and application of an asymmetrical band pass birdcage for hyperpolarised ^{129}Xe MRI that functions without the need of an RF shield, enabling in situ ^{1}H imaging. In vivo FA mapping demonstrated B_1 like those reported in the literature. This study also evaluated various diode configurations for detuning the RF coil, and it was found that the configuration with 4 diodes showed the least distortion of the ^{1}H B_1 field. Although the ^{129}Xe transmit birdcage coil enabled proton imaging, the achieved ^{1}H FA with the ^{129}Xe coil in situ was four times lower for the same transmit power. This reduction is likely due to residual undesired coupling between the RF coils. Increasing the transmit power of the ^{1}H RF amplifier was not an viable solution to mitigate this issue due the local SAR values (9.23 W/kg), which are close to the International Electrotechnical Commission standard for normal level-controlled scans. Therefore, future effort should focus on improving the isolation between the two RF coils in the magnet, potentially using passive trap circuits tuned to the ^{1}H resonance frequency on the ^{129}Xe RF coil. The results obtained demonstrate some improvement in B_1 field homogeneity if compared to flexible vest coil designs reported in the literature. When combined with a separate 8- channel receive array, increased SNR was noticeable despite some drop-off in the sensitivity toward the central slices. The receiver RF coil array permitted acceleration of 2 with low g- factor values (maxi-mum values ~1.4). Also, is

important to note that several mechanical failures occurred due to the complex geometry and the large size of the structure. Additionally, this this design may not be suitable for all patients. In particular, could be not recommended to large size patients or claustrophobic subjects due to the reduced diameter of the coil that caused a reduction of the space available for the patient positioning.

5.5 Further development

The construction of this whole-body setup for imaging hyperpolarised ^{129}Xe allows for both improvements in image quality compared to the standard vest coil and increase the anatomical coverage for some larger anatomies. These enhancements are significant achievements, as there is growing interest in the research of dissolved phase HP ^{129}Xe in the lung, liver, and kidney. Imaging may be performed with the 8-channel array or by developing additional tailored coils for specific anatomy of interest, which would allow to study the dynamic nature of ^{129}Xe transport in blood. This is an important milestone due to recent concerns about gadolinium deposition and toxicity which have recently been brought to the attention of the MRI community [187]. Given the recent advancement in 3T dissolved phase imaging, further comparisons at 1.5T are needed. The development of a tailored sequence for imaging at 1.5T is essential and could allow multiple exams to be carried out with the patient in a single coil, including the comparison of kidney perfusion with and without water loads. This setup also facilitates parallel imaging, dramatically reducing scan time due to the under-sampling of k-space. Further analysis with different reconstruction methods, such as GRAPPA, SPiRiT and Compressed Sensing could also be explored to reduce scan time.

Chapter 6:

Development of a six-channel array for dissolved phase hyperpolarised ^{129}Xe MR imaging in the brain at 3T

Functional imaging of cerebral perfusion is a common clinical exam in MRI [12]. Typically, this procedure requires the injection of an external contrast agent, such as gadolinium. An alternative method that does not require any contrast agent is Arterial Spin labelling MR imaging, but it needs to acquire several averages to produce an adequate SNR [188]. Due to the brain being one of the most vascularized organs, there is growing interest in studying the uptake of dissolved ^{129}Xe in the human brain within the hyperpolarised gas MRI community [187][189][190][191]. Rao et al. [152] developed a custom RF coil system demonstrating the feasibility of hyperpolarised ^{129}Xe dissolved phase brain imaging at 1.5T and further comparisons at the 3T field strength are of interest. Given the low signal from ^{129}Xe in the dissolved phase, designing of tailored receive coils is crucial to obtain high SNR. The first step in developing of a receive array for hyperpolarised ^{129}Xe dissolved phase brain at 3T, involved simulating several designs to determine the optimal one using Ansys HFSS software simulator. This section discusses these designs and the simulations carried out to select the best design for implementation. Additionally, the chapter will cover the construction of the 6-channel receive array and an octagonal transmit coil for human xenon brain MRI at 3T.

6.1 Birdcage coil simulations

The initial phase of the RF setup development focused on designing the transmit coil, adopting an 8-leg low-pass birdcage configuration. Unlike, the conventional circular birdcage, an octagonal profile was chosen to facilitate the construction of the mechanical former using an in-house 3D printer. The end-ring diameter was specified as 36 cm, with

conductors were modelled as a cylindrical copper rod, each having a diameter of 6mm. The legs were designed as a copper strip with 1.4 cm in width, 36 cm of length and modelled as zero thickness sheet. Each leg featured a gap of 8 mm to accommodate a tuning capacitor specified at 27.30 pF modelled as a RLC port. Additionally, two more gaps were incorporated, each shifted by 90^0, to position the lumped port that supplied 1W of power each to feed the coil in quadrature. A cylindrical shaped radiation boundary with a height was applied, having height of 54 cm and a radius of 27 cm. This boundary extended beyond the volume occupied by the coil, as required by the simulation software. To calculate the homogeneity of the octagonal ^{129}Xe B_1^+ birdcage coil, 3D H-fields were exported and post-processed in MATLAB. The mean and standard deviation of the magnetic field were evaluated within a cubical region of 20x20x20 cm at the isocentre of the coil. The simulation involves 10 convergence passes with a Delta S of 0.02. The frequency span was set from 5 MHz to 90 MHz with 425 sampling points.

The results of these simulations, including magnetic field and S parameters, are illustrated in figure 77 below.

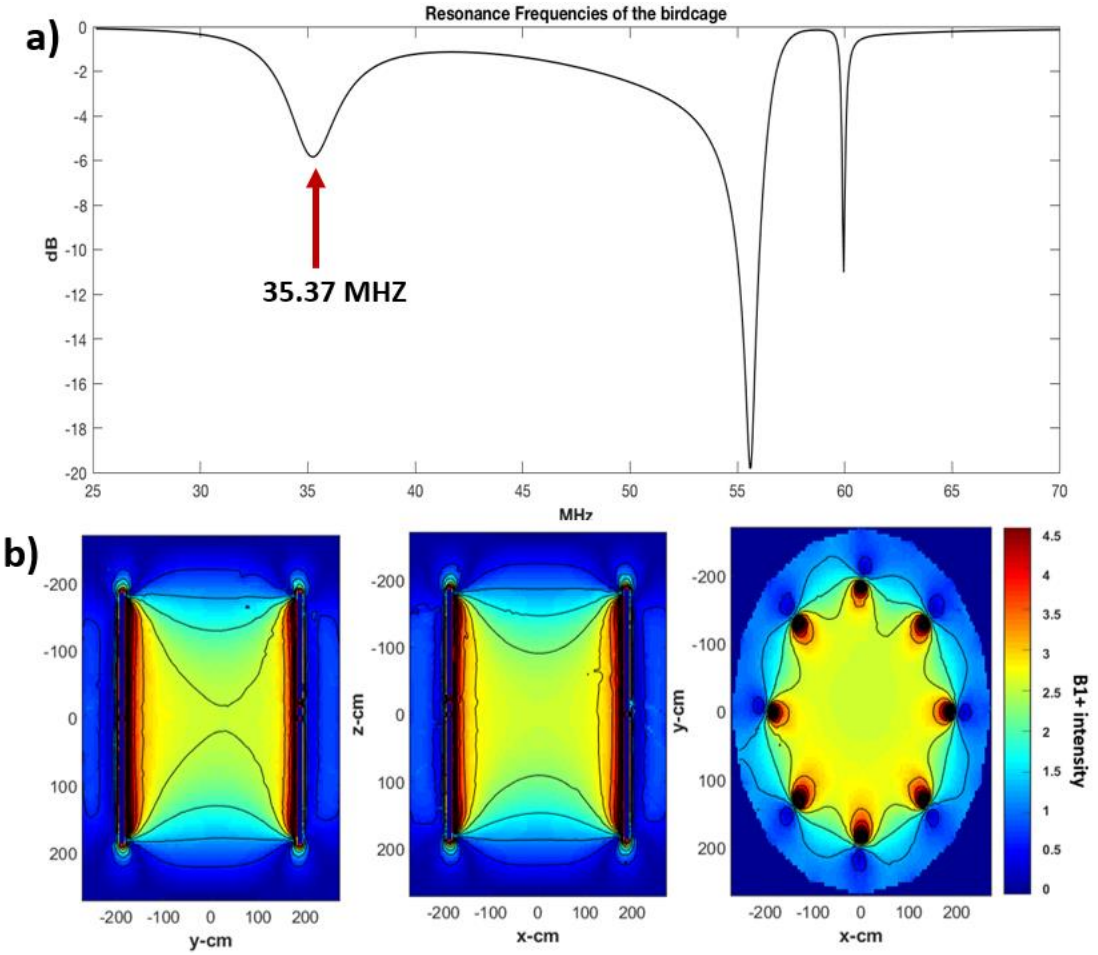

Figure 72: a) Resonant Modes of the birdcage, the first peak is the homogeneous resonant mode at 35.37 MHz. b) B_1^+field simulations for the birdcage in the sagittal, coronal and axial planes.

Additionally, a conventional circular birdcage coil with similar dimensions (diameter 36cm, height 36cm, circular rod diameters 6 mm) was simulated as the octagonal birdcage coil. he magnetic field data for the circular birdcage coil were exported and calculated in MATLAB, following the same procedure used for the octagonal geometry. The calculated magnetic field along the three anatomical axes for circular birdcage coil can be seen in Figure 78.

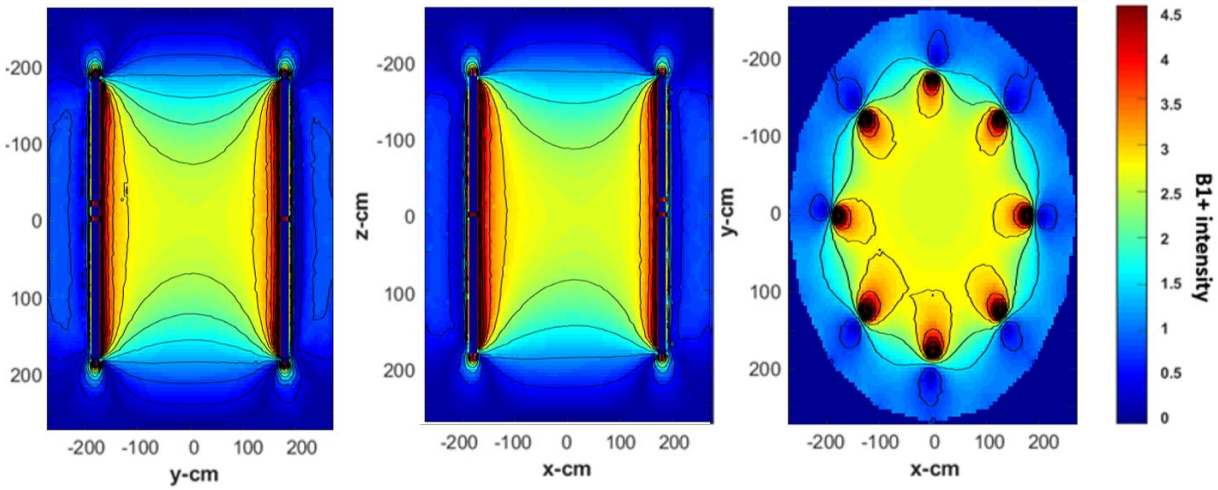

Figure 73: B_1^+field of the circular birdcage in the sagittal, coronal and axial planes.

The comparison of the efficiency of the two coils can be found in table 11. The octagonal birdcage has a better homogeneity despite showing a slightly lower efficiency and B_1 intensity. However, the two coils have a comparable value of transmit field in each plane. The slightly lower efficiency of the birdcage can be related to the higher perimeter length of the end ring conductors, which increases the total coil resistance.

Table 11: Simulated values of the two birdcage models.

Coil	Tuning Capacitance	$\eta = B_1^+ / \sqrt{P}$	B_1^+ axial
Octagonal birdcage	***27.30 pF***	***3.62***	***2.56μT ±5.24%***
Circular birdcage	***28.20 pF***	***3.72***	***2.63μT ±5.49%***

After the assessment of the B_1^+ field uniformity and the tuning capacitance of the birdcage coil, the subsequent step involved evaluating its Local and Average SAR (see figure 79). The birdcage was loaded with the 3D Human Head model embedded in the EM simulation

software. The methods formulas used to calculate SAR were identical to those described earlier for asymmetrical birdcage coil in sections 4.4.2 and 2.5.

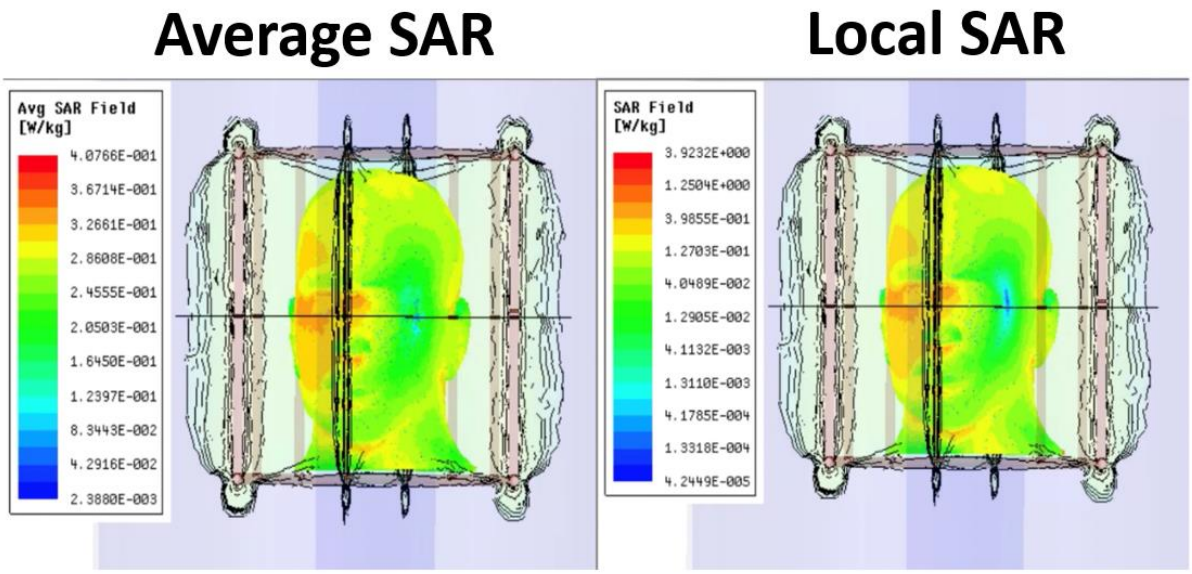

Figure 74: Local and average SAR measurements of the birdcage.

6.2 Array coil simulation

The array design was constrained to six channels, aligning with the available channel connections available in the Philips Ingenia preamplifier box used for ^{129}Xe applications. The optimise the design, the coil shape was adapted to leverage a pre-existing 3D brain array former previously assembled for another coil design [152] (Figure 80).

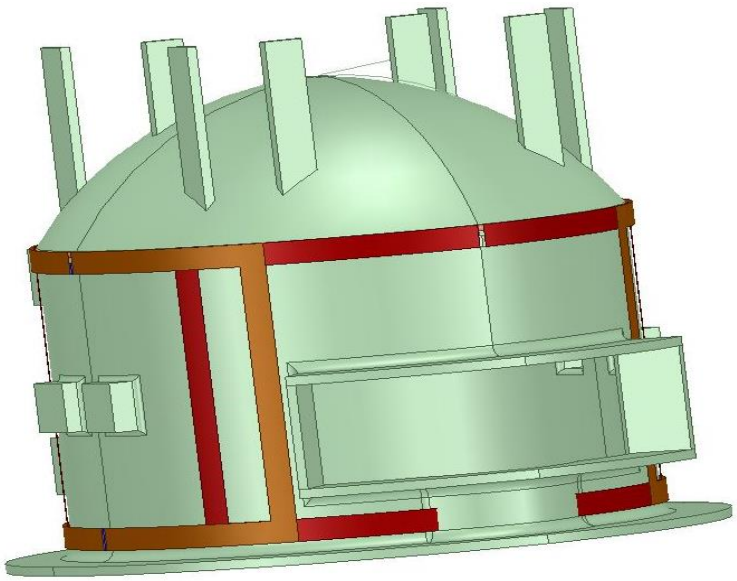

Figure 75: 3D cad of the brain array former. ©University of Sheffield.

Three different designs were simulated:

- The first design featured a 4-channel array surrounding the lateral perimeter of the former coil, incorporating two butterflies coil similar to those described in reference [104]. Each of the 4 elements have 2 tuning capacitors on the top and bottom conductors, while the two butterfly coils have three capacitors in series.
- The second design mirror the first, also consisting of a 4-channel array that surrounding the lateral perimeter of the former coil, and two large saddle coils are positioned on the top. The two-saddle coil are orthogonal to each other and they are placed upper part of the former, whilst the other rectangular elements are placed along the side of the former perimeter. Each of the 4 elements have 2 tuning capacitors on the top and bottom conductors, while the two saddle coils have three capacitors in series.
- The third design is a 6-channel inspired by the work by deZwaart [192]. The front element in this design is the largest and is developed around the gap for the eyes. The other elements have the same dimension. Each element overlaps to enhance decoupling.

6.2.1 Simulation

The simulation was conducted using Ansys HFSS to evaluate the sensitivity of each array design and determine the most suitable option. The coils conductors were modelled as zero thickness strip of copper, with gaps created along them to accommodate the placements of capacitors and source ports. To emulate the capacitors, lumped RLC ports with zero inductance and resistance values were used. A cubical radiation boundary was applied around to simulate the coil shield and truncating infinite free space to a finite calculation domain. Each simulation involved eight convergences passes with a delta S of 0.01. To evaluate the coil tuning parameters, each element was fed with lumped ports, and imaginary part of the impendence were analysed to predict resonance. The frequency sweep ranged from 20 MHz to 50 MHz with 100 samples. To $B1^-$ evaluation, lumped ports were replaced with current ports, each fed with a 1 Ampere if current. The complex H-field data of each element across all volumes were exported to a .txt file and computed in MATLAB to assess the coil sensitivity of each design. The ultimate intrinsic SNR of each array channel was calculated by combining all the receiving fields:

$$SNR = \sqrt{S\Psi^{-1}S^{-1}} \tag{119}$$

where S is the sensitivity of each element given by B_1^-, and Ψ is the noise covariance matrix:

$$\Psi^{\square} = re(Z) * diag((re)Z) \quad (120)$$

re (Z) is the real impendence matrix.

6.2.2 Results

The comparison of each design's sensitivity map is shown in Figure 81.

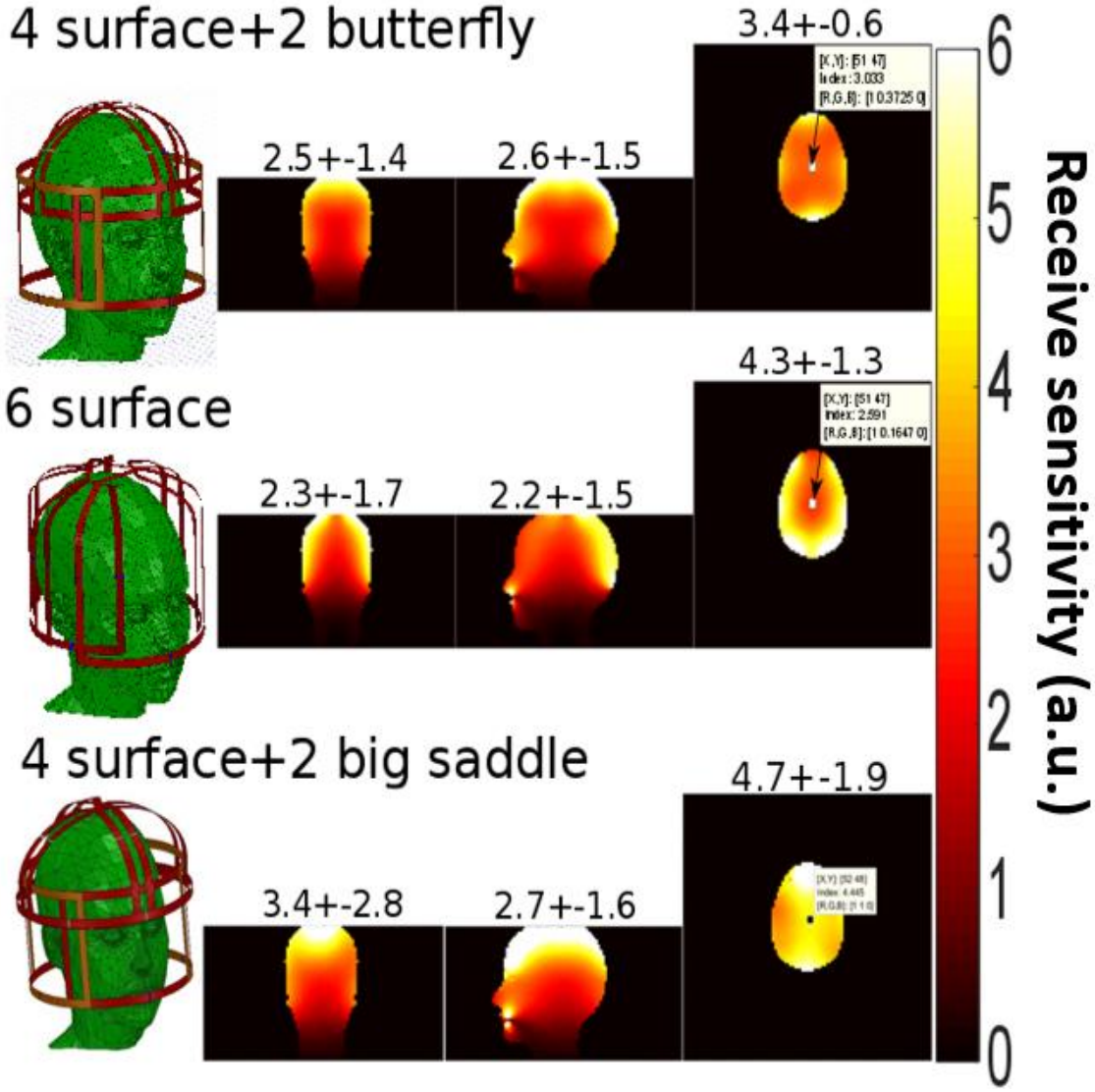

Figure 76: Simulation of the three proposed designs along the three planes, with mean values and standard deviation.

a) Two butterflies design:

This array with two butterflies has the highest homogeneity across the entire coil surface. It shows improved sensitivity in the central portion of the coil compared to the 6-channel design.

b) **Six-Channel Array**:

Despite having higher sensitivity in the peripheral region of the head, it exhibits the lowest overall signal intensity in the central region of the coronal planes compared to the two butterflies design.

c) **Two Large Saddle Coils**:

This design has the highest total mean sensitivity and highest signal in the central region. It achieves also, the best mean sensitivity across the three planes, despite having the highest standard deviation.

Based on these results, it was decided to proceed with the design featuring the 2 large saddle coil. Improved decoupling is expected with the addition of low noise preamplifiers in the coil circuit. In figure 82, the normalised coil sensitivity in the central slice of the ROI across the three anatomical planes is shown. Each element effectively covers its designated area of interest. The two saddle coils cover the upper part of the head, while the two rectangular loops (front and back elements) provide coverage on the front and back side of the brain. The left and right elements, capture the signal from the lateral sides of the brain, with reduced field penetration due the smaller size of these loops compared to the other array elements.

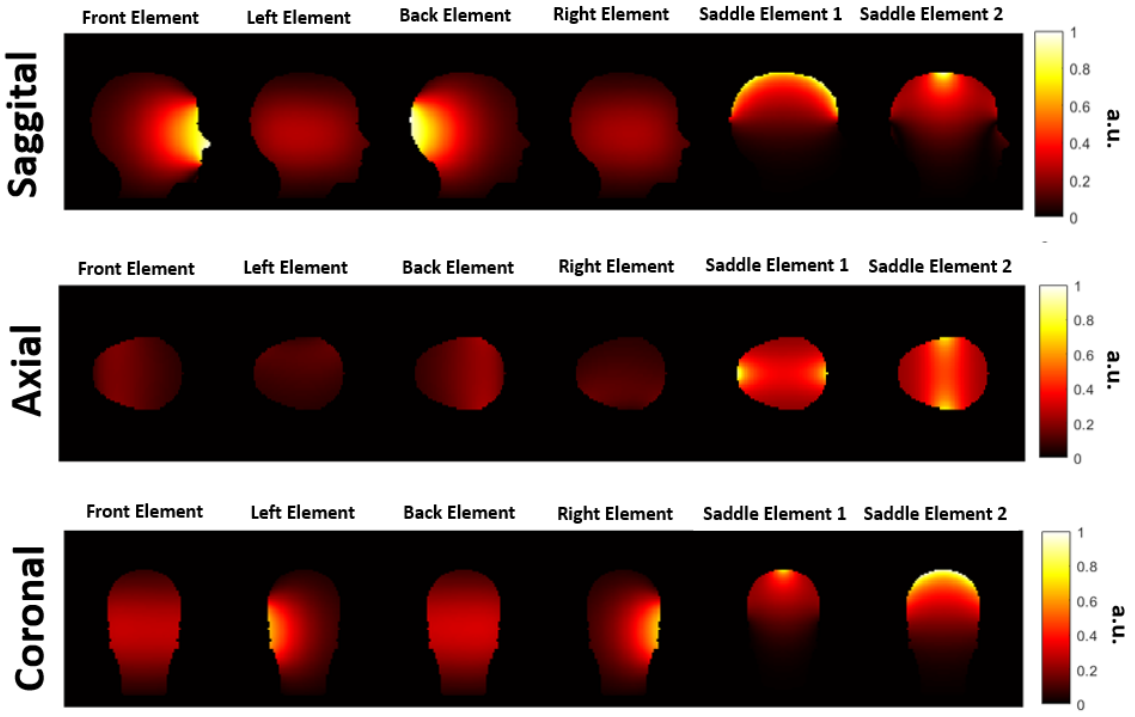

Figure 77: Sensitivity profile of each array elements in the 3 anatomical planes

6.2.3 G-factor calculation

The sensitivity maps allowed for the evaluation of the array design with the best sensitivity. However, it was also important to assess the parallel imaging performance. As described in paragraph 2.9, one of the main parameters to evaluate the efficiency of the parallel imaging reconstruction is the g-factor. According to formula (87), a high of g-factor can significantly decrease the SNR and enhance residual wrap-around artefacts that could affect the diagnostic quality of the acquired images. For example, a g-factor of 2 could decrease the SNR of by factor of 1.41. G-factors maps of the six channel array were calculated from sensitivity maps imported into MATLAB, using the following formula [193]:

$$g = \sqrt{[(\mathbf{\Sigma}^{-1}\Psi^{-1}\mathbf{\Sigma})^{1}]^{-1}[\mathbf{\Sigma}^{-1}\Psi^{-1}\mathbf{\Sigma}]} \qquad (121)$$

Where Σ is the coil sensitivity matrix, with the number of rows and columns determined by the number of coil elements and acceleration rate [192]. Calculated g-factor maps can be seen in figure 83:

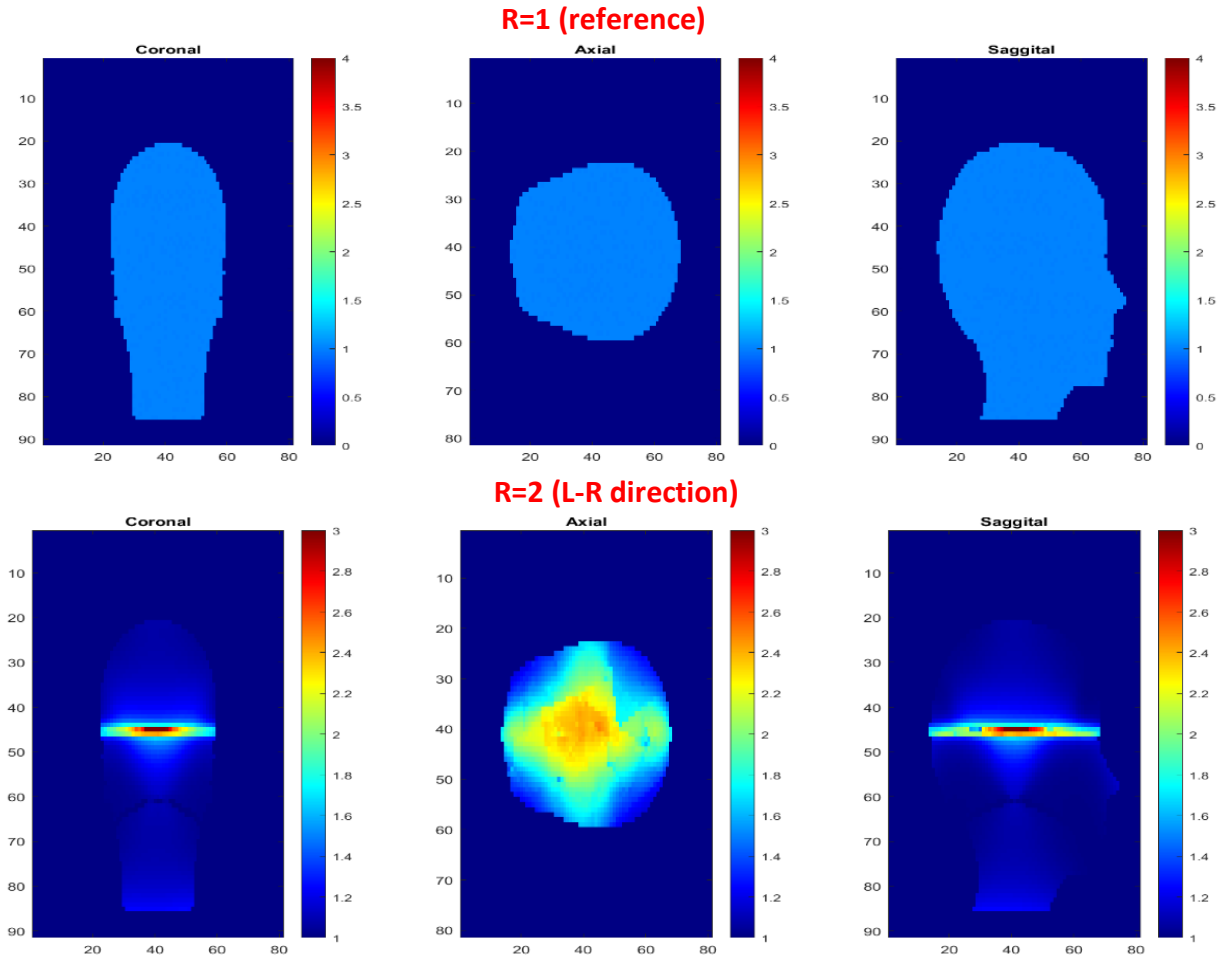

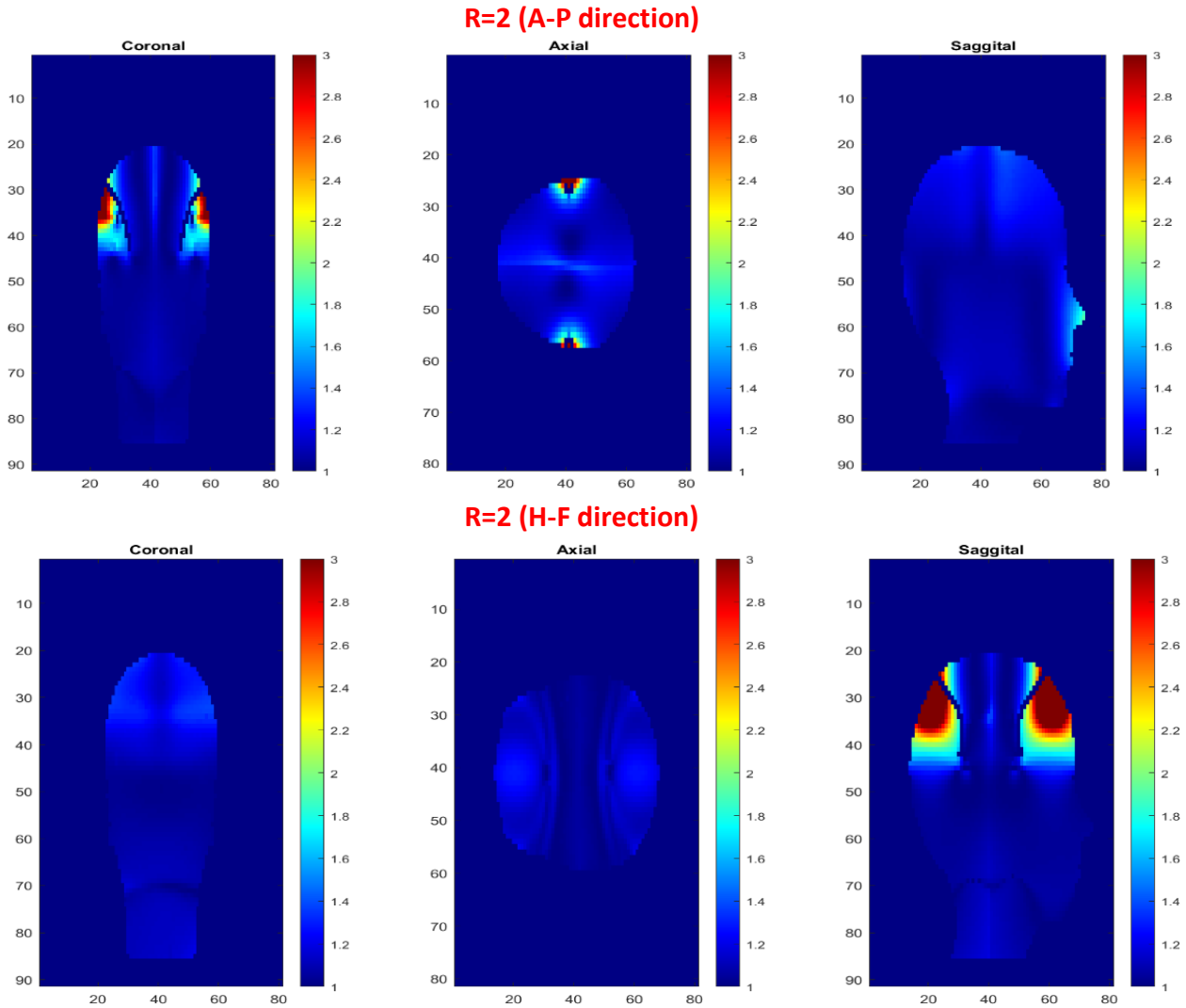

Figure 78: g-factor maps for different values of acceleration along different directions

At the top of figure 83, the reconstruction for R=1 is shown as a reference.

Below, the g-factor maps for an acceleration factor of 2 are displayed along the Anterior-Posterior (A-P), Head-Foot (H-F), and Left-Right (L-R) direction respectively. Regardless the direction of encoding, a region with a high g-factor is always noticeable.

- Referring to the g-factor map with acceleration along the L-R direction, there are axial slices 15 cm deep from top of the head with high g-factors (average 2.1).
- In the maps with acceleration factor along H-F and A-P directions regions with g-factors higher than 3 can be observed in the upper part of the head.

6.2.4 Conclusion

These results suggest that the 6-channel array with the two saddle coils (c) is the optimal design that was considered here for imaging the brain at 3T with HP ^{129}Xe. Despite the non-uniformity expected when using a multiple element array, this is can be mitigated with

post processing reconstruction. This design also showed the best decoupling between all the channels. However, the array has not proven to be the optimal solution for parallel imaging due to some local regions with high g-factor values, even at R=2. The most affected region is particularly around the upper position of the head where the two-saddle coils are located. The birdcage for the transmitting phase was successfully simulated, including the analysis of S-parameters, $B1^+$ field, and SAR measurements. In conclusion, this setup is expected to offer a good sensitivity for dissolved phase hyperpolarised ^{129}Xe in the brain. Since a similar setup was developed for the same purpose at 1.5T, comparisons between the two static field intensities will be possible.

6.3 Comparison of Birdcage T-R and 6-Channel array

A further analysis of the expected SNR between the birdcage and the 6-channel array was performed. The B_1 fields of the two-coil designs were compared to assess effective improvement in sensitivity provided by the 6ch RF array when compared to the octagonal birdcage. The B_1 field of the two designs were calculated by superimposing individual transmission $|B_1^+|$ and receive field $|B_1^-|$[194] using the formula:

$$|B1| = \sqrt{|B1^+|^2 + |B1^-|^2} \tag{122}$$

Considering the 6-channel array the transmit and receive fields of were previously combined using the sum of squares method as in formula (119). The results can be seen in figure 84. As expected, the birdcage coil delivers a more uniform magnetic field, with a slight variation along the Head-Foot direction. On the other hand, the array offers a higher sensitivity in the upper part of the head, with a gradual decay of the coil sensitivity, if we consider the inner part of the head. However, in the region of interest, located in the upper part of the head, the array provides a higher B_1 field intensity. In the coronal plane, the array achieves a maximum intensity ranging from 1.1μT to 0.8 μT, whilst the birdcage has an average field of 0.6 μT, resulting in an approximately 50% increase in field intensity. Similarly, in the axial and coronal planes, there is an improvement of about 33% in B_1 field intensity compared to the birdcage. This results consistent with those obtained in reference [194]. Considering this analysis, the array offers a higher SNR compared to the birdcage in transceiver configuration.

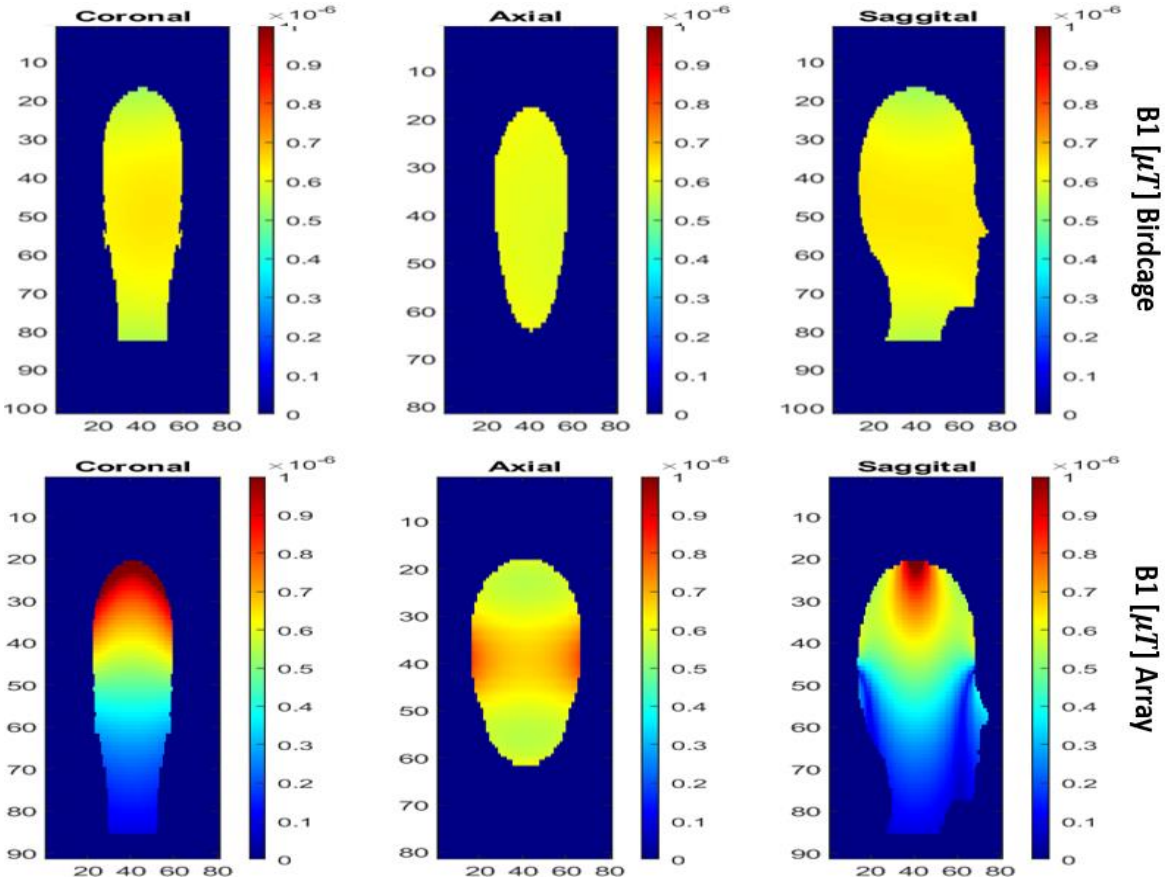

Figure 79: B1 field of the birdcage coil (top), B1 field of the 6 channel array (bottom).

6.4 Birdcage coil construction

The birdcage is an 8-leg low pass birdcage with octagonal end rings (Figure 85). Each leg contains a capacitance of 28.6 pF to tune the coil at 35.33 MHz, the ^{129}Xe Larmor frequency at 3T. Two lattice baluns ensure quadrature feeding of the coil. Active decoupling during the receive phase is achieved with high power PIN diodes placed in the middle of the tuning capacitors, switched by DC through an RF choke (a parallel circuit formed by a $1\mu H$ chip inductance and a 20.2 pF). Proton traps are included along the legs to enable the acquisition of proton images using the system Q-body coil (3TAchieva, Philips). The trap circuit consists of a tuning capacitance of 22pF in series with the trap circuit tuned at 128 MHz (parallel circuit of 186 nH and 8.3 pF) (see figure 86). The coil was loaded with 1 gallon of cylindrical saline solution of 4g NaCl/L, 2g NaCl/L with a height of 25 cm and diameter of 14 cm to simulate the head anatomy. The resulting impedance of the coil measures on the VNA around 4.5 Ohm in both ports. The matching is ensured through two lattice balun matching circuits (304 pF capacitance and 66.87nH inductance), placed perpendicularly to

each other. The two feeding ports are then connected to a quadrature hybrid coupler tuned at 35.3 MHz.

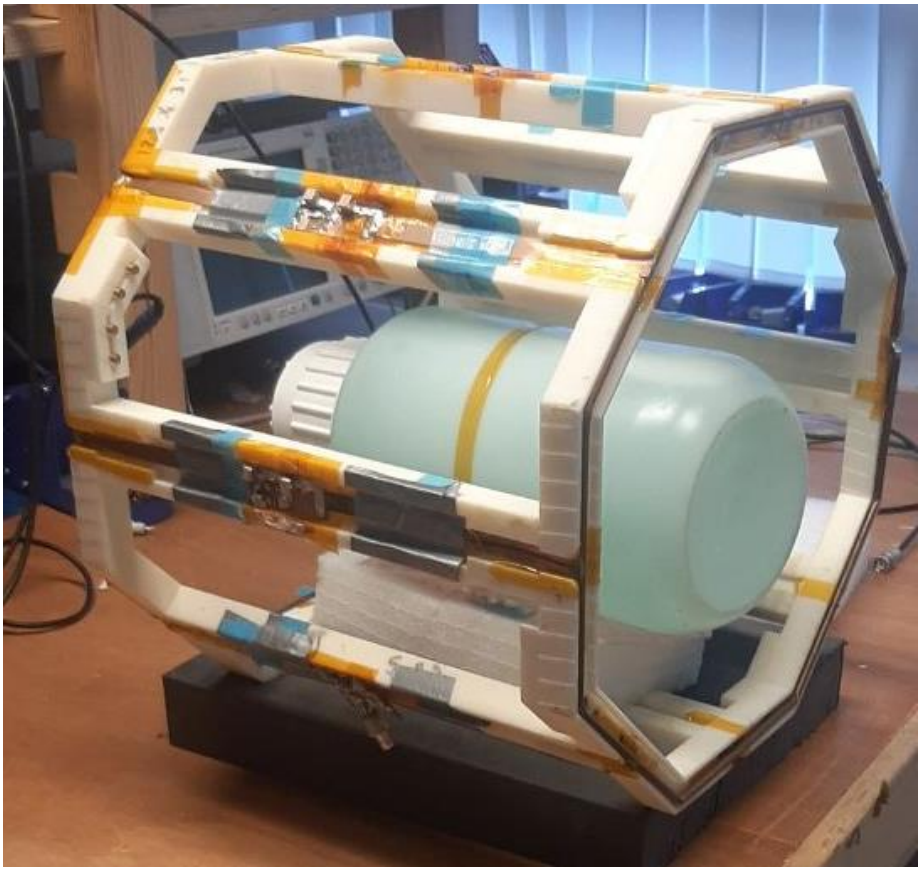

Figure 80: Octagonal birdcage coil, connected to the VNA, loaded with the saline solution phantom. ©University of Sheffield

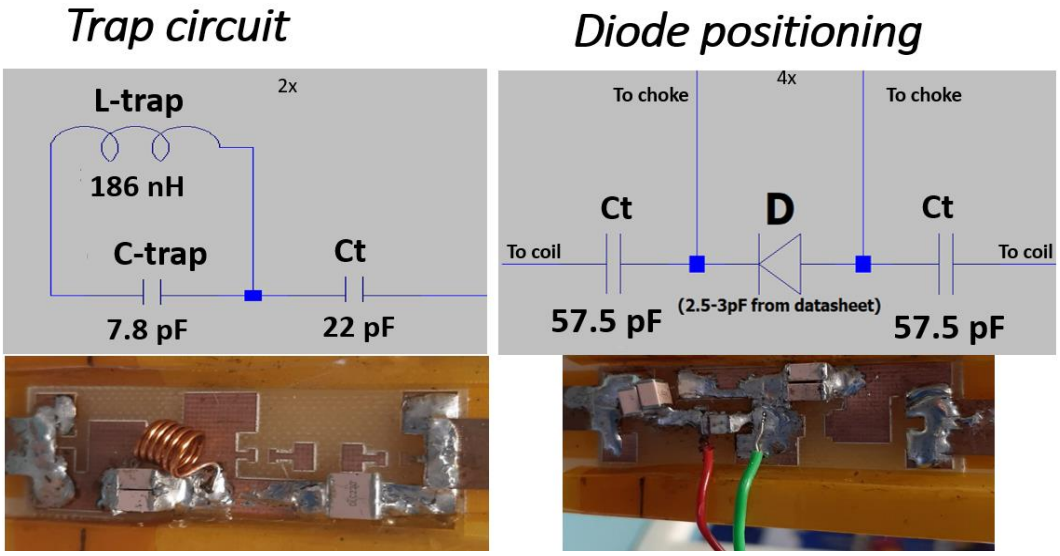

Figure 81: On the left trap circuit, on the right diode circuit. ©University of Sheffield

6.4.1 Results

The unloaded Quality factor of 257 was measured with S_{12} decoupling of two small loops placed nearby the birdcage (Q factor unloaded 257). When loaded with the phantom, the Q factor reduced to 94, giving a ratio $Q_{unloaded}/Q_{loaded}$ of 2.73.

Tuning and matching parameters were measured inside the scanner bore using the referencing a frequency of 34.70 MHz. This adjustment accommodated for a frequency of approximately of 0.6-0.7 MHz, attributable to interaction between the birdcage and the Q-body coil of the 3T scanner. Figure 86 illustrates these measurements on the workbench, depicting both unloaded and loaded coil condition.

At the nominal tuning frequency of 34.70 MHz, the loaded S-parameters were respectively: S_{11} -26.82 dB, S_{22} -19.47 dB, S_{12} -19.522 dB. Further characterisation involved the tuning of a hybrid combiner to 35.35 MHz, achieving isolation levels of -3.16 dB and -3.40 dB on ports S_{12}, S_{13}, respectively. Active decoupling was analysed with the coil connected to the power supply with both ports connected to the hybrid coupler. During transmission, the coil received 5V and 3A (diode on), whereas during reception -12V and 3A (diode off). This setup achieved an effective decoupling of approximatively -23 dB, as measured by the S_{12} parameters with two loops connected to the VNA.

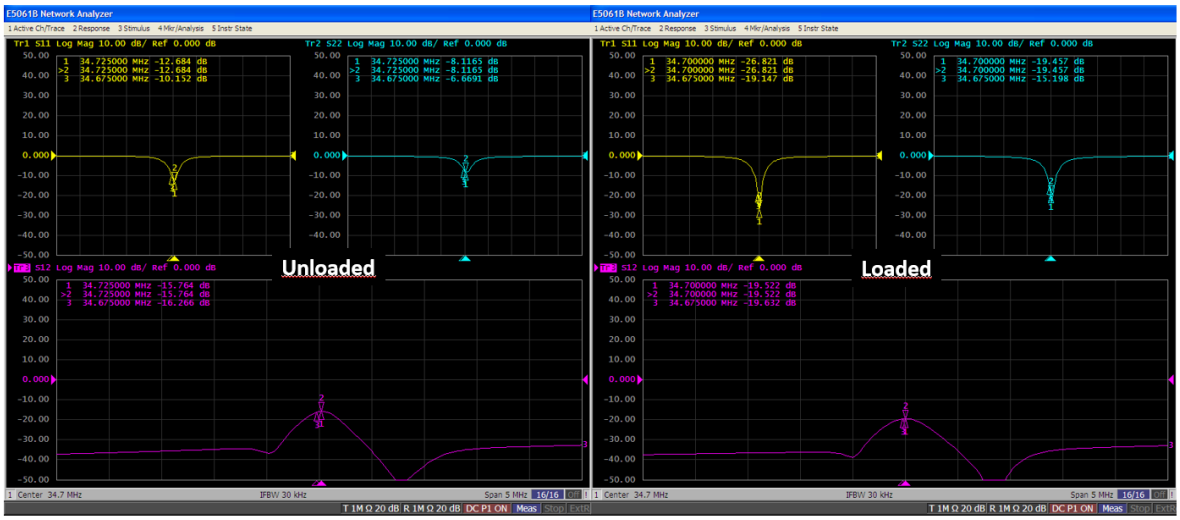

Figure 82: S-parameters measurements, to evaluate tuning and matching of the coil

6.4.2 Dissolved phase ^{129}Xe brain imaging with the octagonal birdcage.

Following the methodology outlined in chapter 4 for evaluating the asymmetrical birdcage coil, we conducted a dissolved ^{129}Xe brain imaging experiment using the octagonal birdcage in transceiver mode. Subsequently, diodes and RF chokes were integrated into the birdcage

circuit to convert it into a transmit-only coil. The experiment was performed on a 3T Philips Ingenia scanner with a healthy male volunteer (36 years old, 185cm, 90Kg). The imaging sequence was a 2D SPGR: FOV 375 mm^2, Matrix 48x30, Pixel size=7.8x12.5 mm, FA=20° degrees, TR=4ms, TE=0.6ms, WFS (Water-Fat shift) =2.45, total BW=2.69 kHz, Offset frequency=9545 Hz (centre frequency shifted to 198 ppm), slice thickness= 100mm, readout encoding direction Right-Left. 7 Dynamics were acquired, one immediately after the inhalation of the Xe dose (1 L, 30% of polarisation), and at intervals of 8 seconds up to 48 seconds. Raw data were exported in MATLAB for images reconstruction. K-space were low pass filtered with a Hamming window and zero padded to achieve a matrix of 95x95. Results from the imaging experiments are presented in figure 87. During the initial scan at 8 and 16 seconds, hyperintense signal were observed, attributed to residual xenon gas phase in the throat and involuntary breathing movements from the patient. Between 16 and 24 seconds, the maximum signal from the dissolved ^{129}Xe in the brain was observed, consistent with the peak signal detected at 22 seconds in the dynamic spectral acquisition. Signal intensity began to decrease at 32 seconds, with some residual signal still present at 40 seconds and

disappears by 48 seconds. These experiments provided valuable insights into the efficacy of the octagonal birdcage for dissolved phase ^{129}Xe in the brain.

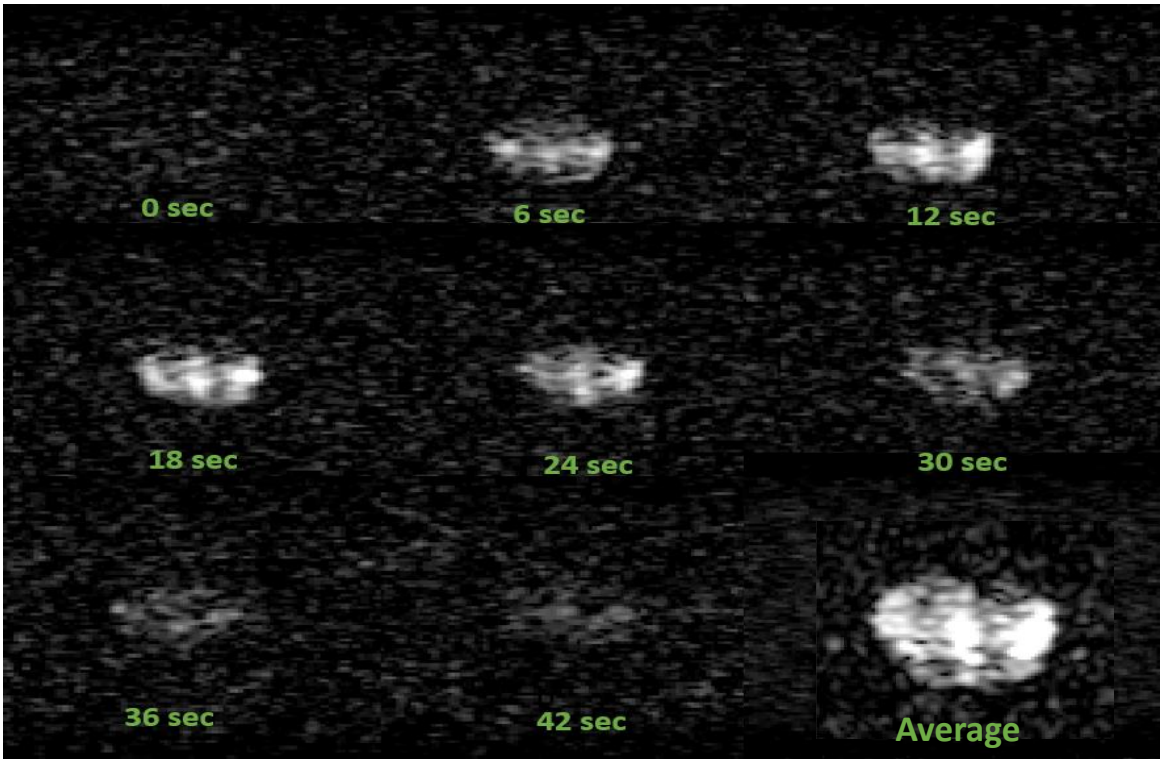

Figure 83: Image of dynamics of dissolved phase ^{129}Xe brain at different scan times. In the end, the resulting image averaging the seven dynamics. ©University of Sheffield

6.5 6-Channel Array construction

As demonstrated in section 5.2, the chosen coil configuration based on optimal results from the simulation was the one with two perpendiculars saddle coil and 4 channels rectangular shaped. However, contrary to simulations, the conductors used were copper cylindrical tubing with an outer diameter 0.4 cm and inner diameter of 0.35 cm. Below are listed in circuital parameters, dimension and results for each single channel.

Channel 1

Channel 1 is located at the front of the helmet (see figure 89). The element is a rectangular shaped loop with a height of 13.56 cm and a length of 20 cm (curvature length 23.2 cm). The maximum radius of curvature is 5 cm from the bottom. Q factor was assessed by measuring the S_{12} coupling of two loop probes placed near the coil. With and without cylindrical saline solution phantom load respectively the Q factors were 243 and 79 respectively, with a Q ratio of 3.53. Active decoupling, achieved with the PIN diode

(MA4P7435NM- 109IT, Macom, Lowell, Massachusetts), was approximately -33 dB. Coil tuning frequency and matching were measured with a minimum peak of -31dB at 35.3 MHz.

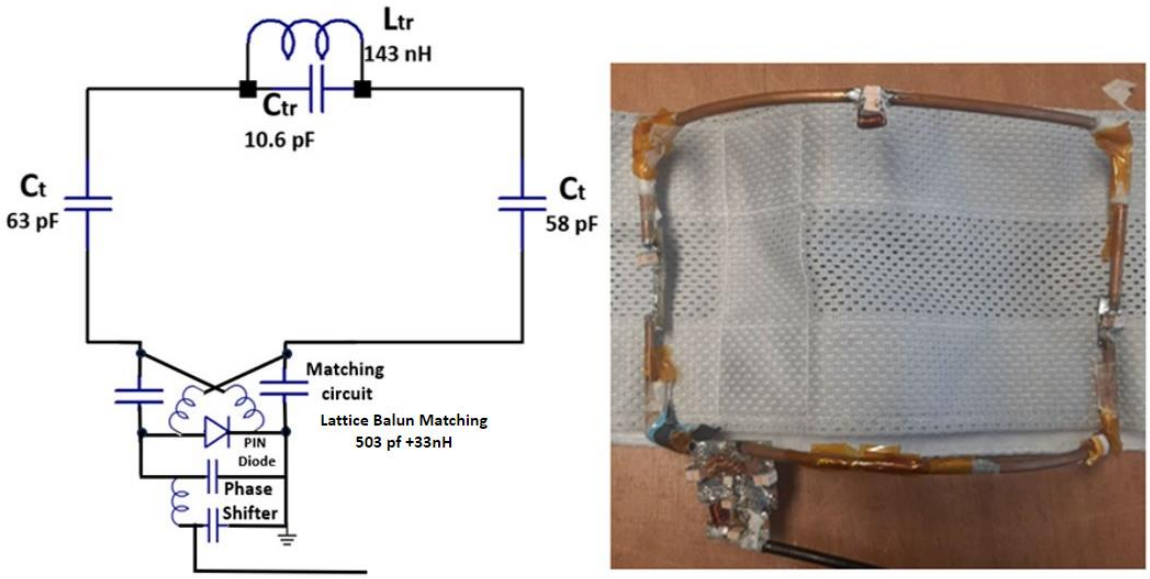

Figure 84: Circuital design of Channel 1 (left) with final construction (right). ©University of Sheffield

6.5.1 Channel 2-4

Channels 2-4 are located at the side of the helmet, sharing identical dimension and circuital design. These elements are rectangular shaped loops with a height of 13.50 cm and a length of 17.5 cm (curvature length 18.8 cm). The maximum radius of curvature is 3 cm from the bottom (Figure 90). Q factor was determined by measuring the S_{12} coupling of two loop probes placed nearby the coil both with cylindrical phantom load (Q-unloaded 84-88) and without load (Q-factor 270-243), resulting in a Q ratio of 3.23. S_{11} was around -25 dB for both loops. Coil tuning frequency and matching were evaluated, revealing a minimum peak of -32 dB at 35.1 MHz.

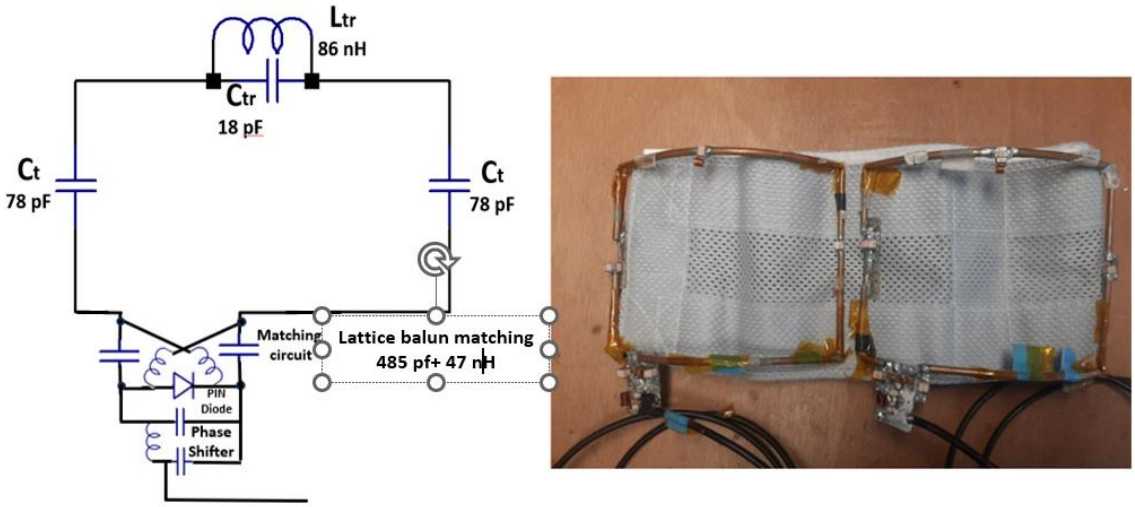

Figure 85: Circuital design of Channel 2-4 (left) with final construction (right). ©University of Sheffield

6.5.2 Channel 3

Channel 3 is situated at the back of the helmet (see figure 91). The element is a rectangular shaped loop with a height of 14 cm and a length of 21.5 cm (curvature length 26.4 cm). The maximum radius of curvature is 6.3 cm from the bottom. Q factor was assessed by measuring the S_{12} coupling of two loop probes placed nearby the coil, both with a cylindrical saline solution phantom load (Q-unloaded 90) and without load (Q factor 257), resulting in a Q ratio of 3.53. Active decoupling achieved with the PIN diode was approximatively -29 dB. Coil tuning frequency and matching were evaluated, showing a minimum peak of -22.33 dB at 35.1 MHz.

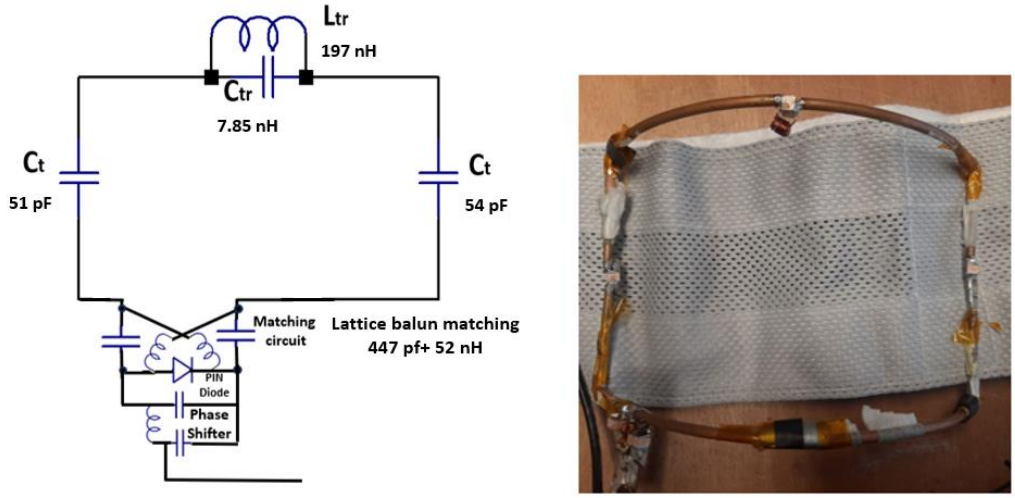

Figure 86: Circuital design of Channel 3 (left) with final construction (right). ©University of Sheffield

6.5.3 Channel 5

Channel 5 features a butterfly type loop design situated at the top of the helmet (see figure 92). The base of the loop is elliptical, with a minimum diameter of 21 cm and a maximum diameter of 24 cm. The conductors forming elliptical base are rectangular strips, with width of 1.5 cm. Two arches, each 35 cm in length, originate from the vertices of the major axis, with a maximum radius of curvature of 10 cm. Q factor was determined measuring the S_{12} coupling of two loop probes placed nearby the coil, both with cylindrical saline solution phantom load (Q-unloaded 83) and without load (Q-loaded 253), resulting in a Q ratio of 3.04. Active decoupling achieved using PIN diode was approximatively -27 dB. Coil tuning frequency and matching were evaluated, revealing a minimum peak of -20.46 dB at 35.3 MHz.

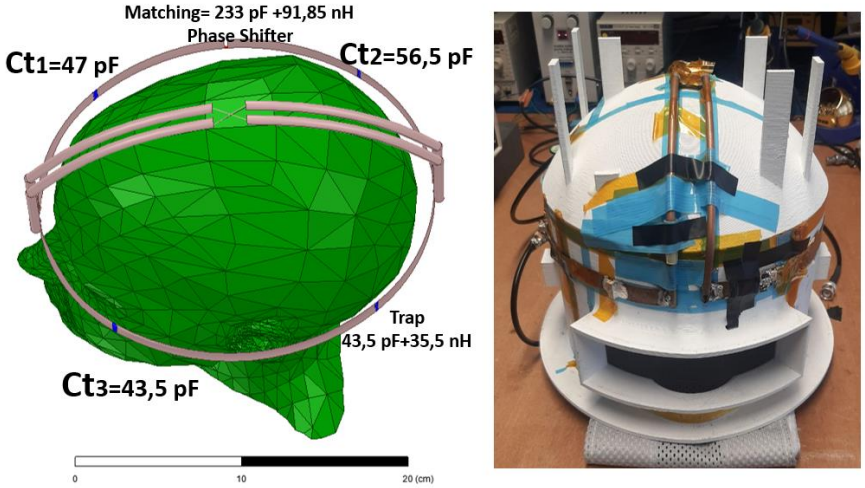

Figure 87: Circuital design of Channel 5 (left) with final construction (right). ©University of Sheffield.

6.5.4 Channel 6

Channel 6 features a butterfly type loop design located on the top of the helmet (see figure 93). The base of the loop is elliptical, with a minimum diameter of 24.5 cm and a maximum diameter of 25 cm. All the conductors used are copper tubes with an outer diameter of 0.4 cm and an inner diameter of 0.35 cm. Two arches, each 34.2 cm in length, originate from the vertices of the major axis, with a maximum radius of curvature of 10 cm. Q factor was assessed by measuring the S_{12} coupling of two loop probes placed near, both with cylindrical saline solution phantom load (Q-unloaded 89) and without load (Q-unloaded 342), resulting in a Q ratio of 3.84. Active decoupling achieved using a PIN diode was

approximatively -32 dB. Coil tuning frequency and matching were evaluated, showing a minimum peak of -23.57 dB at 35.3MHz.

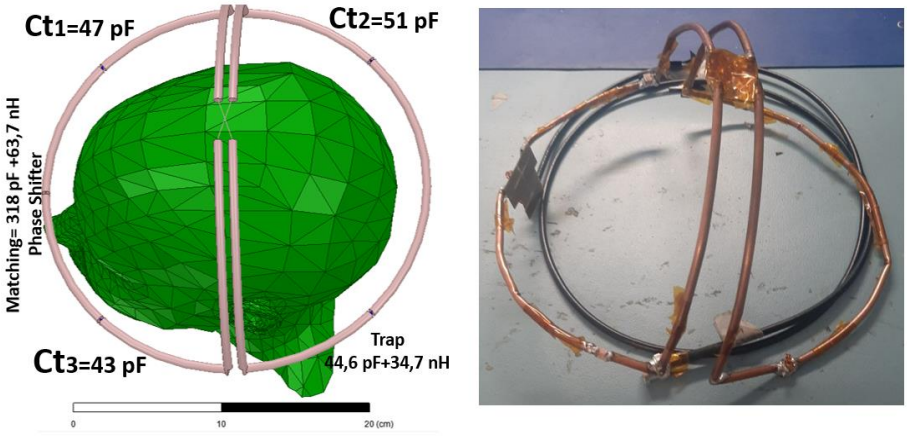

Figure 88: Circuital design of Channel 6 (left) with final construction (right). ©University of Sheffield.

6.5.5 Phase Shifter

Every element is connected to the 6-channel preamplifier box for individual channel isolation. However, the cable connecting the loops to the box introduces a phase shift that hinders optimal preamplifier matching. A cable of length of $\frac{\lambda}{2}$ introduces a phase shift of 180^0, resulting in a null complex impedance. The wavelength in vacuum is given by $\lambda = c/f$, with c being the speed of light $2.99792*10^8$ and f being the tuning frequency of the coil. Considering the tuning frequency of 35.33 MHz the resulting wavelength was 8.49 m. However, considering the velocity factor of the RG-58 cable that is 0.66 (PTFE material), the effective wavelength $\lambda/2$ is reduced to 2.80 m. The phase shifter was designed for a 90^0 degree phase shift ($\lambda/4$), with the remaining phase shift provided by the cable length of 1.40m. This choice was made to ensure the preamplifier boxes outside the scanner bore for safety reasons. Phase shifter design implemented was a simple low pass π-network, chosen for its straightforward implementation. The electrical circuit diagram is presented in figure 94 below, detailing the values of the lumped components.

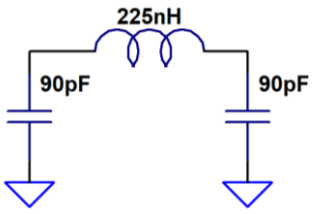

Figure 89 Low pass pi phase shifter. The circuit was soldered immediately after the matching circuit of each array.

The values of the component were calculated using the formulas described in [195]:

$$L = Z_0 \frac{\sin \varphi}{\omega} \tag{123}$$

$$C = \frac{1-\cos \varphi}{Z_0 \omega \sin \varphi} \tag{124}$$

The final coil configuration is shown in figure 95 below:

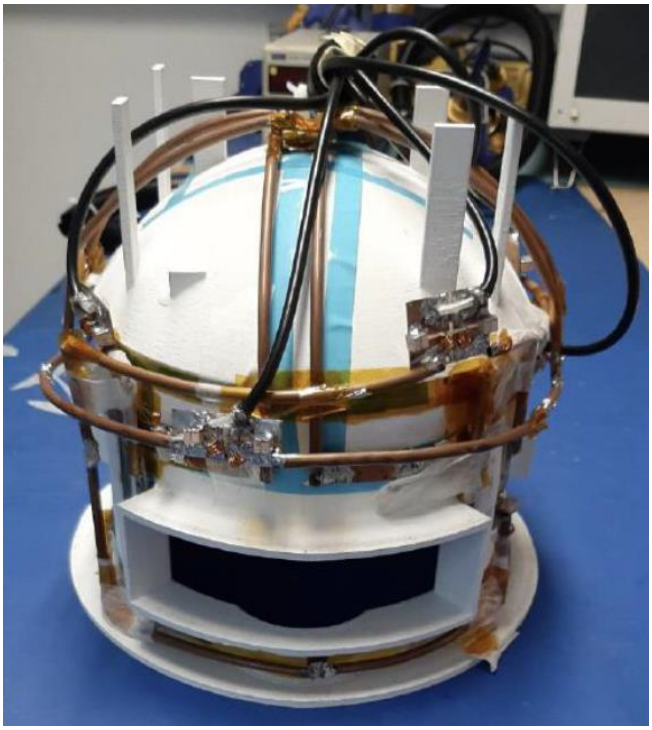

Figure 90: All the 6 channels assembled around the 3D printed head former. ©University of Sheffield

6.6 6-Channel Array ^{129}Xe NMR spectroscopy

The first step in testing the RF setup is to calibrate the flip angle and evaluate $B1^+$ uniformity in the region of interest. To achieve this, the array was loaded with a Tedlar bag containing 500 ml of hyperpolarised ^{129}Xe. Flip angle calibration was then performed using spectroscopy with the following parameters: TR=2000ms; BW=4096 Hz, N samples 256; 30 dynamics; nominal prescribed FA=120°. The decay of dynamic spectra of each element was fitted according to the equation S_n=$S_0[cos(\alpha)]^{(n-1)}$. The actual FA was determined from the average of all channels. The resulting FA decay of each element can be seen in figure 96.

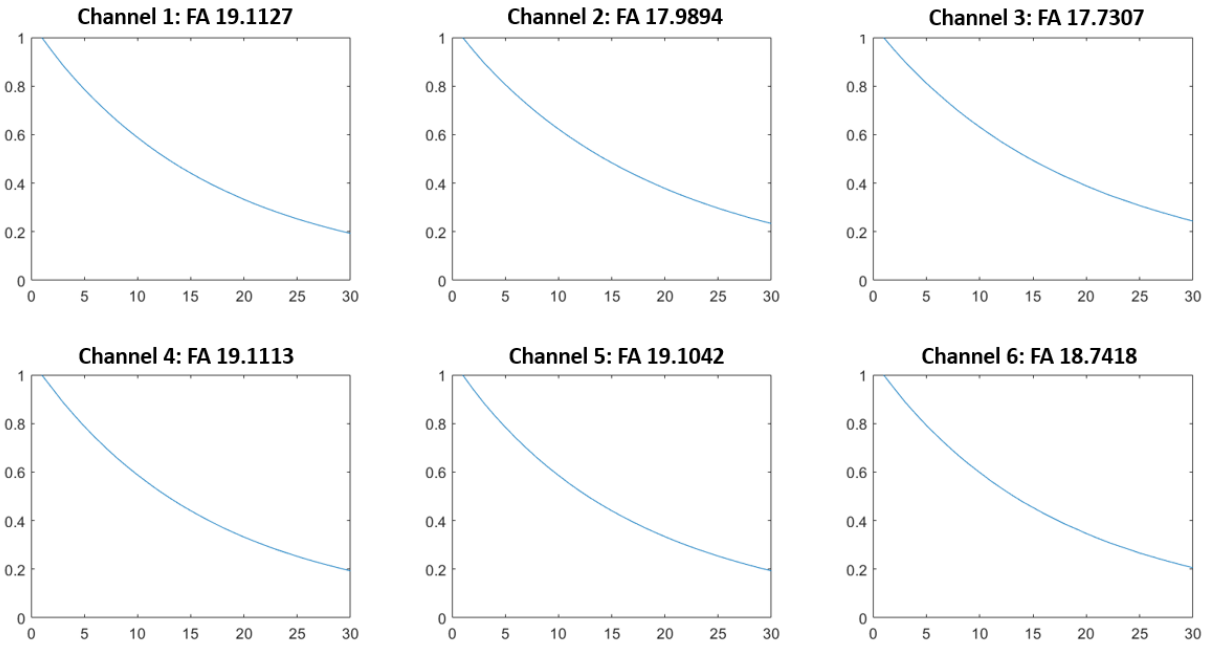

Figure 91: Signal decay of the Xe gas signal in the bag phantom. The peak of every spectrum for each channel was fitted according to the formula described above.

Flip angle decay for all channels fell within the same range, with a maximum of 19.11° observed in channels 1 and 4, and a minimum of 17.73 in channel 2, resulting in a mean flip angle of 18.62±0.62. After evaluating the uniformity of the transmitted flip angle for each channel, the next step was to perform in vivo spectroscopy of dissolved phased ^{129}Xe in the brain.

Dynamic in vivo brain spectroscopy was conducted using five channels due to the malfunction of one preamplifier. The scan was performed on a healthy male volunteer (27 years old, 75Kg), using a pulse acquire sequence with the following parameters: TR=2000ms, BW=4096 Hz, number of sampling points 256 (spectral resolution of 16Hz/point), 25 dynamic scans; FA=16°; inhaled ^{129}Xe Dose=1L (~30% of polarization), breath hold time~20 sec, total scan time~50 sec. The spectra were reconstructed by averaging the FIDs from the 30 dynamic acquisitions and applying an exponential apodization filter for noise reduction. Subsequently, zero-padding was performed to increase the FID to 4096 sampling points, achieving a spectral resolution of 1Hz/point. The FIDs were then Fourier Transformed, rephased and then combined as described in [196]. The final absolute magnitude spectrum can be seen in figure 97.

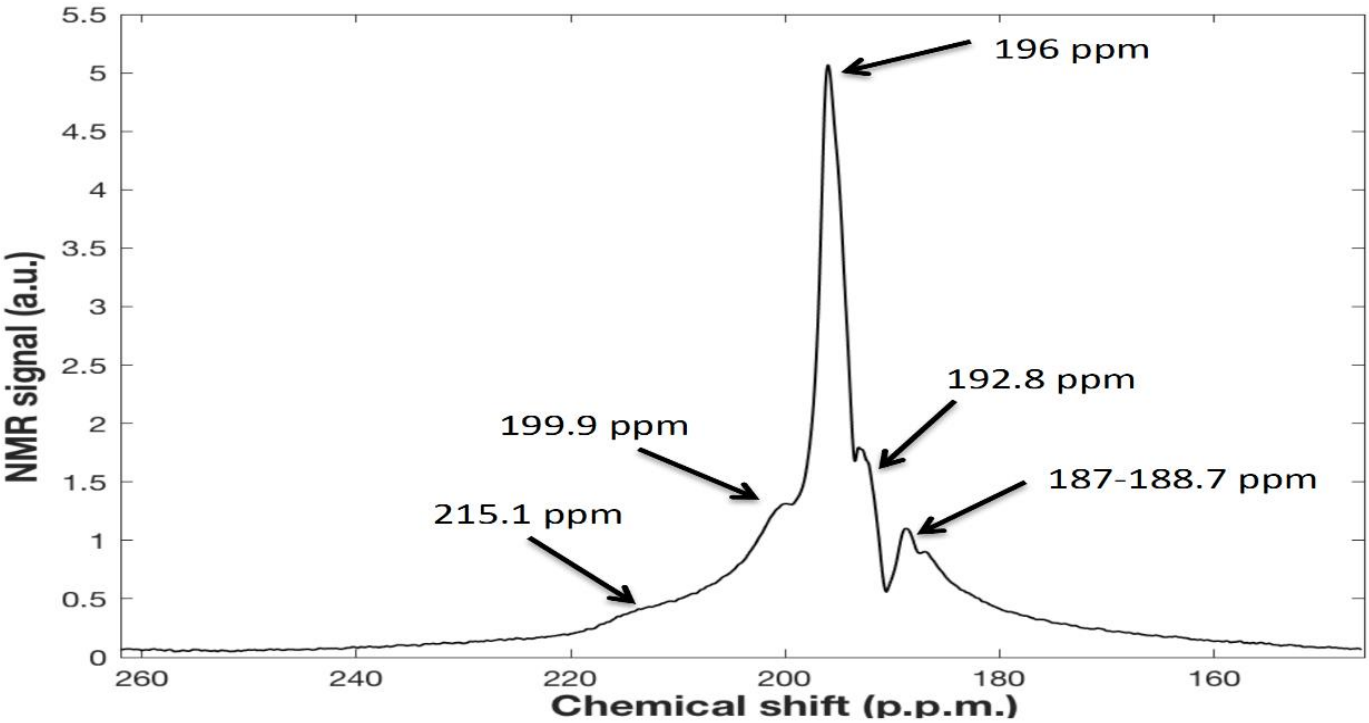

Figure 92: Combined dissolved phase spectra

All the main peaks previously observed in the human brain are visible, and from right to left:

- At 187 ppm, two peaks are observed, likely related to the muscular tissue of the cheeks and midbrains.
- Peaks at 192.8 ppm are attributed to ^{129}Xe dissolved in the white matter and cartilaginous soft tissues.
- The tallest peak at 196 ppm corresponds to the ^{129}Xe dissolved in the grey matter.
- At 199.9 ppm, the peak is likely from hyperpolarised ^{129}Xe dissolved in body interstitial fluid/plasma, fat tissue outside the brain, and cerebrospinal fluid.
- Finally, the peak at 215 ppm represents the ^{129}Xe dissolved in the blood.

All the peaks are consistents with those reported in reference [197]. Additionally, the dynamic behaviour of the spectra was studied over a span of 1 minute. The results can be seen below in figure 98. Xenon in the dissolved phase took almost six seconds to reach the brain, as evidenced in the third dynamic frame where all the peaks become visible. The maximum signal was measured at 22 seconds at the eleventh dynamic, where the grey reached its peak. The white matter peak reached its maximum between the fifth and the

seventh dynamics. Having established the feasibility of hyperpolarised ^{129}Xe spectroscopy, the next step was to attempt brain imaging using the developed 6 channel array.

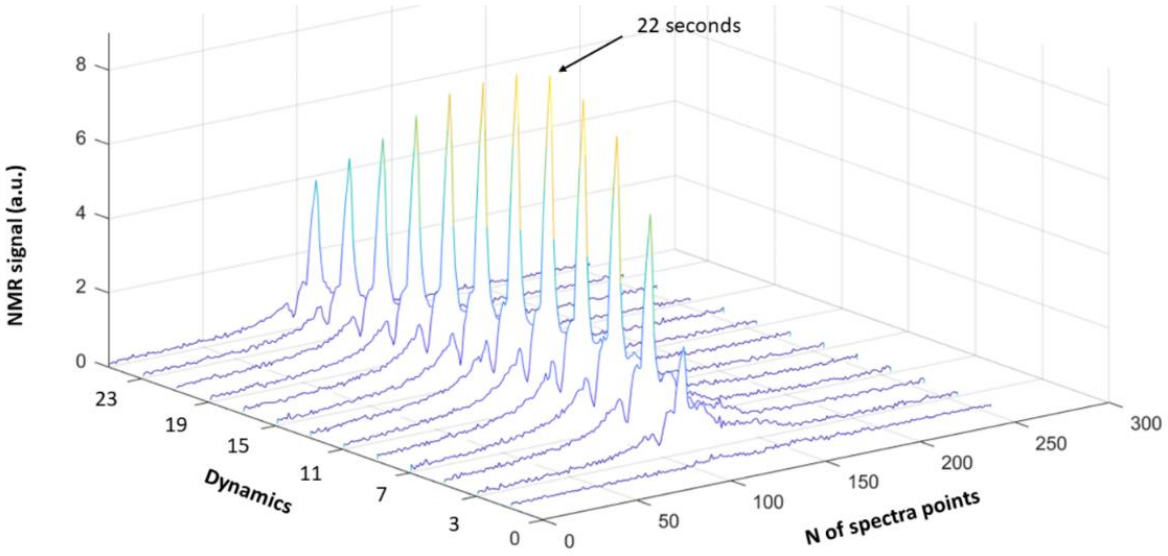

Figure 93: Waterfall plot of dynamic spectra of the dissolved phase ^{129}Xe in the brain.

6.7 Dissolved phase ^{129}Xe brain imaging with the 6-channel array

The first test was performed using a ^{129}Xe bag to evaluate the image quality provided by the 6-channel array. The coil was tested with a ^{129}Xe gas-phase phantom, consisting of a bag of hyperpolarised ^{129}Xe. Imaging was conducted using a 3D spoiled gradient echo, TR/TE=6.7ms/2.5ms, acquisition matrix: 96x72x32, 8mm slice thickness, FA=10°, Receiver bandwidth=8.6 KHz. The result is shown in figure 91. The phantom gas-phase ^{129}Xe images

had a mean SNR~120 in the central slices, with a maximum of 160. These promising results warranted progression to in vivo dynamic imaging of ^{129}Xe in the brain (Figure 99).

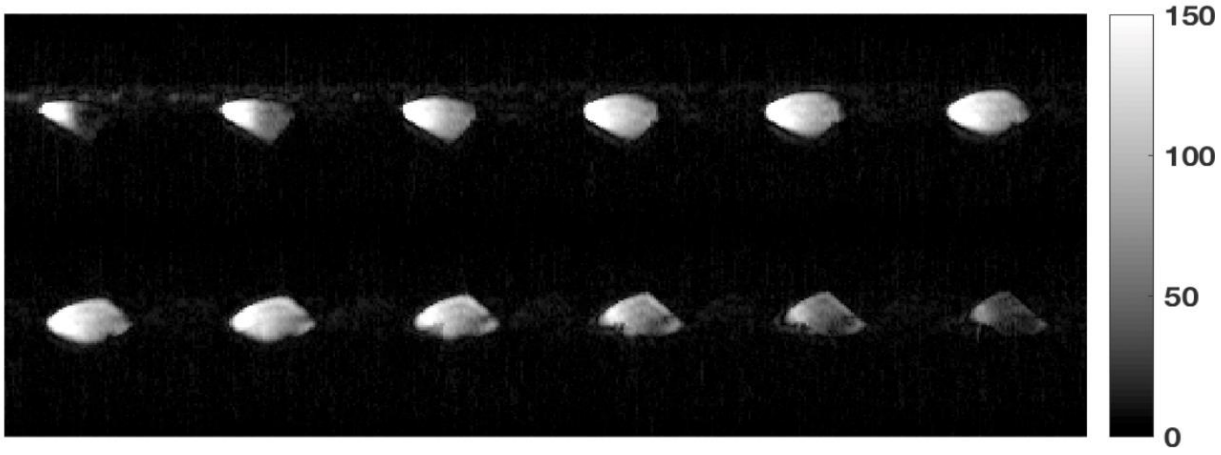

Figure 94: Images of the hyperpolarised ^{129}Xe bag with the 6 channel coil array.

6.7.1 Dissolved phase ^{129}Xe brain imaging with the six-channel array.

Following the successful test with the octagonal birdcage, dissolved phase ^{129}Xe brain was conducted with the 6-channel array combined with the birdcage volume head coil as the transmitter. The experiment was performed on a 3T Philips Ingenia scanner with a healthy male volunteer (36 years old, 185cm, 90Kg). Imaging was conducted using a 2D SPGR sequence with the following parameters: FOV 375 mm^2, Matrix 48x48, Pixel size=7.8x7.8 mm, FA=21° degrees, TR=34ms, TE=1.2 ms, WFS (Water-Fat shift) =2.45, BW=4310 kHz, offset frequency=11512 Hz (centre frequency shifted to 200 ppm), slice thickness= 100mm, encoding direction Right-Left, 10 Dynamics. The sequence lasted one minute, with an image acquisition every six seconds. The inhaled ^{129}Xe dose was 1 L with a 30% polarisation. Raw data were subsequently exported in MATLAB, for image reconstruction of the single channels. K-space data were low pass filtered with a Hamming window and zero padded to reach a matrix of 100x100. Results of the single channels reconstructions can be seen in

figure 100. The images of each channel were then combined using the Sum of Square method. Signal dynamics with averaged images are presented in figure 101.

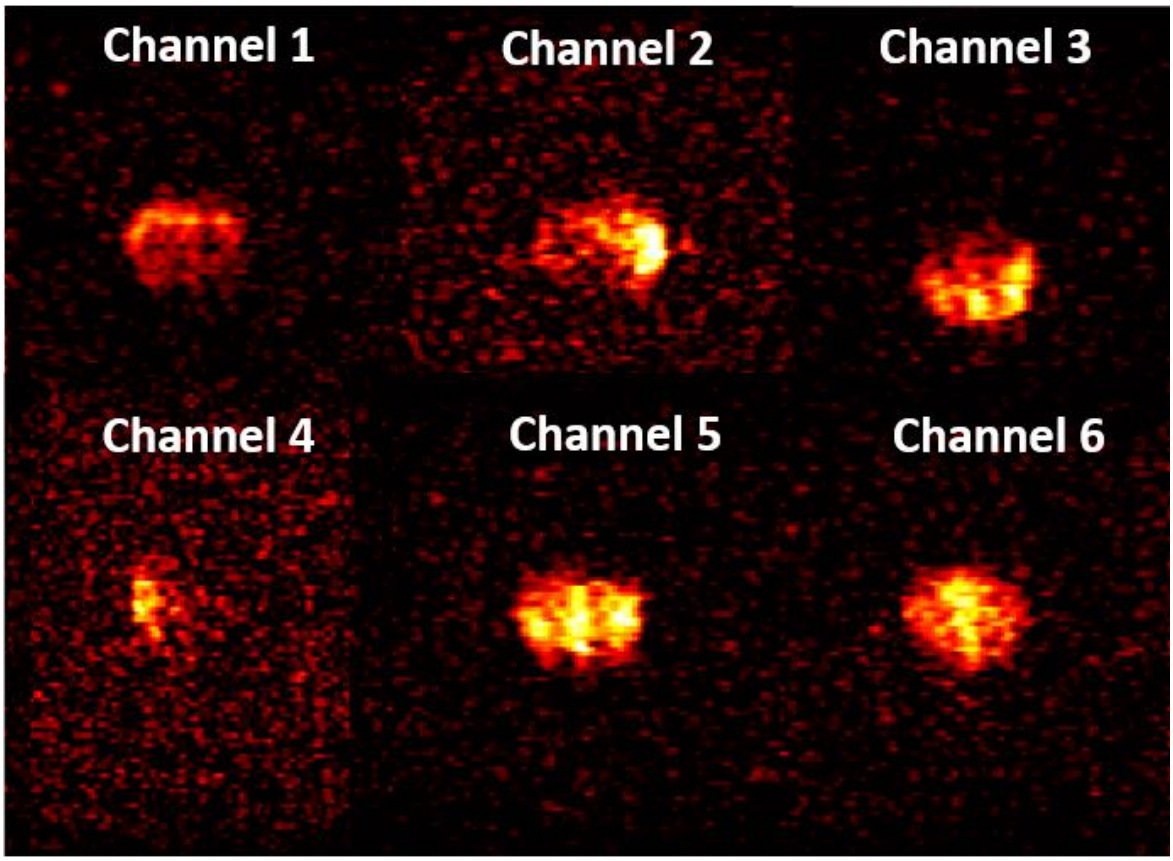

Figure 95: Received signal from each channel of the array. ©University of Sheffield

The first scan began immediately after the inhalation of the Xe dose, the signal become detectabel after six seconds and exhibited a gradual increase, reaching its maximum at 18 seconds. At 30 seconds, a noticeable decrease in the was observed, which subsequently dissipated entirely by 42 seconds. Analysis of the averaged dynamics revealed a higher signal intensity in the central region of the brain. This observation is attributed to the anatomical proximity to channels 5 and 6, which are positioned on the top of the helmet. Table 12 presents a comparison of the Signal-to-Noise Ratio (SNR) for the dissolved phase images obtained using the two different configurations.

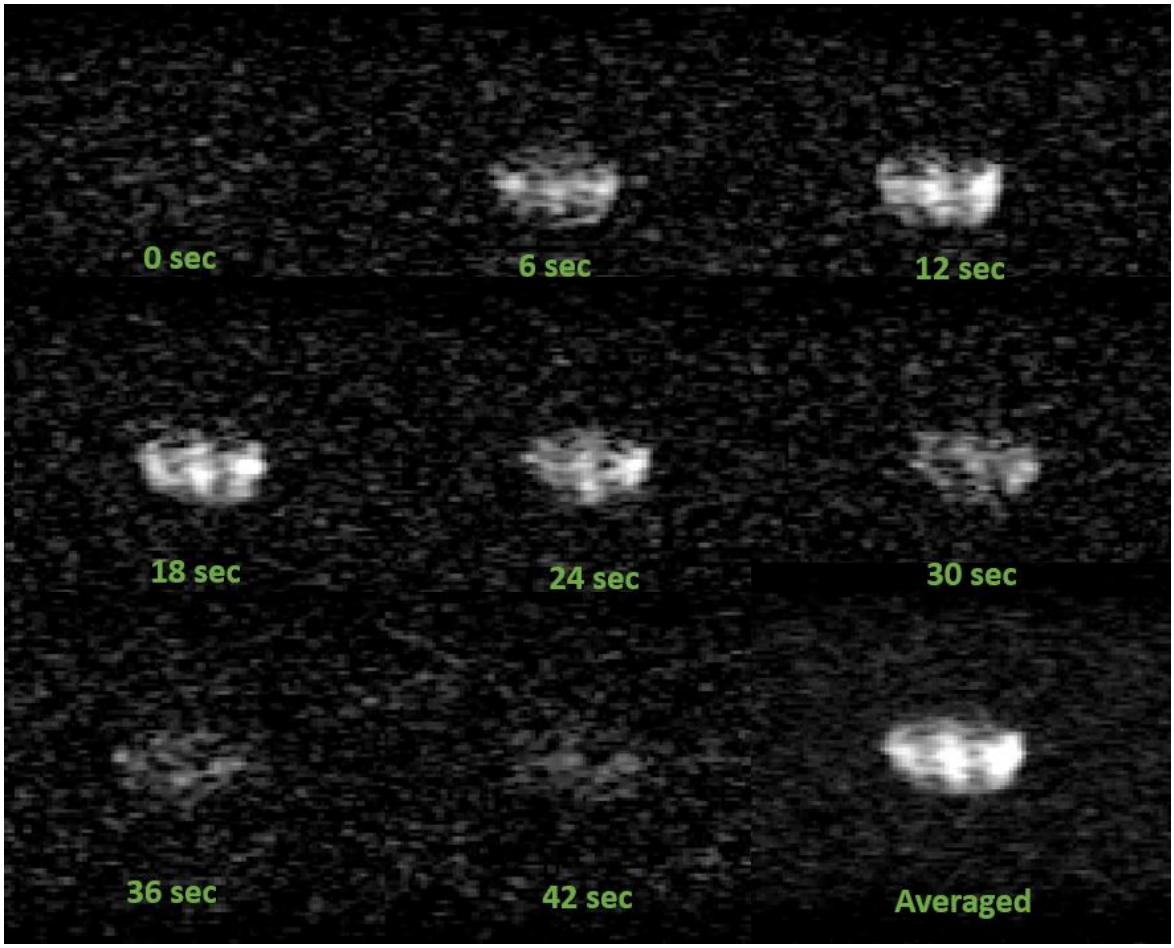

Figure 96: SOS combined images of the 6 channel array hyperpolarised dissolved ^{129}Xe signal dynamics in the brain. ©University of Sheffield.

Table 12: Signal comparison of the Dissolved phase images and spectra obtained with the birdcage and with the 6 channel.

Setup	SNR images
Only birdcage	10
6 Channel Coil receiver	11

6.8 Discussion

6.8.1 Reason of the low SNR of the array coil

The RF coils and electronics described in this study was designed to receive the signal from dissolved ^{129}Xe in the brain. The array functioned effectively in both configurations: with the birdcage in transceiver mode and when combined with the 6-channel array. Both configurations produced dynamic images of the brain and successfully obtained spectra with all relevant peaks visible. The six-channel array was developed to provide an increased SNR and higher spatial discrimination compared to the previous design. However, due to

several unresolved technical issues, Table 12 shows a lower image quality compared to the images obtained in previous study [198]. As demonstrated in Section 6.4.2, the octagonal birdcage was able to provide perfusion imaging of the brain when in transceiver configuration. Preliminary imaging with 6-channel arrays did not increase the SNR of the images nor provided additional physiological or anatomical information, as expected from the analysis in Section 6.3. It should be noted that these results were obtained using different scan parameters: the birdcage scan had a matrix of 48x30 with an echo time (TE) 0.6 ms, while the array scan had a matrix of 48x48, with a TE of 1.2 ms. The primary reason for the suboptimal image quality was due to coupling between the channels.

Table 13: Measured quality factor of the single channels, with the other elements connected to the preamplifiers.

Channel	*Qunload*	*Q load*	*Ratio*
1	***243***	***167***	***1.45***
2	***160***	***105***	***1.52***
3	***173***	***104***	***1.66***
4	***145***	***130***	***1.11***
5	***180***	***87***	***2.06***
6	***231***	***159***	***1.45***

As shown in Table 13, the quality factor of each channel, when assembled around the 3D head former, is reduced compared to measurements taken from each element independently, before array assembly. The ratio between the *Qload* and *Qunload* indicated a reduced sensitivity of each element, with the highest value being 2.06 for channel 5 and a lowest value being 1.11 for element number 4. Previous values of the *Qunload/Qload* ration measured for each channel independently were above 3 (see paragraph 6.6). This reduction in sensitivity is corroborated by the correlation matrix (figure 102), which shows a strong mutual interaction between channels 3 and 6, with a correlation value of 58%. Additionally, the correlations between channels 2 and 6, 3 and 5, and 4 and 5 are higher than 35%. These results suggest a persistent strong mutual interaction between the coil elements when combined, despite the use of low impedance preamplifiers. This mutual interactions contribute to the noisy image obtained, as noise voltage can degrade the SNR from the combination of signals from correlated elements [199].

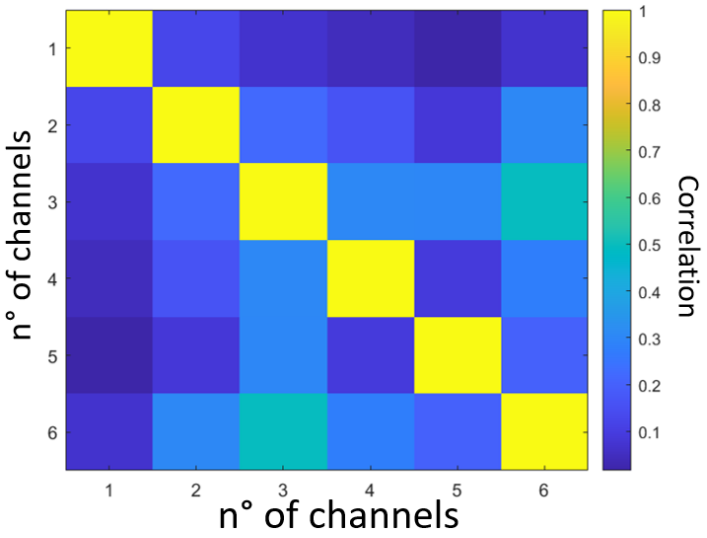

Figure 97: Correlation matrix between coil elements, it can be seen a high coupling between the channels

6.8.2 Parallel imaging and g-factor

Before conducting further experiments in the scanner, a necessary check of the array to thorough examination of the array was necessary to address issues with the receiver coil. However, among many hypotheses and experimental plans, parallel imaging was not considered. Imaging gas-phase hyperpolarised ^{129}Xe and dissolved phase ^{129}Xe involves different considerations, despite both requiring the patient to hold their breath. For lung ^{129}Xe imaging, the gas diffuses immediately after the inhalation, followed by the ventilation scan. As already mentioned in Chapter 4, parallel imaging is crucial to reduce scan time, and consequently, the breath hold time of the patient (typically around 15 seconds without parallel imaging). Since many patients undergoing ^{129}Xe ventilation MRI suffer from pulmonary diseases, reducing scan time through parallel imaging can enhance patient's comfort and improve examination outcomes. In the case of dissolved phase ^{129}Xe imaging, it is important to note that ^{129}Xe take approximatively 6 seconds to reach the brain after inhalation, as can be demonstrated in various imaging and spectroscopy experiments, including the results obtained in paragraph 6.4.2 and 6.7.1 and reaches its maximum signal around 20-22 seconds. Therefore, parallel imaging was not prioritised in the project requirements for the 6-channel array. Instead, the focus was on maximising the signal due to the intrinsically low SNR of dissolved phase ^{129}Xe. The coil was designed to improve upon the results obtained by Rao et al [198] on a 1.5T scanner by increasing the number of channels of the receiver coil and leveraging higher favourable working frequency for RF coil engineered at 3T. As discussed in Section 6.3, the high local g-factor, makes it

unsuitable for parallel imaging; otherwise, a different design would have been chosen. An example could be the 6-channel coil proposed in the work of the Zwaart, which has been shown to work proficiently for parallel imaging purposes [193]. According to the paper of Olingher and Sodickson [200], when an array is built to work in combination with parallel imaging technique, it must be designed to maximize the SNR of the unaccelerated reconstructed data, and to provide spatial information about the magnetization within the sample. The latter factor was not considered in this work of thesis, as it was outside from the initial scope.

6.9 Conclusion and further development

Hyperpolarised ^{129}Xe imaging is an emerging technique that permits brain perfusion imaging. Although still in its development stages, several studies have already demonstrated its potential for several clinical applications. For instance, Hane et al. evaluated ^{129}Xe for the assessing Alzheimer's disease, discovering significant retention of the contrast agent after 60 seconds [201]. Additionally, the same group pioneered the use of the Time of fight methods to acquire the first Hemodynamic response map with ^{129}Xe [189]. Perfusion imaging with ^{129}Xe has also been investigated for evaluating cerebral region damaged by stroke [198]. A kinetic model was recently developed to determine the gas transfer from the blood/brain barrier by analysing the concentration in the grey matter and cerebral blood compartments through in vivo spectroscopy [202]. These studies underscore the potential of ^{129}Xe as a contrast agent for brain perfusions, highlighting its future applications in drug delivery assessments and the investigation several diseases such as intact barrier oedema or arterial plaque. The objective of the 6-channel coil array was to enhance sensitivity to detect the low signal from dissolved phase ^{129}Xe. An improved coil with increased intrinsic SNR allow for higher resolution of the images (typically 32x32 [191], or 48x48 [198]), providing more detailed anatomical information and resolution of anatomical details. Recently, 3D imaging of the hyperpolarised ^{129}Xe has been demonstrated [190], which aids in accurately localising the gas in the brain. Similar to 2D imaging, a coil with increased sensitivity could allow for more slices with reduced thickness. These considerations formed the basis of the development of the 6-channel array. Anyway, the project faced an abrupt interruption due to the COVID-19 pandemics, limiting the access to the RF laboratory and to the scanner at the Royal Hallamshire

Hospital at the Academic Unit of Radiology in Sheffield. This impeded further developments and improvements of the array. Planned enhancement included integrating new preamplifier directly in the circuit of the coil, eliminating the need for a connection cable from the coil to the preamplifier box far from the array. This could potentially improve preamp isolations of each channel by removing dependence on phase shifter and the cable length. A more accurate analysis of the coil geometry, elements positioning and overlapping was also planned. Preliminary assembly revealed suboptimal S_{12} isolation of the channel 2 and 4. When the two loops were connected to the preamplifier box decupling was less than -15 dB (-13.5 dB), indicating inadequate decoupling. Simulations to optimize element positioning and overlap were planned to improve efficiency. Proper mechanical fixing of the coil elements was necessary, as the initial assembly used tape and Kapton for insulation, leading to mechanical failures in some scan attempts (e.g., loose soldering, improperly isolated connectors). Further improvement of the scanning protocol could be envisioned, including a broader bandwidth spectrum to encompass gas phase and dissolved phase peaks, enabling precise scanning at the dissolved phase frequency, specifically at the grey matter peak. These developments could improve the coil robustness, ensuring consistent and repeatable results and enabling systematic comparison of Signal to Noise ratio between octagonal birdcage in transceiver mode and the 6-channel array. In conclusion, these preliminary results and testing of the 6-channel coil and were important to provide insights into the development of a receiver array and the investigation of the dissolved phase hyperpolarised ^{129}Xe in the brain. Despite the project's interruption, the groundwork laid here highlights the potential for future improvements and applications in brain perfusion imaging using ^{129}Xe.

Chapter 7: Conclusions

7.1 Summary

The first three chapters of this thesis serve as an introduction to scientific aspects covered in the subsequent chapters. The first chapter explains the basic theory of MRI, while the second and third chapters focus on the principles of RF and ^{129}Xe MRI, respectively.

7.1.1 Chapter 4

Chapter 4 discusses the development and testing of an RF asymmetrical birdcage coil and its integration and with a receiver 8-channel array. The first part of the chapter is dedicated to the electromagnetic characterization of the asymmetrical birdcage, including evaluation of S-parameters, B_1^+ uniformity and Specific Absorption Rate (SAR). Various decoupling configurations with PIN diodes were tested to achieve optimal B_1 field homogeneity of the ^{1}H transmit coil of the 1.5T and to assess the isolation between the two birdcages. This was followed by the characterising resonance, matching and the Q_{load}/Q_{unload} factor both in the RF lab and inside the scanner.

7.1.2 Chapter 5

Chapter 5 is dedicated to the imaging tests of the asymmetrical birdcage coil as a transceiver and in combination with the receiver 8-channel array. Lung ^{129}Xe ventilation MRI was successfully performed with accelerated imaging using the SENSE algorithm. The experiments yielded good results with both SSFP and SPGR sequences, achieving an acceleration factor of 4. This work also demonstrated the feasibility of simultaneous ^{129}Xe and ^{1}H imaging with the asymmetrical birdcage coil without any RF shield, allowing for co-registration of ^{129}Xe images with anatomical ^{1}H images. Preliminary results of ^{129}Xe imaging with a flexible transmit coil composed of two butterfly coils were also presented, indicating the potential for further comparison with the asymmetrical birdcage coil.

7.1.3 Chapter 6

Chapter 6 involves the development and testing of a 6-channel array for ^{129}Xe dissolved phase imaging of the brain at 3T. A similar design was employed at 1.5T, with this work aiming to replicate and expand the results obtained at lower fields. The RF setup required a transmit birdcage coil, initially simulated to forecast its sensitivity. The birdcage, with its

unusual octagonal profile, was tested and compared to a conventional circular birdcage to evaluate changes in Transmit efficiency and uniformity. Simulation of various permutation of the 6-channel array were conducted, focusing on ROI, coil sensitivity, g-factors map and B_1. The coil was then built, characterized in the RF lab, and finally tested in the 3T scanner. The array demonstrates the capability for ^{129}Xe spectroscopy, obtaining similar results to those obtained in literature. In-vivo ^{129}Xe dissolved phase imaging was also performed with the 6-channel array and with the birdcage in transceiver configuration. However, the 6-channel array did not show the expected increase in SNR, attributed to strong coupling between array elements due to a faulty preamplifier.

7.2 Further developments

7.2.1 Asymmetrical birdcage coil setup

Regarding the Asymmetrical birdcage/8channel setup, having demonstrated an increase in SNR, the next step is to test the coil for dissolved phase ^{129}Xe MRI. Although dissolved phase in the lungs is common practice and has also been already demonstrated with transceiver coils, time limitations prevented the evaluation of the coil setup with the 3D dissolved lung imaging protocol. Future work should work on evaluating the advantages of the added SNR offered by the receiver array in terms of spatial resolution. Additionally, it would be valuable to assess the setup's feasibility for receiving dissolved-phase signals from other anatomies, such as the kidneys, and comparing results with previous studies at 3T. The large ROI of the birdcage could extend spatial coverage of a to the whole abdomen, enabling dissolved phase imaging of other organs like the liver. At the end, comparing the flexible vest coil and with asymmetrical birdcage would be a logical next step, in terms of coil performance, but also in terms of patient comfort and usability.

7.2.2 Octagonal birdcage coil/6 channel

As discussed in paragraph 6.8.1, the array performance was compromised by a faulty preamplifier. An important aspect of improving the array design is to enhance the mechanical robustness of the conductors and the soldering along the 3D former, as the soldering of the PCB failed during movements between the RF lab to the scanner. The cabling system should also be revised to group them together effectively. Additional simulation of both coils together would help to predict coupling between the octagonal

birdcage and the array. The 6-channel array coil aims to increase the inherently low signal from the ^{129}Xe in dissolved phase imaging, potentially enhancing spatial and temporal resolution as demonstrated recently with time resolve spectroscopy [202] and 3D CSI [203].

APPENDIX A

The asymmetrical birdcage coil was successfully built and tested. However, this design, as already mentioned, raised several issues regards the mechanical robustness of the coil and patient comfort. To address these concerns, I also developed a flexible wearable coil design similar to the one already used for clinical practice in Sheffield. This new design was developed to work only as a transmitter, used in conjunction with the 8-channel thorax array as a receiver antenna. This section describes the development and the testing of the flexible coil design.

A.1 Circuit Design

The circuit was designed on an etched flexible FR4 substrate. The flexible substrate allowed the coil to conform to the patient's thorax, making it wearable like a jacket. The coil design, shown in Figure 1.A, consists of two large butterfly coils. Each element comprised two large rectangular loops connected by a 40 cm BNC cable. The conductor thickness is 0.8 cm. Each loop has a rectangular trapezoidal shape with a height of 42 cm, a lower base of 29.5 cm, and an upper base of 25 cm. The conductors are connected on the inner side of the loop 4 cm copper strip. The central part of the PCB, with a width of 8.5 cm houses additional circuitry to insert for matching the two elements and the 180° hybrid coupler.

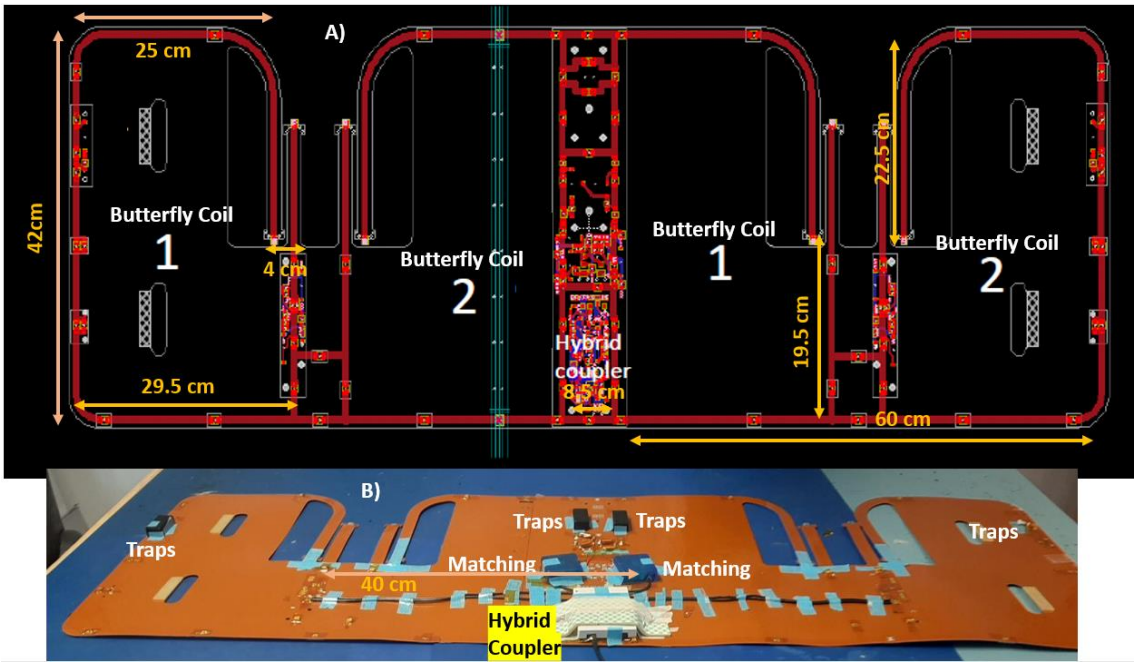

Figure 1.A: A) CAD of the coil with a geometrical dimension of the loops of the butterfly coil. B) Real coil with the description of the main components of the circuit. ©University of Sheffield

Each channel includes two proton traps to permit proton imaging, a decoupling circuit formed by a PIN diode and two RF chokes (1 uH) to separate the DC path from AC path. A lattice balun matching circuit adapts the coil impedance to 50 Ohm (C=545 pF L=149.1 nH). The two butterfly coils are connected to the hybrid coupler located in the central lower bottom of the circuit. The values of the lumped components are shown in figure 2.A below. The two butterflies coils are geometrically decoupled, achieving optimal isolation when the coil is wrapped around the patient 5.5 cm overlap between the two elements.

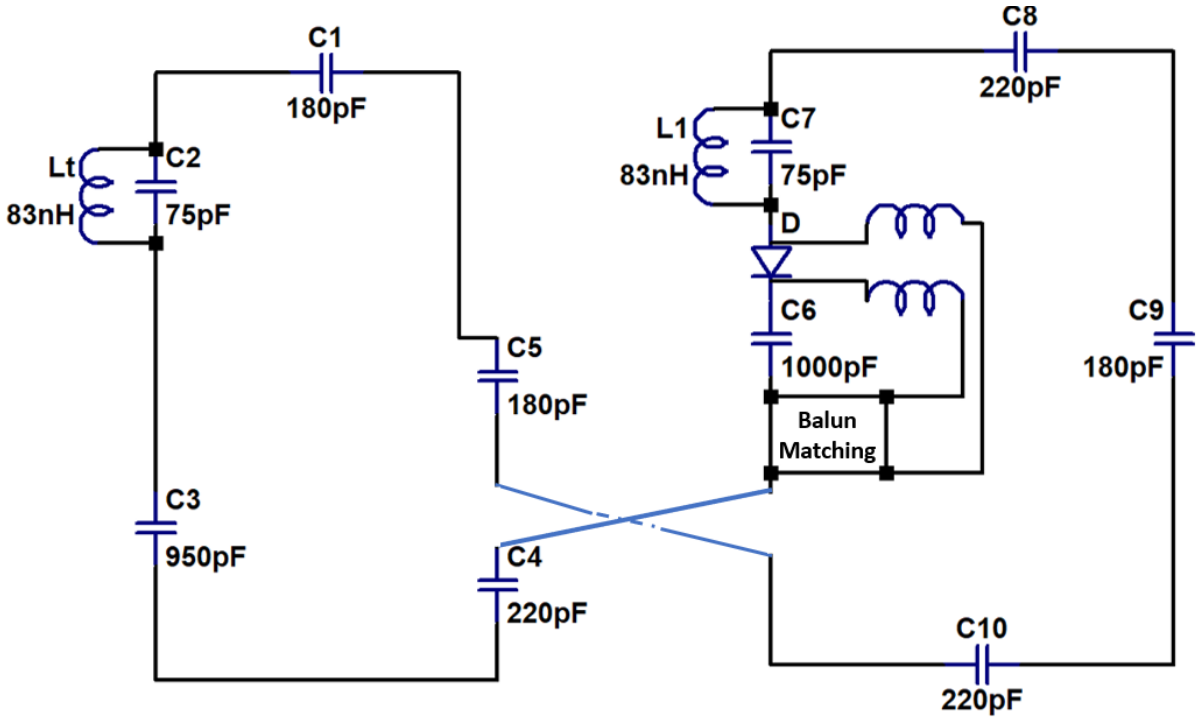

Figure 2.A: Circuital model with values of lumped components of the single butterfly coil. ©University of Sheffield

A.2 Measurements in the RF lab

Tuning and matching of the coil were performed in the RF lab. The quality factor was measured based on the S_{12} coupling bandwidth of two loops placed nearby the vest coil. The unloaded Quality factor was 152.77, and the loaded quality factor was 63, giving a ratio of 2.5. The coil was loaded in vivo with a human patient (78 Kg, 178 cm of height). DC decoupling, achieved by a PIN diode circuit, was evaluated by placing two loops inside the coil and checking the S_{12} parameter. The measured isolation was -53 dB (Diode ON, coil tuned), and -73 (Diode OFF, coil detuned). The hybrid coupler was designed to operate at

a resonating frequency of 17.66 MHz, with the building process and testing in paragraph 4.5.1. The measured impedance of the two elements was 5.5 and 5.3 Ohm. Final tuning and coil matching were tested connecting loaded coil directly to the VNA. Initially, the coil was tuned to 17.66 MHz, but a frequency shift of approximately 0.4 MHz was observed inside the scanner bore (tuning frequency 18.05 MHz). The coil was retuned to account for this shift. The lab resonance frequency was then reduced to 17.24 MHz, with a return loss of -29 dB. Results of the measurements taken in the RF lab can be seen in figure 3.A.

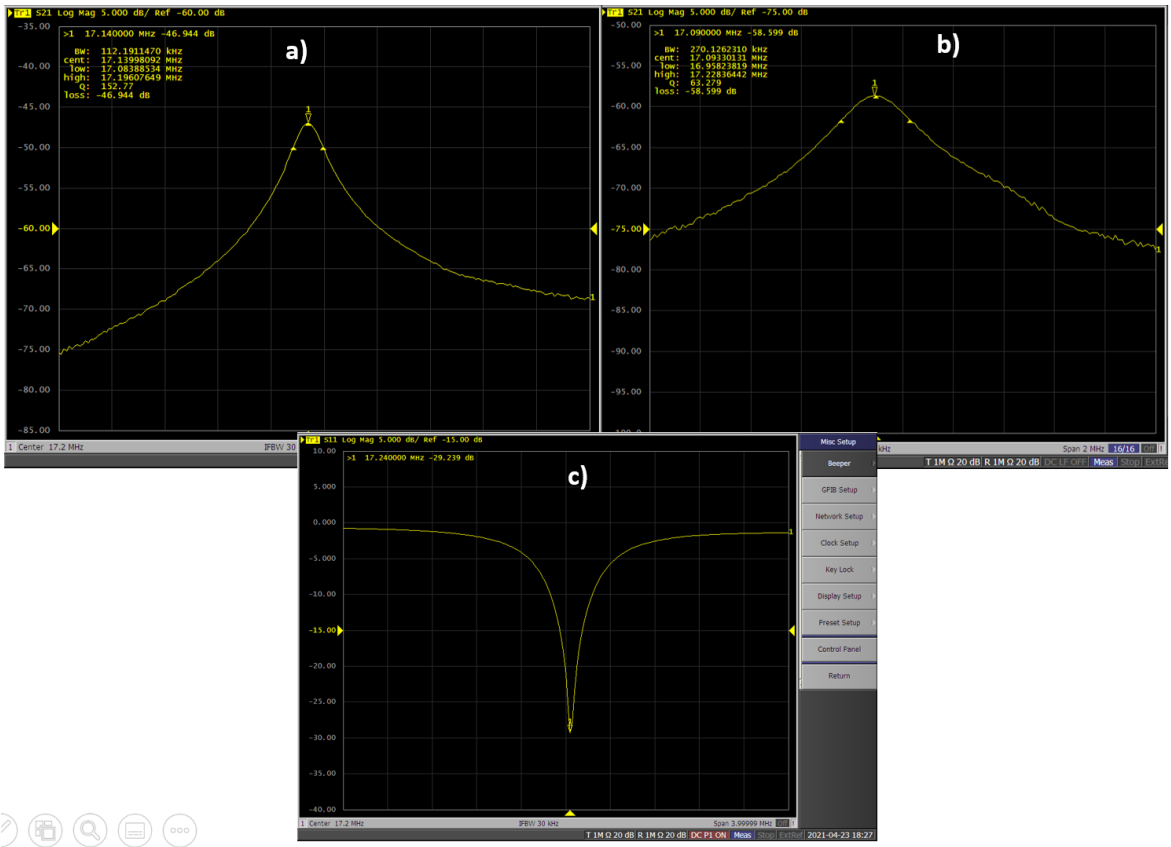

Figure 3.A: Quality factor of the coil in unloaded (a) and loaded (b) condition. Tuning and matching of the coil according to the tuning frequency in the workbench.

A.3 Hyperpolarised ^{129}Xe imaging with the vest coil

After evaluating the tuning and matching parameters, the coil was tested in vivo on the 1.5T Signa HDx scanner (Figure 4.A). The patient was a 36-year-old healthy male volunteer (185 cm 90 Kg). Prior to imaging, a flip angle calibration was performed. The imaging sequence was Steady State Free Precession with an 80x80x20 matrix, TR/TE=6.4/3.1ms, partial echo acquisition, BW=8.06kHz, FoV=40x40cm^2; slice thickness=1cm. A dose of 500 ml of ^{129}Xe was administered to the patient. The raw files were exported on MATLAB, and

images reconstructed with the Sum of Square method. The reconstructed images can be seen in figure 5.A.

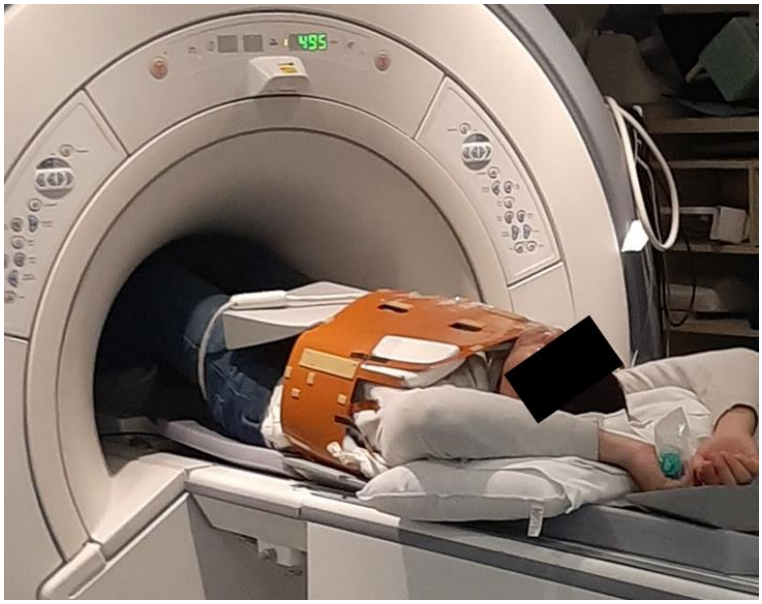

Figure 4.A: In vivo coil testing in the 1.5T scanner. ©University of Sheffield

A.4 Results and discussion

The mean SNR of the central slices was 15, 26 in the posterior slices and 21 in the anterior slices. As expected, the SNR was lower compared to the one acquired with the birdcage coil as a transmitter. The reduction was attributed to the lower dose of inhaled gas, yet the results were comparable to those obtained with the birdcage. The slight decrease in image signal in the anterior slice confirms the gradient effect caused by gravity on the gas. These preliminary images are promising, and further comparison using same dose of gas are anticipated. The vest coil proved to be a viable a whole thorax imaging as a transmitter. Besides similar imaging results, the vest coil design offers several advantages in terms of design and mechanical development. It increases patient comfort due to its wearability and the flexible design can be adapted to various patient sizes. Additionally, is less prone to mechanical failure and does require a trolley to be inserted into the scanner bore. Another potential advantage of the vest coil could its limited interaction with the ^{1}H proton coil embedded in the scanner. Unlike the birdcage, the vest coil has fewer conductors and is not positioned in proximity to the proton body coil. This could improve the ^{1}H birdcage transmission efficiency and resulting better anatomical images for co-registration. However, the vest coil, like similar design may not

offer the same B_1^+ field homogeneity as the birdcage, necessitating further analysis through EM simulation and in vivo flip angle mapping.

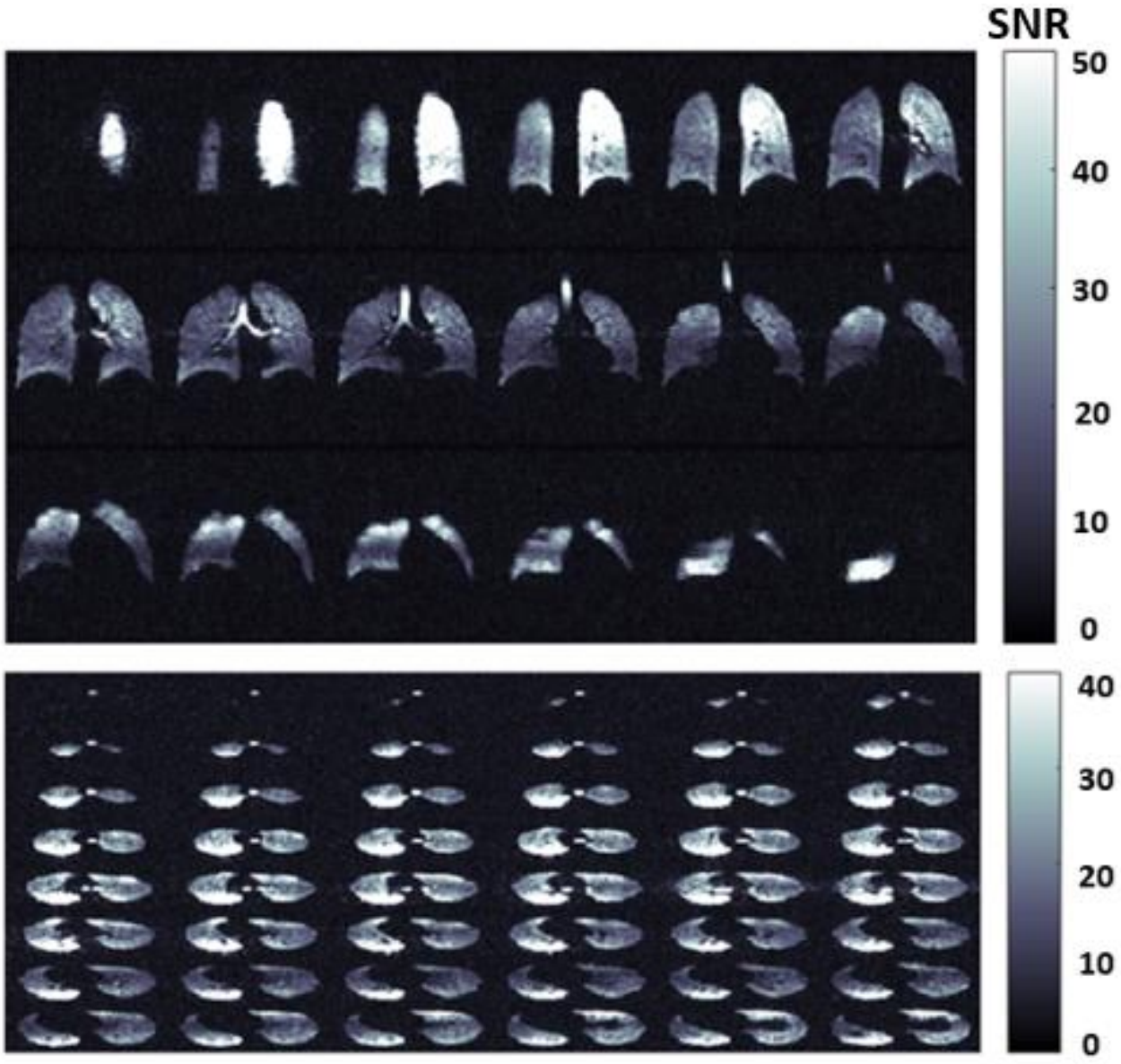

Figure 5.A: Lung ventilation Hyperpolarised^{129}Xe MR imaging acquired with the vest coil as transmission coil and 8-channel as a receiver.

List of figures

List of tables

Bibliography

[1] Rabi I.I.; Zacharias J.R.; S. Millman; P. Kusch, "A new method of measuring Nuclear Magnetic Moment," *Phys.Rev.*, vol. 53, p. 318, 1938.

[2] P. M. Bloch F., Hansen W.W., "Nuclear Induction," vol. 738, no. 69, p. 127, 1939.

[3] E. M. Purcell, H. C. Torrey, and R. V. Pound, "Resonance absorption by nuclear magnetic moments in a solid," *Physical Review*, vol. 69, no. 1–2. pp. 37–38, 1946.

[4] F. Bloch, "Nuclear induction," *Phys. Rev.*, vol. 70, no. 7–8, pp. 460–474, 1946.

[5] R. Damadian, "Tumor detection by nuclear magnetic resonance," *Science (80-.).*, vol. 171, no. 3976, pp. 1151–1153, 1971.

[6] R. Damadian, M. Goldsmith, and L. Minkoff, "NMR in cancer: XVI. FONAR image of the live human body.," *Physiol. Chem. Phys.*, vol. 9, no. 1, pp. 97–100, 108, 1977.

[7] P. C. Lauterbur, "Image formation by induced local interactions: Examples employing nuclear magnetic resonance," *Nature*, vol. 242, no. 5394, pp. 190–191, 1973.

[8] P. Mansfield and A. A. Maudsley, "Medical imaging by NMR," *Br. J. Radiol.*, vol. 50, no. 591, pp. 188–194, 1977.

[9] A. M. J. Hudson, W. Köckenberger, and R. W. Bowtell, "Open access birdcage coils for microscopic imaging of plants at 11.7 T," *Magn. Reson. Mater. Physics, Biol. Med.*, vol. 10, no. 2, pp. 69–74, 2000.

[10] W. A. Edelstein, J. M. S. Hutchison, G. Johnson, and T. Redpath, "Spin warp NMR imaging and applications to human whole-body imaging," *Phys. Med. Biol.*, vol. 25, no. 4, pp. 751–756, 1980.

[11] J. Belliveau *et al.*, "Functional mapping of the human visual cortex by magnetic resonance imaging," *Science (80-.).*, vol. 254, no. 5032, pp. 716–719, Nov. 1991.

[12] S. Ogawa *et al.*, “Intrinsic signal changes accompanying sensory stimulation: Functional brain mapping with magnetic resonance imaging,” *Proc. Natl. Acad. Sci. U. S. A.*, vol. 89, no. 13, pp. 5951–5955, 1992.

[13] M. P. Hartung, T. M. Grist, and C. J. François, “Magnetic resonance angiography: Current status and future directions,” *J. Cardiovasc. Magn. Reson.*, vol. 13, no. 1, pp. 1–11, 2011.

[14] M. S. Albert *et al.*, “Biological magnetic resonance imaging using laser-polarized 129Xe,” *Nature*, vol. 370, no. 6486, pp. 199–201, Jul. 1994.

[15] Diagnostic Imaging Dataset, “Diagnostic Imaging Dataset Annual Statistical,” 2017.

[16] P. E. L. Howell, “United States Patent (19),” no. 19, 1974.

[17] R. H. et al. Hashemi, *MRI : the basics 3rd edition*, 3rd ed. 2004.

[18] P. A. Bottomley, “The Basics,” in *eMagRes*, vol. 4, Chichester, UK: John Wiley & Sons, Ltd, 2015, pp. 505–524.

[19] R. A. Pooley, “Fundamental Physics of MR Imaging,” *RadioGraphics*, vol. 25, no. 4, pp. 1087–1099, Jul. 2005.

[20] S. Currie, N. Hoggard, I. J. Craven, M. Hadjivassiliou, and I. D. Wilkinson, “Understanding MRI: Basic MR physics for physicians,” *Postgrad. Med. J.*, vol. 89, no. 1050, pp. 209–223, 2013.

[21] M. Flower, Ed., *Webb’s Physics of Medical Imaging*. CRC Press, 2016.

[22] D. . Hoult and R. . Richards, “The signal-to-noise ratio of the nuclear magnetic resonance experiment,” *J. Magn. Reson.*, vol. 24, no. 1, pp. 71–85, 1976.

[23] A. Macovski, “Noise in MRI,” *Magn. Reson. Med.*, vol. 36, no. 3, pp. 494–497, 1996.

[24] R. E. Gordon and W. E. Timms, “Magnet systems used in medical NMR,” *Comput. Radiol.*, vol. 8, no. 5, pp. 245–261, 1984.

[25] E. Moser, E. Laistler, F. Schmitt, and G. Kontaxis, “Ultra-high field NMR and MRI-the role of magnet technology to increase sensitivity and specificity,” *Front. Phys.*, vol. 5, no. AUG, pp. 1–15, 2017.

[26] K. M. Koch, D. L. Rothman, and R. A. de Graaf, “Optimization of static magnetic field homogeneity in the human and animal brain in vivo,” *Prog. Nucl. Magn. Reson. Spectrosc.*, vol. 54, no. 2, pp. 69–96, 2009.

[27] C. Juchem, B. Muller-Bierl, F. Schick, N. K. Logothetis, and J. Pfeuffer, “Combined passive and active shimming for in vivo MR spectroscopy at high magnetic fields,” *J. Magn. Reson.*, vol. 183, no. 2, pp. 278–289, 2006.

[28] McGinley et al., “United States Patent 5,532,597,” 1996.

[29] D. I. Hoult and R. Deslauriers, “Accurate Shim-Coil Design and Magnet-Field Profiling by a Power-Minimization-Matrix Method,” *Journal of Magnetic Resonance, Series A*, vol. 108, no. 1. pp. 9–20, 1994.

[30] M. A. Brideson, L. K. Forbes, and S. Crozier, “Determining complicated winding patterns for shim coils using stream functions and the target-field method,” *Concepts Magn. Reson.*, vol. 14, no. 1, pp. 9–18, 2002.

[31] S. S. Hidalgo-Tobon, “Theory of gradient coil design methods for magnetic resonance imaging,” *Concepts Magn. Reson. Part A*, vol. 36A, no. 4, pp. 223–242, Jul. 2010.

[32] R. Turner, “Gradient coil design: A review of methods,” *Magn. Reson. Imaging*, vol. 11, no. 7, pp. 903–920, 1993.

[33] S. A. Winkler *et al.*, “Gradient and shim technologies for ultra high field MRI,” *Neuroimage*, vol. 168, no. 1, pp. 59–70, Mar. 2018.

[34] E. A. Chronik and B. K. Rutt, “Constrained length minimum inductance gradient coil design,” *Magn. Reson. Med.*, vol. 39, no. 2, pp. 270–278, Feb. 1998.

[35] C. Constantinides, S. Angeli, S. Gkagkarellis, and G. Cofer, “Intercomparison of performance of RF coil geometries for high field mouse cardiac MRI,” *Concepts Magn. Reson. Part A Bridg. Educ. Res.*, vol. 38 A, no. 5, pp. 236–252, 2011.

[36] R. Stara *et al.*, “Validation of numerical approaches for electromagnetic characterization of magnetic resonance radiofrequency coils,” *Prog. Electromagn. Res. M*, vol. 29, no. December 2012, pp. 121–136, 2013.

[37] G. Giovannetti, G. Tiberi, and M. Tosetti, “Finite element method-based approach for radiofrequency magnetic resonance coil losses estimation,” *Concepts Magn. Reson. Part B Magn. Reson. Eng.*, vol. 46B, no. 4, pp. 186–190, 2016.

[38] K. M. Gilbert, T. J. Scholl, and B. A. Chronik, “RF coil loading measurements between 1 and 50 MHz to guide field-cycled MRI system design,” *Concepts Magn. Reson. Part B Magn. Reson. Eng.*, vol. 33, no. 3, pp. 177–191, 2008.

[39] D. I. Hoult and P. C. Lauterbur, “The sensitivity of the zeugmatographic experiment involving human samples,” *J. Magn. Reson.*, vol. 34, no. 2, pp. 425–433, 1979.

[40] D. G. Gadian and F. N. H. Robinson, “Radiofrequency losses in NMR experiments on electrically conducting samples,” *J. Magn. Reson.*, vol. 34, no. 2, pp. 449–455, 1979.

[41] J. Mispelter, M. Lupu, and A. Briguet, *NMR Probeheads for Biophysical and Biomedical Experiments*. IMPERIAL COLLEGE PRESS, 2015.

[42] J. Murphy-Boesch and A. P. Koretsky, “An in Vivo NMR probe circuit for improved sensitivity,” *J. Magn. Reson.*, vol. 54, no. 3, pp. 526–532, 1983.

[43] *RF Circuit Design*. Elsevier, 2008.

[44] M. V. Vaidya, C. M. Collins, D. K. Sodickson, R. Brown, G. C. Wiggins, and R. Lattanzi, “Dependence of B1− and B1+ field patterns of surface coils on the electrical properties of the sample and the MR operating frequency,” *Concepts Magn. Reson. Part B Magn. Reson. Eng.*, vol. 46, no. 1, pp. 25–40, Feb. 2016.

[45] G. Glover *et al.*, “Comparison of linear and circular polarization for magnetic resonance imaging,” *J. Magn. Reson.*, vol. 64, no. 2, pp. 255–270, 1985.

[46] D. I. Hoult, “The principle of reciprocity in signal strength calculations?A mathematical guide,” *Concepts Magn. Reson.*, vol. 12, no. 4, pp. 173–187, 2000.

[47] C. M. Collins, S. Li, and M. B. Smith, “SAR and B1 field distributions in a heterogeneous human head model within a birdcage coil,” *Magn. Reson. Med.*, vol. 40, no. 6, pp. 847–856, Dec. 1998.

[48] C. E. Hayes, W. A. Edelstein, J. F. Schenck, O. M. Mueller, and M. Eash, “An efficient, highly homogeneous radiofrequency coil for whole-body NMR imaging at 1.5 T,” *J. Magn. Reson.*, vol. 63, no. 3, pp. 622–628, 1985.

[49] C. N. Chen, D. I. Hoult, and V. J. Sank, “Quadrature detection coils-A further √2 improvement in sensitivity,” *J. Magn. Reson.*, vol. 54, no. 2, pp. 324–327, 1983.

[50] T. S. Ibrahim, Y.-K. Hue, and L. Tang, “Understanding and manipulating the RF fields at high field MRI,” *NMR Biomed.*, vol. 22, no. 9, pp. 927–936, Nov. 2009.

[51] M. C. Leifer, “Resonant Modes of the Birdcage Coil,” *J. Magn. Reson.*, vol. 124, no. 1, pp. 51–60, 1997.

[52] C. Hayes and L. Axel, “Noise performance of surface coils for magnetic resonance imaging at 1.5 T,” *Medical Physics*. 1985.

[53] J. Tropp, “The theory of the bird-cage resonator,” *J. Magn. Reson.*, vol. 82, no. 1, pp. 51–62, Mar. 1989.

[54] P. A. Bottomley *et al.*, “Humanin vivo phosphate metabolite imaging with31P NMR,” *Magn. Reson. Med.*, vol. 7, no. 3, pp. 319–336, Jul. 1988.

[55] J. T. Vaughan *et al.*, “Detunable transverse electromagnetic (TEM) volume coil for high-field NMR,” *Magn. Reson. Med.*, vol. 47, no. 5, pp. 990–1000, 2002.

[56] C. E. Hayes, “The development of the birdcage resonator: A historical perspective,” *NMR in Biomedicine*. 2009.

[57] J. J. Ackerman, T. H. Grove, G. G. Wong, D. G. Gadian, and G. K. Radda, “Mapping of metabolites in whole animals by 31P NMR using surface coils.,” *Nature*, vol. 283, no. 5743, pp. 167–70, 1980.

[58] A. Haase, W. Hanicke, and J. Frahm, “The influence of experimental parameters in surface-coil NMR,” *J. Magn. Reson.*, vol. 56, no. 3, pp. 401–412, 1984.

[59] J. T. Vaughan and Griffiths John, *RF Coils for MRI*. 2012.

[60] C. E. . Hayes and L. Axel, “Noise performance of surface coil for magnetic resonance imaging (Hayes 1984).pdf,” *Medical Physics*, vol. 12, no. 5. pp. 604–607, Sep-1985.

[61] A. Kumar and P. Bottomley, “Optimized Quadrature Surface Coils incorporating Circular, Figure-8 loops, and Strips,” *Proc. Intl. Soc. Mag. Reson. Med*, vol. 15, no. c, p. 1049, 2007.

[62] H. Fujita, T. Zheng, X. Yang, M. J. Finnerty, and S. Handa, “RF Surface Receive Array Coils: The Art of an LC Circuit,” *J. Magn. Reson. Imaging*, vol. 38, no. 1, pp. 12–25, Jul. 2013.

[63] C. C. Guclu, E. Boskamp, T. Zheng, R. Becerra, and L. R. Blawat, “A Method for Preamplifier-Decoupling Improvement in Quadrature Phased-Array Coils,” *J. Magn. Reson. Imaging*, vol. 19, no. 2, pp. 255–258, 2004.

[64] P. B. Roemer, W. A. Edelstein, and C. E. Hayes, “The NMR Phased Array,” vol. 16, no. 2, pp. 192–225, 1990.

[65] C. von Morze *et al.*, “An eight-channel, nonoverlapping phased array coil with capacitive decoupling for parallel MRI at 3 T,” *Concepts Magn. Reson. Part B Magn. Reson. Eng.*, vol. 31B, no. 1, pp. 37–43, Feb. 2007.

[66] J. Jevtic, “Ladder networks for capacitive decoupling in phased-array coils,” *Proc. 9th Annu. Meet. ISMRM,* vol. 9, p. 10437, 2001.

[67] J. A. Nordmeyer-Massner, N. De Zanche, and K. P. Pruessmann, “Noise figure characterization of preamplifiers at NMR frequencies,” *J. Magn. Reson.*, vol. 210, no. 1, pp. 7–15, 2011.

[68] J. R. Corea *et al.*, “Screen-printed flexible MRI receive coils,” *Nat. Commun.*, vol. 7, p. 10839, 2016.

[69] J. R. Corea, P. B. Lechene, M. Lustig, and A. C. Arias, “Materials and Methods for Higher Performance Screen-Printed Flexible MRI Receive Coils,” *Magn. Reson. Med.*, vol. 00, pp. 1–9, 2016.

[70] K. P. McGee *et al.*, “Characterization and evaluation of a flexible MRI receive coil array for radiation therapy MR treatment planning using highly decoupled RF circuits,” *Phys. Med. Biol.*, 2018.

[71] B. Zhang, D. K. Sodickson, and M. A. Cloos, “A high-impedance detector-array glove for magnetic resonance imaging of the hand,” *Nat. Biomed. Eng.*, 2018.

[72] L. Li and C. H. Sotak, “An efficient technique for decoupling NMR transmit coils from surface-coil receivers,” *J. Magn. Reson.*, vol. 93, no. 1, pp. 207–213, Jun. 1991.

[73] P. M. Mellor and D. R. Checkley, “Active coil isolation in NMR imaging and spectroscopy using PIN diodes and tuned transmission line: a practical approach,” *Magma Magn. Reson. Mater. Physics, Biol. Med.*, vol. 3, no. 1, pp. 35–40, Mar. 1995.

[74] S. Kan, M. Fan, and J. Courtieu, “A single-coil triple resonance probe for NMR experiments,” *Rev. Sci. Instrum.*, vol. 51, no. 7, pp. 887–890, 1980.

[75] N. Woodhouse, J. M. Wild, E. J. R. van Beek, N. Hoggard, N. Barker, and C. J. Taylor, “Assessment of hyperpolarized 3 He lung MRI for regional evaluation of interventional therapy: A pilot study in pediatric cystic fibrosis,” *J. Magn. Reson. Imaging*, vol. 30, no. 5, pp. 981–988, Nov. 2009.

[76] G. Adriany and R. Gruetter, “A Half-Volume Coil for Efficient Proton Decoupling in Humans at 4 Tesla,” *J. Magn. Reson.*, no. 125, pp. 178–184, 1997.

[77] A. Asfour and V. Auboiroux, “A new dedicated double-tuned (100 MHz-27 MHz) volume RF coil actively-decoupled form a receive-only simple-tuned (27 MHz) coil: Application to the MRI experiments of hyperpolarized 129Xe in the rat brain,” in

Conference Record - IEEE Instrumentation and Measurement Technology Conference, 2008, pp. 945–950.

[78] A. Dabirzadeh and M. P. McDougall, “Trap design for insertable second-nuclei radiofrequency coils for magnetic resonance imaging and spectroscopy,” *Concepts Magn. Reson. Part B Magn. Reson. Eng.*, vol. 35, no. 3, pp. 121–132, 2009.

[79] M. Meyerspeer, E. S. Roig, R. Gruetter, and A. W. Magill, “An improved trap design for decoupling multinuclear RF coils,” *Magn. Reson. Med.*, vol. 72, no. 2, pp. 584–590, Aug. 2014.

[80] M. Rao, F. Robb, and J. M. Wild, “Dedicated receiver array coil for 1H lung imaging with same-breath acquisition of hyperpolarized 3He and 129Xe gas,” *Magn. Reson. Med.*, vol. 74, no. 1, pp. 291–299, 2015.

[81] M. Rao and J. M. Wild, “RF instrumentation for same-breath triple nuclear lung MR imaging of 1 H and hyperpolarized 3 He and 129 Xe at 1.5T,” *Magn. Reson. Med.*, vol. 75, no. 4, pp. 1841–1848, Apr. 2016.

[82] J. F. Glockner, H. H. Hu, B. M. E. D. W, B. S. L. Angelos, and K. King, “Parallel MR Imaging : A User ’ s Guide 1,” vol. 55905, pp. 1279–1297, 2005.

[83] K. P. Pruessmann, M. Weiger, M. B. Scheidegger, and P. Boesiger, “SENSE sensitivity encoding for fast MRI,” *Magn. Reson. Med. Off. J. Soc. Magn. Reson. Med. / Soc. Magn. Reson. Med.*, vol. 42, no. 5, pp. 952–962, 1999.

[84] M. A. Griswold *et al.*, “Generalized Autocalibrating Partially Parallel Acquisitions (GRAPPA),” *Magn. Reson. Med.*, vol. 47, no. 6, pp. 1202–1210, 2002.

[85] D. K. Sodickson, M. A. Ohliger, R. Lattanzi, and G. C. Wiggins, “Coil Array Design for Parallel Imaging: Theory and Applications,” *eMagRes*, 2011.

[86] R. F. Lee, G. Johnson, R. L. Grossman, B. Stoeckel, R. Trampel, and G. McGuinness, “Advantages of parallel imaging in conjunction with hyperpolarized helium - A new approach to MRI of the lung,” *Magn. Reson. Med.*, vol. 55, no. 5, pp. 1132–1141, 2006.

[87] D. J. Larkman and R. G. Nunes, “Parallel magnetic resonance imaging,” *Phys. Med. Biol.*, vol. 52, no. 7, 2007.

[88] M. Weiger, K. P. Pruessmann, and P. Boesiger, “2D SENSE for faster 3D MRI,” *Magn. Reson. Mater. Physics, Biol. Med.*, 2002.

[89] J. R. MacFall *et al.*, “Human lung air spaces: potential for MR imaging with hyperpolarized He-3.,” *Radiology*, vol. 200, no. 2, pp. 553–558, Aug. 1996.

[90] M. S. Albert *et al.*, “Biological magnetic resonance imaging using laser-polarized 129Xe,” *Nature*, vol. 370, no. 6486, pp. 199–201, Jul. 1994.

[91] M. Ebert *et al.*, “Nuclear magnetic resonance imaging with hyperpolarised helium-3,” *Lancet*, vol. 347, no. 9011, pp. 1297–1299, May 1996.

[92] C. H-f *et al.*, “Lung MRI with hyperpolarised gases: current & future clinical perspectives,” 2021.

[93] J. M. Wild, H. Marshall, M. Bock, L. R. Schad, P. M. Jakob, M. Puderbach, F. Molinari, E.J.R. Van Beek, J. Biederer, "MRI of the Lungs 1/3: methods," *Insights Imaging*, vol. Volume 3, no. Issue 4, p. pp 345--353, 2012.

[94] H. Marshall *et al.*, "Direct visualisation of collateral ventilation in COPD with hyperpolarised gas MRI," *Thorax*, vol. 67, no. 7, pp. 613–617, 2012.

[95] J. P. Mugler and T. A. Altes, "Hyperpolarized 129 Xe MRI of the human lung," *J. Magn. Reson. Imaging*, vol. 37, no. 2, pp. 313–331, Feb. 2013.

[96] J. P. Mugler *et al.*, "MR imaging and spectroscopy using hyperpolarized 129Xe gas: Preliminary human results," *Magn. Reson. Med.*, vol. 37, no. 6, pp. 809–815, 1997.

[97] N. J. Stewart *et al.*, "Experimental validation of the hyperpolarized 129Xe chemical shift saturation recovery technique in healthy volunteers and subjects with interstitial lung disease," *Magn. Reson. Med.*, vol. 74, no. 1, pp. 196–207, 2015.

[98] J. M. Wang *et al.*, "Using hyperpolarized 129Xe MRI to quantify regional gas transfer in idiopathic pulmonary fibrosis," *Thorax*, vol. 73, no. 1, pp. 21–28, 2018.

[99] G. Norquay, G. Leung, N. J. Stewart, G. M. Tozer, J. Wolber, and J. M. Wild, "Relaxation and exchange dynamics of hyperpolarized 129Xe in human blood," *Magn. Reson. Med.*, vol. 74, no. 2, 2015.

[100] M. A. Bouchiat, T. R. Carver, and C. M. Varnum, "Nuclear Polarization in He3 Gas Induced by Optical Pumping and Dipolar Exchange," *Phys. Rev. Lett.*, vol. 5, no. 8, pp. 373–375, Oct. 1960.

[101] F. D. Colegrove, L. D. Schearer, and G. K. Walters, "Polarization of He3 Gas by Optical Pumping," *Phys. Rev.*, vol. 132, no. 6, pp. 2561–2572, Dec. 1963.

[102] J. Leawoods, D. Yablonskiy, B. SAAM, DAVID S. GIERADA, and M. S. CONRADI, "Hyperpolarized 3He gas production and MR imaging of the lung," *Concepts Magn. Reson.*, vol. 13, no. 5, pp. 277–293, 2001.

[103] D. A. Barskiy *et al.*, "NMR Hyperpolarization Techniques of Gases," *Chemistry - A European Journal*, vol. 23, no. 4. pp. 725–751, 2017.

[104] T. G. Walker and W. Happer, "Spin-exchange optical pumping of noble-gas nuclei," *Rev. Mod. Phys.*, vol. 69, no. 2, pp. 629–642, Apr. 1997.

[105] S. R. Schaefer, G. D. Cates, and W. Happer, "Determination of spin-exchange parameters between optically pumped rubidium and 83Kr," *Phys. Rev. A*, vol. 41, no. 11, pp. 6063–6070, Jun. 1990.

[106] E. Babcock *et al.*, "Hybrid spin-exchange optical pumping of 3He.," *Phys. Rev. Lett.*, vol. 91, no. 12, p. 123003, Sep. 2003.

[107] G. D. Cates, F. R. J., A. S. . Barton, P. . Bogorad;, M. Gatzke, and and B. S. N. R.; Newbury, "Rb-129Xe spin-exchange rates due to binary and three-body collisions at high Xe pressures," *Phys. Rev. A*, vol. 45, no. 7, pp. 4631–4639, 1992.

[108] T. Meersmann and E. Brunner, *Hyperpolarized Xenon-129 Magnetic Resonance*. Cambridge: Royal Society of Chemistry, 2015.

[109] B. Driehuys, G. D. Cates, E. Miron, K. Sauer, D. K. Walter, and W. Happer, “High-volume production of laser-polarized 129 Xe,” *Appl. Phys. Lett.*, vol. 69, no. 12, pp. 1668–1670, Sep. 1996.

[110] M. S. Rosen, T. E. Chupp, K. P. Coulter, R. C. Welsh, and S. D. Swanson, “Polarized [sup 129]Xe optical pumping/spin exchange and delivery system for magnetic resonance spectroscopy and imaging studies,” *Rev. Sci. Instrum.*, vol. 70, no. 2, p. 1546, 1999.

[111] F. W. Hersman *et al.*, “Large Production System for Hyperpolarized129Xe for Human Lung Imaging Studies,” *Acad. Radiol.*, vol. 15, no. 6, pp. 683–692, 2008.

[112] T. Hughes-Riley *et al.*, “Cryogenics free production of hyperpolarized 129Xe and 83Kr for biomedical MRI applications,” *J. Magn. Reson.*, vol. 237, no. January 2014, pp. 23–33, 2013.

[113] G. Norquay, S. R. Parnell, X. Xu, J. Parra-Robles, and J. M. Wild, “Optimized production of hyperpolarized 129Xe at 2 bars for in vivo lung magnetic resonance imaging,” *J. Appl. Phys.*, vol. 113, no. 4, p. 044908, 2013.

[114] J. H. Ardenkjaer-Larsen *et al.*, “Increase in signal-to-noise ratio <10,000 times in liquid-state NMR,” *Proc. Natl. Acad. Sci.*, vol. 100, no. 18, pp. 10158–10163, 2003.

[115] H. Johannesson, S. Macholl, and J. H. Ardenkjaer-Larsen, “Dynamic Nuclear Polarization of [1-13C]pyruvic acid at 4.6 tesla,” *J. Magn. Reson.*, vol. 197, no. 2, pp. 167–175, 2009.

[116] J. Natterer and J. Bargon, “Para-Hydrogen Induced Polarization (PHIP),” *Prog. Nucl. Magn. Reson. Spectrosc.*, vol. 31, pp. 293–315, 1997.

[117] G. Norquay, “Large-scale production of highly-polarized 129Xe,” in *Proc. Intl. Soc. Mag. Reson. Med. 25*, 2017.

[118] A. Haase, J. Frahm, D. Matthaei, W. Hanicke, and K. D. Merboldt, “FLASH imaging. Rapid NMR imaging using low flip-angle pulses,” *J. Magn. Reson.*, vol. 67, no. 2, pp. 258–266, 1986.

[119] R. R. Ernst and W. A. Anderson, “Application of Fourier Transform Spectroscopy to Magnetic Resonance,” *Rev. Sci. Instrum.*, vol. 37, no. 1, pp. 93–102, Jan. 1966.

[120] N. J. Pelc, “Optimization of flip angle forT1dependent contrast in MRI,” *Magn. Reson. Med.*, vol. 29, no. 5, pp. 695–699, May 1993.

[121] M. Markl and J. Leupold, “Gradient echo imaging,” *J. Magn. Reson. Imaging*, vol. 35, no. 6, pp. 1274–1289, 2012.

[122] K. Scheffler and S. Lehnhardt, “Principles and applications of balanced SSFP techniques,” *Eur. Radiol.*, vol. 13, no. 11, pp. 2409–2418, 2003.

[123] O. Bieri and K. Scheffler, “Fundamentals of balanced steady state free precession MRI,” *Journal of Magnetic Resonance Imaging*, vol. 38, no. 1. pp. 2–11, 2013.

[124] J. P. Mugler, “Optimization of Gradient-Echo Sequences for Hyperpolarized Noble Gas MRI,” p. 1997, 1997.

[125] G. W. Miller, T. A. Altes, J. R. Brookeman, E. E. De Lange, and J. P. Mugler, “Hyperpolarized3He lung ventilation imaging with B1-inhomogeneity correction in a single breath-hold scan,” *Magn. Reson. Mater. Physics, Biol. Med.*, vol. 16, no. 5, pp. 218–226, 2004.

[126] J. M. Wild, M. N. J. Paley, M. Viallon, W. G. Schreiber, E. J. R. van Beek, and P. D. Griffiths, “k-Space filtering in 2D gradient-echo breath-hold hyperpolarized3He MRI: Spatial resolution and signal-to-noise ratio considerations,” *Magn. Reson. Med.*, vol. 47, no. 4, pp. 687–695, Apr. 2002.

[127] J. M. Wild, M. N. J. Paley, M. Viallon, W. G. Schreiber, E. J. R. Van Beek, and P. D. Griffiths, “k-space filtering in 2D gradient-echo breath-hold hyperpolarized3He MRI: Spatial resolution and signal-to-noise ratio considerations,” *Magn. Reson. Med.*, vol. 47, no. 4, pp. 687–695, 2002.

[128] M. H. Deppe and J. M. Wild, “Variable flip angle schedules in bSSFP imaging of hyperpolarized noble gases,” *Magn. Reson. Med.*, vol. 67, no. 6, pp. 1656–1664, 2012.

[129] J. M. Wild *et al.*, “Comparison between 2D and 3D gradient-echo sequences for MRI of human lung ventilation with hyperpolarized3He,” *Magn. Reson. Med.*, vol. 52, no. 3, pp. 673–678, Sep. 2004.

[130] H. Marshall, S. Ajraoui, M. H. Deppe, J. Parra-Robles, and J. M. Wild, “K-space filter deconvolution and flip angle self-calibration in 2D radial hyperpolarised 3He lung MRI,” *NMR Biomed.*, vol. 25, no. 2, pp. 389–399, 2012.

[131] H. E. Möller *et al.*, “MRI of the lungs using hyperpolarized noble gases,” *Magn. Reson. Med.*, vol. 47, no. 6, pp. 1029–1051, 2002.

[132] J. Wolber, A. Cherubini, A. S. K. Dzik-Jurasz, M. O. Leach, and A. Bifone, “Spin-lattice relaxation of laser-polarized xenon in human blood,” *Proc. Natl. Acad. Sci.*, vol. 96, no. 7, pp. 3664–3669, Mar. 1999.

[133] H. E. Möller, Z. I. Cleveland, and B. Driehuys, “Relaxation of hyperpolarized 129Xe in a deflating polymer bag,” *J. Magn. Reson.*, vol. 212, no. 1, pp. 109–115, Sep. 2011.

[134] W. Zheng, Z. I. Cleveland, H. E. Möller, and B. Driehuys, “Gradient-induced longitudinal relaxation of hyperpolarized noble gases in the fringe fields of superconducting magnets used for magnetic resonance,” *J. Magn. Reson.*, vol. 208, no. 2, pp. 284–290, Feb. 2011.

[135] X. Xu *et al.*, “Hyperpolarized 129Xe gas lung MRI-SNR and T2* comparisons at 1.5 T and 3 T,” *Magn. Reson. Med.*, vol. 68, no. 6, pp. 1900–1904, 2012.

[136] M. H. Deppe *et al.*, “Susceptibility effects in hyperpolarized 3He lung MRI at 1.5T and 3T,” *J. Magn. Reson. Imaging*, vol. 30, no. 2, pp. 418–423, 2009.

[137] B. Driehuys, G. P. Cofer, J. Pollaro, J. B. Mackel, L. W. Hedlund, and G. A. Johnson, “Imaging alveolar-capillary gas transfer using hyperpolarized 129Xe MRI,” *Proc Natl Acad Sci U S A*, vol. 103, no. 48, pp. 18278–18283, 2006.

[138] J. P. Mugler *et al.*, “MR imaging and spectroscopy using hyperpolarized 129Xe gas:

Preliminary human results," *Magn. Reson. Med.*, vol. 37, no. 6, pp. 809–815, 1997.

[139] K. Ruppert, J. R. Brookeman, K. D. Hagspiel, and J. P. Mugler, "Probing lung physiology with xenon polarization transfer contrast (XTC)," *Magn. Reson. Med.*, vol. 44, no. 3, pp. 349–357, Sep. 2000.

[140] I. Dregely *et al.*, "Hyperpolarized Xenon-129 gas-exchange imaging of lung microstructure: First case studies in subjects with obstructive lung disease," *J. Magn. Reson. Imaging*, vol. 33, no. 5, pp. 1052–1062, 2011.

[141] N. J. Stewart *et al.*, "Reproducibility of quantitative indices of lung function and microstructure from129Xe chemical shift saturation recovery (CSSR) MR spectroscopy," *Magn. Reson. Med.*, vol. 77, no. 6, pp. 2107–2113, 2017.

[142] S. H. Robertson *et al.*, "Uncovering a third dissolved-phase 129Xe resonance in the human lung: Quantifying spectroscopic features in healthy subjects and patients with idiopathic pulmonary fibrosis," *Magn. Reson. Med.*, vol. 78, no. 4, pp. 1306–1315, 2017.

[143] Z. I. Cleveland *et al.*, "Hyperpolarized 129Xe MR imaging of alveolar gas uptake in humans," *PLoS One*, vol. 5, no. 8, 2010.

[144] J. P. Mugler *et al.*, "Simultaneous magnetic resonance imaging of ventilation distribution and gas uptake in the human lung using hyperpolarized xenon-129.," *Proc. Natl. Acad. Sci. U. S. A.*, vol. 107, no. 50, pp. 21707–21712, Dec. 2010.

[145] S. S. Kaushik *et al.*, "Probing the regional distribution of pulmonary gas exchange through single-breath gas- and dissolved-phase 129Xe MR imaging.," *J. Appl. Physiol.*, vol. 115, no. 6, pp. 850–60, 2013.

[146] S. S. Kaushik *et al.*, "Single-breath clinical imaging of hyperpolarized 129xe in the airspaces, barrier, and red blood cells using an interleaved 3D radial 1-point Dixon acquisition," *Magn. Reson. Med.*, vol. 75, no. 4, pp. 1434–1443, 2016.

[147] G. J. Collier *et al.*, "Dissolved 129Xe lung MRI with four-echo 3D radial spectroscopic imaging: Quantification of regional gas transfer in idiopathic pulmonary fibrosis," *Magn. Reson. Med.*, vol. 85, no. 5, pp. 2622–2633, May 2021.

[148] G. Norquay, G. Leung, N. J. Stewart, G. M. Tozer, J. Wolber, and J. M. Wild, "Relaxation and exchange dynamics of hyperpolarized 129 Xe in human blood," *Magn. Reson. Med.*, vol. 74, no. 2, pp. 303–311, Aug. 2015.

[149] G. Norquay, G. Leung, N. J. Stewart, J. Wolber, and J. M. Wild, "129 Xe chemical shift in human blood and pulmonary blood oxygenation measurement in humans using hyperpolarized 129 Xe NMR," *Magn. Reson. Med.*, vol. 77, no. 4, pp. 1399–1408, Apr. 2017.

[150] M. S. Albert, D. F. Kacher, D. Balamore, A. K. Venkatesh, and F. A. Jolesz, "T1 of 129Xe in Blood and the Role of Oxygenation," *J. Magn. Reson.*, vol. 140, no. 1, pp. 264–273, Sep. 1999.

[151] M. Rao, N. J. Stewart, G. Norquay, P. D. Griffiths, and J. M. Wild, "High resolution spectroscopy and chemical shift imaging of hyperpolarized (129) Xe dissolved in the

human brain in vivo at 1.5 tesla.," *Magn. Reson. Med.*, vol. 75, no. 6, pp. 2227–34, 2016.

[152] M. Rao, N. J. Stewart, P. D. Griffiths, G. Norquay, and J. M. Wild, "Imaging Human Brain Perfusion with Inhaled Hyperpolarized 129Xe MR Imaging," *Radiology*, vol. (epub), pp. 1–7, 2017.

[153] J. Chacon-Caldera *et al.*, "Dissolved hyperpolarized xenon-129 MRI in human kidneys," *Magn. Reson. Med.*, vol. 83, no. 1, pp. 262–270, Jan. 2020.

[154] J. Chacon Caldera *et al.*, "Dynamic MRI of Hyperpolarized Xenon-129 Uptake in the Human Kidney Using a Dedicated Transmission-Only-Reception-Only Array at 3 Tesla," in *Proc. Intl. Soc. Mag. Reson. Med. 26* , 2018.

[155] M. A. Antonacci, L. Zhang, A. Burant, D. McCallister, and R. T. Branca, "Simple and robust referencing system enables identification of dissolved-phase xenon spectral frequencies," *Magn. Reson. Med.*, vol. 441, no. November 2017, pp. 431–441, 2017.

[156] G. T. Mussell *et al.*, "Xenon ventilation MRI in difficult asthma: Initial experience in a clinical setting," *ERJ Open Res.*, vol. 7, no. 3, pp. 10–19, 2021.

[157] G. Norquay, G. J. Collier, O. I. Rodgers, A. B. Gill, N. J. Screaton, and J. Wild, "Standalone portable xenon-129 hyperpolariser for multicentre clinical magnetic resonance imaging of the lungs," *Br. J. Radiol.*, p. 20210872, Jan. 2022.

[158] J. E. Roos, H. P. McAdams, S. S. Kaushik, and B. Driehuys, "Hyperpolarized Gas MR Imaging: Technique and Applications," *Magnetic Resonance Imaging Clinics of North America*, vol. 23, no. 2. pp. 217–229, 2015.

[159] R. L. Eddy and G. Parraga, "Pulmonary xenon-129 MRI: New opportunities to unravel enigmas in respiratory medicine," *Eur. Respir. J.*, vol. 55, no. 2, 2020.

[160] J. M. Wild *et al.*, "Simultaneous imaging of lung structure and function with triple-nuclear hybrid MR imaging," *Radiology*, vol. 267, no. 1, pp. 251–5, 2013.

[161] N. De Zanche, A. Yahya, F. E. Vermeulen, and P. S. Allen, "Analytical approach to noncircular section birdcage coil design: Verification with a cassinian oval coil," *Magn. Reson. Med.*, vol. 53, no. 1, pp. 201–211, 2005.

[162] M. C. Leifer, "Theory of the quadrature elliptic birdcage coil," *Magn. Reson. Med.*, vol. 38, no. 5, pp. 726–732, 1997.

[163] T. A. Riauka, N. F. De Zanche, R. Thompson, F. E. Vermeulen, C. E. Capjack, and P. S. Allen, "A numerical approach to non-circular birdcage RF coil optimization: Verification with a fourth-order coil," *Magn. Reson. Med.*, vol. 41, no. 6, pp. 1180–1188, 1999.

[164] N. De Zanche, N. Chhina, K. Teh, C. Randell, K. P. Pruessmann, and J. M. Wild, "Asymmetric quadrature split birdcage coil for hyperpolarized 3He lung MRI at 1.5T," *Magn. Reson. Med.*, vol. 60, no. 2, pp. 431–438, 2008.

[165] F. Wetterling *et al.*, "Whole body sodium MRI at 3T using an asymmetric birdcage resonator and short echo time sequence: first images of a male volunteer.," *Phys.*

Med. Biol., vol. 57, no. 14, pp. 4555–67, Jul. 2012.

[166] M. H. Deppe, J. Parra-Robles, H. Marshall, T. Lanz, and J. M. Wild, "A flexible 32-channel receive array combined with a homogeneous transmit coil for human lung imaging with hyperpolarized 3He at 1.5 T," *Magn. Reson. Med.*, vol. 66, no. 6, pp. 1788–1797, 2011.

[167] I. Dregely *et al.*, "32-channel phased-array receive with asymmetric birdcage transmit coil for hyperpolarized xenon-129 lung imaging," *Magn. Reson. Med.*, vol. 70, no. 2, pp. 576–583, 2013.

[168] K.-N. Kim *et al.*, "An Asymmetric Birdcage Coil for Small-animal MR Imaging at 7T," *Magn. Reson. Med. Sci.*, vol. 16, no. 3, pp. 253–258, 2017.

[169] N. De Zanche, N. Chhina, K. Teh, C. Randell, K. P. Pruessmann, and J. M. Wild, "Asymmetric quadrature split birdcage coil for hyperpolarized 3He lung MRI at 1.5T," *Magn. Reson. Med.*, vol. 60, no. 2, pp. 431–438, 2008.

[170] T. A. Riauka, N. F. De Zanche, R. Thompson, F. E. Vermeulen, C. E. Capjack, and P. S. Allen, "A numerical approach to non-circular birdcage RF coil optimization: Verification with a fourth-order coil," *Magn. Reson. Med.*, vol. 41, no. 6, pp. 1180–1188, Jun. 1999.

[171] N. De Zanche, A. Yahya, F. E. Vermeulen, and P. S. Allen, "Analytical approach to noncircular section birdcage coil design: Verification with a cassinian oval coil," *Magn. Reson. Med.*, vol. 53, no. 1, pp. 201–211, 2005.

[172] C. Puddu *et al.*, "An asymmetrical whole-body birdcage RF coil without RF shield for hyperpolarized 129Xe lung MR imaging at 1.5 T," *Magn. Reson. Med.*, vol. 86, no. 6, pp. 3373–3381, Dec. 2021.

[173] N. De Zanche, N. Chhina, K. Teh, C. Randell, K. P. Pruessmann, and J. M. Wild, "Asymmetric quadrature split birdcage coil for hyperpolarized 3 He lung MRI at 1.5T," *Magn. Reson. Med.*, vol. 60, no. 2, pp. 431–438, Aug. 2008.

[174] "IEC 60601-2-33:2010 Medical electrical equipment - Part 2-33: Particular requirements for the basic safety and essential performance of magnetic resonance equipment for medical diagnosis."

[175] J. A. Hou and Y. H. Wang, "A compact quadrature hybrid based on high-pass and low-pass lumped elements," *IEEE Microw. Wirel. Components Lett.*, vol. 17, no. 8, pp. 595–597, 2007.

[176] S. C. L. Deoni, "High-resolution T1 mapping of the brain at 3T with driven equilibrium single pulse observation of T1 with high-speed incorporation of RF field inhomogeneities (DESPOT1-HIFI)," *J. Magn. Reson. Imaging*, vol. 26, no. 4, pp. 1106–1111, Oct. 2007.

[177] A. Maunder, M. Rao, F. Robb, and J. M. Wild, "An 8-element Tx/Rx array utilizing MEMS detuning combined with 6 Rx loops for 19 F and 1 H lung imaging at 1.5T," *Magn. Reson. Med.*, vol. 84, no. 4, pp. 2262–2277, Oct. 2020.

[178] H. Gudbjartsson and S. Patz, "The rician distribution of noisy mri data," *Magn.*

Reson. Med., 1995.

[179] N. J. Stewart, G. Norquay, P. D. Griffiths, and J. M. Wild, “Feasibility of human lung ventilation imaging using highly polarized naturally abundant xenon and optimized three-dimensional steady-state free precession,” *Magn. Reson. Med.*, vol. 74, no. 2, pp. 346–352, 2015.

[180] F. C. Horn, M. Rao, N. J. Stewart, and J. M. Wild, “Multiple breath washout of hyperpolarized 129 Xe and 3 He in human lungs with three-dimensional balanced steady-state free-precession imaging,” *Magn. Reson. Med.*, vol. 77, no. 6, pp. 2288–2295, Jun. 2017.

[181] S. Wright and L. Wald, “Theory and Applications of Array Coils in MR Spectroscopy,” *NMR Biomed.*, vol. 10, pp. 394–410, 1997.

[182] M. H. Deppe, J. Parra-Robles, H. Marshall, T. Lanz, and J. M. Wild, “A flexible 32-channel receive array combined with a homogeneous transmit coil for human lung imaging with hyperpolarized 3He at 1.5 T,” *Magn. Reson. Med.*, vol. 66, no. 6, pp. 1788–1797, 2011.

[183] P. Kellman and E. R. McVeigh, “Image reconstruction in SNR units: A general method for SNR measurement,” *Magn. Reson. Med.*, vol. 54, no. 6, pp. 1439–1447, 2005.

[184] C. A. McKenzie, E. N. Yeh, M. A. Ohliger, M. D. Price, and D. K. Sodickson, “Self-calibrating parallel imaging with automatic coil sensitivity extraction,” *Magn. Reson. Med.*, 2002.

[185] J. M. Wild *et al.*, “Steady-state free precession with hyperpolarized 3He: Experiments and theory,” *J. Magn. Reson.*, vol. 183, no. 1, pp. 13–24, Nov. 2006.

[186] N. J. Stewart, G. Norquay, P. D. Griffiths, and J. M. Wild, “Feasibility of human lung ventilation imaging using highly polarized naturally abundant xenon and optimized three-dimensional steady-state free precession,” *Magn. Reson. Med.*, vol. 74, no. 2, pp. 346–352, Aug. 2015.

[187] C. Olchowy *et al.*, “The presence of the gadolinium-based contrast agent depositions in the brain and symptoms of gadolinium neurotoxicity-A systematic review,” *PLoS ONE*. 2017.

[188] D. C. Alsop *et al.*, “Recommended implementation of arterial spin-labeled perfusion MRI for clinical applications: A consensus of the ISMRM perfusion study group and the European consortium for ASL in dementia,” *Magn. Reson. Med.*, vol. 73, no. 1, pp. 102–116, Jan. 2015.

[189] Y. Shepelytskyi, F. T. Hane, V. Grynko, T. Li, A. Hassan, and M. S. Albert, “Hyperpolarized 129Xe Time-of-Flight MR Imaging of Perfusion and Brain Function,” *Diagnostics*, vol. 10, no. 9, pp. 14–18, 2020.

[190] V. Grynko, Y. Shepelytskyi, T. Li, A. Hassan, K. Granberg, and M. S. Albert, “Hyperpolarized 129Xe multi-slice imaging of the human brain using a 3D gradient echo pulse sequence,” *Magn. Reson. Med.*, vol. 86, no. 6, pp. 3175–3181, Dec. 2021.

[191] Y. Shepelytskyi, V. Grynko, T. Li, A. Hassan, K. Granberg, and M. S. Albert, “The

effects of an initial depolarization pulse on dissolved phase hyperpolarized 129Xe brain MRI," *Magn. Reson. Med.*, vol. 86, no. 6, pp. 3147–3155, Dec. 2021.

[192] J. A. De Zwart, P. J. Ledden, P. Kellman, P. Van Gelderen, and J. H. Duyn, "Design of a SENSE-optimized high-sensitivity MRI receive coil for brain imaging," *Magn. Reson. Med.*, vol. 47, no. 6, pp. 1218–1227, 2002.

[193] J. a de Zwart, P. van Gelderen, and J. H. Duyn, "Receive coil arrays and parallel imaging for functional magnetic resonance imaging of the human brain.," *Conf. Proc. IEEE Eng. Med. Biol. Soc.*, vol. 1, pp. 17–20, 2006.

[194] K. N. Kim *et al.*, "Quantitative assessment of phased array coils with different numbers of receiving channels in terms of signal-to-noise ratio and spatial noise variation in magnetic resonance imaging," *PLoS One*, vol. 14, no. 7, pp. 1–13, 2019.

[195] D. M. Pozar, *Microwave Engineering, 4th Edition*. Wiley, 2011.

[196] S. M. Wright and L. L. Wald, "Theory and application of array coils in MR spectroscopy," in *NMR in Biomedicine*, 1997.

[197] M. Rao, N. J. Stewart, G. Norquay, P. D. Griffiths, and J. M. Wild, "High resolution spectroscopy and chemical shift imaging of hyperpolarized 129 Xe dissolved in the human brain in vivo at 1.5 tesla," *Magn. Reson. Med.*, vol. 75, no. 6, pp. 2227–2234, Jun. 2016.

[198] M. R. Rao, N. J. Stewart, P. D. Griffiths, G. Norquay, and J. M. Wild, "Imaging Human Brain Perfusion with Inhaled Hyperpolarized 129 Xe MR Imaging," *Radiology*, vol. 286, no. 2, pp. 659–665, Feb. 2018.

[199] T. W. Redpath, "Noise correlation in multicoil receiver systems," *Magn. Reson. Med.*, vol. 24, no. 1, pp. 85–89, Mar. 1992.

[200] M. A. Ohliger and D. K. Sodickson, "An introduction to coil array design for parallel MRI," *NMR Biomed.*, vol. 19, no. 3, pp. 300–315, 2006.

[201] F. Hane, T. Li, J.-A. Plata, A. Hassan, K. Granberg, and M. Albert, "Inhaled Xenon Washout as a Biomarker of Alzheimer's Disease," *Diagnostics*, vol. 8, no. 2, p. 41, Jun. 2018.

[202] M. R. Rao, G. Norquay, N. J. Stewart, and J. M. Wild, "Measuring 129Xe transfer across the blood-brain barrier using MR spectroscopy," *Magn. Reson. Med.*, vol. 85, no. 6, pp. 2939–2949, Jun. 2021.

[203] Collier G.J., Schulte R.F., Rao M., Norquay G., Ball J., Wild J.M. Imaging gas-exchange lung function and brain tissue uptake of hyperpolarized 129 Xe using sampling density-weighted MRSI. Magn Reson Med. 2023 Jun;89(6):2217-2226